Nanoscale imaging of synapse morphology in the mouse neocortex in vivo by two-photon STED microscopy

Mirelle Jamilla Tamara ter Veer

université de BORDEAUX

THESIS FOR THE DEGREE OF

DOCTOR IN NEUROSCIENCE

FROM THE UNIVERSITY OF BORDEAUX

DOCTORAL SCHOOL OF LIFE SCIENCES AND HEALTH

SPECIALISATION: NEUROSCIENCE

By Mirelle Jamilla Tamara TER VEER

Nanoscale imaging of synapse morphology in the mouse neocortex *in vivo* by two-photon STED microscopy

Supervised by Prof. U. Valentin NÄGERL

Defended on November 25, 2016

Committee members:

M. Giovanni Marsicano, Directeur de Recherche	Chair
M. Bruno Weber, Professor	Reviewer
M. Fritjof Helmchen, Professor	Reviewer
M. Laurent Cognet, Directeur de Recherche au CNRS	Examiner
M. Detlev Schild, Professor	Examiner
M. Valentin Nägerl, Professor	PhD supervisor

université de BORDEAUX

THÈSE POUR OBTENIR LE GRADE DE

DOCTEUR EN NEUROSCIENCES

DE L'UNIVERSITÉ DE BORDEAUX

ÉCOLE DOCTORALE SCIENCES DE LA VIE ET DE LA SANTÉ

SPÉCIALITÉ: NEUROSCIENCES

Par Mirelle Jamilla Tamara TER VEER

Imagerie nanométrique de la morphologie synaptique dans le néocortex de souris *in vivo* par microscopie deux-photon STED

Sous la direction du Pr. U. Valentin NÄGERL

Soutenue le 25 Novembre, 2016

Membres du jury:

M. Giovanni Marsicano, Directeur de Recherche	Président
M. Bruno Weber, Professeur	Rapporteur
M. Fritjof Helmchen, Professeur	Rapporteur
M. Laurent Cognet, Directeur de Recherche au CNRS	Examinateur
M. Detlev Schild, Professeur	Examinateur
M. Valentin Nägerl, Professeur	Directeur de Thèse

SUMMARY

Nanoscale imaging of synapse morphology in the mouse neocortex *in vivo* by two-photon STED microscopy

Abstract:

The brain is a complex organ consisting of neurons and non-neuronal cells. Communication between neurons takes place via synapses, whose morphological remodeling is thought to be crucial for information processing and storage in the mammalian brain. Recently, this neuro-centric view of synaptic function has evolved, also taking into account the glial processes in close vicinity of the synapse. However, as their structure is well below the spatial resolution of conventional light microscopy, progress in investigating them in a physiological environment, the intact brain, has been impeded. Indeed, little is known on the nanoscale morphological variations of dendritic spines, the interaction with glial processes, and how these affect synaptic transmission *in vivo*.

Here, we aim to visualize the dynamic nano-morphology of dendritic spines in mouse somatosensory cortex *in vivo*. We implemented super-resolution 2P-STED time-lapse imaging, which allows for high spatial resolution and deep tissue penetration, in anesthetized mice, and show that the nano-morphology of spines is diverse, variable, but on average stable, and that differences in spine morphology can have an effect on spine biochemical compartmentalization *in vivo*. Moreover, implementation of dual color *in vivo* super-resolution imaging and a novel astrocytic labeling approach provided the first steps towards nanoscale characterization of neuron-glia interactions *in vivo*.

These findings bring new insights in synapse dynamics at the nanoscale *in vivo*, and our methodological endeavors help pave the way for a better understanding of how nanoscale aspects of spine morphology and their dynamics might contribute to brain physiology and animal behavior.

Keywords:
Super-resolution microscopy, Two-Photon (2P-) STED microscopy, *in vivo* brain preparation, dendritic spines, FRAP, spine compartmentalization, dual color imaging, glial processes

Research unit:
Interdisciplinary Institute for Neuroscience – CNRS UMR5297
146 rue Léo Saignat
33077 Bordeaux Cedex

Imagerie nanométrique de la morphologie synaptique dans le néocortex de souris *in vivo* par microscopie deux-photon STED

Résumé:

Le cerveau est un organe complexe composé de neurones et des cellules non-neuronales. La communication entre les neurones a lieu via les synapses, dont le remodelage morphologique est considéré essentiel pour le traitement et le stockage des informations dans le cerveau des mammifères. Récemment, ce point de vue neuro-centrée de la fonction synaptique a évolué, en prenant également en compte les processus gliales à proximité immédiate de la synapse. Cependant, comme leur structure est bien en deçà de la résolution spatiale de la microscopie optique conventionnelle, les progrès dans les enquêtes dans leur environnement physiologique, le cerveau intact, a été entravée. En effet, on sait peu sur les variations nanométriques de la morphologie des épines dendritiques et l'interaction avec les processus gliales, et, finalement, comment elles affectent la transmission synaptique *in vivo*.

Dans cette thèse, nous cherchons à visualiser la dynamique de la nano-morphologie des épines dendritiques et les processus gliales dans le cortex à tonneaux de souris *in vivo*. Nous avons donc mis en place l'imagerie super-résolution 2P-STED en temps réel, ce qui permet une haute résolution spatiale et la pénétration profonds des tissus, chez la souris anesthésiée *in vivo*. Nous montrons que la nano-morphologie des épines est diversifiée, variable, mais globalement stable, et que les différences dans la morphologie des épines peut avoir un effet sur leur compartimentation *in vivo*. En outre, la mise en œuvre de l'imagerie super-résolution en double couleur *in vivo* et le développement d'une approche de marquage astrocytaire, nous a permis de fournir la caractérisation à l'échelle nanométrique des interactions neurone-glie.

Ces résultats apportent un aperçu sans précédent dans la dynamique de la synapse à l'échelle nanométrique *in vivo*, et ouvrir la voie à une meilleure compréhension de la façon dont les réarrangements morphologiques des synapses contribuent à la physiologie du cerveau.

Mots clés:
Microscopie super résolution, microscopie à deux photons (2P) et STED, la préparation *in vivo* du cerveau, épines dendritiques, FRAP, compartimentation des épines, imagerie double couleur, processus gliales

Unité de recherche :
Institut Interdisciplinaire de Neurosciences – CNRS UMR5297
146 rue Léo Saignat
33077 Bordeaux Cedex

CURRICULUM VITAE Mirelle Jamilla Tamara ter Veer

Education and degrees

2013 Msc in *Neuroscience*, Faculty of Earth and Life Sciences at the VU University Amsterdam

2011 Bsc in *Medische Natuurwetenschappen*, Faculty of Exact Sciences at the VU University Amsterdam.

Professional appointments

2013 - 2016 PhD student via the ENC network, both in the Interdisciplinary Institute for Neuroscience, UMR 5297 CNRS / Université Bordeaux Segalen, and in the Brain Research Institute , University of Zurich.

Communications

Posters

2016 July Mirelle J.T. ter Veer, T. Pfeiffer, P. Bethge, J. Angibaud, M. Arizono, F. Helmchen, and U.V. Nägerl, *Two photon-STED microscopy to visualize glial cells and dendritic spines in mouse neocortex* in vivo. Poster at the 19th FENS forum in Copenhagen, Denmark

2016 June Mirelle J.T. ter Veer, T. Pfeiffer, P. Bethge, J. Angibaud, M. Arizono, F. Helmchen, and U.V. Nägerl, *Two photon-STED microscopy to visualize glial cells and dendritic spines in mouse neocortex* in vivo. Poster at the 3rd ENCODS meeting in Helsingør, Denmark

2016 June Thomas Pfeiffer, Mirelle J.T. ter Veer, V.V.G. Krishna Inavalli, and U. Valentin Nägerl, *Visualizing microglia-synapse interactions using two-photon STED microscopy*. Poster at the Jacques Monod conference in Roscoff (Brittany), France

2015 Oct. Thomas Pfeiffer, Mirelle J.T. ter Veer, Elena Avignone, and U. Valentin Nägerl, *The induction of hippocampal long-term potentiation increases the motility of microglial processes and their engagement with dendritic spines*. Poster at the SfN meeting in Chicago, USA

2015 Sept. TER VEER Mirelle J.T., PFEIFFER Thomas, BETHGE Philipp, ANGIBAUD Julie, ARIZONO Misa, HELMCHEN Fritjof, and NÄGERL U Valentin, *Two-photon STED imaging of synapses and their glial partners* in vivo. Poster at the GliSyn meeting in Bordeaux, France.

2015 April Mirelle J.T. ter Veer, T. Pfeiffer, P. Bethge, J. Angibaud, M. Arizono, F. Helmchen, and U.V. Nägerl, *2P-STED imaging of synapses and their glial partners in vivo*. Poster at the ENC annual meeting in Coimbra, Portugal

2015 April Mirelle J.T. ter Veer, T. Pfeiffer, P. Bethge, J. Angibaud, M. Arizono, F. Helmchen, and U.V. Nägerl, *2P-STED imaging of synapses and their glial partners in vivo*. Poster at the 2nd ENCODS meeting in Sesimbra, Portugal

2014 July Mirelle J.T. ter Veer, Philipp Bethge, Fritjof Helmchen, U. Valentin Nägerl, *STED microscopy of dendritic spines in vivo*. Poster at the annual meeting of the ENC network in Milan, Italy.

Oral communications

2016 June *2P-STED microscopy* in vivo – *nanoscale investigation of the morphology of dendritic spines and their glial partners*. Pecha-Kucha at the ENC annual meeting in Helsingør, Denmark.

2015 May *Imaging synapses and their glial partners at nanoscale resolution **in vivo***. Oral communication at the monthly meeting of the Interdisciplinary Institute for Neuroscience in Bordeaux, France.

2015 April *Imaging synapses and their glial partners at nanoscale resolution in vivo*. Oral report at the ENC annual meeting in Coimbra, Portugal.

2014 July *2P-STED microscopy of the (tripartite) synapse **in vivo***. Pecha-Kucha at the ENC annual meeting in Milan, Italy.

Honours

2013 – 2016 Erasmus Mundus Joint Doctorate fellowship within the ENC network
2015 Selected for best poster at the Journee d'Ecole Doctorale in Arcachon, France.
2015 Selected for best poster at the IINS retreat in Lacanau, France
2015 Award for best oral presentation at the ENC annual meeting in Coimbra, Portugal
2015 Travel grant to attend ENCODS 2015 in Lisbon and Sesimbra, Portugal

Publications:

(PhD). ter Veer MJT, Pfeiffer T, Nägerl UV (2016), Two-photon STED microscopy for nanoscale imaging of neural morphology *in vivo*, Springer - Methods in Molecular Biology, in preparation

(Msc). Schotten S, Meijer M, Walter AM, Huson V, Mamer L, Kalogreades L, Ter Veer M, Ruiter M, Brose N, Rosenmund C, Sørensen JB, Verhage M, Cornelisse LN. (2015), Additive effects on the energy barrier for synaptic vesicle fusion cause supralinear effects on the vesicle fusion rate, Elife, 4, doi: 10.7554/eLife.05531. Erratum in Elife. 2015;4. doi: 10.7554/eLife.09036

(Bsc). van Oort B, ter Veer MJ, Groot ML, van Stokkum IH. (2012), Excited state proton transfer in strongly enhanced GFP (sGFP2), Phys Chem Chem Phys, 14 (25), 8852 – 8858.

Extracurricular Activities

2015-2016	Coordinator of the Organizing Committee, and main organizer, of the European Neuroscience Conference by/for Doctoral Students (ENCODS2016) in Helsingør, Denmark.
2015	Jury member for master student presentations at the NBA symposium in Bordeaux, France.
2015	Organizer of non-scientific activities for IINS retreat in Lacanau, France.
2013-2015	Member of PhD student get together and institute non-scientific gatherings organization in Bordeaux, France.

Languages

Native: *Dutch*
Fluent: *English, French*
Moderate: *German*
Basic: *Spanish*

Acknowledgements

This work was conducted at the Interdisciplinary Institute for Neuroscience (UMR 5297 CNRS) in Bordeaux in the group of Prof. U. Valentin Nägerl from September 2013 until September 2016.

First of all, I would like to thank my supervisor, Prof. U. Valentin Nägerl, for giving me the opportunity to carry out my PhD work in his lab with funding support from the ENC-Network. I am particularly thankful for the support as well as independence he granted me during these exciting three years.

I would like to thank the committee members for the evaluation of this work, Prof. Bruno Weber and Prof. Fritjof Helmchen for their written report of my PhD thesis, Dr. Laurent Cognet and Prof. Dr. med. Dr. rer. nat. Detlev Schild for their examination, and Dr. Giovanni Marsicano for serving as president of the thesis committee.

A special thanks to my fellow “puppy” Thomas Pfeiffer, with whom I started this adventure of getting an academic degree, helped me constructing my social life in Bordeaux, and joint me on our (hiking) trip to the top of the mountain: the PhD title. I also wish to thank former members of the team: Jan Tønnesen for his advice on the FRAP approach and analysis, Philipp Bethge for training me on the 2P-STED setup; Ronan Chereau for his advices and explanations on STED-microscopy and analysis; Martin Lenz for his great explanations on optics and computer issues; and Aude Panatier for very helpful discussions.

A lot of gratitude for Thomas and the other current members of the team, especially Ezequiel Saraceno for not only supporting me scientifically but also mentally, as well as Misa Arizono for the fruitful discussions about astrocytes and work-strategies. I would like to thank Julie Angibaud for the technical and mental support. And last, but therefore not less, thanks to the other members of the team: Lasani Wijetunge and Krishna Inavalli.

My gratitude also goes out to Prof. Arjen Brussaard and Maaike Leusden, the director and secretary of the ENC network, respectively, for their support in my decision to organize the PhD conference ENCODS2016 together with Amber Kerkhofs. She deserves a special word here as well for sharing the enthusiasm about organizing a European conference within a year, a crazy idea, which became a very successful event!

I would here also like to acknowledge Luigi Bellochio, who introduced me to stereotactic injections, and Wenrui Liu, I-Wen Chen, and Jill Stobart who advised me on the *in vivo* strategies. Thanks to all people involved in the animal care-taking, and of course all the mice who sacrificed their lives for my project.

Many thanks as well for Corey Butler for his friendship in- and outside of the lab, he is the best person one could wish for to meet. Also special thanks to Julien Dupuis as my local tutor, and of course, thanks to all the members of the institute who made working here a pleasure!

My final appreciation goes to those who have supported me through many difficult episodes of my life, as well as this adventure: my family, in particular Arnold, Joke, Jessica and Natasja; and my best friend Annelieke.

TABLE OF CONTENT

SUMMARY..... I

Curriculum Vitae..... III

Acknowledgements..... VI

TABLE OF CONTENT..... 1

List of Figures..... 4

ABBREVIATIONS..... 6

Résumé détaillé en français..... 7

INTRODUCTION..... 11

1 Brain structure and function..... 12

1.1 The somatosensory cortex..... 12

1.2 Cellular structures of the brain..... 13

1.2.1 Neurons..... *13*

1.2.2 The synapse and synaptic communication..... *14*

1.2.3 Glial cells..... *16*

1.2.3.1 Astrocytes..... 16

1.3 The tripartite synapse..... 18

2 Dendritic spine morphology and physiology..... 21

2.1 Spine morphology described by ultrastructural studies..... 21

2.2 Structural plasticity of dendritic spines..... 22

2.3 Spine compartmentalization..... 25

3 STED microscopy..... 30

3.1 Basic principles of fluorescence microscopy..... 30

3.2 Confocal and two-photon excitation fluorescence microscopy..... 31

3.2.1 Absorption and scattering of light in thick tissue..... *32*

3.2.2 Optical aberrations..... *33*

3.3 Super-resolution approaches and the principle of 2P-STED microscopy. 34

3.4 Development of STED as imaging modality in the life sciences..... 37

3.5 STED microscopy *in vivo*..... 39

4 AIMS…… 40

5 MATERIALS AND METHODS…… 41

5.1 Animals…….. 41

5.2 *In vivo* surgery – window implantation…… 41

5.3 Viral infection…… 42

5.3.1 Synthesis of constructs and viral particles…… 42

5.3.2 Stereotactic injection…….. 42

5.4 Immunohistochemistry and confocal imaging…….. 43

5.5 Upright two-photon STED setup…… 43

5.6 Image acquisition…… 44

5.6.1 2P-STED imaging of dendritic spines…… 44

5.6.2 Dual color 2P-STED experiments and imaging astrocytes alone….. 45

5.6.3 FRAP experiments on dendritic spines…… 45

5.7 Image analysis…….. 46

5.7.1 Analysis of spine morphology…….. 46

5.7.2 Analysis of FRAP experiments…… 46

5.7.3 Deconvolution of astrocyte images…… 47

5.8 Statistics…… 47

6 RESULTS…….. 48

6.1 Establishment of *in vivo* 2P-STED microscopy…… 49

6.1.1 Point-spread function and resolution of the 2P-STED microscope.. 49

6.1.2 Performance of the 2P-STED microscope in acute slices…… 52

6.1.3 Optimization of in vivo preparation…….. 53

6.1.4 Performance of the 2P-STED microscope in vivo…… 54

6.1.5 Conclusion…… 60

6.2 *In vivo* 2P-STED microscopy to study the nanoscale morphology of dendritic spines …… 61

6.2.1 Quantitative analysis of spine morphology in vivo at the nanoscale.61

6.2.2 Analysis of morphological dynamics of spines using STED time-lapse imaging…….. 63

6.2.3 Biochemical and electrical compartmentalization of spines in vivo.. 66

6.2.4 Conclusion…… 71

6.3 Further applications of *in vivo* 2P-STED microscopy……. 72

6.3.1 Validating the capability of the 2P-STED setup to perform dual color imaging in vivo…… 72

6.3.2 The tripartite synapse in vivo…… 73

6.3.2.1 Development of an astrocytic label suitable for STED microscopy…….. 73

6.3.2.2 2P-STED microscopy as a tool to study tripartite synapse in vivo……..77

6.3.3 Conclusion…… 78

7 DISCUSSION…….. 81

7.1 Summary of the findings…… 81

7.2 Improvements of the *in vivo* STED approach as a tool in neuroscience… 83

7.2.1 Optimization of the preparation…… 84

7.2.2 Adding optical imaging methods to study brain cell physiology... 85

7.2.3 Optimization of the setup…… 87

7.3 Imaging dendritic spine morphology and compartmentalization *in vivo*… 88

7.3.1 Resolving spine morphology at the nanoscale in vivo…….. 88

7.3.2 Dynamics of spine morphological parameters in vivo…….. 89

7.3.3 Spine morphological parameters' link to spine compartmentalization in vivo…….. 90

7.4 Studying neuron-glia interactions *in vivo*……92

7.5 Outlook for 2P-STED microscopy as an imaging tool in neuroscience…… 93

7.6 Concluding remarks…….. 95

REFERENCES…… 96

APPENDICES…… 115

Appendix 1 – Springer – Methods in Molecular Biology manuscript…….. 115

Appendix 2 – Time lines of experiments…… 145

List of Figures

Figure 1: The somatosensory cortex of mice..... 12
Figure 2: Schematic model of the glutamatergic excitatory synapse..... 15
Figure 3: Schematic of cellular structures in the brain..... 16
Figure 4: The well-established homeostatic functions of the astrocyte..... 17
Figure 5: Schematic showing the proposed lateral astrocyte synaptic regulation..... 19
Figure 6: The concept "tripartite synapse" and its signalling pathways..... 20
Figure 7: Variation in dendritic spine morphology..... 22
Figure 8: Spine dynamics at different timescales..... 23
Figure 9: Experience-dependent spine plasticity in the adult neocortex..... 25
Figure 10: Compartmentalization in dendritic spines..... 28
Figure 11: Energy levels and transitions of a fluorophore..... 30
Figure 12: Reduction of refractive index mis-match by a silicon-oil objective while imaging through a glass coverslip..... 34
Figure 13: The 2P-STED principle..... 36
Figure 14: Representation *in vivo* surgery and imaging..... 42
Figure 15: Schematic of the setup..... 44
Figure 16: Schematic of spine analysis plugin..... 46
Figure 17: Beam profiles through a glass coverslip..... 50
Figure 18: Performance 2P-STED microscope, water versus silicon-oil objective..... 51
Figure 19: Resolution improvement with 2P-STED in depth..... 52
Figure 20: Imaging dendritic spines over time in acute slices..... 52/53
Figure 21: Signal intensities over depth..... 55
Figure 22: Signal intensities over time..... 56
Figure 23: Performance 2P-STED over depth and time *in vivo*..... 57
Figure 24: Negligible direct excitation by STED-light..... 58
Figure 25: Imaging spine structure *in vivo* with the silicon-oil objective..... 58
Figure 26: Morphological parameters of dendritic spines imaged with a silicon-oil objective..... 59
Figure 27: Spatial resolution improvement with 2P-STED microscopy..... 61
Figure 28: Spine morphological parameters span a broad range..... 62

Figure 29: Spine morphological parameters are variable but on average stable…….. 64
Figure 30: Spine morphological parameters investigated at higher temporal resolution show lower variability…… 65
Figure 31: Spine morphology and biochemical compartmentalization *in vivo*…… 67
Figure 32: Spine morphology and spine compartmentalization…….. 69
Figure 33: Spine neck resistance and spine morphological parameters…….. 70
Figure 34: Validation setup – two color 2P-STED microscopy *in vivo*…….. 72
Figure 35: Testing and validating viral labelling approach for astrocytes……..74
Figure 36: Validation of vimentin antibody……..75
Figure 37: Establishment of an astrocytic label for 2P-STED microscopy *in vivo*…….. 76
Figure 38: Bleaching of astrocytic label…… 77
Figure 39: Imaging of dendritic spines and astrocytes labelled with cytosolic GFP…… 78
Figure 40: Astrocytic coverage of neuronal processes visualized with membrane bound Clover as label for astrocytes…… 79/80
Figure 41: X-ray images showing boney structures that could be used to head-fix a mouse…… 84
Figure 42: A cranial window with PDMS……85
Figure 43: Attenuation of electrical signals through spines……92
Figure 44: The quad-partite synapse and its modifications in depression…… 95

ABBREVIATIONS

2P	Two-photon
AAV	Adeno-associated virus
APD	Avalanche photodiode
Ca^{2+}	Calcium
CNS	Central nervous system
CV	Coefficient of variation
DM	Dichroic mirror
EM	Electron microscopy
EOM	Electrical optical modulator
FOV	Field of view
FRAP	Fluorescent recovery after photo bleaching
FWHM	Full width at half-maximum
GFAP	Glial fibrillary acidic protein
GFP	Green fluorescent protein
λ	wavelength
MIP	Maximum intensity projection
NA	Numerical aperture
OPO	Optical parametric oscillator
PMT	Photomultiplier tube
PSF	Point spread function
$R_{neck,xxx}$	Neck resistance, estimated on morphology or diffusion
ROI	Region of interest
STED	Stimulated emission depletion
τ	Time constant
TEM_{00}	Gaussian beam profile
WT	Wild type
YFP	Yellow fluorescent protein

Résumé détaillé en français

Le cerveau est un organe complexe et compartimenté constitué de neurones et de cellules gliales adaptant constamment leurs propriétés fonctionnelles en réponse à des stimuli environnementaux. Cette dynamique et la communication cellulaire a lieu principalement au niveau des synapses, qui sont formées par des boutons axonales présynaptiques et des épines dendritiques postsynaptiques des neurones. Il a été montré que ces structures présentent une morphologie variable et que la morphologie des épines jouerait un rôle essentiel dans le fonctionnement synaptique. En outre, les cellules gliales peuvent également interagir via de fins prolongements avec les synapses. Malheureusement, l'étude des synapses, ainsi que leurs partenaires gliaux, est souvent entravée par leur petite taille et l'inaccessibilité optique par microscopie optique conventionnelle limitée par la diffraction de la lumière. Cependant, comprendre les propriétés nanométriques structurelles des épines dendritiques, permettrait de définir leurs propriétés biochimiques et électriques, mais également de comprendre leur régulation par les cellules gliales. Le développement récent de la microscopie d'excitation deux photons avec déplétion par émission stimulée (2P-STED) permet de contourner la barrière de diffraction de la microscopie optique conventionnelle et aide ainsi à la pénétration des tissus profonds, permettant l'étude des neurones et des structures gliales à l'échelle nanométrique dans le tissu cérébral *in vivo*.

Comme décrit précédemment, en raison du manque de résolution dans les approches d'imagerie des tissus, peu de choses sont connues sur l'effet des changements de la morphologie des épines et des prolongements gliaux sur la physiologie des synapses. La transmission synaptique est affectée par les changements morphologiques des épines mais aussi des prolongements astrocytaires. Il devient donc important de développer une approche super résolutive pour élucider la dynamique de ces changements.

Objectifs

Pour étudier la dynamique morphologique des épines dendritiques ainsi que leur compartimentation dans le cortex à tonneaux de souris vivantes, j'ai combiné la microscopie 2P-STED super résolutive avec la technologie 2P-FRAP *in vivo*. D'autre part, j'ai développé un marquage stable des cellules gliales, adapté pour l'imagerie STED *in vivo*, que j'ai associé à l'utilisation du microscope 2P-STED assemblé sur mesure.

En utilisant la microscopie 2P-STED *in vivo*, nous surmontons la limitation de résolution liée à la diffraction de la lumière afin d'étudier la morphologie des épines et leurs proximités avec les prolongements gliaux à l'échelle nanométrique dans le cortex à tonneaux de souris anesthésiées.

Nous présumons que la morphologie des épines dendritiques est variable à l'échelle nanométrique *in vivo* et que ces changements ont une incidence sur la compartimentation des épines. De plus, en raison du rôle supposé des cellules gliales dans la plasticité synaptique, nous nous sommes également intéressés à l'interaction neurone-glie au niveau subcellulaire.

Les principaux objectifs de ma thèse étaient donc les suivants:

1) Mettre au point la microscopie super résolutive *in vivo* dans le cortex à tonneaux de souris.

2) Examiner à l'échelle nanométrique la dynamique morphologique des épines dendritiques et la relation entre la morphologie des épines et leur compartimentation *in vivo* par imagerie en temps réel dans des conditions basales.

3) Mettre au point l'imagerie super résolutive deux couleurs *in vivo* au niveau de l'interaction épines-glie et tester la faisabilité de notre approche en imageant la structure de la synapse tripartite *in vivo*.

Les différents sujets seront abordés dans le reste de la thèse comme suit: (i) Partie 1 décrit l'élaboration du microscope 2P- STED *in vivo* dans notre laboratoire et détaille le microscope 2P-STED et son application en tant qu'outil pour l'imagerie des épines dendritiques *ex* et *in vivo*; (ii) Partie 2 couvre la morphologie à l'échelle nanométrique des épines dendritiques, leur dynamique et leur relation avec la compartimentation biochimique *in vivo*; et (iii) Partie 3 décrit une nouvelle approche pour étudier la morphologie de la synapse tripartite (les synapses entourées par des prolongements astrogliaux) *in vivo*. Tous les résultats sont mis en perspective dans la discussion, qui est suivie par des matériaux supplémentaires.

Résumé des conclusions

Mettre en place la microscopie 2P-STED in vivo

Dans cette thèse, j'ai présenté la mise en œuvre des expériences *in vivo* dans le laboratoire, le principe de base de la microscopie 2P-STED, ainsi que des conseils pratiques sur la façon de mettre en place notre système et de le faire fonctionner. Dans la première partie (Partie 1) de résultats, j'ai décrit l'optimisation de la chirurgie et l'imagerie *in vivo*, ainsi que l'utilisation d'un objectif à huile de silicone pour visualiser les épines dendritiques dans la couche 1 du cortex à tonneaux de la souris.

Par la suite, j'ai montré l'acquisition à l'échelle nanométrique, et en temps réel, des épines dendritiques marquées avec l'YFP et des prolongements microgliaux marqués avec la GFP, dans des tranches aiguës de cerveau *in vivo*.

Imagerie in vivo de la morphologie des épines dendritiques

J'ai ensuite montré dans la deuxième partie des résultats que l'imagerie 2P-STED peut révéler les paramètres morphologiques des épines dendritiques, à savoir la largeur du cou, la longueur du cou, la longueur totale des épines, et le volume de leur tête, à l'échelle nanométrique dans le cortex à tonneaux de souris anesthésiées. Ces paramètres morphologiques couvrent une large gamme et tous - sauf pour la longueur totale des épines - ont montré une différence significative entre les mesures à partir des données 2P par rapport aux données 2P-STED, comme attendu grâce à la résolution améliorée obtenue en microscopie STED. Pour la longueur totale des épines on a prévu d'afficher les mêmes résultats dans les deux modalités d'imagerie, car il est bien au-dessus de la limite de résolution. La morphologie des épines a été suivie à différentes résolutions temporelles et pour un maximum de 50 minutes, et n'a montré aucune corrélation entre les différents

paramètres morphologiques. Tous les paramètres étaient globalement stables au fil du temps, même si une grande variabilité existe entre les épines et que leur morphologie montre des variations au cours du temps.

Compartimentation des épines in vivo

Semblable à la morphologie des épines, nos expériences préliminaires ont montré que les valeurs du facteur 'tau' (τ), la constante de temps pour la compartimentation biochimique engendre une large gamme, avec des gammes similaires trouvées dans τ calculé (à partir de données 2P-STED) et τ démesuré (à partir des données de FRAP). Les tau calculés et mesurés ne sont pas corrélés, ce qui pourrait être expliqué par des données morphologiques qui ne prennent pas en compte quel est le pourcentage de l'espace qui est réellement impliqué dans la diffusion, et quel est le pourcentage de l'espace qui est repris par des structures intracellulaires tels que l'appareil des épines qui est riche en actine, le réticulum endoplasmique (RE), les mitochondries et autres organites. Ce qui est intéressant est qu'une corrélation modérée a été observée entre la longueur du cou des épines et le τ mesuré, ainsi qu'une faible corrélation entre la largeur du cou des épines et le τ mesuré. Tandis que la longueur du cou des épines explique que 4 % de la variation des vitesses de diffusion, la largeur du cou des épines représentait 1.6 % de la variabilité. Le volume de la tête n'a pas de corrélation avec, ni expliqué plus de la variabilité, du facteur de compartimentage biochimique (le τ). En outre, la résistance du cou a été calculée soit sur la base de la loi d'Ohm ou sur la loi de Fick et leurs résultats se sont révélés pas considérablement différents l'un de l'autre.

La microscopie 2P-STED en deux couleurs in vivo

Enfin, j'ai vérifié que notre système est capable d'effectuer la double couleur pour la microscopie 2P-STED *in vivo* et j'ai montré cette application en imageant le complexe neurones-glie et leur co-localisation. Les astrocytes sont très sensibles à la lumière STED, ils ont donc été difficiles à imager. Avec notre nouvelle approche de marquage, j'ai réussi à visualiser l'apposition des structures neuronales et des prolongements astrocytaires.

Pris dans leur ensemble, les résultats présentés ici montrent que notre microscope 2P-STED permet l'étude des structures cérébrales, en particulier des épines dendritiques avec une super résolution. Il a été montré que la morphologie des épines dendritiques est globalement stable à l'échelle nanométrique tenant compte de la variabilité de la compartimentation des épines *in vivo*. En outre, il a été démontré qu'il est possible avec notre système d'effectuer l'imagerie super résolutive deux couleurs *in vivo* et de l'appliquer à l'étude de l'apposition morphologique des épines dendritiques et des prolongements gliaux dans la couche 1 du cortex à tonneaux de souris anesthésiées.

Remarques finales

En conclusion, le travail présenté ici nous permet d'étudier des structures neuronales et gliales à l'échelle nanométrique dans l'environnement intact grâce à l'amélioration de l'imagerie *in vivo* et d'une nouvelle approche de marquage des astrocytes. La corrélation entre la morphologie à l'échelle nanométrique des épines dendritiques et leur

compartimentation biochimique a été explorée *in vivo*. Les résultats peuvent éventuellement être confirmés en combinant la microscopie 2P-STED avec 1) la technique du patch-clamp en électrophysiologie *in vivo*, 2) la libération de molécules cagées avec un laser deux-photons pour activer sélectivement des épines, 3) l'imagerie calcique et / ou 4) l'imagerie par des colorants sensibles au voltage, tous apportant des informations fonctionnelles.

L'émergence de marqueurs astrocytaires plus forts dans les longueurs d'onde verte et les adaptations de notre microscope permettront de découvrir de nombreuses facettes intéressantes de la morphologie de la synapse tripartite et sa relation avec la physiologie du cerveau. Cela pourrait alors permettre l'étude des questions biologiques pertinentes *in vivo*, tels que les types de couverture d'épines par les astroglies, la dynamique de ces structures variables, et le type d'interaction des épines avec des (multiples) cellules gliales à l'échelle nanométrique. Cela nous aiderait à obtenir un meilleur aperçu des dynamiques morphologiques des (tri-) synapses, les conséquences sur la compartimentation des épines dendritiques, et peut-être une meilleure compréhension de la communication synaptique et donc de la physiologie et de la pathologie du cerveau.

INTRODUCTION

In this thesis, I describe the development and application of dual color two-photon excitation stimulated emission (2P-STED) microscopy *in vivo* in our laboratory. The ultimate goal of my PhD was to establish *in vivo* super-resolution imaging and use this approach to elucidate spine dynamics and visualize spine – glia morphological interactions in the living brain (*in vivo*).

The brain is a very complex structure, with a capability to produce thoughts and feelings, memories, and actions. Those brain functions rely on the many cellular structures present in the brain, with an estimate of $8 \cdot 10^{10}$ nerve cells – the neurons – and a similar number of non-neuronal cells in the human brain (Azevedo et al. 2009). Santiago Ramón y Cajal, using the Golgi staining method (Golgi 1873), was the first to identify differences between neuronal structures. He also outlined the basic connectivity pattern within several brain regions (Ramón y Cajal 1888; Ramón y Cajal 1891; Ramón y Cajal 1899). This connectivity pattern represents the communication between the neurons via their synapses, which can consist of a pre-synaptic bouton and a postsynaptic spine. Spine morphology plays an important role in synaptic function and thus it is of great interest to study the morphological dynamics of spines in the most intact environment possible. However, some of the morphological parameters of spines (e.g. neck width) cannot be fully resolved with conventional light microscopy. Thus, little is known about their nanoscale changes and subsequent effects on spine physiology in the intact brain. We are interested in filling the knowledge gap between the quantification of nanoscale structures in fixed tissue and the scarce super-resolved imaging of spines in the intact environment. We aim to add a quantification of those structures in the *in vivo* brain. Live brain tissue is the ultimate preparation for neuroscience studies as it preserves all long range neuronal projections, it keeps cells in their natural environment, and it allows to monitor morpho-functional changes over time in a living animal. The low amount of users of this *in vivo* preparation is explained by the fact that for certain questions it comes with a cost in amongst others optical accessibility, ease of performing electrophysiological recordings, and most importantly vibrational artefacts due to breathing and heartbeat of the animal. However, imaging deep in the brain has been facilitated by the use of two-photon (2P) microscopy since it allows for up to 1 mm of penetration depth due to the reduced scattering of the excitation light. In addition, the introduction of cranial windows facilitated the chronic access to the cerebral tissue. STED microscopy furthermore allows for the nanoscale investigation of subcellular structures. Eventually, an *in vivo* 2P-STED imaging approach will enable to tackle questions such as “what are the nanoscale morphological variations and dynamics of neuronal structures, e.g. the dendritic spine?” and “how does spine nanoscale morphology affect spine physiology?”.

In the following chapters, I will introduce the neurobiological aspects that are relevant for my project and the principles of STED microscopy. Finally, I will describe the aims of my PhD project.

1 Brain structure and function

The complexity of the brain can already be appreciated by its anatomy. Firstly, the two hemispheres of the brain are interconnected via the corpus callosum and can each be subdivided in sub-regions who are involved in various functions. In addition, the surface of the brain – the cortex – exists of many folds and deep clefts, respectively the gyri and sulci, thereby constituting most of the brain's surface area. As evolutionarily the most recent brain structure, the cerebral cortices are capable of performing higher cognitive functions and the outer layer of the cerebral cortex can be referred to as the neocortex. For example, they can control incoming information and outgoing behavior via the sensory and the motor cortex, respectively, thereby showing their role as the integrative center of the brain.

Since much of the brain is devoted to deal with stimuli arising from the internal and external environments, studying the mechanisms of sensation, such as its signaling pathways, will give us a better understanding of higher brain functions. Processing of the sensory signals is performed by the neurons via both ascending and descending connection pathways within the cortex (Bernardo et al. 1990) and with other brain regions. Those connections are structurally well organized, as it is for example seen in the mouse neocortex. Neocortical connections are organized via the segmentation of the cortex into horizontal layers as well as vertical columns. On top of that, one can find a clear somatosensory topography in rodents. There is a direct relation between the facial whiskers of the animal and the cortical signal processing area (barrels) in layer 4 (L4) of the rodent's somatosensory cortex (Woolsey & Van der Loos 1970; Fox 2008; Bosman et al. 2011). This organization makes this system an excellent model to better understand neocortical function (Petersen 2007; Feldmeyer et al. 2013).

1.1 The somatosensory cortex

The specific relation of the sensory systems with their cortical area in mice can be represented with the mouseunculus as shown in Figure 1 (Fig. 1, right; (Zembrzycki et al. 2013)). The direct connections between the whiskers on the snout, the barrelettes in the hindbrain, the barreloids in the ventral posterior nucleus (VPN) of the thalamus, and the

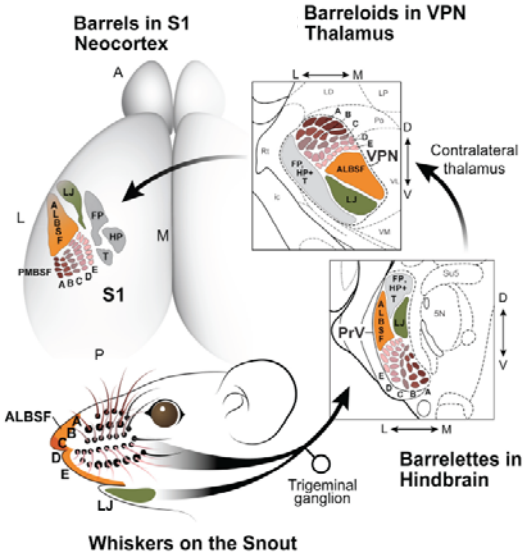

Figure 1: The somatosensory cortex of mice. *The somatosensory system in mice, showing the different pathways between brain regions (left) and a scaled representation in the mouseunculus (right). Figure adapted from* (Zembrzycki et al. 2013).

barrels in the primary somatosensory (S1) cortex are shown here (Fig. 1, left). Even though different layers of the cortex are hard to distinguish, L4 and layer 1 (L1) can be easily identified due to their high and low cell density, respectively. This makes those layers favorable to study intra- and intercortical microcircuits structure and function (Feldmeyer 2012). The neuronal structures found in L1 are mainly apical tufts originating from neurons located in layer 5 (L5), which is the main output layer of the barrel cortex (Hooks et al. 2011). The many inter- and intracortical connections, as well as the broad receptive fields compared to the single-whisker receptive fields in the trigeminal ganglion (Simons 1978; Moore & Nelson 1998; Zhu & Connors 1999; Brecht et al. 2003; Higley & Contreras 2003) and the highly variable response to stimuli due to amongst others the interaction with spontaneous activity (Petersen et al. 2003; Sachdev et al. 2004), makes it conceivable that synapses in L1 serve an integrational role (Feldmeyer 2012). A better understanding of this integrational layer might help getting a better insight into cortical functioning and eventually brain physiology. The direct link between the sensory system and the cortical connections makes the mouse barrel cortex thus a perfect model to study the type of connections in such interconnected pathways. In addition, because of their higly dynamic nature (Gilbert & Sigman 2007), it is of great interest to characterize not only the structure but also the function of the different neuronal connections in and between the various layers and cortices. Altogether, it can be concluded that sensory processing, and thus higher brain functioning, can very well be studied in the well-defined synaptic pathways of the rodent whisker-related sensorimotor system (Petersen 2007). Even though one should keep in mind that a combined microscopic and macroscopic view will facilite a full understanding of the sensory system its functioning (Feldmeyer et al. 2013), an understanding of the single cell its actions is crucial to explain network activity.

1.2 Cellular structures of the brain

The two cell types of utmost importance for brain functioning are the nerve cells – the neurons – and non-neuronal cells – the glial cells. In general, the neurons are perceived as the main communicators in the brain via their tremendous amount of synaptic connections. Glial cells on the contrary have for a long time been regarded as playing a merely supporting role for neurons and brain function.

1.2.1 Neurons

Since Ramon y Cajal's pioneering description of neuronal morphology and synapses as the building blocks of neuronal communication, one of the principle goals in neuroscience has been to decipher the function and structure of neurons and their connections.

Most neurons share the same general structure, but the morphology of individual neurons varies and is adapted to their specific function. Generally speaking, neurons are polarized structures, which process and transmit information through both chemical and electrical signals. A typical neuron consists of a soma wherefrom processes, the dendrites and axon, extend. Here the focus lays on the multipolar neurons, where the dendrites are mainly the input region. Dendrites are in charge of the reception and integration of neuronal signals, while axons mainly communicate those signals to other target cells. Dendrites have many

branch points and are covered with protrusions, called dendritic spines. Axons, on the contrary, don't have spines but do have enlargements in the diameter of their shaft, which are called axonal boutons. Axonal boutons and dendritic spines can form a connection through which neurons communicate with each other. This structure is called the synapse and a single axon can make many synaptic connections. Likewise, a single dendrite can receive inputs from multiple axon terminals. Synapses can be formed between a dendritic spine and an axonal bouton, between an axonal bouton and the dendritic shaft, and between an axonal bouton and the cell soma.

1.2.2 The synapse and synaptic communication

The synapse is a dynamic structure in charge of information processing in the central nervous system. The communication between synapses, synaptic transmission, can be chemically or electrically defined. In the electrical synapse the membranes of the pre- and post-synaptic cells are in direct contact forming a gap-junction via which small ions can flow. Thereby, currents (the electric signal) can be transmitted from one cell to the other. Here the focus lays on the chemical synapse, which transmits the electrical signal (action potentials (APs)) via a chemical intermediate, called neurotransmitter. The pre- and post-synaptic cell are not in direct contact with each other, but separated by a 10 – 30 nm wide synaptic cleft (De Robertis & Bennett 1955). Upon the arrival of an AP in the pre-synapse, neurotransmitters are released in the synaptic cleft. Those neurotransmitters can activate post-synaptic receptors, which can subsequently induce a synaptic potential.

In the pre-synapse, besides the active zone, various diversely sized vesicles can be found as well as a range of scaffolding and adhesion molecules (Li & Jimenez 2008; McAllister 2007). Most of those vesicles contain the neurotransmitters, which can be inhibitory or excitatory. Synaptic vesicles fuse with the membrane upon the arrival of an AP so that they can release those signaling molecules at the active zone. In the case of an excitatory synapse, the neurotransmitter is often glutamate, while inhibitory synapses usually contain gamma-aminobutyric acid (GABA) or glycine.

Similar to the pre-synapse, the post-synapse can have many different shapes and sizes, often proportional to the presynaptic vesicle content (Lisman & Harris 1993; Harris & Stevens 1989). The post-synaptic spines are small appendages from the dendrite, characteristically described by a bulbous head and slender neck (Peters & Kaiserman-Abramof 1969; Peters et al. 1976). The spine architecture is dependent on its underlying structural elements forming the cytoskeleton (Matus 2000). While the dendrite is mainly build up by microtubules (Peters et al. 1976; Matus et al. 1982), the spine cytoskeleton consists mainly of microfilaments which form longitudinal bundles in the neck and core of the head, and a meshwork of fine fibers in the periphery (Peters et al. 1976; Landis & Reese 1983). An important molecule present throughout both synaptic components (Dillon & Goda 2005) and composing the microfilaments in the spines, is actin (see Fig. 2; (Fifková & Delay 1982; Matus et al. 1982; Cohen et al. 1985)). Actin can, mainly in large spines, form together with the smooth endoplasmic reticulum (SER) a spine apparatus (Spacek & Harris 1997; Gray & Guillery 1963; Westrum et al. 1980). The actin microfilaments are thus concentrated in spines (Gray 1959b) and are closely associated to an organelle attached to the post-synaptic

membrane – the post-synaptic density (PSD). The PSD is positioned across a vesicle-containing presynaptic bouton and is proportional to the number of vesicles in the pre-synapse, as well as the total spine volume and number of organelles in the spine (Spacek & Harris 1997; Harris et al. 1992). Most importantly, the PSD contains a large collection of signal processing devices (Kennedy 1998; Kennedy 2000), including important neurotransmitter receptors such as the ionotropic α-amino-3-hydroxy-5-methyl-4-isoxazole propionate (AMPA) and N-methyl-D-aspartate (NMDA) glutamate receptors (also represented in Fig. 2) and metabotropic glutamate receptors (Nusser et al. 1998; Takumi et al. 1999; Husi et al. 2000; Walikonis et al. 2000). NMDA and AMPA receptors play an important role in the regulation of spine formation, stabilization (discussed in (Matus 2000)), and excitatory synaptic transmission (e.g. see (Shi et al. 1999; Zhu et al. 2002; Noguchi et al. 2011; Sala & Segal 2014)). When glutamate binds the NMDARs and AMPARs, the channels open and AMPARs allow for sodium and potassium exchange, resulting in depolarization of the cell. NMDARs are originally blocked by magnesium ions, but AMPAR-dependent depolarization can lead to the efflux of magnesium, thereby unblocking the NMDARs. The

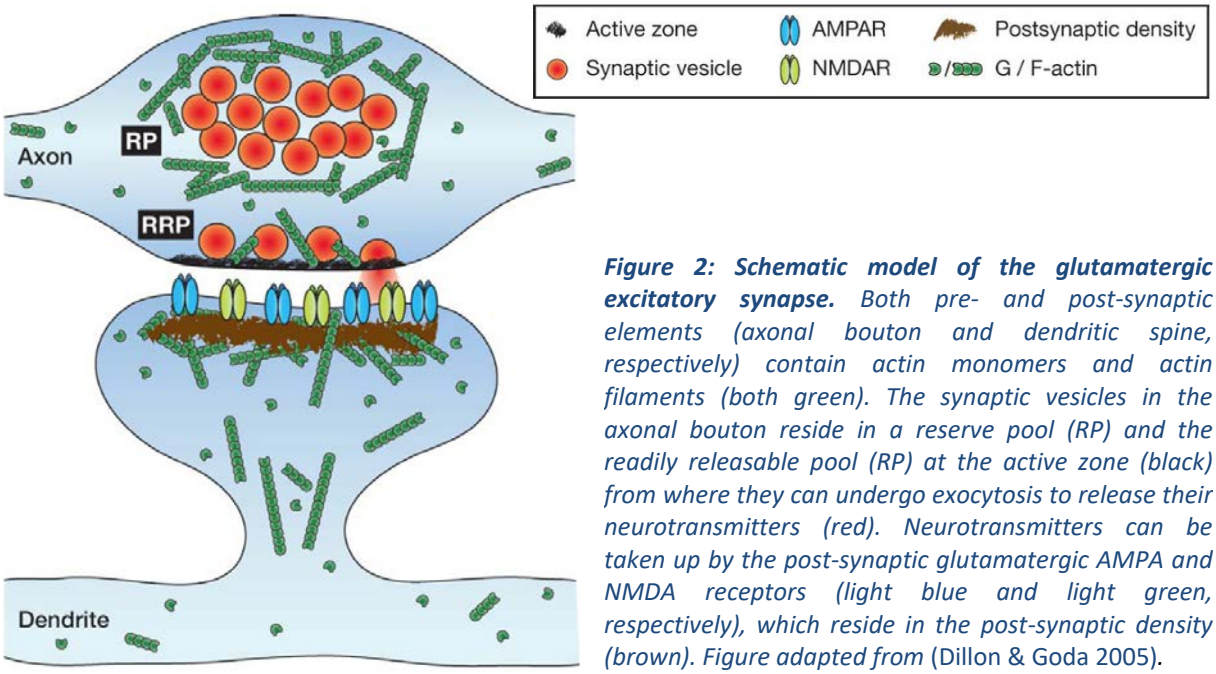

Figure 2: Schematic model of the glutamatergic excitatory synapse. *Both pre- and post-synaptic elements (axonal bouton and dendritic spine, respectively) contain actin monomers and actin filaments (both green). The synaptic vesicles in the axonal bouton reside in a reserve pool (RP) and the readily releasable pool (RP) at the active zone (black) from where they can undergo exocytosis to release their neurotransmitters (red). Neurotransmitters can be taken up by the post-synaptic glutamatergic AMPA and NMDA receptors (light blue and light green, respectively), which reside in the post-synaptic density (brown). Figure adapted from* (Dillon & Goda 2005).

open NMDARs allow for both sodium and calcium influx. Subsequently, calcium is implicated in the induction of several phenomena like long-term potentiation (LTP) corresponding to a persistent increase in the efficacy of transmission. In addition, the NMDAR magnesium block is not only relieved by AMPAR activation. It can also be relieved by other, voltage-sensitive, channels and be due to the high sensitivity of NMDAR to calcium (Bloodgood & Sabatini 2007; Svoboda et al. 1999; Sabatini et al. 2001). Glutamate is thus an important neurotransmitter for excitatory synaptic activity and requires to be highly controlled. In order to maintain glutamate concentration at optimal levels during synaptic transmission, glutamate transporters can take up excessive glutamate from the synaptic cleft (Danbolt 2001). Those glutamate transporters are not only present on the two neuronal elements of synapses, but more importantly also on glial cells (Lehre et al. 1995; Rothstein et al. 1994;

Sullivan et al. 2004). The glutamate transporters expressed on astrocytes were shown to be of great importance for the shaping of glutamate transients since approximately 90 % of excessive glutamate can be taken up by astrocytes (discussed in (Bergles & Edwards 2014)). The variable glial coverage of spines influences the clearance of glutamate at specific locations (Lehre & Rusakov 2002) thereby emphasizing the important role of glial cells in synaptic transmission (discussed in e.g. (Panatier & Robitaille 2016)).

1.2.3 Glial cells

Originally, the glial cells were only seen as supporter cells for the neurons. However, nowadays it has been more and more accepted that they also play a role in the modulation of synaptic transmission. The different types of glial cells found in the central nervous system (CNS) are NG2 glial cells, microglia, oligodendrocytes, and astrocytes (see Fig. 3). NG2 glial cells, or polydendrocytes, are multifunctional cells, mainly related to as being the precursor cells for oligodendrocytes. Microglia are the resident immune cells of the brain, but have also been shown to be involved in synaptic plasticity (Pfeiffer et al. 2016). Oligodendrocytes

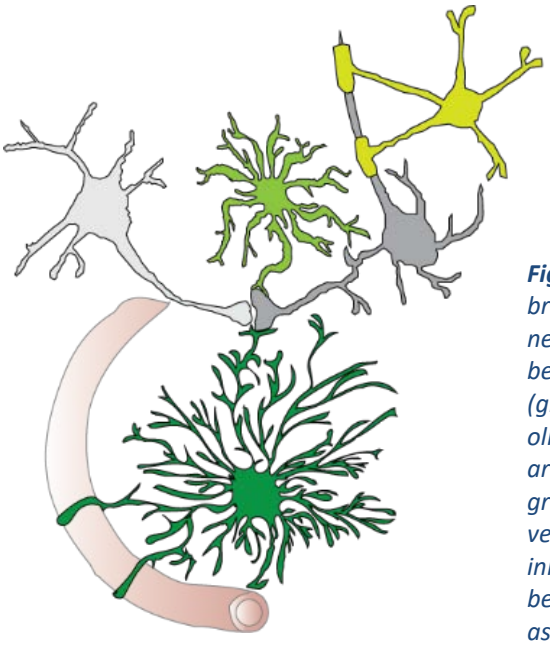

Figure 3: Schematic of cellular structures in the brain. *The brain does not only exist of neurons, but contains many non-neuronal cells as well. In this schematic a synapse is shown between the pre-synaptic (light grey) and post-synaptic (grey) neuron. The glial cells surround the neurons, with oligodendrocytes (yellow-green) forming myelin sheets around the output branch of the neuron. Astrocytes (dark green) form an intermediary between the (cerebral) blood vessels (red) and the pre- and post-synaptic neurons. The innate immune cells of the brain, the microglia (green), have been shown to touch and interact with neuronal structures as well.*

provide myelin and form an insulating sheath around a subset of neuronal structures, thereby speeding up the transmission of the electrical signals. Astrocytes, the most numerous type of glial cells in the brain, are involved in synaptogenesis during brain development and contribute to the formation of the blood-brain-barrier. Most importantely, they have more recently been accepted to play a role in basal synaptic transmission as well (e.g. see (Panatier et al. 2011)). A complete understanding of brain function thus requires insights in astrocytic function as well as the interaction between astrocytes and neurons (discussed in (Volterra & Meldolesi 2005)).

1.2.3.1 Astrocytes

Astrocytes create a large syncytium of connected cells via their coupling by gap junctions through which they exchange metabolites (Rouach et al. 2008; Giaume et al. 2010). They have for a long time not received a lot of attention, maybe because they do not generate

action potentials and were thus considered to be passive cells unable to communicate (Steinhäuser et al. 1992). This view has however changed with the finding of gliotransmission, the communication between neighbouring astrocytes and neurons (Bezzi & Volterra 2001) in response to various neurotransmitters (e.g. glutamate) and other signaling factors (see (Halassa & Haydon 2010; Volterra & Meldolesi 2005; Perea et al. 2009). Using glial fibrillarly acidic protein (GFAP) labelling, astrocytes were hallmarked by their star-shaped morphology and numerous protrusions surrounding bloodvessels and neurons. They are heterogeneous in morphology, which is dependent on their location and function (discussed in (Wang & Bordey 2008)). Due to improved labelleling strategies, astrocytes are nowadays described as spongiform structures with stubby main processes and irregularly shaped dense ramifications (Bushong et al. 2002; Bushong et al. 2004; Hama et al. 2004). Since astrocytes occupy a key position between blood vessels and synapses (Reichenbach 1989; Derouiche & Frotscher 2001; Bushong et al. 2002; Halassa et al. 2007; Oberheim et al. 2008), they are amongst others in charge of coupling neuronal activity and local blood flow changes (Petzold & Murthy 2011). Furthermore, some of their well-established functions include their importance for the homeostasis of ions and the clearance of neuronal messenger molecules, such as glutamate, and their involvement in trophic functions such as angiogenesis (discussed in (Wang & Bordey 2008) and see Fig. 4).

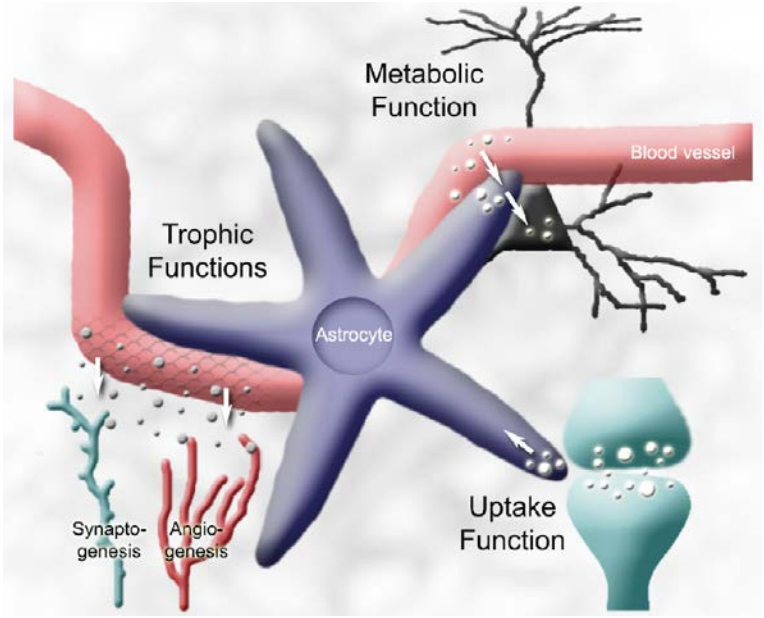

Figure 4: The well-established homeostatic functions of the astrocyte. *In order to maintain a viable environment for neurons, astrocytes are involved in many homeostatic functions including the uptake of potassium and neurotransmitters, maintenance of the blood-brain-barrier and providing metabolic support for neurons, and synapto- and angiogenesis. Figure taken from* (Wang & Bordey 2008).

After pioneering work from several groups (e.g. see Araque et al. 2001; Oliet et al. 2001), it became clear that changes in astrocytic coverage of the synapse affected neurotransmission. This led to more studies focusing on, and giving more insight in, the role of astrocytes in synaptic transnmission (e.g. see (Perea & Araque 2005; Panatier et al. 2006; Henneberger et al. 2010)). In addition to having a complex structure and to adapt to their many functions (some of them described in e.g. (Weber & Barros 2015)), astrocytes do also express a large repertoire of receptors, including ionotropic glutamate receptors (Lalo et al. 2006) and glutamate transporters (Anderson & Swanson 2000; Murphy-Royal et al. 2015)). Those

proteins and other ion channels enable the sensing of neuronal activity by the astrocytes. This can result in elevations of the intracellular calcium levels (see e.g. (Dani et al. 1992; Porter & McCarthy 1996; Pasti et al. 1997)) in subcellular compartments (Panatier et al. 2011; Di Castro et al. 2011), microdomains, or the whole cell (Grosche et al. 1999). Spontaneous calcium transients have been observed *in vivo* and were found to indeed be regulated by neuronal activity (e.g. see (Hirase et al. 2004; Wang et al. 2006; Winship et al. 2007; Petzold et al. 2008)). Intracellular calcium waves are thus representing the excitability of astrocytes and their capability to sense synaptically released neurotransmitters emphasizes their relation to synaptic transmission ((Porter & McCarthy 1996; Pasti et al. 1997; Latour et al. 2001; Fellin et al. 2004) and discussed in (Wang & Bordey 2008)). However, little is known about the existense of intercellular calcium waves, while also only little data exists on the presence of sodium waves (for the latter see e.g. Bernardinelli et al. 2004). The increased sodium levels in astrocytes might lead to increased astrocytic intracellular calcium levels, which, similar to the calcium elevations due to receptor activation, can result in fast release of gliotransmitters such as D-serine, adenosine triphosphate (ATP) and glutamate (Fellin et al. 2004; Pascual et al. 2005; Perea & Araque 2005; Panatier et al. 2006; Serrano et al. 2006; Henneberger et al. 2010). These gliotransmitters can in turn act on other glial cells and at the level of synapses regulate neuron excitability and synaptic transmission efficacy (discussed in e.g. (Volterra et al. 2014)). Altogether, calcium signalling is thus a key mechanism for astrocytic function. It has been shown to be capable of integrating neuronal activities of different strengths, at different timescales. In addition, calcium signalling can differ between different astrocytic locations (globally and locally) and can take place via different mediators (De Pittà et al. 2012; Shigetomi et al. 2013). For efficient neuron-astrocyte interaction, a close apposition of the two structures seems to be of importance. Indeed, mature astrocytes were shown to be capable of contacting thousands of synapses with non-overlapping domains of individual astrocytes (Bushong et al. 2002; Halassa et al. 2007), and the degree of ensheathment of synapses has been found to be variable and complex (Bernardinelli et al. 2014).

1.3 The tripartite synapse

The small astrocytic processes can contact or enwrap the synapses, as has already been shown with electron microscopy (EM) in the early 90's (Peters et al. 1991). Almost a decade later, the concept of the so-called tripartite synapse was introduced by Alfonso Araque, implying that the astrocytic processes are functionally integrated components of synapses and are as such of great importance for neuronal communication (Araque et al. 1999). Astrocytes have recently been proposed to laterally regulate synaptic transmission through their network activity, thereby resulting in increased connectivity of the synapses (see Fig. 5; (Covelo & Araque 2016)). The influence of astrocytic processes on the synapses can be easily conceived given their close apposition and possible invasion of the synaptic cleft by particularly small astrocytic processes (Ventura & Harris 1999; Witcher et al. 2007; Pannasch et al. 2014). The mechanisms mediating neuron-astrocyte interaction include the previously described clearance of glutamate from the synaptic cleft and the release of gliotransmitters (see Fig. 6 and e.g. (Araque et al. 2001)), as well as the buffering of potassium ions in the extracellular space (e.g. see (Bay & Butt 2012)) and physically shaping the available space for synaptic diffusion (Panatier et al. 2014). Glutamate is thus not only an important

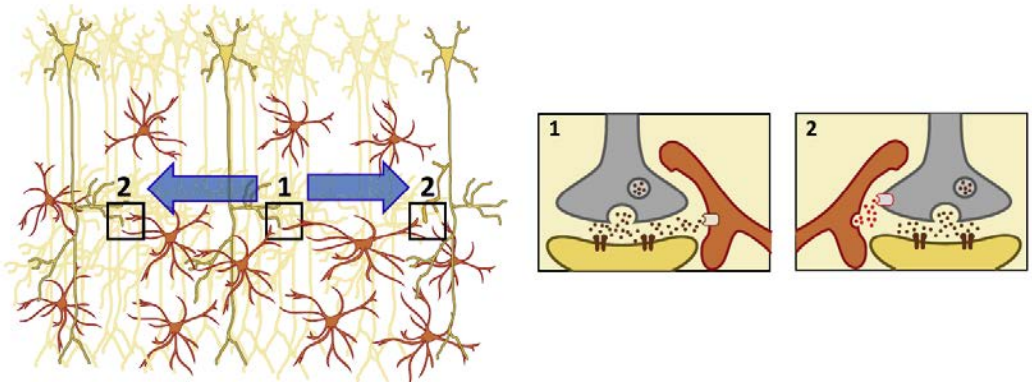

Figure 5: Schematic showing the proposed lateral astrocyte synaptic regulation. *Neurotransmitters released from the first synapse (1) can be taken up by the surrounding astrocytic process, thereby possibly evoking astrocytic calcium signals which can extend intracellularly (and maybe even intercellularly) and stimulate the release of gliotransmitters at a second synapse (2) which would otherwise not be affected by the activity of the first synapse. Figure taken from* (Covelo & Araque 2016).

neurotransmitter, but also a well characterized gliotransmitter capable of influencing synaptic transmission. As schematically represented in Figure 6, upon release of neurotransmitters (1), the surrounding astrocyte can respond with elevated calcium levels and possibly fast depolarization (2), thereby inducing the release of gliotransmitters, such as D-serine or glutamate. These gliotransmitters can act on both pre- and post-synaptic, as well as extra-synaptic, metabotropic or ionotropic receptors (3). Activation of those receptors on the neuronal elements of the tripartite synapse can result in synaptic currents sufficiently large to depolarize the cells and regulate synaptic efficacy (Angulo et al. 2004; Fellin et al. 2004; Perea & Araque 2005; Navarrete & Araque 2008). In addition, astrocytes are capable of clearing glutamate from the synaptic cleft via their glutamate transporters (4). Thus, the morphological arrangement of the astrocytic processes around the synapse can be seen as a structural substrate for tight functional interactions within the tripartite synapse (e.g. see (Theodosis et al. 2008; Bernardinelli et al. 2014)). The extent of astrocytic coverage, and thereby functional impact, varies between and within brain regions and upon neuronal activity (e.g. see (Hirase et al. 2004)). Indeed, using EM, Genoud and colleauges showed that the tripartite synapse is a heterogeneous structure and a dynamic structure upon stimulation (Genoud et al. 2006). Modelling studies also predicted that the spatial proximity of, and coverage by, astrocytes plays an important role in synaptic transmission (Rusakov 2001; Theodosis et al. 2008; Panatier et al. 2011). Recently, a combined use of EM and field stimulations showed that small displacements of the astrocytic process around the synapse have a big effect on synaptic function, more specifically, the neuronal field potentials (Pannasch et al. 2014). However, the functional read-out was from a live network, while morphology was determined on fixed single synapses. As the interaction of astrocytic processes with synapses can influence synaptic strength, it would be of great interest to now have a tool to study the morphological displacements within the tripartite synapse in live tissue. Confocal microscopy has been used to study basal astrocytic process movements in hippocampal slice cultures which gives indicative information about the spine-astrocyte interaction (Bernardinelli et al. 2014). However, confocal microscopy is resolution limited, and neurovascular coupling is absent in slices and slice cultures, thereby arguing for the preferred use of studies on the tripartite synapse in a more intact and physiological

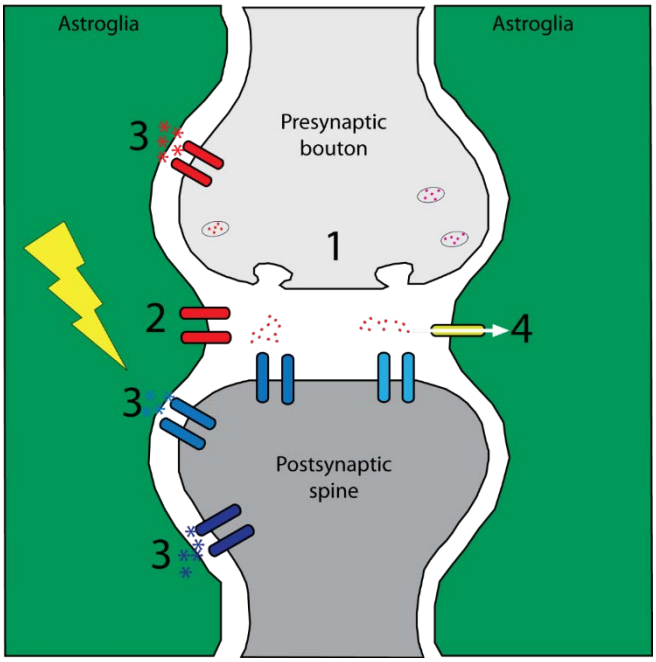

Figure 6: The concept "tripartite synapse" and its signalling pathways. *The tripartite synapse is a description for a structures consisting of a pre- and post-synaptic element as well as a surrounding astrocytic process. In the excitatory synapse, upon the release of neurotransmitters in the synaptic cleft (1), astrocytic receptors can take those transmitters up, which induces calcium elevation in the astrocytic process (2). Subsequently, the calcium elevation can induce the transmission of so-called gliotransmitters, such as glutamate, which can affect both the pre- and the post-synapse (3). 'Left-over' glutamate in the synaptic cleft can be cleared via the action of astrocytic glutamate transporters (4). Process (1) – (4) show the interaction between the three elements, thereby emphasizing the role of astrocytes in synaptic communication.*

environment: the *in vivo* brain. Using 2P-microscopy, it was shown that indeed astrocytic processes displace upon sensory stimulation *in vivo* (Perez-Alvarez et al. 2014). However, because of the diffraction-limited resolution, it is hard to tell how exactly the synapse and astrocytic processes co-localize and how this co-localization affects synaptic physiology. Altogether, with EM showing astrocytic process nanoscale displacements and live studies showing an apparent change upon stimulation, it is emphasized that there is a need for a nanoscale imaging technique to study astrocytic processes and synapses in the physiological relevant and intact brain. In order to fully understand tri-synaptic functioning, it is of great importance to understand the function of each individual element. Since the post-synaptic element of the tripartite synapse, the dendritic spine, contains many receptors on which the astrocytic gliotransmitters can act, and dendritic spines have been found a reliable read-out for synaptic function as well, the focus will now be on the post-synaptic dendritic spine.

2 Dendritic spine morphology and physiology

The development of two-photon microscopy (Denk et al. 1990; Denk et al. 1994) and the possibility of imaging synapses in living brain tissue led to the discovery of activity-dependent morpho-functional changes of synapses. This can be considered as the cellular substrate for learning and memory in mammals, and has been shown both *in vitro* and *in vivo* (Engert & Bonhoeffer 1999; Yuste & Bonhoeffer 2001; Nägerl et al. 2004; Matsuzaki et al. 2004; Nägerl et al. 2007; Becker et al. 2008; Holtmaat & Svoboda 2009; Hayashi-Takagi et al. 2015). The dendritic spine morphology has been found to determine synaptic strength, with spine neck length being related to electrical and biochemical isolation of the spine from the dendrite (Majewska, Brown, et al. 2000; Yuste et al. 2000), while spine head volume was shown to be correlated with the number of postsynaptic receptors (Matsuzaki et al. 2001) and thus the size of the postsynaptic density (Harris & Stevens 1989). To better understand the variability in synaptic strength it is thus of interest to characterize spine morphology. Though two-photon microscopy enabled to create estimates of synaptic function based on its structure (Bloodgood & Sabatini 2005), it has been a STED-based approach leading to the discovery of the plasticity of spine necks (Tønnesen et al. 2014), underlining the necessity of resolving synapses at the finest detail.

2.1 Spine morphology described by ultrastructural studies

Already since the 19th century it has been described that dendritic spine nanoscale morphology is very diverse (Ramón y Cajal 1892; Gray 1959a; Gray 1959b; Jones & Powell 1969; Peters & Kaiserman-Abramof 1969; Peters & Kaiserman-Abramof 1970), but in general spine length ranges from 500 nm to 2 µm and spine head diameter is approximately 1 µm, with total spine volumes ranging from 0.01 femtoliter (fL) to 0.8 fL (Harris & Kater 1994; Harris 1999; Sorra & Harris 2000; Arellano et al. 2007). The spine neck is said to be about 500 nm in length and tens to hundreds of nm in width (e.g. (Nishiyama & Yasuda 2015)). The classification of spine types has been proposed by Peters and Kaiserman-Abramof and is based on optical microscopy and observations in electron microscopy (EM). Spines were classically divided in stubby, thin, mushroom, and cup-shaped spines (Peters & Kaiserman-Abramof 1970; Chang & Greenough 1984; Harris et al. 1992). Their hypothesized role in synaptic functioning led to further ultrastructural studies describing spine morphology (Spacek & Hartmann 1983; Špaček 1985). Typically, thin spines have a small head and slender neck, mushroom spines a larger head, and stubby spines do not show a clear neck (Jones & Powell 1969). However, spines do not always fall in either one of those categories, and more often show an intermediary phenotype, which has continuously been stressed in literature (Peters & Kaiserman-Abramof 1970; Spacek & Hartmann 1983; Harris et al. 1992; Harris & Kater 1994; Arellano et al. 2007). Indeed, dendritic spine morphologies show a continuum of variability in their shape and size, with no clear subgrouping being possible based on the distribution of their morphological parameters (see Fig. 7; Arellano et al. 2007). Both in EM and light microscopy studies, spine neck length and head volume were found to not be correlated (Benavides-Piccione et al.; Arellano et al. 2007), whereas neck width did correlate with head volume (Arellano et al. 2007). However, one should take into account that differences in correlation might exist between apically and basally positioned dendritic spines and that the angle from which spines are imaged can influence their categorization (Arellano et al. 2007). Originally having been studied mainly with EM, the variability of spine

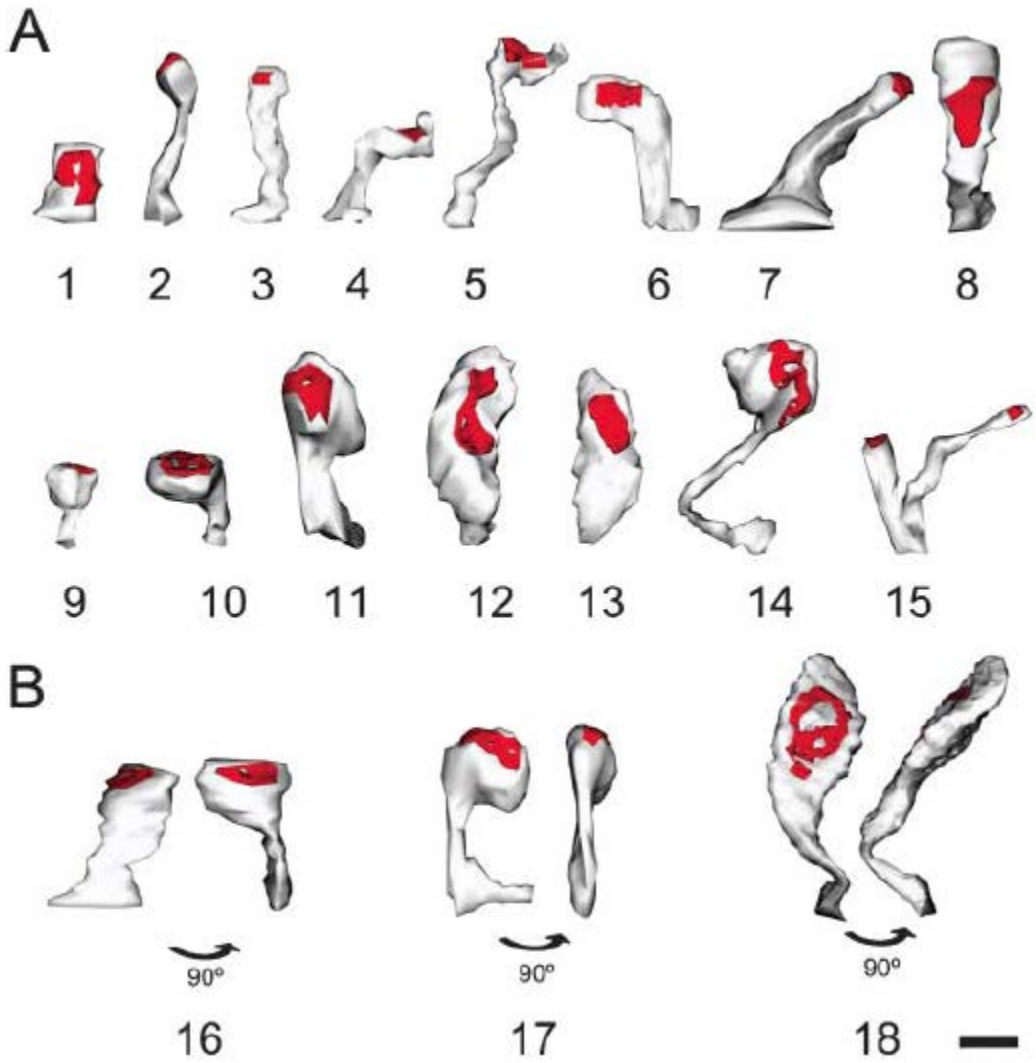

***Figure 7: Variation in dendritic spine morphology**. (A) An ultrastructural study showed the wide range in dendritic spine morphology with the existence of classically designed spine shapes as well as intermediate forms. (B) Dependent on the angle of imaging, spines might be classified in a certain class even though they belong to a different class. Figure taken from Arellano et al., 2007.*

morphology and the early hypothesis of the presence of a morpho-functional relation (Chang 1952; Rall 1978; Crick 1982; Koch, C., Poggio 1983; Segev & Rall 1988; Nusser et al. 1998; Schikorski & Stevens 1997; Bourne & Harris 2008), more specifically morphological changes related to long term potentiation (LTP; (Fifková & Van Harreveld 1977; Fifková & Anderson 1981; Desmond & Levy 1986)), led to an increased interest in morphological dynamics. Understanding the correlation between spine morphological dynamics, spine- and neuronal network activity, and different behaviors is crucial for obtaining a better understanding of brain mechanisms (Chen et al. 2014) and thus shows the need for live imaging. This need is further emphasized by recent work indicating that fixation for EM approaches might cause structural artefacts (reviewed in (Araya 2014); (Chen et al. 2012; Knott et al. 2006)).

2.2 Structural plasticity of dendritic spines

Utillizing live imaging approaches, spine morphological parameters showed similar values to ultrastructural studies (Takasaki & Sabatini 2014; Tønnesen et al. 2014), and could

additionally show their dynamic nature (Blanpied et al. 2008). By receiving mostly excitatory signals on pyramidal neurons (Spacek & Harris 1998; Arellano et al. 2007; Chen et al. 2012), dendritic spines are proposed to be the gateway of excitatory synaptic transmission in the brain (Gray 1959b). Indications for excitatory synaptic plasticity and its modifications can thus be investigated through the study of spines and their structural dynamics (Segal 2005; Tada & Sheng 2006; Harms & Dunaevsky 2007). Several membrane receptors (Lin et al. 2007; Tran et al. 2009; Li et al. 2007) have been found to be involved together with changes in spine morphology to influence synaptic plasticity. Those changes also appeared upon environmental manipulations (Greenough & Volkmar 1973; Connor & Diamond 1982). Work from the last decades emphasizes that spines are indeed motile structures (Blomberg et al. 1977; Crick 1982; Fischer et al. 1998; Korkotian & Segal 2001; Mysore et al. 2007). While most studies focus on spine dynamics as determined by the formation and elimination of spines, dynamics of spines at shorter timescales (see Fig. 8; Mysore et al. 2007) and smaller spatial scales, do take place as well.

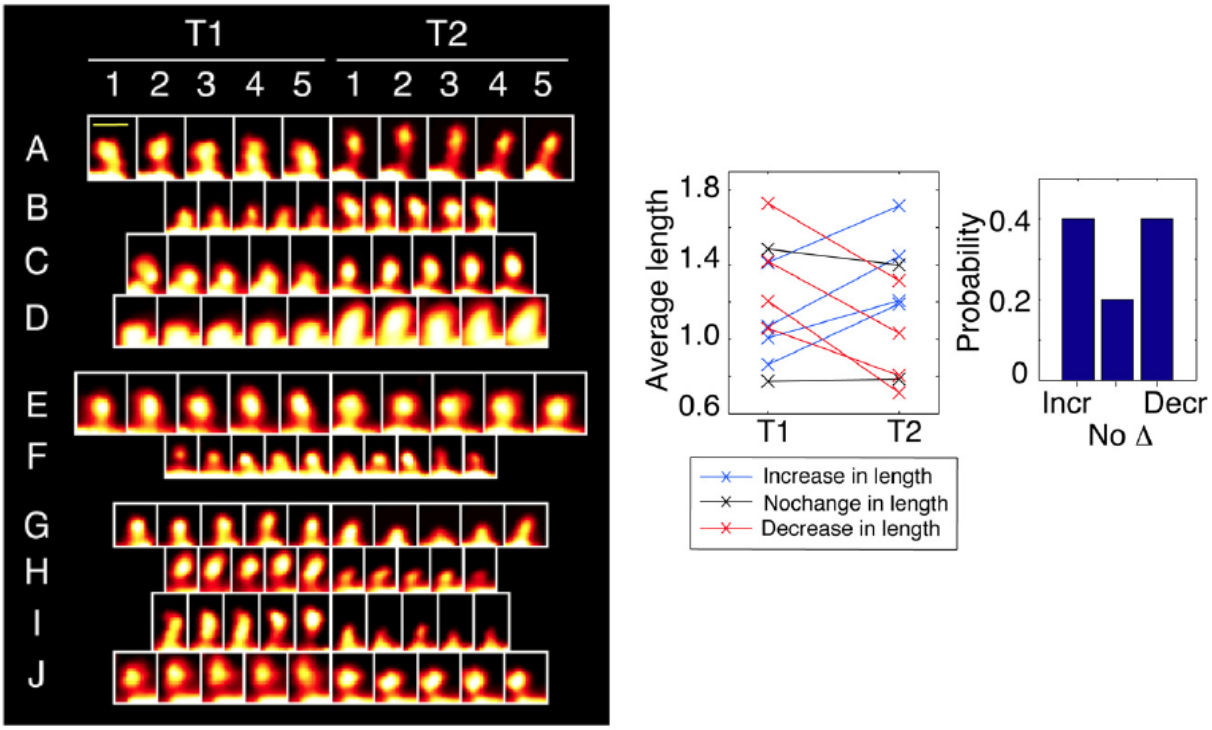

Figure 8: Spine dynamics at different timescales. *Left: Confocal time-lapse images of dendritic spines on cultured neurons showing the variability in spine dynamics. T1 represents images taken every minute at the start of the imaging session, T2 represents images taken every minute hours after the start of the imaging session. Right: Quantification of changes in spine length, average length calculated for 1-5 from both T1 and T2. Image adapted from* (Mysore et al. 2007).

Dendritic spines are capable of changing their morphology upon functional manipulations such as LTP (Toni et al. 2001) or specific stimulation of group 1 metabotropic glutamate receptors (Vanderklish & Edelman 2002). Those morphological rearrangements are taking place both *ex*- and *in vivo* (Fischer et al. 1998; Dunaevsky et al. 1999; Lendvai et al. 2000). Various studies reported the expansion of spine head volume upon stimulation (Matsuzaki et al. 2004; Sapoznik et al. 2006; Yang et al. 2008; Lee et al. 2009; (Lai et al. 2012; Zhang et al. 2013), showing different magnitudes of changes as well as different durations. This might

depend on initial spine morphology (Lai et al. 2012; Matsuzaki et al. 2004) and/or the insertion, or absence thereof, of ionotropic glutamate receptors into the spine head (Korkotian & Segal 2001; Kopec et al. 2007). Furthermore, Hosokawa and colleagues were the first to show that small spines increase in length upon the induction of chemical LTP (Hosokawa et al. 1995), but, most probably due to the resolution limit of conventional light microscopes, little structural data on the smaller structures, such as the spine neck width, exist. On the contrary, molecular processes underlying spine motility have been studied in more detail. The developmentally regulated (Dunaevsky et al. 1999) motility can depend on many different proteins involved in synaptic transmission (Hering & Sheng 2001). It might also change the morphological classification of spines in the case of rapid motility (Parnass et al. 2000). In contrast to morphological plasticity, which is at a timescale of hours or days, this rapid motility appears on a timescale of seconds to minutes in various brain preparations, is actin-remodeling dependent, and sensitive to input-deprivation at a brief critical period of development (Fischer et al. 1998; Dunaevsky et al. 1999; Lendvai et al. 2000; Matus 2000). The *in vivo* work from Lendvai and colleagues showed the retraction and extension, a phenomenon called turnover, of spines (Lendvai et al. 2000). A role for the actin network in this spine motility has throughout the decades been proposed (e.g. see (Blomberg et al. 1977; Hall 1994; Fischer et al. 1998; Honkura et al. 2008; Kessels et al. 2011). The authors of a recent EM study predicted that the dynamic nature of actin is indeed crucial for spine plasticity, as changes in the actin network can change the shape of the synapses, and even retract or sprout spines (Korobova & Svitkina 2010). More recently, actin (de)polymerization and formation of a new stable population of actin in the center of the spine head has been proposed as the underlying mechanism for spine enlargement during LTP (Bosch & Hayashi 2012). However, it remains to be elucidated whether the exact same mechanism is present for spine morphology changes in the absence of any stimulus. The first steps to enable such a study, have been made by the group of S.W. Hell, who showed, by labelling actin, the morphological plasticity of spines *in vivo* and at the nanoscale using a stimulated emission depletion (STED) microscope (Willig et al. 2014). It has been hypothesized that in the adult mouse, spines are largely stable across cortical areas and cell types (Alvarez & Sabatini 2007; Bhatt et al. 2009). However, this does not mean that spine dynamics do not take place in the adult mouse, as was shown by the structural rearrangements of spines in multiple cortical areas including barrel cortex, visual cortex, and motor cortex (Holtmaat et al. 2005; Zuo et al. 2005; Majewska 2006; Yu & Zuo 2011; Noguchi, et al. 2011; Moczulska et al. 2013). Most studies on spine dynamics have so far mainly focused on spine turnover during development and morphological changes upon stimulation or deprivation (see Fig. 9, discussed in (Holtmaat & Svoboda 2009)).

A big advancement in the field of neuroscience was the possibility to track the same spine for a longer time in the living brain (Grutzendler et al. 2002; Trachtenberg et al. 2002; Gu et al. 2014). This allowed for the visualization of spine morphology and dynamics throughout the animal's lifespan (Chen et al. 2014), and revealed a great variability amongst different regions of interest and upon different types of stimuli (reviewed in (Holtmaat & Svoboda 2009; Fu & Zuo 2011)). Part of this variability originates from the differences in the history of activity of different regions of interest, as well as the type of *in vivo* preparation. It has

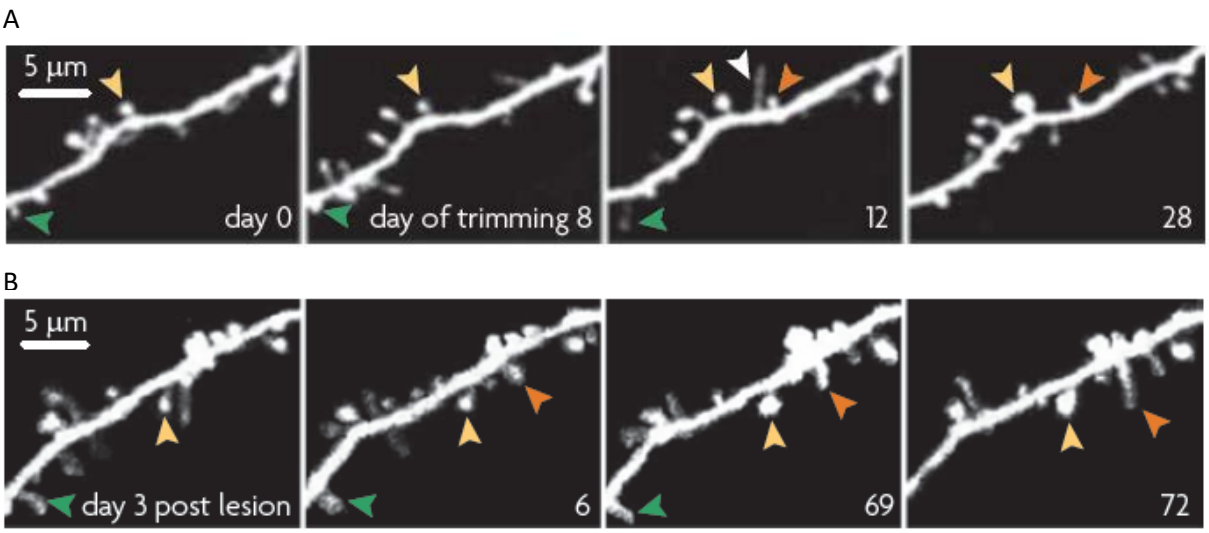

Figure 9: Experience-dependent spine plasticity in the adult neocortex. *(A)* In vivo *time-lapse imaging of dendritic spines in the barrel cortex before (day 0) and after trimming of the whiskers in a chessboard pattern. Most spines are stable, but others are dynamic. (B)* In vivo *time-lapse imaging of dendritic spines in the visual cortex upon a uni-lateral focal lesion of the retina. Some spines are lost, while others get replaced or are stable. Yellow arrowhead: stable spines, green arrowhead: lost spines, orange arrowhead: newly formed persistent spines, white arrowhead: transient spine. Figure adapted from* (Holtmaat & Svoboda 2009).

indeed been shown that the stability of dendritic spines depends on the pattern of neuronal activity rather than the strength (Wyatt et al. 2012) and that synapse remodeling is associated with different types of learning and deprivation (Majewska & Sur 2003; Oray et al. 2004; Keck et al. 2008; Hofer et al. 2009; Holtmaat & Svoboda 2009; Xu et al. 2009; Yang et al. 2009; Lai et al. 2012). Additionally, it has been shown that indeed the type of cranial window affects the dynamics and turnover of spines (Grutzendler & Gan 2006; Xu et al. 2007; Pan & Gan 2008). For example, under thinned skull conditions spines are largely stable, while open skull preparations showed high spine plasticity and turnover (Xu et al. 2007; Pan & Gan 2008). Recently, a direct link was shown between the functional plasticity of cortical circuits and the structural plasticity of the dendritic spines in the somatosensory cortex (Wilbrecht et al. 2010). On top of that, the nanoscale morphology of dendritic spines could be resolved in the cortex of a living mouse by utilizing STED microscopy (Berning et al. 2012), a technique which might advance our understanding in the relation between spine morphology and physiology since it allows for the investigation of nanoscale changes in spine morphology. One characteristic of spine physiology, is their capacity to compartmentalize biochemical and electrical signals.

2.3 Spine compartmentalization

Even though compartmentalization of signals can occur at different scales (Nishiyama & Yasuda 2015), the focus in the field of neuroscience has more and more shifted to the nanoscale. The intrinsic relationship between spine nanoscale morphology and spine functioning is still not fully understood (Lee et al. 2012), but might support spine-specific synaptic plasticity independent of the parent dendrite (e.g. (Gulledge et al. 2012; Takasaki & Sabatini 2014) and reviewed in (Adrian et al. 2014)). However, synaptic signals might also spread beyond the spine, a mechanism which depends on many factors, including dendrite

and spine geometry (Yasuda & Murakoshi 2011). In order to better understand this relation, it is of great interest to study spine morphological dynamics and synaptic plasticity (Bosch & Hayashi 2012). It has been suggested that septin and Ankyrin-G are implemented in the regulation of spine morphology and function during structural plasticity (Tada et al. 2007; Xie et al. 2007; Ewers et al. 2014; Smith et al. 2014; Nishiyama & Yasuda 2015). Furthermore, it has been shown that neuronal activity regulates diffusional coupling through the spine neck (Bloodgood & Sabatini 2005), and that this thin spine neck allows the spine to act as a semi-autonomous compartment to alter diffusional coupling and thus, for example, calcium kinetics (Volfovsky et al. 1999; Korkotian & Segal n.d.; Majewska, Tashiro, et al. 2000; Majewska, Brown, et al. 2000; Yuste et al. 2000). Spines have therefore been proposed to fulfill a role in biochemical compartmentalization (Müller & Connor 1991; Koch & Zador 1993; Svoboda et al. 1996), as well as in the compartmentalization of neurotransmitter receptors (e.g. see (Richards et al. 2004; Triller & Choquet 2005; Ashby et al. 2006), and electrical compartmentalization due to the resistance at the spine neck (Segev & Rall 1988; Tsay & Yuste 2004; Araya et al. 2006; Grunditz et al. 2008; Harnett et al. 2012; Yuste 2013). Those compartmentalization mechanisms can alter synaptic plasticity (Harnett et al. 2012; Tønnesen et al. 2014; Grienberger et al. 2015). A key process for both functional and structural plasticity, and an extensively studied mechanism, is calcium signaling and diffusion (Nishiyama & Yasuda 2015; Kennedy et al. 2005; Bloodgood & Sabatini 2007), which involves the activity of glutamate receptors. By now, many isolated spine calcium signals have been observed in various cell types (Yuste & Denk 1995; Denk et al. 1995; Koester & Sakmann 1998; Nevian & Sakmann 2004; Humeau et al. 2005), and by selectively addressing the diffusion of single spines via either fluorescent recovery after photo bleaching (FRAP) or glutamate uncaging, it was shown that the geometry of dendritic spines was indeed an important factor for the determination of diffusion rates in the spine (Svoboda et al. 1996). More specifically, diffusional rates for calcium where found to be correlated to the resistance of the spine neck, positively correlated with spine neck length, and negatively correlated with diffraction-limited measurements of spine neck width, as well as the surface to volume ratio of the spine (Majewska et al. 2000; Holthoff et al. 2002; Sabatini et al. 2002; Korkotian et al. 2004; Noguchi et al. 2005; Grunditz et al. 2008). In contrast, other studies show that spine morphology cannot predict the amplitude of calcium signals in dendritic spines (Sobczyk et al. 2005; Araya et al. 2006; Araya et al. 2014; Takasaki & Sabatini 2014), the effect of which might be explained by the fact that calcium signaling does not solely depend on spine morphology but on other intracellular (synaptic) mechanisms as well (discussed in (Araya 2014)).

The assumed relation between spine morphology and diffusional rates has been theoretically calculated (Holcman & Schuss 2011) and can be justified by a compartmentalization model, the latter being proven to be highly predictable for cytosolic diffusion in dendritic spines in live tissue (Tønnesen et al. 2014; Takasaki & Sabatini 2014). The model determines passive diffusional coupling of a molecule ‘x’ with the following formula:

$$\tau_x = \frac{Vl}{DA} \qquad (1)$$

with V being the spine volume, *l* the spine neck its length, D the diffusion coefficient of molecule 'x' and A the cross-sectional area of the spine neck calculated as $A = \pi(r_{neck})^2$. Based on this formula, it was found that indeed spine neck width relates inversely with diffusional rates while spine neck length correlates positively with τ (Tønnesen et al. 2014; Takasaki & Sabatini 2014). A decrease in neck width could in addition possibly affect negatively the active transport of endosomes (Kusters et al. 2014). The passage of membrane-bound proteins through the spine neck is indeed partly due to its morphology restricted (Kusters et al. 2013), with neck length being positively correlated with τ (Hugel et al. 2009). However, whether or not head morphology is correlated with diffusional rates was differently predicted by the different studies (positively correlated in (Tønnesen et al. 2014) and (Hugel et al. 2009), but a weak decrease in (Takasaki & Sabatini 2014)) and thus remains to be elucidated. Nonetheless, it can be concluded that spine neck geometry is crucial for dendrite to spine communication (reviewed in (Adrian et al. 2014)).

Whereas biochemical compartmentalization can be defined by changes in the axial and lateral diffusion of signaling molecules in the spine (see Fig. 10a,b; (Lee et al. 2012; Kusters et al. 2013) and reviewed in (Adrian et al. 2014)), electrical compartmentalization is predicted to amplify local electrical signals due to amongst others the resistance of the spine neck (see Fig. 10c-e; (Gulledge et al. 2012; Segev & Rall 1988)). However, whether spine geometry can regulate synaptically evoked electrical activity, has long been controversial (Tsay & Yuste 2004). The spine neck has nevertheless been proposed to produce a voltage gradient between the spine and the rest of the neuron, the effect of which can be amplified further in spines with a voltage-dependent conductance (Grunditz et al. 2008; Yuste 2013; Nishiyama & Yasuda 2015). Since spine head somatic excitatory postsynaptic potentials (EPSPs) can be calculated by

$$EPSP_{sphead} \approx I_{syn} * (R_N + Z) \qquad (2)$$

with I_{syn} the synaptic current, R_N spine neck resistance, and Z dendritic impedance, insight into neck resistance would advance insight into synaptic electrical signals. Neck resistance can be estimated based on Fick's law or Ohm's law (Svoboda et al. 1996), respectively:

$$R_N = \frac{\tau \rho D}{V} \qquad (3)$$

and

$$R_N = \frac{\rho L}{A} \qquad (4)$$

with ρ the cytoplasmic resistivity, τ the diffusion time constant, D the diffusion coefficient, *L* spine neck length, and A cross-sectional area of the spine neck. Thus, spine head EPSPs can be modified by changes in spine geometry (Koch 2004), which might eventually affect synaptic efficacy (reviewed in (Araya 2014)). For example, when spines of pyramidal neurons with a longer neck were stimulated, EPSPs were smaller than those where shorter spines were stimulated, a finding done both in hippocampus and cortex (Araya et al. 2006; Araya et

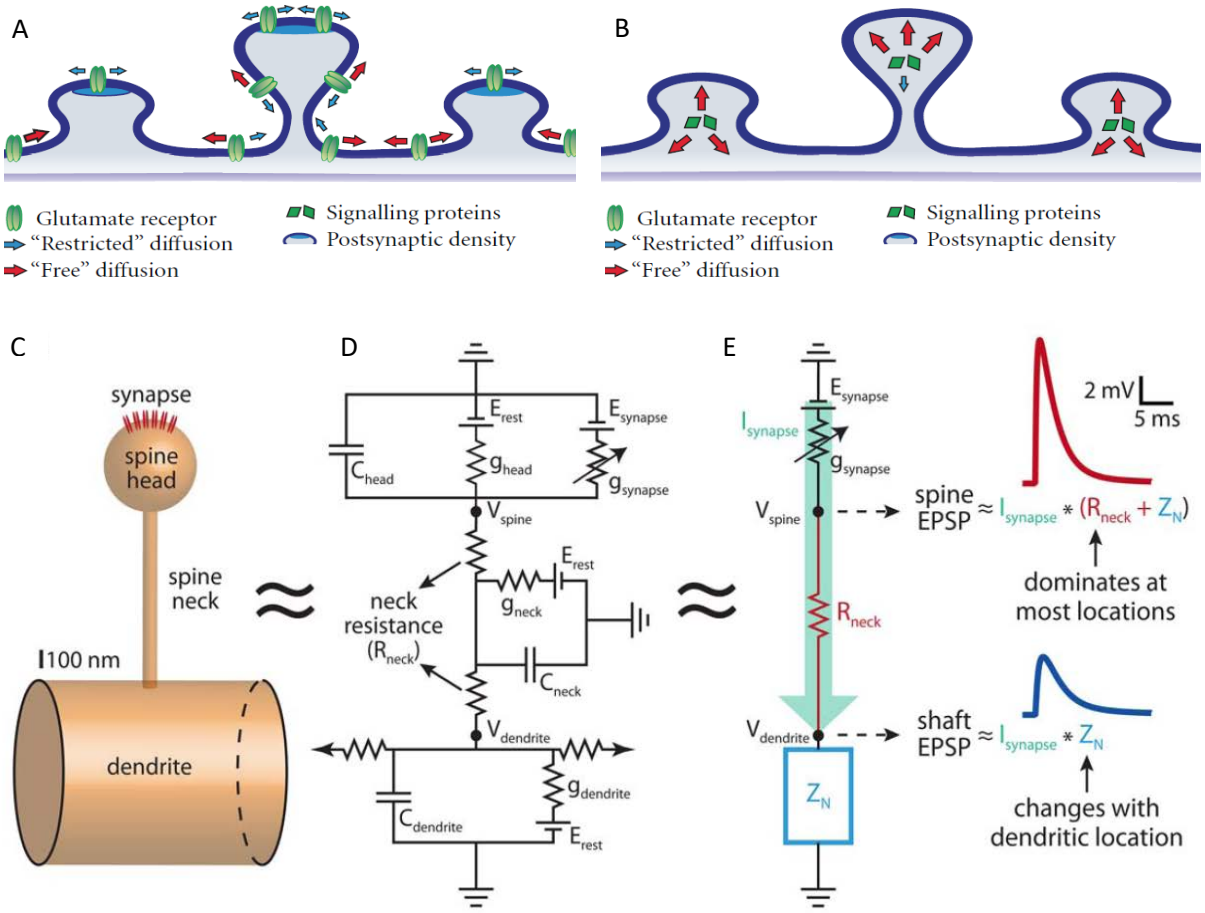

Figure 10: Compartmentalization in dendritic spines. *(A,B) Schematic representation of biochemical compartmentalization in dendritic spines. Figure taken from* (Lee et al. 2012) *(A) Longer spine necks attenuate lateral mobility of surface glutamate recpetors. (B) Spine specific compartmentalization of cytosolic signaling proteins, smaller necks constrain diffusion. (C-E) Electrical properties of dendritic spines. Figure adapted from* (Gulledge et al. 2012). *(C) Diagram representing a dendritic spine. (D) Electrical circuit to model spines, taking into consideration the membrane conductances (g_{xxx}) and capacitances (C_{xxx}) which are determined by the surface area of each compartment. Neck resistance comes forth from cytoplasm conductivity and the cross-sectional area and length of the spine neck. (E) Simplified model for spine electric circuitry, assuming that the small surface area of spines minimizes their membrane g and C. $I_{synapse}$ = synaptic current, Z_N = input impedance as defined by the dendritic electrical properties, R_{neck} = spine neck resistance. Spine EPSPs depend strongly on R_{neck}, while dendritic shaft EPSPs are mainly affected by Z_N. The dynamic regulation of spine neck geometry together with synaptic conductances allows for the adaptation of local EPSPs.*

al. 2014; Takasaki & Sabatini 2014). Besides this passive mechanism, an active mechanism where voltage-gated spine channels are recruited does underlie electrical compartmentalization as well (Araya et al. 2014). Indeed, by activating voltage-sensitive channels, spine neck resistance was revealed to reach values of 500 MΩ, thereby amplifying the depolarization in spine heads (Harnett et al. 2012). However, the exact value of spine neck resistance is still unknown, or, at least shown to have a broad range, and to be affected by high neuronal activity (Nishiyama & Yasuda 2015) such as the induction of LTP (Tønnesen et al. 2014). Indeed, it was shown that spine necks become wider and shorter upon LTP induction, thereby reducing spine neck resistance as estimated by Ohm's law (Formula 4) (Tønnesen et al. 2014). Importantly, diffusional equilibration during structural LTP seemingly does not alter because of the increase in head volume and the widening and shortening of the spine neck having inverse effects on biochemical compartmentalization (Tønnesen et al.

2014). Likewise, using mathematical simulations and STED microscopy data, upon spine neck plasticity only a minor effect was expected on somatic EPSPs, thereby emphasizing the local role spine neck plasticity plays (Tønnesen et al. 2014; Nishiyama & Yasuda 2015). Indeed, voltage signals originating from the dendrite propagate non-attenuated into the dendritic spines (Holthoff et al. 2010; Carter et al. 2012; Popovic et al. 2015), while voltage signals from the spine head towards the dendrite are filtered (Araya et al. 2006; Harnett et al. 2012; Araya et al. 2014).

Altogether, it can thus be stated that the regulation of spine structure and function is highly complex. A robust quantification of spine nanoscale morphology in a physiological relevant environment is currently lacking. In addition, the exact relation between spine morphology and spine compartmentalization remains controversial and thus needs more in depth studies. For those in depth investigations of the relationship between spine structural plasticity, spine compartmentalization, and thus synaptic functioning, it is of importance to visualize those structures. For this purpose, one can make use of fluorescently labelled cells, which can be imaged by utilizing fluorescence microscopy. However, in order to resolve the nanoscale structures of the spines, a super-resolution approach, such as stimulated emission depletion (STED) microscopy, is required.

3 STED microscopy

Fluorescence microscopy is a powerful technique, which is widely used in neuroscience and is the basis for super-resolution microscopy techniques such as stimulated emission depletion (STED) microscopy, single particle localization microscopy (PALM / STORM), and (saturated) structured illumination microscopy ((S)SIM).

3.1 Basic principles of fluorescence microscopy

In fluorescence microscopy, fluorophores are excited from the ground state (S_0) to a higher electronic state (e.g. S_1) upon the absorption of an incident photon with an energy equal to the difference between the two states (S_1-S_0), see Figure 11. The emission process from the excited state to ground state is categorized into two different radiative processes, which are fluorescence and phosphorescence. In the fluorescence process, the excited molecules will relax via vibrational relaxation of an electron to the lowest vibrational level of the excited state (non-radiative relaxation) and then relax to the molecules' lowest energy electronic state while emitting a photon (radiative relaxation). The emitted photon has a lower energy than the original excitation photon due to the vibrational relaxation, which is called the Stoke shift (range: ~20 – 100 nm). The relaxation through the vibrational levels defines the relatively broad emission spectra of the fluorophores. Similarly to regular relaxation, molecules can relax non-radiatively to the lowest vibrational level of the excited triplet state (T_1), and further to S_0 via phosphorescence or non-radiative triplet relaxation. Phosphorescence is different from fluorescence in that the absorbed photon undergoes an

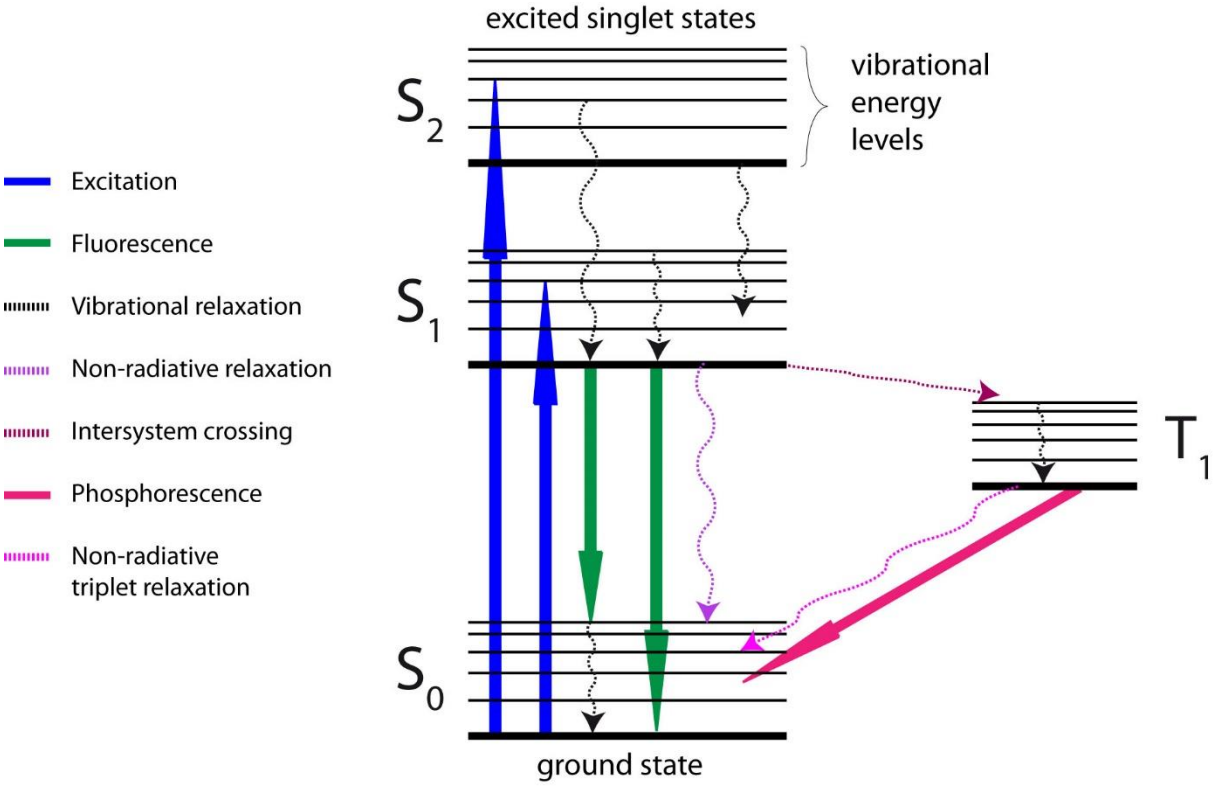

Figure 11: Energy levels and transitions of a fluorophore. *The Jablonski diagram shows the main molecular pathways upon the absorption of a single photon (blue). Transitions from and to the ground and excited singlet states ($S_0 – S_2$), as well as the excited triplet state (T_1) are shown. Both radiative (solid arrows) and non-radiative (dashed curved arrows) transitions are represented.*

unusual intersystem crossing into a higher energy state (e.g. T_1) with only "forbidden" transitions available to return to a lower energy level. This kinetically unfavorable transition due to the spin flip results in longer life times for phosphorescence than fluorescence. When molecules in T_1 react with molecular oxygen, this will alter or destroy the molecules and can accordingly lead to photo bleaching and photo damage of the sample preparation.

By making use of fluorescence microscopy and suitable fluorophores, such as green and yellow fluorescent protein (GFP and YFP, respectively), biological structures can be visualized at the cellular level with high specificity and sensitivity in living samples.

3.2 Confocal and two-photon excitation fluorescence microscopy

Confocal microscopy and two-photon (2P) excitation fluorescence microscopy are examples of laser scanning microscopy techniques and these two are amongst the most commonly used fluorescence imaging approaches in the life sciences. In confocal microscopy, fluorophores absorb a single incident photon to arrive to the excited state whereas in 2P microscopy fluorophores need to absorb two incident photons simultaneously (within ~0.5 fs; discussed in Helmchen & Denk 2005) to get to the excited state.

In confocal microscopy fluorophores are excited below and above the focused spot, and thus absorption of light occurs throughout the specimen. However, the signal is only obtained from a thin focal plane, since out of focus signals are spatially filtered by inserting a pinhole in the detection pathway at a plane conjugated to the focal plane. Thus, only ballistic (non-scattered) photons contribute to the signal, while scattered photons are rejected. Since these scattered photons are often the majority of the signal, an increase in excitation power is necessary to compensate for this signal loss, which can lead to photo-destruction of the fluorophores (photo bleaching) or photodynamic damage to the specimen (Denk & Svoboda 1997).

In 2P microscopy, excitation occurs only in the focal plane due to the steep dependence of the absorption rate on the light intensity, since the light has to be concentrated in space and time in order to generate sufficient signal (discussed in Denk & Svoboda 1997; Helmchen & Denk 2005). This allows for high optical sectioning within thick samples and accordingly reduced out-of-focus bleaching of fluorophores. Since the signal is only generated from the focal spot, and thus both ballistic and scattered photons constitute useful signal, there is no need for a pinhole in the detection pathway. The absence of a pinhole increases the amount of photons which can be detected and thus improves the signal-to-noise ratio. The longer wavelengths (near-infrared light), which are used for excitation in 2P microscopy, further reduces the chance for scattering in the thick sample and thereby enables imaging deep inside the tissue. In addition, using pulsed near-infrared light (lower average energy) reduces the chance for photo toxicity because scattered excitation light is too dilute to randomly 2P excite and too long in wavelength to be absorbed otherwise (Denk et al. 1994; Denk 1996).

Both confocal and 2P microscopy make use of an objective lens to focus the light on the sample, which creates a diffraction pattern. This phenomenon of diffraction of light leads to the theoretical resolution (Δr) of the optical system being limited as described by Abbe's formula (Abbe 1873):

$$\Delta r \cong \frac{\lambda}{2\,NA}.$$

where λ is the wavelength of the excitation light and NA the numerical aperture of the objective used. In practice, Δr represents the minimal distance at which two closely spaced objects can still be resolved. From Abbes law, it becomes clear that 2P microscopy has its inherent disadvantages. The resolution of a microscope is namely proportional to the excitation wavelength, the latter being longer in 2P microscopy (excitation wavelength ~800 nm) than in confocal microscopy (excitation wavelength ~500 nm). However, due to the non-linearity of excitation, the 2P emission PSF gets tighter, and thus the resolution improved, in 2P microscopy. Beyond this fundamental limitation, in fluorescence microscopy, the quality of the images is further determined by the aberrations of the system, absorption and scattering of light in thick tissue, and how well these phenomena are corrected.

3.2.1 Absorption and scattering of light in thick tissue

When using 2P excitation, one should keep in mind the possibility for 1P absorption, three photon (3P) effects, and second harmonic generation (SHG). While linear absorption of the infrared light is usually very low, upon usage of high excitation powers, the 1P absorption can become significant. In addition, the chance for 3P excitation is very low, as often the excitation and emission spectra of the chosen fluorophores are not conform with it and the cross-section is lower. Again, when using higher excitation powers, the chance for 3P excitation becomes higher. Together, the increased chance for 1P absorption in for example water and the increased chance for 3P effects, make very high excitation powers disadvantageous in general. While 2P excitation depends on the dye properties and is non-coherent, SHG is coherent and does not involve relaxation in vibrational levels. This virtual state will give exactly half the wavelength of the incidental photon for the emitted photon, which can thus easily be filtered out with an excitation filter in a setup. In addition, the endogenous SHG from for example microtubules is rather weak compared to the exogenous 2P excitation signals from the fluorophores. Absorption of the light by the sample preparation will lead to a loss of the signal. However, the effect of absorption on fluorescence efficiency is in most biological tissues negligible compared to scattering, and thus the focus lays here on scattering.

Scattering is the deflection of light rays from their original direction. Scattering of light in the excitation pathway will lead to lower effective excitation powers, the latter being a crucial factor in 2P microscopy. In addition, scattering of light in the detection pathway will further reduce the intensity of the signal. The probability of scattering depends on the properties of the excitation light (its wavelength) as well as the properties of the sample, such as the variation in refractive indices and the size of the object of interest (Helmchen & Denk 2005). Shorter wavelengths scatter more following Rayleighs law for very small objects ($\propto \lambda^{-4}$), and less than Rayleigh scattering for brain tissue (Oheim et al. 2001). The contribution of shorter wavelengths to the signal is thus reducing over depth and becomes minor beyond approximately one scattering mean-free-path. Depending on the type of tissue and the excitation wavelength, approximately half of the incident photons are scattered every 50 – 200 µm (~50 – 100 µm with 630 nm excitation compared to ~200 µm *in vivo* with 800 nm

excitation light; (Kleinfeld et al. 1998; Oheim et al. 2001; Yaroslavsky et al. 2002)). For imaging deep inside tissue, the confocal detection pathway is thus insufficient and attention should be paid to the detection of the scattered photons (Helmchen & Denk 2005), which is beneficial in 2P microscopy.

Taken together, with increasing depth, the amount of incident photons reaching the focus reduces (Svoboda & Yasuda 2006). The higher-angle light rays have longer paths to reach this focus and are more likely to scatter, thereby additionally decreasing the resolution of a scanning system with imaging depth. The scattering of the light rays can be quantified by the anisotropy parameter. This parameter is generally high in brain tissue (approximately 0.9) since cells are heterogeneous and have variable molecular polarizabilities (Helmchen & Denk 2005). One can compensate for the consequences of scattering by making use of higher laser powers. However, the achievable imaging depth does not infinitely increase with increasing laser power, as the sample might get damaged by the high intensity light. Even though scattering can affect signal detection, little signal loss is expected in epi-detection mode when using appropriate detectors. The area of scattered light emerging from the tissue surface is much wider than the focus is deep, and thus either detectors with a large sensitive area and a reasonable quantum efficiency are needed, or one needs to focus the emitted light onto detectors with a small sensitive area and high quantum efficiency. Lastly, scattering of light can reduce the effective numerical aperture (NA) of an objective when imaging deeper in thick tissue. This is due to the large-angle rays which are more likely to be scattered than the central rays (Helmchen & Denk 2005).

3.2.2 Optical aberrations

In optical microscopy, aberrations originating from the optical path or the sample can distort the point spread function (PSF). High NA objectives are typically corrected for astigmatism by the manufacturers. Additionally, curvature and distortion do not affect the point spread function (PSF), therefore we do not focus on these aberrations here. However, other aberrations such as coma (away from the optical axis) and especially spherical aberrations (on the optical axis) are of interest to us.

In three dimensional (3D) live imaging, one can expect spherical aberrations, that is, differential focusing of axial versus peripheral light rays. Spherical aberrations occur due to a refractive index mismatch in the optical path, especially between the sample, its type of mounting, and the immersion medium used. These aberrations result in a larger focal spot, which accordingly reduces the peak intensity of the light and the spatial resolution of the system. The correction for spherical aberrations depends strongly on the imaging depth and the presence of a glass coverslip to mount the sample. The spherical aberrations are dependent on the coverslip thickness and increase with the NA of the objective. Spherical aberrations due to the coverslip can be minimized by the use of specifically designed objectives. For example, the Plan Apo water immersion objectives with a correction collar for coverslip thickness (and thus refractive index mismatch), and additionally the use of immersion and sample media with similar refractive indices to those of the front lens of the objective and the coverslip. The correction collar's working principle relies on the movement of a set of lens elements inside the objective to adapt the space in between the several lenses in such a way that spherical aberrations become minimal. Other approaches to adjust for spherical aberrations, include the usage of adaptive optics where aberrations are both measured and corrected by compact deformable mirrors or spatial light modulators

(discussed in e.g. Booth 2007, 2014). These elements introduce an aberration that cancels out the specimen induced aberration, thereby restoring the diffraction limited focus.

In living tissue, it is usually advantageous to use a water immersion objective since it maintains its performance into depth, and reduces the difference in refractive index between tissue (brain, n ≈ 1.38) and immersion media (water, n = 1.33). However, it does not correct for usage of a glass coverslip (n ≈ 1.52) as required for *in vivo* preparations with a cranial window (such as used in the current thesis). Instead, one should consider the usage of a silicon-oil objective, which minimizes spherical aberrations due to a limited refractive index mismatch (see Fig. 12). Besides minimizing spherical aberrations, silicon-oil objectives can reach higher NA, thereby optimizing the diffraction-limited spatial resolution.

Figure 12: Reduction of refractive index mis-match by a silicon-oil objective while imaging through a glass coverslip. *Using a water-immersion objective, light rays refract differently in the immersion medium (water) and the glass coverslip, while an objective with silicon-oil immersion medium reduces the mismatch in refractive indices between the different elements (tissue, glass coverslip, medium) and thus reduces spherical aberrations. Image taken from Olympus Brochure.*

Furthermore, the use of a focusing lens is not without drawbacks, since lenses intrinsically focus different wavelengths in different positions. This phenomena is known as chromatic aberration. Chromatic aberration occurs both in the lateral and the axial axis. Especially when performing two-color experiments, the axial shift makes co-localizing two structures more challenging. The overlap of two different laser beams becomes also challenging because of the chromatic aberrations. Lateral chromatic aberrations can be minimized by only analyzing structures in the center of the imaging field. Axial chromatic aberrations can be corrected by measuring the axial offset and correct the imaging acquisition for this offset. These corrections can for example be done by using spatial light modulators or by shifting the focus and alignment of one beam before the objective. Specifically designed objectives correcting for chromatic aberrations are recommended for imaging experiments. Luckily, 2P microscopy is inherently unaffected by chromatic aberrations and can thus be seen as one of the optimal imaging approaches suitable for super-resolution microscopy.

3.3 Super-resolution approaches and the principles of 2P-STED microscopy

Besides any needed corrections, confocal or 2P excitation microscopy can possibly be used as the basis for super-resolution approaches. In order to reach super-resolution, Eric Betzig proposed that one needs to add a dimension to the conventional imaging approaches (Betzig 1995). This can either be a temporal dimension, which is used in the stochastic approaches photo-activated localization microscopy (PALM) and stochastic optical reconstruction microscopy (STORM) (Betzig et al. 2006), or a spatial dimension as used in the deterministic

approaches (saturated) structured illumination microscopoy ((S)SIM; Neil et al. 1997; Gustafsson 2005) and stimulated emission depletion (STED; Hell & Wichmann 1994; Klar et al. 2000).

The fluorophores used in PALM and STORM are activated at different time points. In PALM one makes use of conversion by wavelengths while in STORM the chemical state of the molecules is converted. The successive activation and imaging of the fluorophores results in multiple wide-field images, which each contain only a few isolated single fluorescent emitters. Due to the different subsets of fluorophores being imaged without spatial overlap, they can be localized with high precision. The super-resolution image is then generated by reconstructing the localization of each individual molecule from the many acquired images. Resolutions down to some 50 nm can be reached with PALM and STORM. However, in PALM and STORM, one makes use of a total internal reflection angle, and thus an evanescent wave, to illuminate the sample. Therefore, the light does not penetrate into the tissue (~100 nm), which limits the imaging depth. In addition, the acquisition time is rather long (in the minutes range) and intensive post-processing of the images is required.

A technique, which requires less intense post-processing than PALM/STORM and which can penetrate deeper into the tissue (up to 20 µm), is structured illumination (SIM). In SIM, a sinusoidal illumination pattern is applied to the sample, which generates a Moiré pattern at a much lower spatial frequency than that of the sample structures. By rotating and scanning the excitation pattern over the sample, multiple wide-field images are acquired. Those images are then used to reconstruct the sample structure at high resolution. However, the resolution obtained in SIM (down to ~100 nm) is lower than in PALM/STORM and the approach still requires post-processing of the images. Furthermore, in regular SIM, fine structures with spatial frequencies well above the excitation pattern are not better resolved, as mixing the two frequencies (sample and excitation pattern) does not generate a lower spatial frequency in the Moiré pattern. This can be overcome by making use of saturated SIM (SSIM), where a high frequency component is used in the excitation pattern, thereby allowing structures with a size far below the diffraction limit to be resolved.

The diffraction limit can also be bypassed by utilizing the process of stimulated emission depletion (STED). In STED microscopy, the excited states of fluorescent molecules are spatially controlled, which leads to a reduced size of the effective point spread function (PSF) and thus a direct increase in spatial resolution. This approach allows for imaging deeper inside tissue (~40 µm) than the previously discussed approaches, without losing resolution (~50 nm). The biggest advantage of STED microscopy is that the super-resolution image is directly obtained, and thus no post-processing of the images is required.

Similar to conventional fluorescence microscopy, in STED microscopy fluorophores are used to label and visualize biological structures of interest. However, in addition to the excitation of the fluorophores from their ground state to their excited state, part of the molecules in the excited state are forced back to their ground state (‘quenched’) before spontaneous fluorescence occurs (see Fig. 13). This stimulated emission will only occur if the photons from a second laser exactly match the energy difference between the ground state and the excited state. The photon emits in the propagation (forward) direction and can hence be

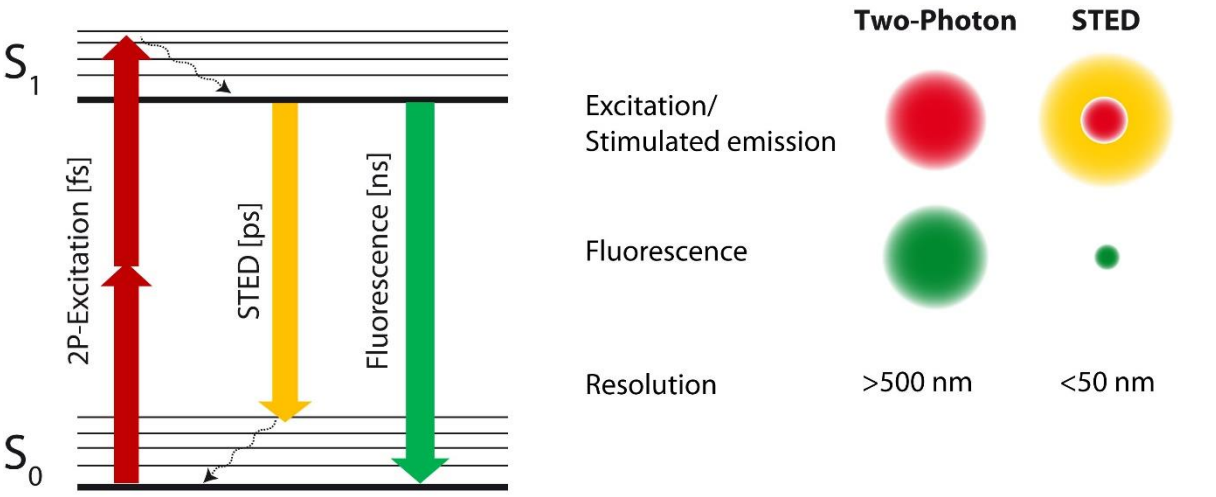

Figure 13: The 2P-STED principle. *Left: In 2P-STED microscopy, molecules are excited by the coincident arrival of two photons of the same wavelength, together spanning the difference in energy between the ground state (S_0) and the first excited singlet state (S_1). A red-shifted STED beam quenches the excited molecules before actual fluorescence can take place. Right: The effective excitation PFS is reduced by the doughnut-shaped STED PSF and thus a higher resolution can be obtained, allowing for the separation of closely spaced structures.*

separated from the excitation and signal light, as it is not detected in the backward direction. This principle was first described by S.W. Hell (Hell & Wichmann 1994), and in theory allows for diffraction-unlimited resolution. However, in practice the resolution is nevertheless limited by the properties of the used lasers, as well as the previously discussed aberrations of the optics, and fluorophore stability.

Because of the advantages of pulsed 2P excitation and its shown compatibility with STED microscopy (Ding et al. 2009; Li et al. 2009; Moneron & Hell 2009; Bethge et al. 2013; Takasaki et al. 2013), the focus here lays on 2P-STED microscopy. The longer wavelength of the STED light can be easily separated from the fluorescence signal by standard optical filters and dichroic mirrors. In addition, the chance for direct excitation of the fluorophores by the STED light is reduced since the longer wavelength is further away from the excitation spectrum. The Gaussian STED beam is modulated by a helical vortex phase plate to create a vortex of light, the intensity distribution of which is still doughnut-shaped upon travelling through a focusing lens and being projected on a flat surface. The doughnut-shape allows for depletion of the fluorescent molecules in the outer rim of the excitation signal (see Fig. 13). In addition, the deep zero-intensity of the doughnut-shaped STED beam allows for specific collection of fluorescent signals from the center of the PSF. The size of the center can be adjusted by in- or decreasing the intensity of the STED laser, which results in a smaller or bigger (respectively) PSF, which can be described by:

$$\Delta r = \frac{\lambda}{2 \times NA \times \sqrt{1 + I_{STED}/I_S}},$$

with I_{STED} being the intensity of the STED beam used and I_S the intensity of the STED beam at which half of the molecules are quenched (Harke et al. 2008). By using a high intensity doughnut-shaped STED beam, saturation of the quenching process can be reached, thereby allowing for an effective PSF, and thus resolution, below the diffraction limit (see Fig. 13). However, in order to perform STED imaging in live tissue, the STED laser power should not

be too high, otherwise the cellular structures will get damaged by the produced heat upon absorption of the high light intensities. The use of pulsed lasers offers an efficient way to overcome this limitation. Indeed, the pulsed light allows for low average powers, which preserves the sample while imaging, and at the same time provides high peak intensities, which ensures the super-resolution. Since the quasi-simultaneous absorption of multiple photons necessitates a high temporal and spatial photon density, pulsed light is indeed required for multi-photon excitation, and can also be used for the STED light in order to force molecules to their ground state. After 2P absorption, molecules in the excited state decay non-radiatively within several picoseconds before to spontaneously fluoresce on the nanosecond timescale, and thus a long STED pulse would be more effective for optimal quenching of the molecules. Moreover, a long STED pulse decreases the peak intensity, and thus reduces the chance for 2P excitation by the STED beam. Altogether, the usage of pulsed excitation and pulsed depletion light leads to more efficient quenching of the fluorescent signal. The use of multiphoton excitation allows to excite fluorophores deep within tissues. However, since the super-resolution relies on the quality of the STED beam, which drastically decreases in depth, the depth penetration of 2P-STED is actually limited by the single photon STED light and further depends on the sample properties and brightness of the label. Nevertheless, the advantage of 2P-STED over 1P-STED is the reduced chance for photo bleaching and – damage, especially outside the focal plane. Further, 2P-STED microscopy is, as many other super-resolution approaches, a compromise of achievable signal intensity, maximum reachable imaging depth and highest obtainable resolution. Despite the challenges of super-resolution microscopy, many scientists believe that the nanoscale morphology of cells is of importance for their function and thus the scientific community continued to develop STED as an imaging modality in the life sciences.

3.4 Development of STED as imaging modality in the life sciences

In neuroscience, it has long been very challenging to study subdiffraction-limited sized structures such as the postsynapse in live tissue, an issue which can be circumvented by the use of the STED principle. The first proof of the STED principle after its invention (Hell & Wichmann 1994) was delivered by Klar and colleagues in 2000 (Klar et al. 2000), but its application to neuroscience research manifested only 6 years later with studies precisely localizing synaptic proteins, which were immuno-labeled in fixed neuronal cultures (Sieber et al. 2006; Kittel et al. 2006; Willig et al. 2006). Using STED microscopy, the spatial organization of the presynaptic protein Bruchpilot could be resolved (Kittel et al. 2006), as well as the nuclear protein SC35 (Donnert et al. 2006), and various other biological structures (Wildanger et al. 2009). The vesicular soluble NSF attachment protein reporter (SNARE) protein synaptotagmin-1 was found to stay clustered in the cell membrane upon synaptic vesicle fusion (Willig et al. 2006) and dual-color isoSTED with its improved axial resolution could show that those clusters are in the vicinity of the axonal active zones (Schmidt et al. 2008).

When comparing STED to other super-resolution techniques such as SIM and the stochastic approaches PALM and STORM, STED achieves a satisfying temporal resolution while keeping a high spatial resolution. In addition, STED has been demonstrated to be capable of both

dual (Donnert et al. 2007; Pellett et al. 2011; Tønnesen et al. 2011) and 3-color imaging (Bückers et al. 2011). Moreover, STED microscopy can be combined with 2P excitation to image for example microtubules in immuno-labeled cells (Bianchini et al. 2012). By using continuous wave fiber lasers for fast STED microscopy, vimentin filaments and the endoplasmic reticulum (ER) of living cells could be studied (Moneron et al. 2010). Another combination, namely those of selective plane illumination microscopy (SPIM) and STED, was used to image structures at high-resolution and fast acquisition deep inside zebrafish embryo (Friedrich et al. 2011). Furthermore, nicotinic acetylcholine receptor's nanoscale organization (Kellner et al. 2007) was investigated, and with the STED approach single clusters of SNARE proteins in neuroendocrine PC12 cells could be measured (Sieber et al. 2006). Besides that, the nanoscale morphology and dynamics of the ER (Hein et al. 2008) as well as the localization of β_1-integrin were revealed with STED microscopy (Schröder et al. 2009). Additionally, phosphatidylinositol-4,5-bisphosphate (PIP_2) clusters were quantified using STED microscopy and were found to be much smaller than originally thought (van den Bogaart et al. 2011). The listed studies are not exhaustive, but demonstrate the power of STED in neuroscience and more generally in biology.

In the last decade it has been demonstrated that STED imaging can also be performed on more complex live materials, both in single and multicolor (Sidenstein et al. 2016). The STED laser intensities were similar to those used in 2P imaging, while also still achieving super-resolution (Nägerl et al. 2008; Rankin et al. 2011). STED microscopy allowed for the topological mapping of various synaptic proteins (Liu et al. 2011; Blom et al. 2011; Blom et al. 2012; Blom et al. 2013). In cultured brain preparations, such as dissociated neurons and organotypic brain slices, it was possible to image the dynamics of synaptic vesicles in nerve terminals, as well as the fine morphological changes of dendritic spines (Westphal et al. 2008; Nägerl et al. 2008). It was furthermore shown that the movement of vesicles is more rapid outside axonal boutons compared to within the boutons (Westphal et al. 2008), with newly endocytosed vesicles being highly mobile before getting immobilized into clusters for proper reorganization (Kamin et al. 2010; Hoopmann et al. 2010). The STED approach is not limited to only describing nanoscale structures, as it can be combined with other techniques for physiological readouts, such as patch-clamp electrophysiology, 2P glutamate uncaging, and other (optical) techniques. For example, the combined use of STED and fluorescence correlation spectroscopy (FCS) revealed the nanoscale dynamics of lipids in the living cell (Eggeling et al. 2009; Müller et al. 2012). In addition, the combined use of multiple of the aforementioned techniques also allowed for the discovery of spine neck plasticity and its role in the compartmentalization of synapses in cultured brain slices (Tønnesen et al. 2014). An interesting study recently showed that an all-optical method can also be used to study dendritic spine morphology upon stimulation of these spines (Lauterbach et al. 2016). The authors showed that upon holographic stimulation and imaging with STED microscopy, spines would first compact and then further shrink, while non-stimulated spines did not change their nanoscale morphology (Lauterbach et al. 2016).

Nowadays, STED microscopy and its applications are no longer limited to cultured slices (Urban et al. 2011; Willig & Nägerl 2012), since it has also been successfully extended to thick tissue preparations, with imaging being possible both in single and dual color

(Tønnesen et al. 2011). The nanoscale structure of dendritic spines could be studied, and it was shown that it is dynamic and prone to morphological changes upon induction of long-term potentiation (LTP; (Urban et al. 2011)). The adaptation of STED microscopy with 2P excitation has been proven successful not only in fixed cells/fluorescent spheres but also in acute brain slices (Moneron & Hell 2009; Ding et al. 2009; Bethge et al. 2013). Reversible saturable optical fluorescence transition (RESOLFT) microscopy, which is a more generalized formulation of the STED approach, generally allows for deep-tissue imaging too, advantageously with low light intensities in large field of views (Hofmann et al. 2005; Grotjohann et al. 2012; Chmyrov et al. 2013). In hippocampal slice cultures, it enabled the study of spine morphology and revealed rearrangements in actin filaments in baseline conditions and upon stimulation (Testa et al. 2012). Besides the recent development of all-optical cell stimulation and monitoring (Lauterbach et al. 2016), 3D-STED by using adaptive optics in specimen prone to aberrations (Gould et al. 2012) may be a promising tool to perform STED microscopy *in vivo*.

3.5 STED microscopy *in vivo*

As pointed out by Schnorrenberg and colleagues, *in vivo* nanoscopy is rarely realized and unsatisfactorily established (Schnorrenberg et al. 2016). *In vivo* imaging has been shown in the fairly simple organism C. elegans as well as in D. melanogaster (Rankin et al. 2011; Schnorrenberg et al. 2016). Further, using RESOLFT the microtubule network in living transgenic flies could be visualized with super-resolution (< 60 nm), relatively low light intensities and short irradiation times (Schnorrenberg et al. 2016). With the development of instrumentation, such as the parallelized STED microscopy approach (Yang et al. 2014), and labelling approaches, it is expected that *in vivo* nanoscopy will be further expanded to other multicellular organisms as well (Schnorrenberg et al. 2016). The group of S.W. Hell lately did indeed show that nanoscopy could be applied to other *in vivo* preparations. They showed that dendritic spines could be resolved in the cortex of a living mouse by STED microscopy and that subcellular protein structures could be studied *in vivo* (Berning et al. 2012; Willig et al. 2014). Even though little quantification was done, by investigating the actin network they could resolve morphological plasticity in the brain (Willig et al. 2014). The authors suggest that *in vivo* STED microscopy will thus help provide insights into the basic working principles of the brain (Willig et al. 2014).

Based on the previously described literature (chapter 1 – 3), one can think of many biological structures which might require approaches that reconcile nanoscale spatial resolution with an intact tissue environment. For example, since previous studies showed that spine morphology plays an important role in synaptic functioning, it is of great interest to study spine morphological dynamics in the most intact state possible. However, the nanoscale morphological parameters of spines (e.g. neck width) cannot be properly resolved with conventional light microscopy, and thus little is known about their nanoscale changes in the intact brain. Likewise, the particularly small processes of glial cells are only poorly resolved by conventional imaging approaches. It would thus be of great interest to apply STED microscopy to those nanoscale structures and study them in their intact environment.

4 AIMS

As discussed in the previous chapters, only little is known about the effect of small changes in spine and/or glial process morphology on synaptic physiology. This might be due to the lack of resolution in conventional light microscopy approaches. Since the dynamic nanoscale changes of spine morphology have been suggested to influence spine compartmentalization, the need to study this structure-function relationship with high resolution is emphasized. In addition, astrocytic processes and in particular the changes in their nanoscale morphology, have been suggested to play an important role in synaptic transmission. To investigate this subcellular interaction, it is thus necessary to study both neuronal and astrocytic elements in great detail. Thus, again, there is a need for a super-resolution approach to elucidate these nanoscale structural dynamics.

One super-resolution approach suitable for live tissue imaging, is two photon excitation stimulated emission depletion (2P-STED) microscopy. With this approach, one obtains a higher resolution than with regular 2P microscopy, while maintaining low average excitation/depletion powers due to the pulsed light. The advantage of 2P-STED over 1 photon excitation STED is that the chance for out-of-focus photo bleaching and damage is smaller due to the characteristics of 2P excitation. Since quenching with multiphoton STED light would possibly require such high laser powers that it would damage the sample, single photon STED light is commonly used. These shorter wavelengths do however scatter more and thereby limit the maximum achievable imaging depth of any 2P-STED system.

However, applying 2P-STED microscopy *in vivo* offers the opportunity to overcome the otherwise diffraction-limited resolution of conventional light microscopy and thus allows us to study the nanoscale morphology of dendritic spines and glial processes in the barrel cortex of anesthetized mice. We hypothesize that dendritic spine morphology is variable at the nanoscale *in vivo*. We further hypothesize that this variability in nanoscale morphology will accordingly affect *in vivo* spine compartmentalization. In addition, we are interested in the neuron–glia interaction at a subcellular level and thus the main goals of my PhD thesis were the following:

1) To establish *in vivo* super resolution microscopy in mouse barrel cortex

2) To examine the morphological nanoscale dynamics and compartmentalization of dendritic spines *in vivo*

3) To establish super-resolution (dual color) imaging of spine-glia interactions *in vivo*

The different topics will be discussed in the rest of the thesis as follows: (i) Part 1 describes the implementation of *in vivo* 2P-STED microscopy and elaborates on 2P-STED microscopy and its application as a tool to image dendritic spines *ex*- and *in vivo*, (ii) Part 2 covers the nanoscale morphology of dendritic spines, their dynamics, and their relation to biochemical compartmentalization *in vivo*, and (iii) Part 3 describes a novel approach to study spine-glia interactions *in vivo*. All those results are put in perspective in the Discussion, which is followed by a list of references and supplementary information.

5 MATERIALS AND METHODS

5.1 Animals

Mice were kept under a 12 h light/ 12 h dark cycle with *ad libitum* access to food and water. All experiments were carried out in accordance with the European directive on the protection of animals used for scientific purposes (2010/63/EU), approved by the Ethic Committee N°50 of Bordeaux, and is under review by the Ministry of the Higher Education and Research.

In this study we used transgenic adult (post-natal day (P) 55 – P75) male mice (Jackson Labs, Bar Harbor, ME) which were implanted with a cranial window and acutely imaged at the indicated age. Firstly, Thy1-YFP-H mice that express YFP in a subpopulation of pyramidal neurons in the hippocampus as well as in layer 4/5 of cortex (Feng et al. 2000), and second, double transgenic mice, which were obtained from crossbreeding Thy1-YFP-H homozygous female ($Thy1^{eYFP}/^{eYFP}$) with a Cx3CR1 homozygous ($Cx3CR1^{eGFP/eGFP}$) male mice were used. The resulting progeny ($Thy1^{+/eYFP}$ x $Cx3Cr1^{+/eGFP}$) expresses GFP in all microglial cells (Jung et al. 2000) and YFP in pyramidal neurons in the hippocampus and layer 5 of the cortex. Third, a Thy1-YFP-H homozygous female ($Thy1^{eYFP}/^{eYFP}$) was crossbred with a homozygous GFAP male ($GFAP^{eGFP}/^{eGFP}$) in order to obtain $Thy1^{+/eYFP}$ x $GFAP^{+/eGFP}$ crossbred mice expressing GFP in astrocytes containing GFAP (Zhuo et al. 1997) and YFP in pyramidal neurons in the hippocampus and layer 4/5 of the cortex. Wildtype (WT) mice on a C57BL/6 background (Jackson Labs, Bar Harbor, ME) were used for testing the different viral labelling strategies.

5.2 *In vivo* surgery – window implantation

Male mice in the age range of P55 – P75 were implanted with a cranial window. All surgical devices were pre-sterilized and the chronic cranial windows were implanted in the barrel cortex as previously described (Holtmaat et al. 2009).

In short, mice were intraperitoneally and intramuscularly injected with buprecare (buprenorphine, Centravet; 10x diluted in PBS, 100 µl per 30 gram mouse) and dexamethasone (dexadresone, Centravet; 30 µL at 4mg/mL), respectively, 25 minutes before anesthesia induction at 4% isoflurane (Vetflurane, Centravet) at a 1 L/min flow rate of oxygen. Mice were maintained under anesthesia at 1.5 % isoflurane at 0.6 L/min flow rate of oxygen, and subsequently placed on a heating pad to keep body temperature at 36°C. An anal probe to measure body temperature was inserted and eye ointment (Ocry gel) was applied. Hereafter, mice were injected subcutaneously with Lidocaïne 2% (Lurocaïne®) and the skin was treated with Lidocaïne 2% cream (Xylocaïne®). The area for incision was disinfected with betadine, upon which the incision was made in the skin. The surface of the skull was then cleaned of any remaining tissue and roughened for a better adhesion of the liquid glue (Loctite Colle SuperGlue 3 Liquide) fixing the head holder to the skull. A helmet from dental cement (Palavit® G, Heraeus; resin and dental cement powder) was created for a more stable fixation of the head holder and a craniotomy of 3 mm in diameter was performed above the barrel cortex (see Fig. 14a), that is, approximately 1 mm anterior-posterior (AP) and laterally (L) 3 mm of bregma. The opened skull was rinsed with cortex

buffer (123mM NaCl, 5mM KCl, 10mM Glucose, 10mM Hepes, 2mM $CaCl_2$, and 2mM $MgSO_4$; at pH = 7.3) and coagulant sponges (Gelita no. 2, ref. 2070014) were used to get rid of any bleeding that occurred. A 0.15 ± 0.02 mm glass coverslip with a 3 mm diameter (#1 Cover Glass, Small Diameter 3mm (100), CS-3R, Cat:64-0720, Warner Instruments, 203-776-0664) was gently positioned on the brain and sealed with gel glue (Loctite Colle SuperGlue 3 Power Flex). Gel glue was left to dry for 10 minutes, after which mice were placed below the objective of the microscope for acute imaging (see Fig. 14b,c).

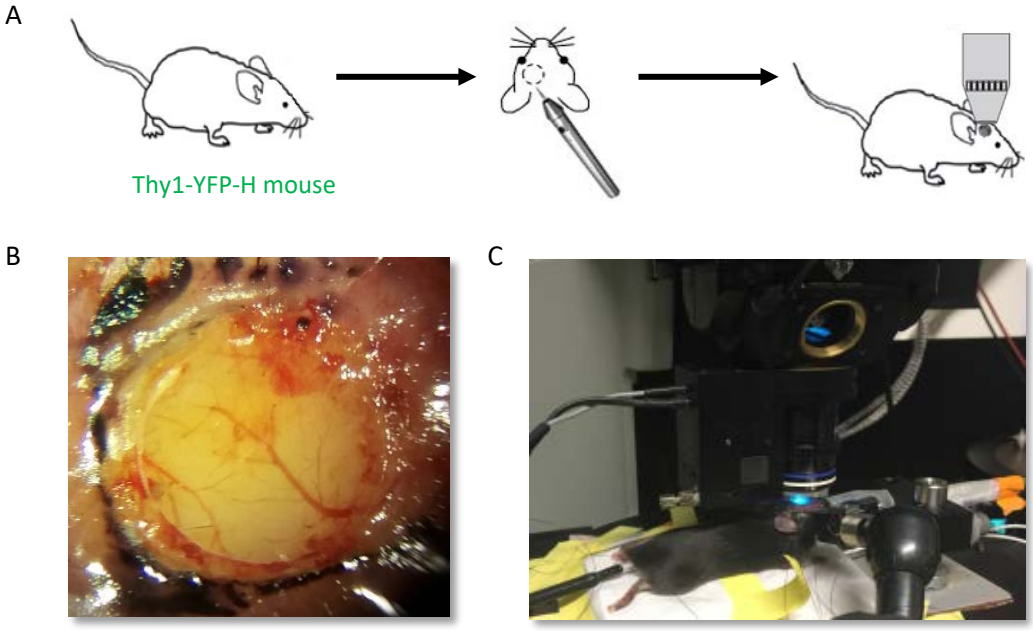

Figure 14: Representation* in vivo *surgery and imaging. *(A) Schematic representation of the implementation of a cranial window in the Thy1-YFP-H mouse and subsequent positioning below the objective. (B) Live image of the cranial window, showing the sealing of the coverslip with gel glue. (C) Live example of the position of the mouse below the objective in our system.*

5.3 Viral infection

5.3.1 Synthesis of constructs and viral particles

Construction of the pZac2.1-gfaABC$_1$D-Clover, pZac2.1-gfaABC$_1$D-GFP, pZac2.1-gfaABC$_1$D-Lck-Clover, and pZac2.1-gfaABC$_1$D-Lck-GFP plasmids from an original plasmid adeno-associated virus (AAV) vector (Addgene, plasmids from Baljit Khakh lab) was performed by Julie Angibaud (a technician in the Nägerl group). Additionally, she produced the new AAVs, the backbone of which (AAV2/1) was a kind gift from Luigi Bellochio (University of Bordeaux, INSERM U862, Bordeaux, France).

5.3.2 Stereotactic injection

In order to specifically label cortical astrocytes, a nanofil syringe (World Precision Instruments, Inc.) was back-filled with AAV2/1.GFAP-GFP (a kind gift from Luigi Bellochio), AAV2/1.gfaABC$_1$D-Clover, or AAV2/1.gfaABC$_1$D-Lck-Clover. Male mice in the age of P23 - P27 were anesthetized with 4 % isoflurane at a 2 L/min flowrate of oxygen, and to maintain anesthesia 2 % isoflurane at a 0.4 L/min flowrate of oxygen was used. Eyes were protected with eye ointment (Ocry gel), and the mice were subcutaneously injected with Lidocaine 2%

(Lurocaïne®). Upon incision a small drill bit was used to make a tiny craniotomy via which the virus could be applied. The syringe was inserted and positioned in the second/third cortical layer of the barrel cortex. The virus injection was stereotactically guided (AP = - 1 mm, L = + 3 mm from bregma) into the tissue at a rate of 500 nL/min, with a total injection volume of 1200 - 1500 nL per site. After injection the syringe was kept in the brain tissue for 3 minutes and then slowly retracted from the brain tissue to have a total of 5 minutes for the virus to spread out in the brain. Subsequently, the skin was stitched back together and mice were placed on a heated pad in a ventilated cage for recovery. After 1 hr of recovery they were placed back in their home cage and provided with *ad libitum* food and water access. Experiments were conducted 6 weeks post-injection, giving bright GFP or Clover expression while preserving the physiological health of the cells as tested online by visual inspection and post-hoc with immunohistochemistry.

5.4 Immunohistochemistry and confocal imaging

Six weeks following injection, WT and Thy1-YFP-H animals were perfused with phosphate buffered saline (PBS) followed by 4 % paraformaldehyde (PFA). Brains were post-fixed in 4 % PFA for 18 hours and sunk in PBS. 40 µm thick sections cut on a vibratome (Leica VT1200S) were stained with one or more of the following antibodies: Chicken anti-vimentin (ABCAM, ab24525; 1:1000), Rabbit anti-GFAP (DAKO, Z0334; 1:1000), and mouse anti-MAP2 (Sigma Aldrich, M9942; 1:1000). As secondary antibodies we used the following: TRITCH (Jackson ImmunoResearch, 103-025-155; 1:500), Alexa Fluor 647 (ABCAM, ab150107; 1:500), Alexa Fluor 568 (ABCAM, ab175471; 1:500); with the fluorophore conjugated antibodies raised against the appropriate species. Sections were dehydrated and mounted with a moviol embedding medium including DAPI (VectaShield) to counterstain the sections. Images were acquired via the LAS AF (Leica) software on the confocal SP8 system (Leica) at the Bordeaux Imaging Center (BIC) in Bordeaux, France. Image acquisition parameters were generally set to 1024 x 1024 pixels at an imaging speed of 700 Hz, having 142.49 nm pixel size and 600 ns pixel dwell time. Sequential scans with 4 line averages were done, as well as a 4-steps autofocus. Images were exported from the LAS AF software into a 16-bit or 8-bit tiff file format. NIH ImageJ was then used for processing of the acquisitions, such as creating maximum intensity projections and the application of a 1-pixel median filter.

5.5 Upright two-photon STED setup

For *in vivo* imaging of dendritic spines and astrocytes in layer 1 of mouse barrel cortex, we used a home-built two-photon (2P) STED microscope based on pulsed excitation and depletion (Fig. 15). The microscope was constructed around a standard upright microscope (BX51WI, Olympus) using a 60x, 1.1 NA water-immersion objective with a long working distance (1.5 mm) and equipped with a correction collar (LUMFI, Olympus) or a 60x 1.3 NA silicon-oil objective with a shorter working distance (0.3 mm) and equipped with a correction collar (UPLSAPO, Olympus). The system used pulsed 2P excitation at ~908 nm and 80 MHz (Ti:Sapphire (Ti:Saph) laser, Tsunami, Spectra-Physics) and pulsed quenching at 598 nm, the latter being generated by the combination of a femtosecond mode-locked Ti:Saph laser (834 nm at 80 MHz, Chameleon, Coherent) and an optical parametric oscillator (OPO BASIC Ring fs, APE). Before combining the 2P and STED beam with a dichroic mirror, the 2P beam

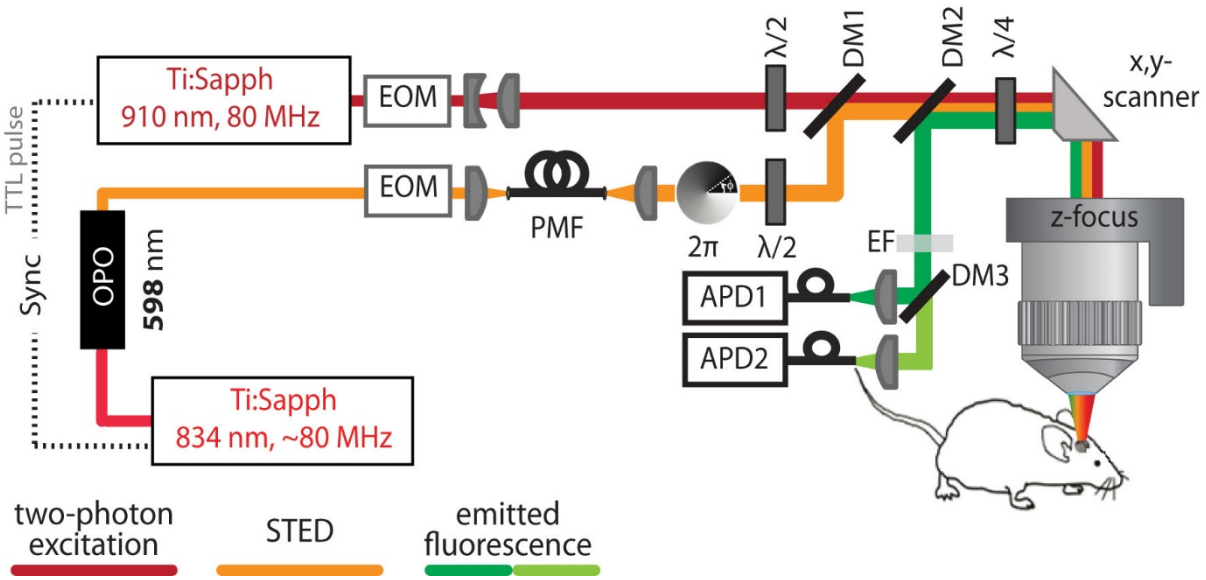

Figure 15: Schematic of the setup. *Simplified schematic of the setup showing the excitation, STED, and emission beam pathways to the various optical components as described in the main text. OPO = Optical Parametric Oscillator, EOM = Electrico-Optical Modulator, PMF = Polarization Maintaining Fiber, 2π = helical 2π phase mask, λ/2 = half-wave plate, DM = Dichroic Mirror, λ/4 = quarter-wave plate, EF = Excitation Filter, APD = Avalanche PhotoDiode.*

diameter was expanded by a factor of 2 by a telescope to sufficiently overfill the back aperture of the objective. The STED light pulses were pre-widened using a glass rod and subsequently the beam was coupled into a 20 m long polarization maintaining single-mode optical fiber to create the optimal pulse length (around 100 ps) and laser propagation mode (TEM_{00}). A helical 2π phase mask created the doughnut-shaped STED beam. Its shape was then fine-tuned by adjusting a half-wave and quarter-wave plate. Laser intensities were controlled by electro-optical modulators (EOM, Conoptics) and scanning of the sample with the two laser beams was enabled by a telecentric scanner (Yanus IV, TILL Photonics) with a customized scan and tube lens combination. The z-position of the objective was controlled by a piezo actuator (P-721 PIFOC, PI Physik Instrumente) and emitted fluorescence was detected in de-scanned mode. The emitted fluorescence was sent via a long-pass dichroic mirror towards the detectors. The emitted fluorescence of two green fluorophores, such as GFP and YFP, could be spectrally separated via a dichroic mirror and was eventually focused into optical multi-mode fibers, which were coupled to avalanche photo diodes (APDs). Image acquisition was controlled by the IMSpector software (courtesy of A. Schönle, Max Planck Instituite for Biophysical Chemistry, Göttingen, Germany) via data-acquisition cards (PCI 6259 M DAQ, 2090A, National Instruments).

5.6 Image acquisition

5.6.1 2P-STED imaging of dendritic spines

Anesthesia levels during image acquisition were set to an oxygen supply of 0.6 L/min with 1.5 % isoflurane. At these rates the breathing of the mouse was calm and abdominal, thereby reducing vibrations of the brain compared to diaphragmatic breathing. The parameters of acquisition were set so that neither apparent photo damage nor excessive

photo bleaching was occurring over the course of the experiment. Image acquisitions were performed with an excitation power of ~12 mW and a STED power of ~28 mW (objective back aperture measurements). The image stacks for the analysis of spine morphology were acquired with a voxel size of 19.5 nm (xy), 500 nm (z), and a pixel dwell time of 10 µs, unless stated otherwise. Single frames were extracted for comparison of spines in 2P and 2P-STED mode in the same focal plane. Imaging into the depth of layer 1 of the barrel cortex was determined by the z-piezo focus, with the fluorescence on top of the brain defining the reference z-position, and ranged between 30 – 90 µm. Z-stacks of 20x20x10 µm (x, y and z dimensions, respectively) were acquired for morphological investigation of dendritic spines, while z-stacks of 20x20x5 µm with a pixel dwell time of 5 µs were acquired every 1 min for 5-6 minutes and/or every ~10 min for 1 hour for analysis of spine morphological dynamics.

5.6.2 Dual color 2P-STED experiments and imaging astrocytes alone

Similar to 2P-STED experiments on dendrites, parameters of acquisition were set to minimize photo damage and bleaching over the course of the experiment. Excitation power was similar as described above. The image stacks of astrocytes alone were acquired with a voxel size of 19.5 nm (xy), 250nm (z), and a pixel dwell time of 2 - 5 µs for the small field of views (FOVs). Larger FOV image stacks were acquired with a voxel size of 195 nm or 97.6 nm (xy), 500 nm or 1 µm (z), and a pixel dwell time of 10 µs, unless stated otherwise. Full stacks were extracted to compare 2P and 2P-STED images of astrocytic processes. The imaging depth within layer 1 of the barrel cortex was determined by the z-piezo focus similar to the 2P-STED experiments on spines, and ranged between 15 – 45 µm. Z-stacks of 100x100x10 µm (x, y, z) and 50x50x20 µm (x, y, z) were acquired to investigate astrocytic labelling in large FOVs, while z-stacks of 10x10x1 µm (x, y, z) were acquired to compare 2P and 2P-STED images of astrocytic processes in a smaller FOV. The image stacks of spine-glia interactions were acquired with a voxel size of 39nm (xy), 500nm (z), and a pixel dwell time of 5 µs for the small FOVs. Larger FOVs image stacks were acquired with a voxel size of 195nm (xy), 1 µm (z), and a pixel dwell time of 10 µs. The imaging depth within layer 1 of the barrel cortex was determined by the z-piezo focus and ranged between 30 – 50 µm. Z-stacks of 100x100x20 µm (x, y, z) and 50x50x10 µm (x, y, z) were acquired to investigate spine-glia co-appearance in large FOVs, while z-stacks of 20x20x5 µm (x, y, z) were acquired to allow for 2P and 2P-STED image comparison of spine-glia interactions in a small FOV.

5.6.3 FRAP experiments on dendritic spines

The 2P laser beam was used for both bleaching of YFP in - and 2P-STED imaging of - the dendritic spines. The bleaching was performed by line scanning the spine head for a period of 20-30 ms, concomitant with 2P excitation line scanning to read out fluorescence levels. Bleaching power was around 40 mW in the back aperture of the objective, with the power being adjusted so that bleaching levels were in the range of 40 – 70 %. Before bleaching, a 0.5 s baseline scan of fluorescence was performed, while after bleaching at least 3 s of scanning was done to measure fluorescence recovery.

5.7 Image analysis

Images of neuronal and astrocytic structures as well as the raw FRAP measurements were exported from IMSpector into a 16-bit tiff file format. NIH ImageJ was then used for processing of the images. Image analysis was done on raw data of single frames and images presented in the figures were filtered by a 1- or 2-pixel median filter to reduce noise. Regions of interest were visualized by performing a maximum intensity projection (MIP) of the z-stacks.

5.7.1 Analysis of spine morphology

To automatically measure the full width at half maximum (FWHM) of spine necks, as well as to measure spine neck length and spine head volume, a custom made ImageJ plugin was used (courtesy of Florian Levet, Institute Interdisciplinaire de NeuroSciences, UMR 5297 CNRS, Bordeaux, France). At multiple positions on the spine neck, the plugin automatically estimated the best fit orthogonal to the skeleton and plotted the intensity profile (Fig. 16). Having multiple fits in parallel helped to find the best measurement for smallest neck width, as it reduced the noise coming from single measurements and the imaging itself. The FWHM value could then be extracted from the non-linear Gaussian fits of the intensity profiles. Spine length and spine neck length values could be obtained from the skeleton of the structures in the ROI and by indicating the edges of dendrite-neck and neck-head. For spine head size an ellipsoid was fitted to the manually indicated edges of the spine head, thereby allowing for an estimation of spine head volume (see Fig. 16).

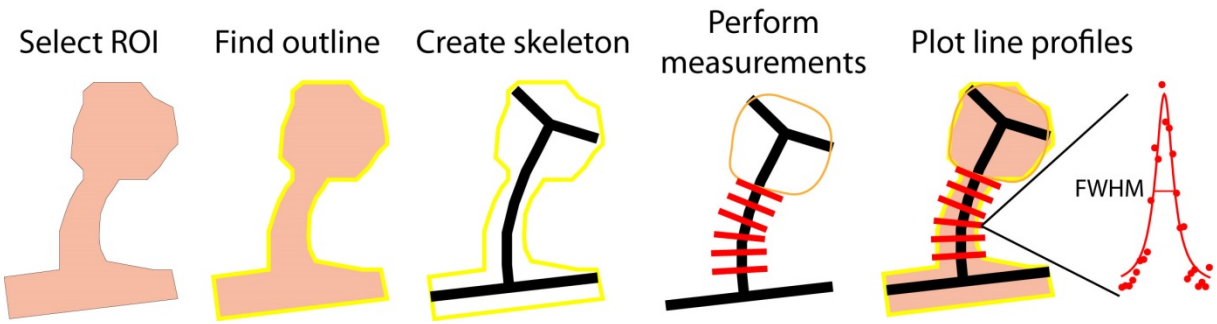

Figure 16: Schematic of spine analysis plugin. *The steps taken within the custom-made ImageJ plugin in order to measure spine morphological parameters. First the region of interest (ROI) is selected, then an outline and skeleton are created upon which measurements rely. The measurements at given positions allow for the plotting of line profiles and determination of full-width at half-maximum (FWHM).*

5.7.2 Analysis of FRAP experiments

Fluorescence recovery after photobleaching (FRAP) was plotted as emission intensity versus time and fitted with a single-exponential function ($y = a\,(1 - e^{-bx}) + c$) in ImageJ. The recovery time constant (τ) could be derived from the fit ($\tau = \frac{1}{b}$), with the average τ value of 2-3 repeats per spine being used for further statistical analysis.

Calculated τ was based on the morphological parameters' values found with 2P-STED imaging and was calculated as following:

$$\tau_{calc} = \frac{V_{head} L_{neck}}{D_{YFP} A_{neck}} \qquad (1),$$

where V_{head} is the volume of the spine head estimated by an ellipsoid, L_{neck} the length of the spine neck, D_{YFP} the diffusion coefficient of YFP (assumed to be 16 μm^2; Petrásek & Schwille 2008), and A_{neck} the cross-sectional area of the spine neck.

Spine neck resistance was estimated either based on morphology (Ohm's law) or on diffusion (Fick's law) (Svoboda et al. 1996), as calculated by

$$R_{morph} = \frac{\rho L}{A} \quad (2)$$

and

$$R_{\tau} = \frac{\tau \rho D}{V} \quad (3),$$

where ρ is cytoplasmic resistivity (assumed to be 150 Ω cm, (Major et al. 1994; Nevian et al. 2007)), L is neck length, A is the neck cross-sectional area, τ the diffusion time constant, D the diffusion coefficient (assumed to be 16 $\mu m^2/s$, Petrásek & Schwille 2008), and V is the spine head volume.

5.7.3 Deconvolution of astrocyte images

In order to increase the signal to noise ratio, images of astrocytes were treated with Huygens software for deconvolution for visualization purposes only. The amount of iterations for deconvolution ranged from 3 – 12, but was in general 6 iterations for astrocytes alone and 3 iterations for spine-astrocyte interactions. Two channel signal detection was linearly unmixed to visualize spine-astrocyte co-localizations. Regions of interest were visualized by performing a maximum intensity projection (MIP) of the z-stacks acquired.

5.8 Statistics

The dynamic range of the morphological parameters of dendritic spines, as well as the range of measured τ and calculated τ, and calculated neck resistance based on Ohm's law and Fick's law, were presented as boxplots including the median, first- and third quartile. A Wilcoxon Signed Rank Test was performed to test for significant difference between 2P and 2P-STED measurements. The Sign Test was used to verify whether the estimated τ (from 2P-STED morphology data) differed significantly from measured τ (from FRAP data), and whether calculated neck resistance differed between the two methods. Correlations between morphological parameters, between calculations for neck resistance, and between morphological parameters and measured τ, were investigated via a Spearman correlation test. To test the effect of time on spine morphology and the significance of changes in the morphological parameters over time, a one-way repeated measures ANOVA was performed with post-hoc Bonferroni test.

6 RESULTS

The results section is comprised of 3 parts:

6.1 This part describes the establishment of *in vivo* 2P-STED microscopy. The performance of the setup, the testing of two specific objectives (water-immersion and silicon-oil), and the first results on *in vivo* spine morphology are described. In this project I designed, performed and analyzed the *in vivo* imaging experiments. These *in vivo* experiments, together with dual color imaging experiments in acute slices (performed by Thomas Pfeiffer), as well as a description of how to set up and use a home-build 2P-STED microscope were also used for a protocol article in preparation for Springer - Methods in Molecular Biology (see Appendix 1). Together we designed the figures for this article and wrote the first draft of the manuscript, which is being revised by our supervisor, Prof. Valentin Nägerl.

6.2 This part describes the feasibility of 2P-STED microscopy as a tool to study the dynamic morphology of spines at the nanoscale *in vivo* in mouse barrel cortex, as well as exploratory experiments to study morpho-functional correlations regarding biochemical compartmentalization of dendritic spines. The results are also used for a research article in preparation for a scientific journal. In this part I designed, performed and analyzed all experiments.

6.3 This part includes other applications of 2P-STED microscopy, demonstrating dual color 2P-STED imaging *in vivo*. The enhanced resolution obtained with 2P-STED in combination with two-color imaging makes the first steps towards the visualization of spine-glia interaction *in vivo* at the nanoscale. The development of a novel labelling strategy for astrocytes, in order to be able to perform 2P-STED microscopy on 'tripartite synapses', is explained here as well. In this part I designed, performed and analyzed all *in vivo* experiments and immunohistochemistry experiments (for the controls), while constructs and viruses were produced by Julie Angibaud, who also verified the expression of constructs in astrocytic cultures.

6.1 Establishment of *in vivo* 2P-STED microscopy

Following Ramon y Cajal's pioneering description of neuronal morphology and synapses, which constitute the building blocks of neuronal communication, one of the principle goals in neuroscience has been to decipher the function and structure of neuronal synapses. The development of two-photon (2P) microscopy (Denk et al. 1990; Denk et al. 1994) allowed for the investigation of synaptic morphology and function (Bloodgood & Sabatini 2005). Unfortunately, the resolution of 2P microscopy is limited by light diffraction. In contrast to 2P microscopy and other conventional light microscopy approaches, the recent development of stimulated emission depletion (STED) microscopy bypasses this diffraction limit. Nowadays, STED microscopy has been successfully used with thick tissue preparations such as organotypic slice cultures, acute slices and *in vivo* preparations in single and dual color (Tønnesen et al. 2011; Berning et al. 2012). Recently, we showed that STED microscopy can also be applied to acute brain slices by using 2P excitation in an upright system (Bethge et al. 2013). By making use of 2P excitation, one can reduce the extent of photo damage and bleaching, and the resolution power of STED combined with its adaptability to *in vivo* paradigms should lead to a widespread adoption of the technique in the field of neuroscience.

In this chapter I first discuss the performance of our custom-made 2P-STED microscope and then describe its application for imaging dendritic spines in the intact brain tissue (*in vivo*) of mice.

6.1.1 Point-spread function and resolution of the 2P-STED microscope

The resolution enhancement of the 2P-STED microscope was first optimized by aligning the system through the imaging of reflections of gold spheres and the fluorescence emission of fluorescent nano-spheres. Since I am interested in using the setup for *in vivo* experiments, where a cranial (glass) window is used, it was important to optimize the imaging through a glass coverslip. The presence of a glass coverslip can distort the excitation and depletion beam-profiles (see examples for STED beam in Figure 17a,b, compare left to middle in a), which can accordingly lead to a need in higher excitation powers and a weaker STED effect. An efficient STED effect, the gain in resolution, largely depends on the symmetry and center null of the donut-shaped beam. Without using a coverslip, one can see a deep null and a tight z-profile (Figure 17a, left). However, upon the presence of a glass coverslip, both the symmetry in x,y, and z, as well as the null of the donut, get distorted (Figure 17a, middle). By adjusting the correction collar, one can correct for these spherical aberrations, which leads to an improved symmetry, null, and z-profile of the donut (Figure 17a, right). It is thus of great importance to verify the settings of the correction collar of the objective before every imaging session, in order to optimize the shape of the donut (Figure 17a,b). Optimization of the donut is not the only purpose of correcting spherical aberrations with the correction collar. Modulating the correction collar also leads to a tighter z-PSF with maximum intensity when imaging fluorescent nano-spheres. These spheres are 170 nm in diameter (see examples in Figure 17c,d), and imaging them shows the better optical sectioning due to the improved axial resolution. Altogether, I can conclude that the performance of the 2P-STED

microscope partly depends on whether the user optimized the settings of the correction collar to minimize the spherical aberrations before and during every imaging session.

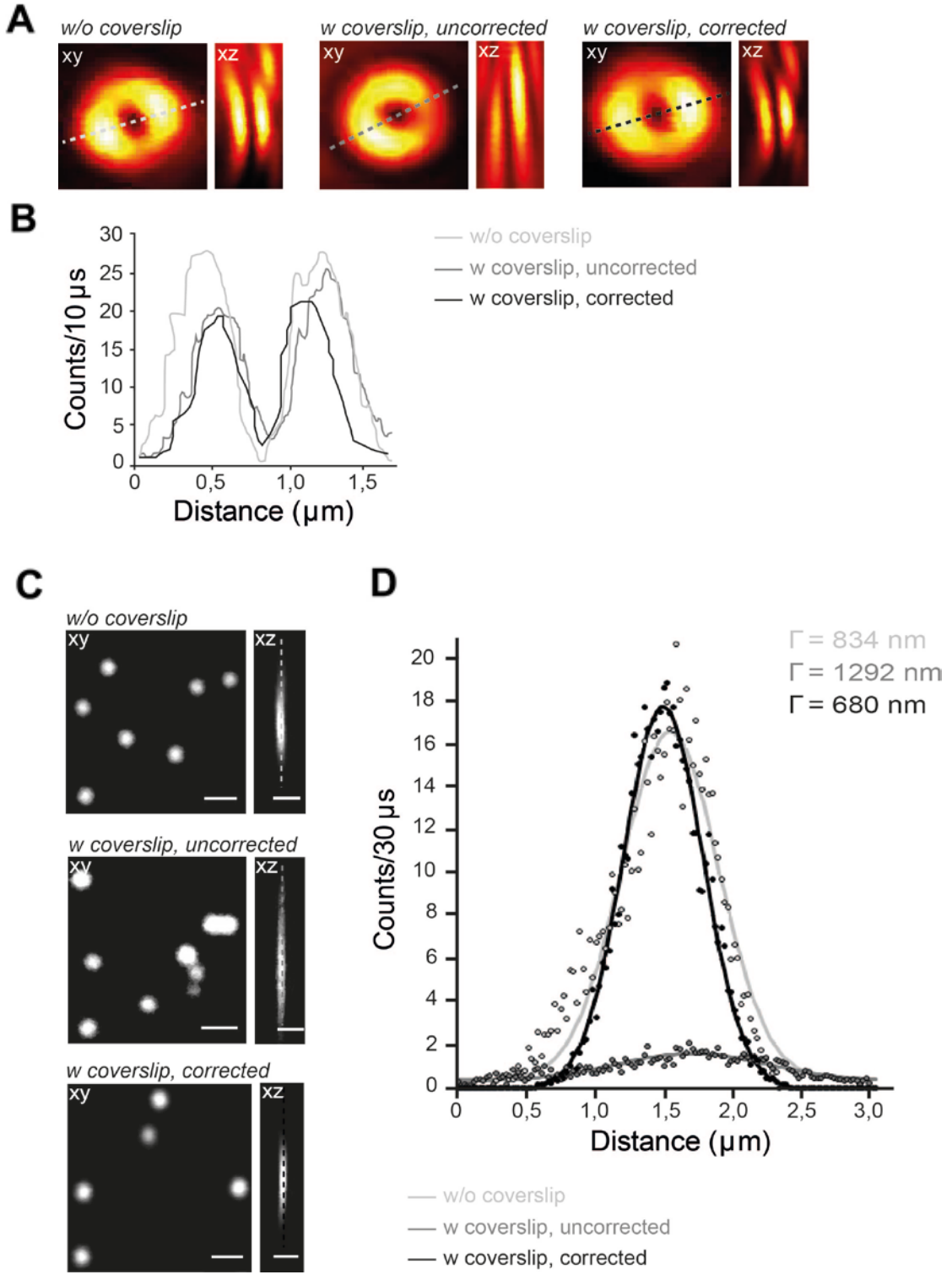

Figure 17: Beam profiles through a glass coverslip. *(A) Examples of reflections of gold beads in xy and xz, visualizing the distortion of the donut shape upon the presence of a glass coverslip (left compared to centre image), and the correction of this distortion by having modulated the correction collar of the objective (centre compared to right image). (B) Line profiles of the indicated axes in the xy images in (A), showing the differences in depth and width of the null of the donut. (C) Examples of xy and xz profiles of fluorescent nano-spheres without (top) and with coverslip (middle and bottom), showing the tighter z-profile upon modulation of the correction collar (compare middle to bottom image). (D) Line profiles of the indicated axes in the xz profiles in (C), showing the tighter z-profile as measured by the FWHM of the line profile.*

The next step was to determine whether by better matching the refractive indices, image quality could be improved. To test this, I assessed the performance of the silicon-oil objective against the water-immersion objective on nano-spheres first. The water-immersion objective (n = 1.33) has the advantage of having a long working-distance, while the silicon-oil objective (n = 1.40) allows for a better correction of the mismatch in refractive indices between the brain (n ≈ 1.36) and glass (n = 1.51). The silicon-oil objective produces a tighter z-PSF than, and improved super-resolution compared to, the water objective. This was confirmed by imaging the gold and fluorescent spheres, which were mounted below a glass coverslip, in 2P-STED mode compared to 2P mode (examples in Fig. 18a-c, quantification and statistics on a population of beads in Fig. 18d).

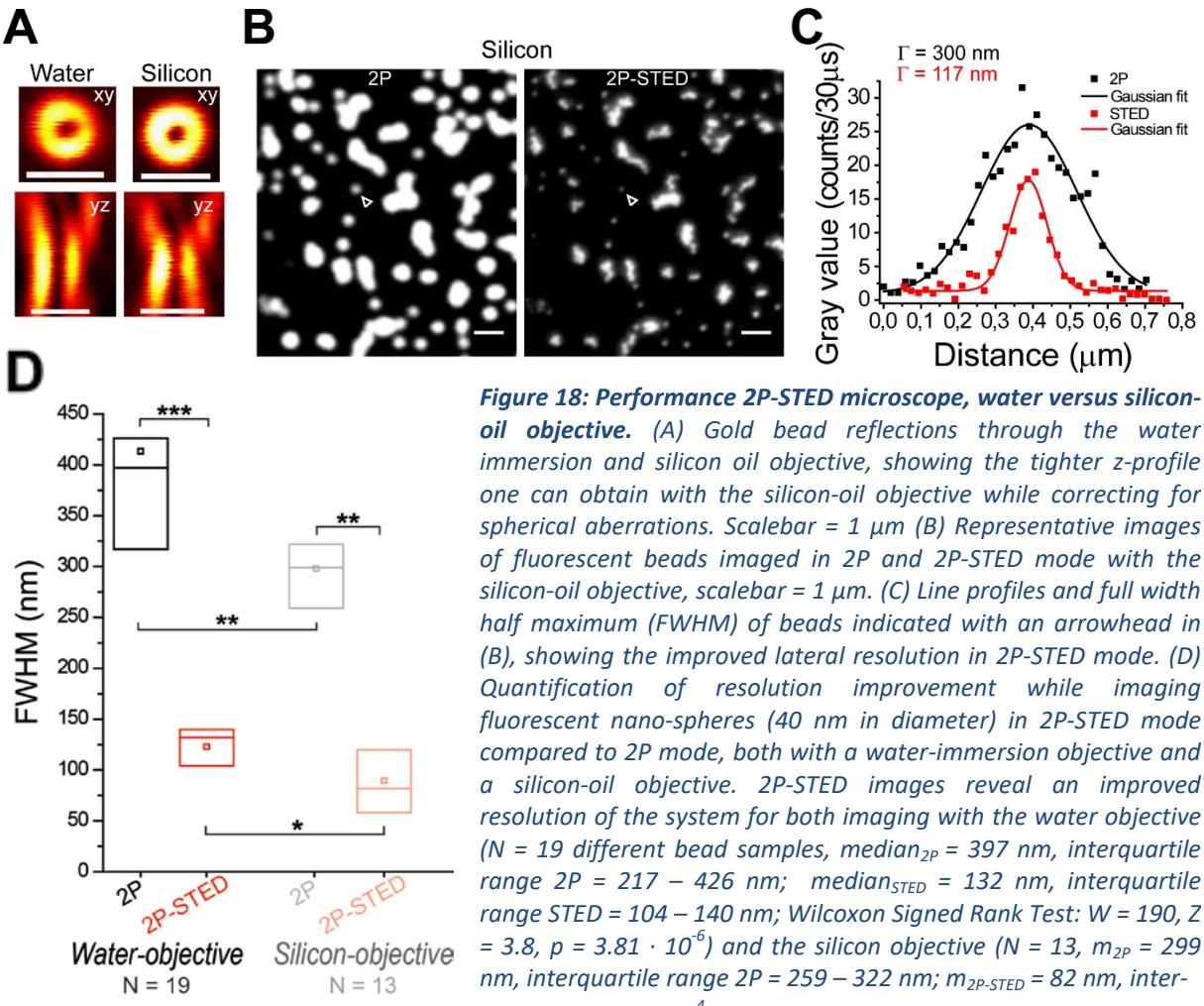

Figure 18: Performance 2P-STED microscope, water versus silicon-oil objective. *(A) Gold bead reflections through the water immersion and silicon oil objective, showing the tighter z-profile one can obtain with the silicon-oil objective while correcting for spherical aberrations. Scalebar = 1 µm (B) Representative images of fluorescent beads imaged in 2P and 2P-STED mode with the silicon-oil objective, scalebar = 1 µm. (C) Line profiles and full width half maximum (FWHM) of beads indicated with an arrowhead in (B), showing the improved lateral resolution in 2P-STED mode. (D) Quantification of resolution improvement while imaging fluorescent nano-spheres (40 nm in diameter) in 2P-STED mode compared to 2P mode, both with a water-immersion objective and a silicon-oil objective. 2P-STED images reveal an improved resolution of the system for both imaging with the water objective (N = 19 different bead samples, median$_{2P}$ = 397 nm, interquartile range 2P = 217 – 426 nm; median$_{STED}$ = 132 nm, interquartile range STED = 104 – 140 nm; Wilcoxon Signed Rank Test: W = 190, Z = 3.8, p = 3.81 · 10^{-6}) and the silicon objective (N = 13, m$_{2P}$ = 299 nm, interquartile range 2P = 259 – 322 nm; m$_{2P\text{-}STED}$ = 82 nm, inter-quartile range STED = 58 – 120 nm; W = 91, Z = 3.1, p = 2.44· 10^{-4}) Performance of the silicon-oil objective is in general better than the water-immersion objective (Kruskall-Wallis 2 sample test Water versus Silicon;2P: D = 0.61, Z = 1. 69, p = 0.004; 2P-STED: D = 0.53, Z = 1.48, p = 0.014).*

Quantification of the resolution improvement while imaging fluorescent nano-spheres (40 nm in diameter) in 2P-STED mode compared to 2P mode, both with a water-immersion objective and a silicon-oil objective, revealed a significantly improved resolution of the system in 2P-STED mode (N_{water} = 19 different bead samples, median$_{2P}$ = 397 nm, interquartile range 2P = 217 – 426 nm; median$_{2P\text{-}STED}$ = 132 nm, interquartile range STED = 104 – 140 nm; Wilcoxon Signed Rank Test: W = 190, Z = 3.8, p = 3.81 · 10^{-6} and $N_{silicon}$ = 13, median$_{2P}$ = 299 nm, interquartile range 2P = 259 – 322 nm; median$_{2P\text{-}STED}$ = 82 nm,

interquartile range 2P-STED = 58 – 120 nm; W = 91, Z = 3.1, p = 2.44· 10^{-4}). The performance of the silicon-oil objective was in 2P mode already significantly better than the water-immersion objective (Kruskall-Wallis 2 sample test water versus silicon objective; 2P: D = 0.61, Z = 1. 69, p = 0.004) and indeed outperformed the water-immersion objective in 2P-STED mode as well (KW 2 sample test; 2P-STED: D = 0.53, Z = 1.48, p = 0.014).

6.1.2 Performance of the 2P-STED microscope in acute slices

I next tested the ability of the 2P-STED microscope on imaging deep inside living tissue with the water-immersion objective. I thus first verified that our system allows for better resolving dendritic spines in 2P-STED mode compared to 2P-mode at different depths in light scattering tissue. In order to do so, I made use of acute slice preparations of adult Thy1-YFPH mice. Indeed, our system allowed for the imaging of the nanoscale morphology of dendritic spine necks at different depths, as exemplified in Figure 19.

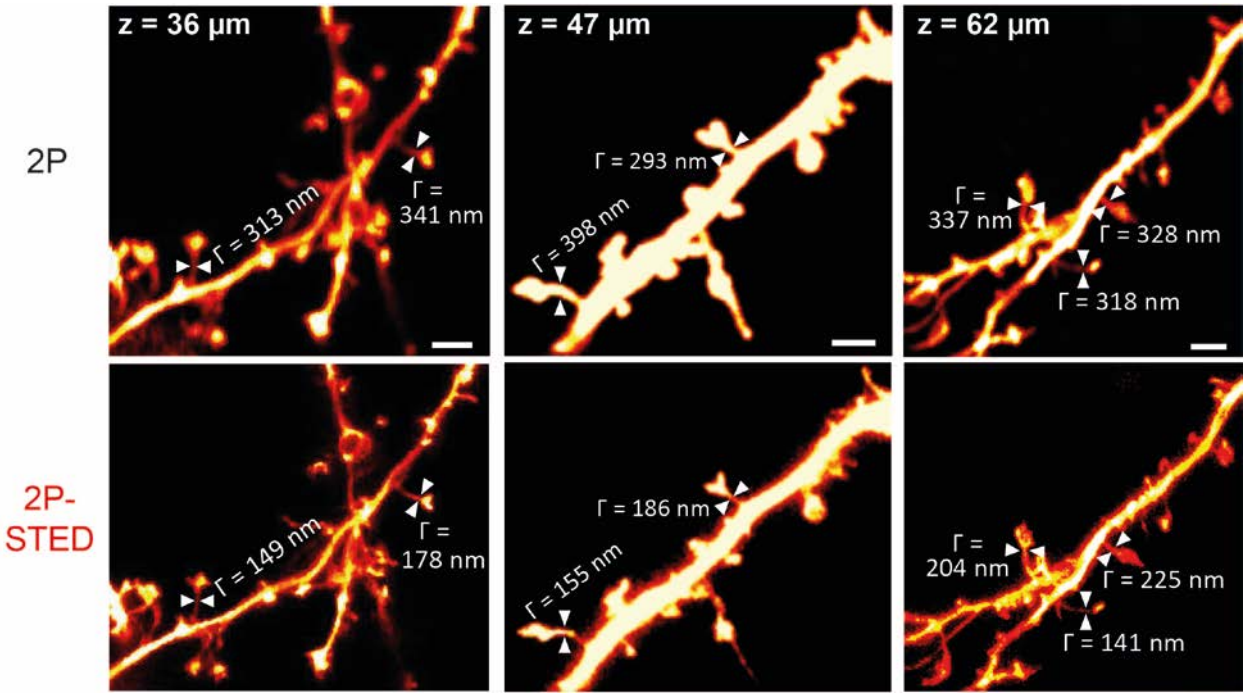

Figure 19: Resolution improvement with 2P-STED in depth. *Examples of various dendritic stretches with dendritic spines at 36 µm away from the surface of the brain (left), at 47 µm depth (middle), and 62 µm depth; all stretches imaged in both 2P (top) and 2P-STED mode (bottom). Scalebars = 2 µm.*

Furthermore, using acute slices, I could show that with our microscope, dendritic stretches and single spines can be imaged over time in single color (Figure 20a,b) and together with microglial processes in dual color (Figure 20c).

Figure 20: Imaging dendritic spines over time in acute slices. *(A) Time-lapse imaging of dendritic spines of a L5 apical oblique showing that nanoscale morphological changes can be followed up to 60 minutes in acute brain slices. MIP of three z-planes approximately 30 µm deep. (B) Dendritic spines can be followed with a temporal resolution enabling the assessment of their fine morphological dynamics during changes in their synaptic transmission. Single z-plane approximately 35 µm deep in an acute brain slice. (C) Two-color 2P-STED time-lapse imaging can be used to dissect the dynamic morphological interactions between microglial processes and dendritic spines in acute brain slices (Thy1H$^{+/YFP}$ x Cx3Cr1$^{+/eGFP}$ mouse). MIP of two z-planes 45 µm deep. All images are taken during basal synaptic transmission. Scale bars: 500 nm (A,B); 2 µm (C).* →

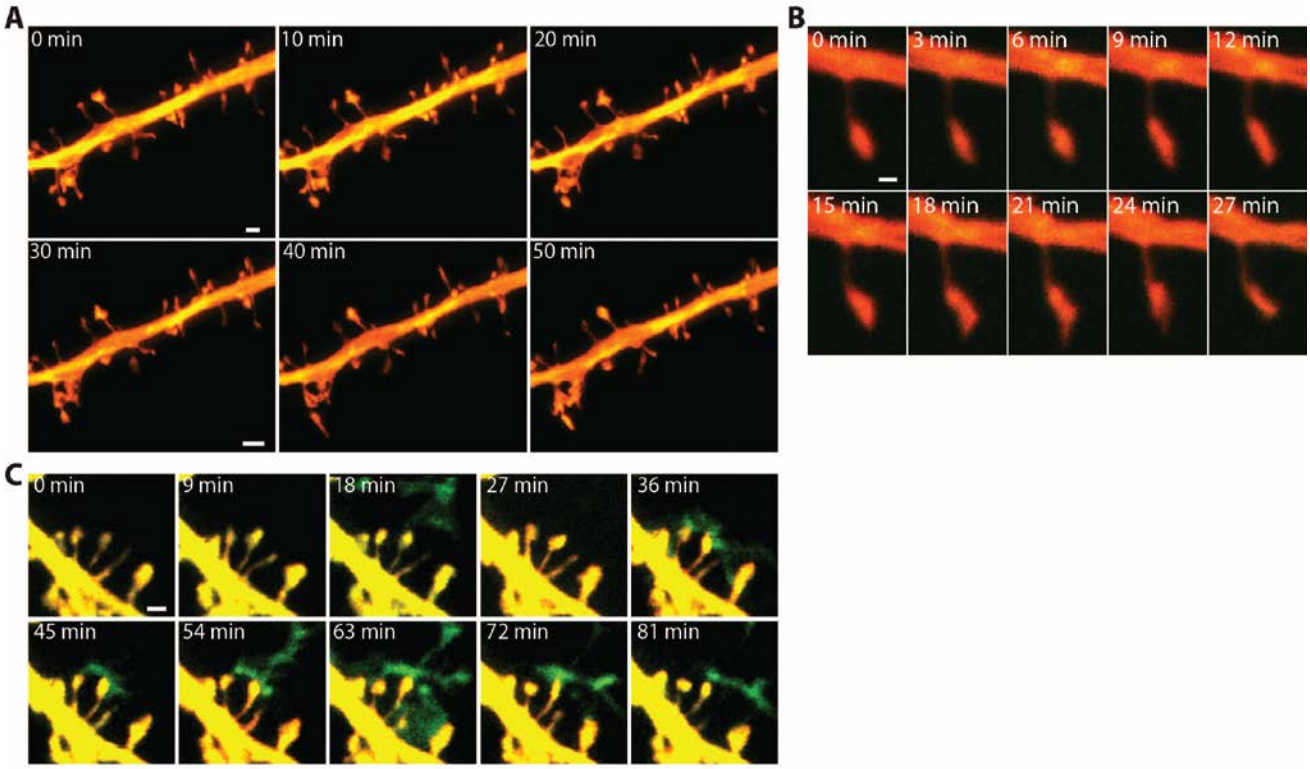

6.1.3 Optimization of *in vivo* preparation

Next to the optimization of the performance of our system it was of great importance to establish an improved protocol for *in vivo* experiments while utilizing our 2P-STED microscope. The basic surgery skills for the implementation of a cranial window could simply be improved by practicing the preparation, this also allowed for the improvement of different aspects of the *in vivo* preparation. For example, several body postures of the mice were tested in order to find an optimal position in our setup while maintaining as many parameters (e.g. body temperature, anesthesia levels, and drug application) as possible in accordance with previously published protocols (e.g. Holtmaat et al. 2009).

A successful *in vivo* imaging experiment greatly relied on the mechanical stability of the sample. Stability of the brain was first of all ensured by gluing the head holder to the skull, which maintained the head at a fixed position during image acquisition. All other parameters for a successful *in vivo* experiment, that is, stable imaging, were also verified. Firstly, the head of the mouse was turned in such a way that breathing was not obstructed, while ensuring that the brain would not be pulled away from the window by gravity, but the region of interest could still be easily accessed without an angle. Secondly, the body posture of the mouse was adjusted so that the lungs could easily expand during respiration, while the front paws were still resting on the heating pad to stabilize the full body posture. Thirdly, the body temperature of the mouse was continuously measured and regulated by in- or decreasing the temperature of the heating pad below the mouse. A stable body temperature (in our case around 36°C) should allow for minimal changes in blood flow, thereby decreasing vibrations originating from the blood vessel pulsations in the brain. Fourthly, the entrance of

the nostrils of the mouse into the mask, which applied the isoflurane, was verified so that the anesthetic appropriately reached the nostrils while respiration was not obstructed (verified by absence of gasping). By doing so, vibrations originating from jaw movements (in case of gasping) were reduced. Fifthly, hydration of the mouse was verified during the experiments, applying water in case of signs of dehydration (e.g. loss of suppleness of skin). Lastly, anesthesia levels during image acquisition were set to an oxygen supply of 0.6 L/min with 1.5 % isoflurane. The usage of isoflurane for longer periods of time should not affect dynamics of dendritic spines (Yang et al., 2011), and at these rates the breathing of the mouse was calm and abdominal, thereby reducing vibrations of the brain compared to diaphragmatic breathing. Furthermore, it has been shown that with these anesthesia settings, mean values of arterial pressure and heart rate are stable and comparable to those observed in awake animals (Constantinides et al., 2011), suggesting that the mouse is maintained close to its physiological health during the experiments.

6.1.4 Performance of the 2P-STED microscope *in vivo*

Having optimized the stability of the sample, I verified the stability of the signals. First of all, this could be done while imaging a homogenous sea of fluorescein or calcein, which did not show any loss of signal within the commonly used imaging depth (~50 µm). Brightness of the signal strength over depth in light scattering tissue without adjusting excitation power was also tested (Fig. 21a,b). When comparing the average signal intensity per frame over depth, signal strength would decrease to 23 % of the highest value of this average signal. The presence of bright structures in the field of view (FOV) would affect the average signal intensity for that frame, but on average I found that 55 ± 19 % (s.d.) of the highest average signal intensity per frame remained (Fig. 21b,c). Bright structures, such as axonal boutons and large dendritic branches diving into the depth, would give an increase in the otherwise decreasing signal intensity over depth (Fig. 21c). In contrast, when adjusting excitation power upon a depth of 100 µm, neuronal structures could still be imaged with an average intensity of at least 69 % of the maximal observed signal (Fig. 21d,e). Again, the amount and type of bright structures present in the FOV can make one perceive the maximal penetration depth different than the actual penetration depth. When comparing signal intensities at different depths, changes were however minimal, with the brightest structures having a comparable brightness (Fig. 21f).

In order to determine whether neuronal structures could be repeatedly imaged, time-lapse acquisitions of different FOVs and at different temporal resolutions were acquired without adjusting excitation power. Imaging every 10 min over half an hour, signal intensity dropped to a minimum of 83 % of the original signal, but 88 % of the signal was on average preserved (Fig. 22a,b). Images acquired in 2P mode at higher temporal resolution (every 30 s) showed a similar average loss in signal, with no significant differences over time (n = 11 FOVs from 5 animals, 1-way ANOVA repeated measures + post-hoc Bonferroni correction, $F = 2.06$, $p = 0.13$; Fig. 22c,d).

In summary, the excitation light seems to neither induce photo bleaching nor photo toxicity (as indicated by the absence of unnatural swelling of the structures). More importantly, I

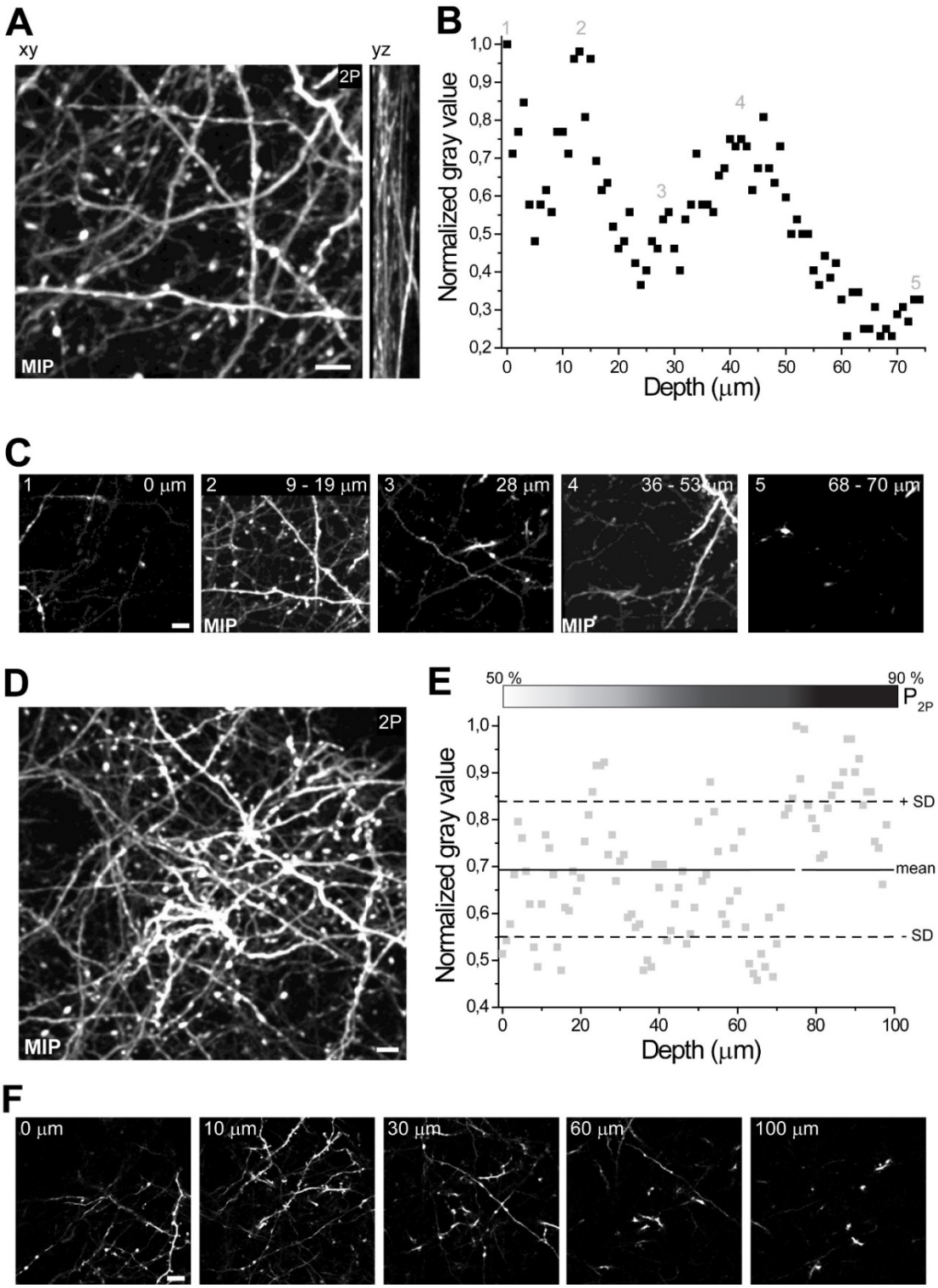

Figure 21: Signal intensities over depth. *(A) Maximum intensity projection (MIP) of a 70 µm long z-stack acquired in 2P mode without adjusting laser power, left: xy view, right: yz view. (B) Full frame highest intensity value normalized to the first frame in the z-stack. Numbers indicate locations of bright structures. (C) Single frame (1, 3, and 5) and MIPs (2, 4) of locations indicated in (B), showing bright structures as a source for increase in otherwise decreasing signal intensity. (D) MIP of a 100 µm z-stack acquired in 2P mode while adjusting laser power, view = xy. (E) Full frame highest intensity value normalized to the frame with the highest value in the z-stack. Signal is on average 69 ± 14 % (s.d.) of highest value. Intensity bar indicates progressive adjustment of the 2P laser power as a percentage of its maximal possible power. (F) Single frames at different depth showing similar signal intensities for the structures present. All scalebars represent 5 µm.*

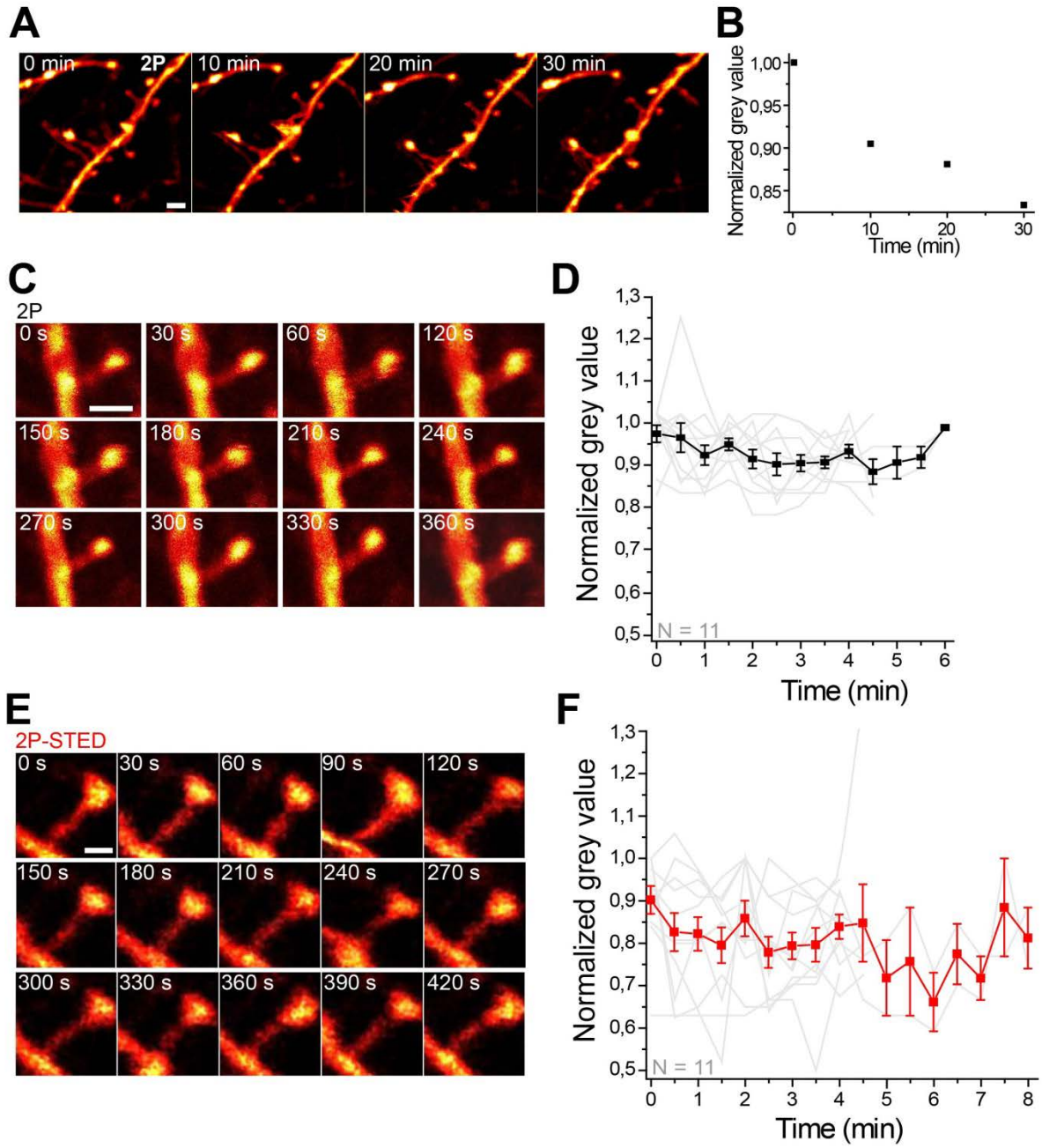

Figure 22: Signal intensities over time. *(A) MIPs of 5 µm z-stacks of a dendritic stretch followed over 30 min to study possible bleaching of the signal. Scalebar = 2µm. (B) Full field of view (FOV) highest intensity value normalized to the first MIP, signals would drop to 83 % of first MIP but on average 88 % of signal would be preserved. (C) MIPs of 3 µm z-stacks in a smaller FOV, imaging spines in 2P mode at higher temporal resolution. Scalebar = 2 µm. (D) Full FOV highest intensity value normalized to brightest MIP in time, average loss of intensity 17 %, no significant differences over time (1-way ANOVA repeated measures + post-hoc Bonferroni correction, F = 2.06, p = 0.13). (E) MIPs of 3 µm z-stacks imaging single spines with 2P-STED in a small FOV at higher temporal resolution. Scalebar = 1 µm. (F) Full FOV highest intensity value normalized to highest value in time (occurred 4x). Average loss of 19.9 % with no significant differences between each and every time point (p ranging from 0.07 – 1). Overall signal loss just reaches significance (F = 2.07, p = 0.05).*

also tested the effects of imaging at faster rates (every 30 s; Fig. 22e). I found that the signal intensity in 2P-STED images dropped to 82 % of its highest values after 8 minutes. Over time, signal intensity decreased significantly (F = 2.07, p = 0.049; Fig. 22f), but individual time points did not differ from each other (p >> 0.05; Fig. 22f). In addition, on average 80 % of the maximum obtained signal was preserved.

Taken together, 2P-STED imaging at high temporal resolution did not seem to induce any photo toxicity or excessive photo bleaching. I then tested whether 2P-STED imaging could be performed in depth and over longer time intervals as well. Similarly to the 2P mode, I could reach an imaging depth of approximately 60 µm, with the present structures having similar counts upon adjustments of the excitation power (Figure 23a) and I was able to repeatedly image the same dendritic stretch for at least 30 minutes (Figure 23b).

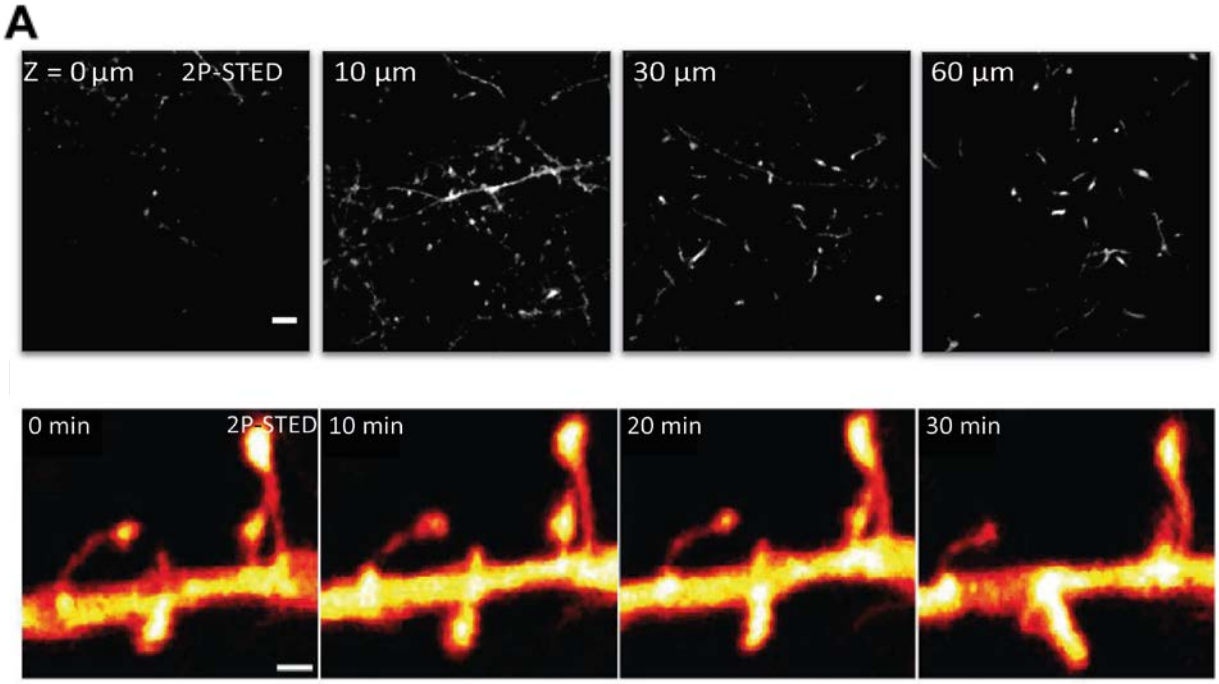

***Figure 23: Performance 2P-STED over depth and in time* in vivo.** *(A) Example of single frames at different distance from the brain surface showing neuronal structures with similar brightness because of the adaptation of the excitation power. Scalebar = 5 µm. (B) Example of a dendritic stretch imaged every 10 minutes for a total of 30 minutes. Scalebar = 1 µm.*

Furthermore, I tested whether direct excitation of the sample by the STED light was occurring. Several structures *in vivo* were imaged with 2P-STED, 2P alone, and STED alone, which led to an observation of negligible direct excitation by the STED light (example in Figure 24). Profiting from the better correction of aberrations by the silicon-oil objective, and the optimization of the previously described factors during *in vivo* experiments, I was able to acquire highly resolved images of dendritic spines (see example in Figure 25a,b). I determined the morphological parameters of dendritic spines at the nanoscale when using 2P-STED microscopy (Figure 25c) and in a population of spines I found that spine neck widths were significantly better resolved in 2P-STED mode compared to 2P mode (N = 16 spines from 4 animals, paired data; $median_{2P}$ = 305 nm, interquartile range 2P = 271 – 349 nm; $median_{2P\text{-}STED}$ = 180 nm, interquartile range 2P-STED = 143 – 228 nm; Wilcoxon Signed Rank Test: W = 134, Z = 3.39, p = $9.16 \cdot 10^{-5}$; Fig. 26a). In addition, due to the improved resolution in 2P-STED mode, I was better able to discern the transition from spine neck to spine head, thereby enabling improved quantification of actual spine head volume. I found a significant difference in spine head volume based on imaging in 2P versus 2P-STED mode (N= 16, $median_{2P}$ = 0.17 femtoliter (fL), interquartile range 2P = 0.12 – 0.29 fL; $median_{2P\text{-}STED}$ = 0.11 fL, interquartile range 2P-STED = 0.07 – 0.19 fL; W = 131, Z = 3.23, p = $3.05 \cdot 10^{-4}$; Fig. 26b).

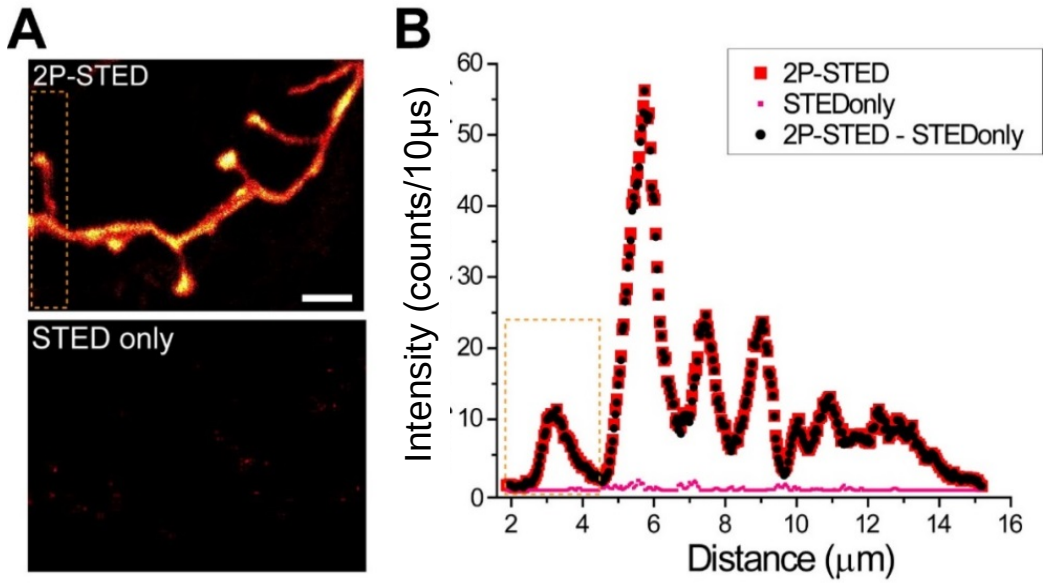

Figure 24: Negligible direct excitation by STED light. *(A) Maximum Intensity Projection (MIP) of a 5 µm z-stack. Dendritic stretch imaged with 2P-STED (upper) and STED light alone (lower). Orange box indicates area representative for part of the intensity plot in (B). Scale bar = 2µm. (B) Fluorescence intensity of the full MIP for 2P-STED (red), STED alone (STED only, magenta), and STED only subtracted from the 2P-STED signal (black). Orange box is signal as indicated by the orange box in (A). Image and plot show negligible direct excitation by the STED light.*

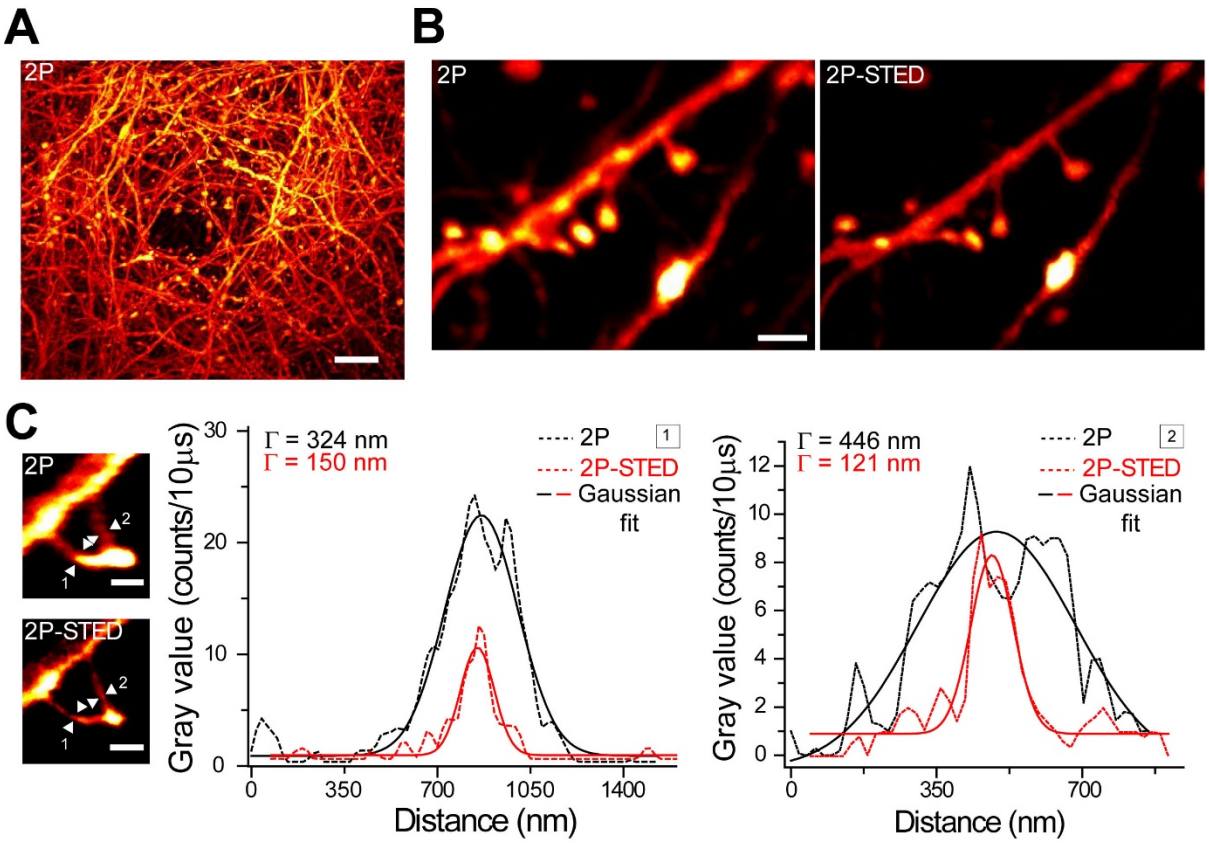

Figure 25: Imaging spine structure* in vivo *with the silicon-oil objective. *(A) Overview image of dendritic and axonal stretches in the mouse barrel cortex* in vivo*. Image taken in 2P mode, scalebar = 10 µm. (B) Comparison of the same dendritic stretch imaged both in 2P- (left) and in 2P-STED mode (right), showing that structures become crisper and thus better resolved in 2P-STED mode. Scalebar = 2 µm. (C) Quantification of resolution improvement seen in 2P-STED (red) compared to 2P mode (black). A line profile through both spine necks (1 and 2) is drawn and the FWHM is determined via a Gaussian fit. Scalebar = 1 µm.*

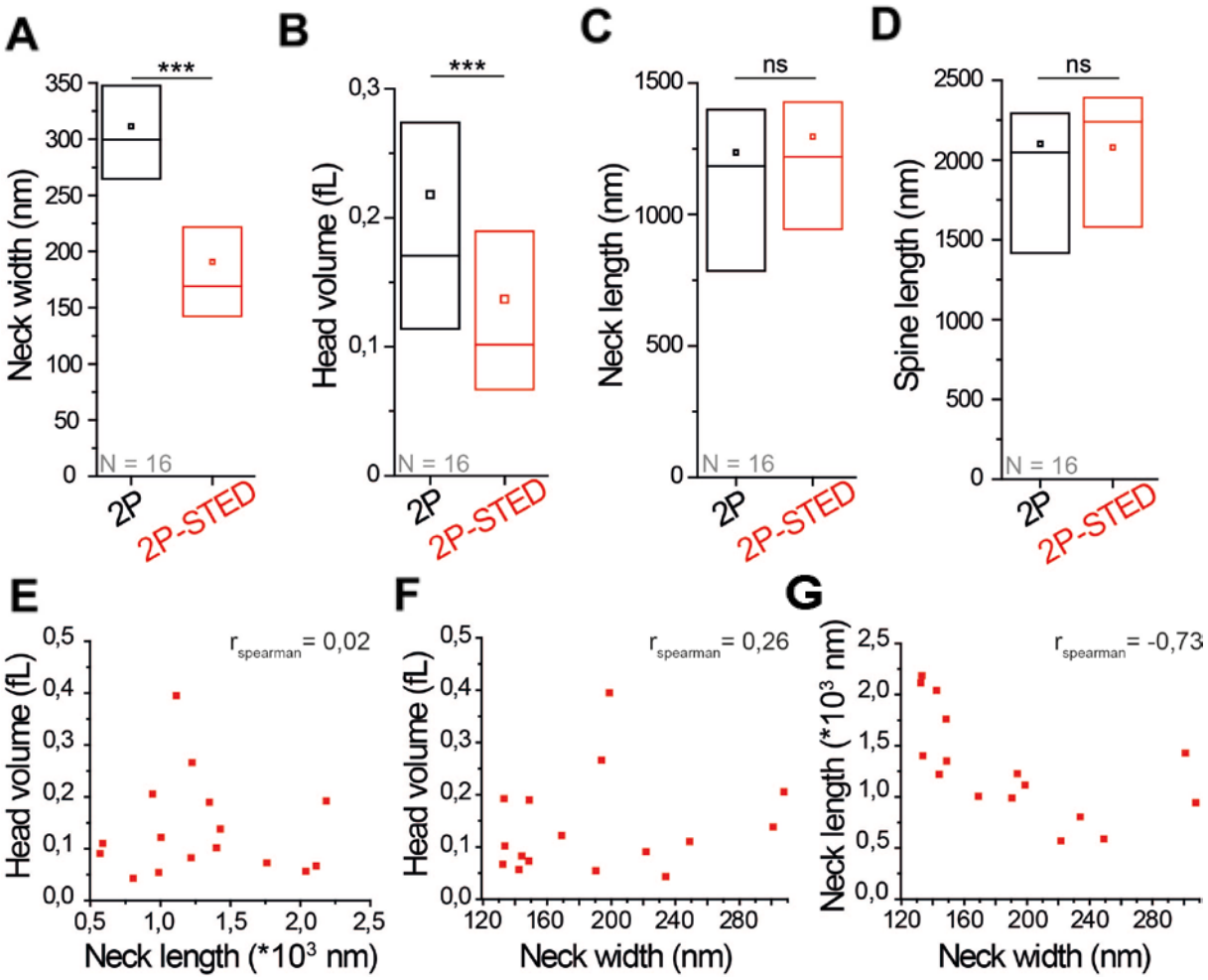

Figure 26*: Morphological parameters of dendritic spines imaged with a silicon-oil objective.* *(A-D) Distribution of morphological parameters of dendritic spines imaged* in vivo *with 2P and 2P-STED. Box plots of the non-normal dataset show interquartile range, median and mean value. For all distributions N = 16 spines from 4 animals, paired data, and Wilcoxon Signed Rank Test was performed to test for significant differences. (A) Distribution of neck width measurements (***Z = 3.39, p = 9.16 · 10^{-5}). (B) Head volume distribution (***Z = 3.23, p = 3.05 · 10^{-4}). (C) Distribution of neck length measurements (Z = -1.27, p = 0.21). (D) Spine length distribution (Z = -0.28, p = 0.78). (E-G) Morphological parameters measured in 2P-STED mode are differently inter-correlated (E) Correlation neck length and head volume, $r_{spearman}$ = 0.02. (F) Correlation neck width and head volume, $r_{spearman}$ = 0.26. (G) Correlation neck width and neck length, $r_{spearman}$ = -0.73.*

The morphological parameters with values well above the diffraction limit were similarly measured in 2P and 2P-STED mode (N = 16; neck length: $median_{2P}$ = 1198 nm, interquartile range 2P = 785 – 1522 nm; $median_{2P\text{-}STED}$ = 1223 nm, interquartile range 2P-STED = 966 – 1594 nm; W = 43, Z = -1.27, p = 0.21; and spine length: $median_{2P}$ = 2112 nm, interquartile range 2P = 1513 – 2357 nm; $median_{2P\text{-}STED}$ = 2283 nm, interquartile range 2P-STED = 1611 – 2429 nm; W = 62, Z = -0.28, p = 0.78; Fig. 26c,d). Neck length and head volume were not correlated to each other ($r_{spearman}$ = 0.02, p = 0.93; Fig. 26e), but neck width and head volume were weakly positively correlated ($r_{spearman}$ = 0.26, p = 0.32; Fig. 26f), while spine neck length and spine neck width showed a strong negative correlation ($r_{spearman}$ = -0.73, p = 0.001; Fig. 26g). These findings will need to be confirmed by increasing the sample size. However, the silicon-oil objective has a major disadvantage in that it has a large diameter (ranging from

5.4 mm (front lens) to 22.8 mm in the first 0.17 mm after the front lens) and short working distance (0.3 mm), thereby hindering the easy access to the small mouse crane and even smaller craniotomy. For ease of access, all remaining experiments were therefore performed only with the water-immersion objective.

6.1.5 Conclusion

In conclusion, these results show that I can successfully perform 2P-STED microscopy *ex*- and *in vivo*, with a water-immersion and a silicon-oil objective. Besides the successful implementation of 2P-STED microscopy *in vivo*, I optimized the conditions to obtain high-resolution images with minimal spherical aberrations and was able to stably image dendritic spines in layer 1 of mouse barrel cortex *in vivo*. I quantified the nanoscale morphology of these spines when imaged with the silicon-oil objective, but in the following chapters 2P-STED microscopy with the usage of a long working distance water-immersion objective will be discussed. I will show a more elaborate application of the *in vivo* 2P-STED microscopy approach as well as two-color *in vivo* imaging of nanoscale brain structures.

6.2 *In vivo* 2P-STED microscopy to study the nanoscale morphology of dendritic spines

By combining STED microscopy with FRAP measurements, 2P glutamate uncaging, and patch-clamping electrophysiology in hippocampal organotypic brain slices, it was shown that biochemical and electrical compartmentalization are distinctly shaped and dynamically regulated by nanoscale spine morphology (Tønnesen et al., 2014). The combined application of these techniques was necessary to overcome the shortcomings of EM and 2P microscopy, which either cannot be combined with functional assays or does not have sufficient spatial resolution to resolve spine nanostructure, respectively. Spines are often studied in the hippocampus because of its important role in learning and memory. In addition, the whisker to barrel cortex system is a well-appreciated approach to study morpho-functional correlations of spines upon stimulation. Single whiskers are represented at individual barrels in the cortex, and thus stimulation of one whisker will allow for a more precise read-out of neuronal activity. One can then more specifically study spines which were stimulated. Finally, layer 1 of mouse neocortex is of interest because of its important integrative role.

I here show the combined use of 2P-STED microscopy and FRAP measurements in anesthetized adult Thy$^{eYFP/eYFP}$ mice. I studied the morphology of dendritic spines in layer 1 of mouse barrel cortex, as well as those spines' morphological dynamics. Exploratory experiments were performed to investigate whether spine morphology can predict spine compartmentalization *in vivo*.

6.2.1 Quantitative analysis of spine morphology *in vivo* at the nanoscale

To visualize dendritic spines, 55 – 70 days old Thy1$^{eYFP/eYFP}$ mice were implanted with cranial windows and acutely imaged in the barrel cortex by 2P-STED microscopy while under anesthesia. Our home-built 2P-STED microscope offered a spatial resolution of around 70 nm (Fig. 27a) when using the water immersion objective, providing sufficient resolution to reliably quantify morphological parameters of the dendritic spines. Indeed, spines were better resolved while using the 2P-STED modality compared to 2P-imaging alone, with spine

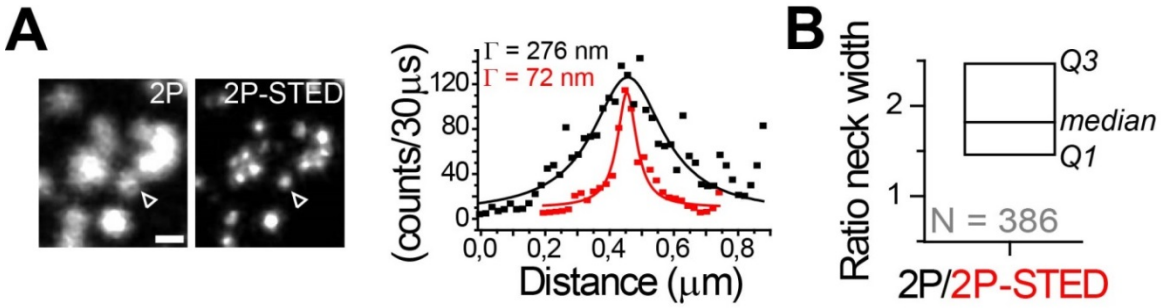

Figure 27: Spatial resolution improvement with 2P-STED microscopy. *The performance of the setup is tested on 40 nm fluorescent spheres (left, 2P versus 2P-STED), which show a substantial gain in spatial resolution. Intensity profiles (right) corresponding to the bead indicated with the arrowhead are depicted (scatter plot, black = 2P, red = 2P-STED) and the full width half maximum from the Lorentzian fit (line graphs) illustrates the gain in resolution: 72 nm in 2P-STED compared to 276 nm in 2P mode. (B) Spine neck widths were better resolved* in vivo *while using the 2P-STED modality compared to 2P-imaging alone with on average at least a factor 2 (n = 386 spines from 26 animals).*

neck measurements differing on average by a factor of 2 (Figure 27b), as exemplified in Fig. 28a. From the Gaussian fits to the line profiles through the spine neck, its width was found to be distributed around a median of 307 nm and ranged from 267 nm to 606 nm in 2P mode, while the same spines were significantly better resolved in 2P-STED mode with a median of 172 nm, ranging from 48 nm to 423 nm (n = 386 spines from 26 animals, Wilcoxon

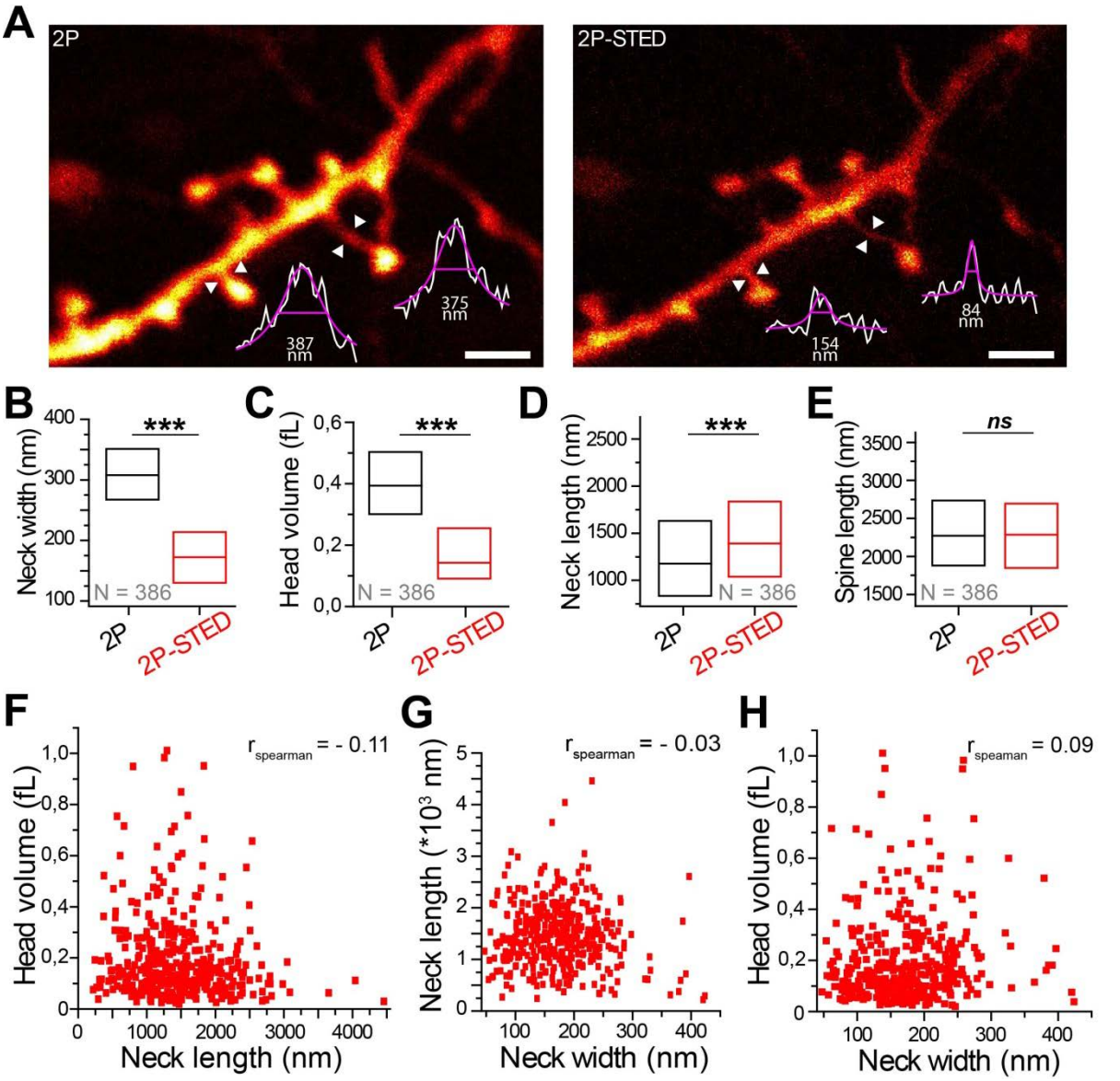

Figure 28: Spine morphological parameters span a broad range. *(A) 2P and 2P-STED images of a dendritic segment showing that with the 2P-STED approach dendritic spines are better resolved. The image is a maximum-intensity projection (MIP) of 5 z-planes 500 nm apart. The intensity profile in raw data of neck width (between the white arrowheads) is depicted (white) with a Gaussian fit (magenta); the full width at half maximum (magenta line) indicates the neck width and is given in nm. Scale bar represents 2 µm. (B–E) Distribution of morphological parameters of dendritic spines imaged in vivo with 2P and 2P-STED. Box plots of the non-normal dataset show interquartile and median value. For all distributions N = 386 spines from 26 animals, and Wilcoxon Signed Rank Test was performed to test for significant differences. (B) Distribution of neck width measurements (***Z = 16.5, p << 0.05). (C) Head volume distribution (***Z = 16.5, p << 0.05). (D) Distribution of neck length measurements (***Z = -10.9, p = $6.28 \cdot 10^{-28}$). (E) Spine length distribution does not significantly differ (Z = 1.32, p = 0.18). (F-H) Morphological parameters measured in 2P-STED mode are not inter-correlated (F) Correlation neck length and head volume (G) Correlation neck width and neck length (H) Correlation neck width and head volume.*

Signed Rank Test: Z = 16.5, p << 0.05; Fig. 28b). The difference in measured neck width is reflecting the resolution enhancement provided by STED microscopy. In addition, I found that spine head volume was significantly smaller when imaged with 2P-STED as indicated by a median of 0.14 femto-liter (fL) compared to 0.39 fL in 2P (Z = 16.5, p << 0.05; Fig. 28c). The improved resolution with 2P-STED most probably allowed for better resolving the transition from spine neck to head, thereby resulting in different head measurements for the two modalities. While neck length measurements in STED modality were significantly larger than those in 2P measurements, total spine length did not differ, indicating that differences between 2P and 2P-STED measurements were not due to imaging artifacts such as bleaching of signals and thus less emitted fluorescence being detected (median $L_{neck,2P}$ = 1177 nm, median $L_{neck,2P\text{-}STED}$ = 1391 nm, Z = -10.9, p = $6.28 \cdot 10^{-28}$; $L_{spine,2P}$ = 2288 nm, $L_{spine,2P\text{-}STED}$ = 2303 nm, Z = 1.32, p = 0.18; Fig. 28d,e). The ratio of neck to spine length differed significantly between 2P and 2P-STED measurements (Z = 13.8, p = $3.1 \cdot 10^{-43}$; not shown), most probably as a result of the improved capability to resolve transitions from dendrite to spine neck and from spine neck to spine head. None of the morphological parameters as measured in 2P-STED mode were found to be inter-correlated, as shown by $r_{spearman}$ ranging from - 0.11 to + 0.09 (p > 0.05; Fig. 28f-h), a result which is consistent with previous work in the hippocampus in organotypic slice cultures (Tønnesen et al. 2014), but contradictory with work in the hippocampus in acute slices where a weak correlation was found between neck width and neck length (Tønnesen et al. 2014; Wijetunge et al. 2014). However, spine morphology is age and region specific (Wijetunge et al. 2014), both of which are different in our preparation (L1 cortex of P55 – P70 old mice versus CA1 of P14, P28-P35 (Tønnesen et al. 2014), and P37 old mice), and thus a direct comparison between the studies cannot be made.

6.2.2 Analysis of morphological dynamics of spines using STED time-lapse imaging

Dendritic spine morphology was followed for 30 min (or in some cases 50 min) with a 10 min time interval to determine the stability of spine morphology over time (Fig. 29a). All morphological parameters showed subtle fluctuations over time. However, neck width did on average not significantly change over time (n = 77 spines from 13 animals, 1-way repeated measures ANOVA with post-hoc Bonferroni correction, overall F = 1.93 with p = 0.14; comparison of each time point to each other time point: p >> 0.05; Fig. 29b). In contrast, head volume, neck length and spine length were slightly decreased over time compared to the first time point, but neck and spine length values were back to initial values when following the spines longer than 30 minutes (overall $F_{head\ volume}$ = 3.00 with $p_{head\ volume}$ = 0.02; overall $F_{neck\ length}$ = 3.74 with $p_{neck\ length}$ = 0.02 and overall $F_{spine\ length}$ = 11.9 with $p_{spine\ length}$ = $7.21 \cdot 10^{-5}$; Fig. 29d,e). Each time point compared to each other time point did not show any significant differences for spine length and neck length (p >> 0.05). However, neck length was significantly smaller at 30 minutes compared to 0 minutes ($p_{30\ min}$ = 0.03) and spine length was significantly smaller at 20 and 30 minutes after its first measurement ($p_{20\ min}$ = $5.68 \cdot 10^{-4}$ and $p_{30\ min}$ = $9.53 \cdot 10^{-7}$). Spine length did however come back to its initial value at 40 and 50 minutes. The observed decrease in neck and spine length could be due to the fact that I could not follow all spines for more than 30 minutes, with part of those spines possibly

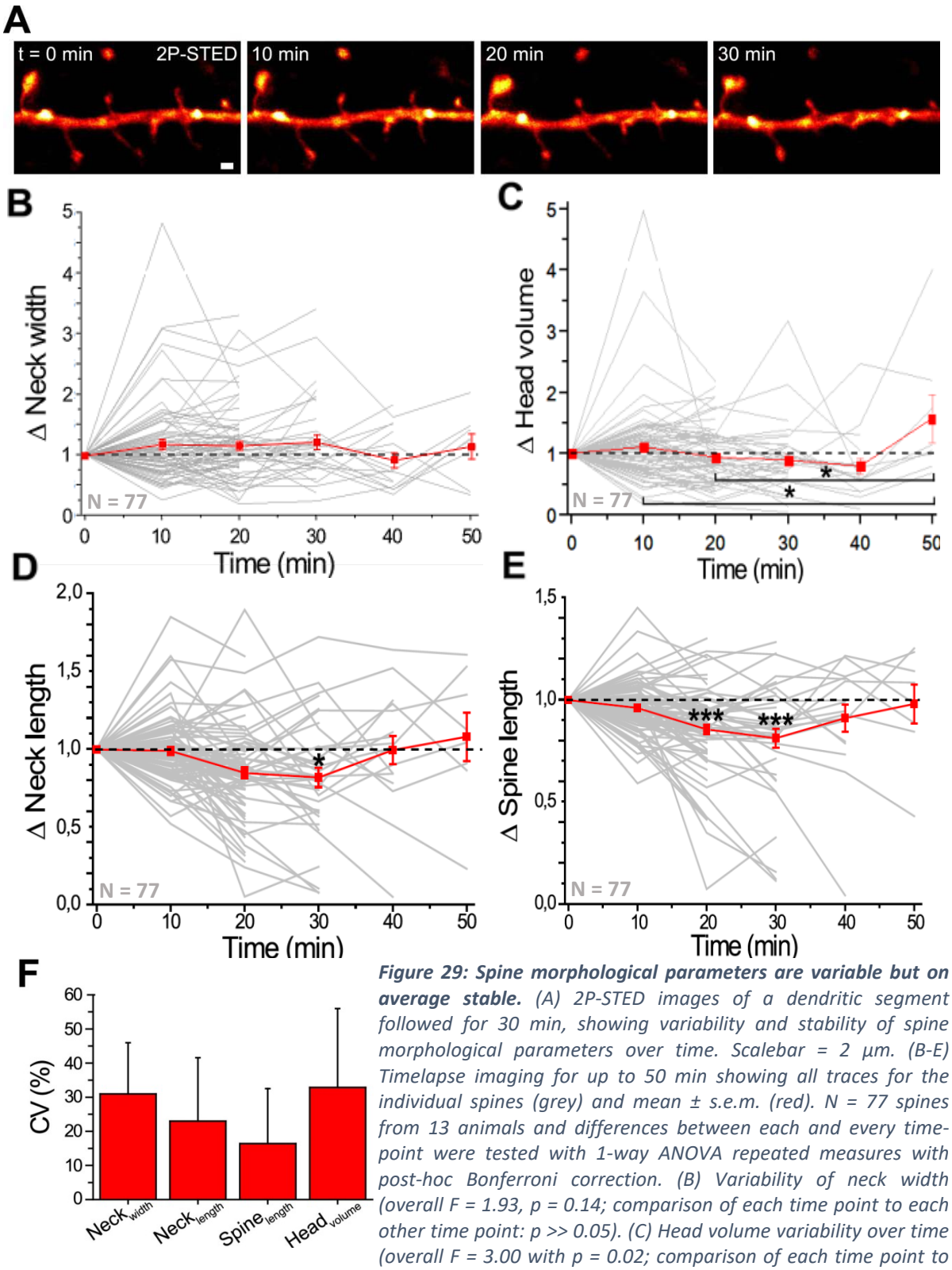

Figure 29: Spine morphological parameters are variable but on average stable. *(A) 2P-STED images of a dendritic segment followed for 30 min, showing variability and stability of spine morphological parameters over time. Scalebar = 2 µm. (B-E) Timelapse imaging for up to 50 min showing all traces for the individual spines (grey) and mean ± s.e.m. (red). N = 77 spines from 13 animals and differences between each and every time-point were tested with 1-way ANOVA repeated measures with post-hoc Bonferroni correction. (B) Variability of neck width (overall F = 1.93, p = 0.14; comparison of each time point to each other time point: p >> 0.05). (C) Head volume variability over time (overall F = 3.00 with p = 0.02; comparison of each time point to each other time point: p >> 0.05; $p_{10\text{-}50}$ = 0.048; $p_{20\text{-}50}$ = 0.03). (D) Variability of neck length (overall F = 3.74, p = 0.02; each time point compared to each other time point did not show any significant differences (p >> 0.05), except at 30 minutes compared to 0 minutes ($p_{30\ min}$ = 0.03). (E) Spine length variability (overall F = 11.9, p = 7.21·10-5; no significant difference when comparing each time point to each other one, except at 20 and 30 minutes compared to the first measurement ($p_{20\ min}$ = 5.68·10-4 and $p_{30\ min}$ = 9.53·10-7). (F) Variability of morphological parameters within spines as indicated by the coefficient of variation (CV) in mean + s.d. (red + black). $CV_{neck\ width}$ = 30.9 ± 15.0 %, $CV_{head\ volume}$ = 32.8 ± 23.1 %, $CV_{neck\ length}$ = 23.0 ± 18.6 %, $CV_{spine\ length}$ = 16.4 ± 16.1 %.*

being affected by the imaging itself and thus showing deformation over time. Because of the absence of blebbing of the sample, it might rather be due to a change in focal plane, which was however controlled for by always making small z-stacks. As spines might turn in space, differences found over time might be due to looking at the spine from a different angle (Arellano et al. 2007). Furthermore, transient shortening of the spine might be due to changes in synaptic transmission, but I cannot state a direct link here since I lack a functional readout. Head volume did not significantly differ over time compared to the first time point, but did significantly differ between 10 and 50 minutes and between 20 and 50 minutes (p_{10-}

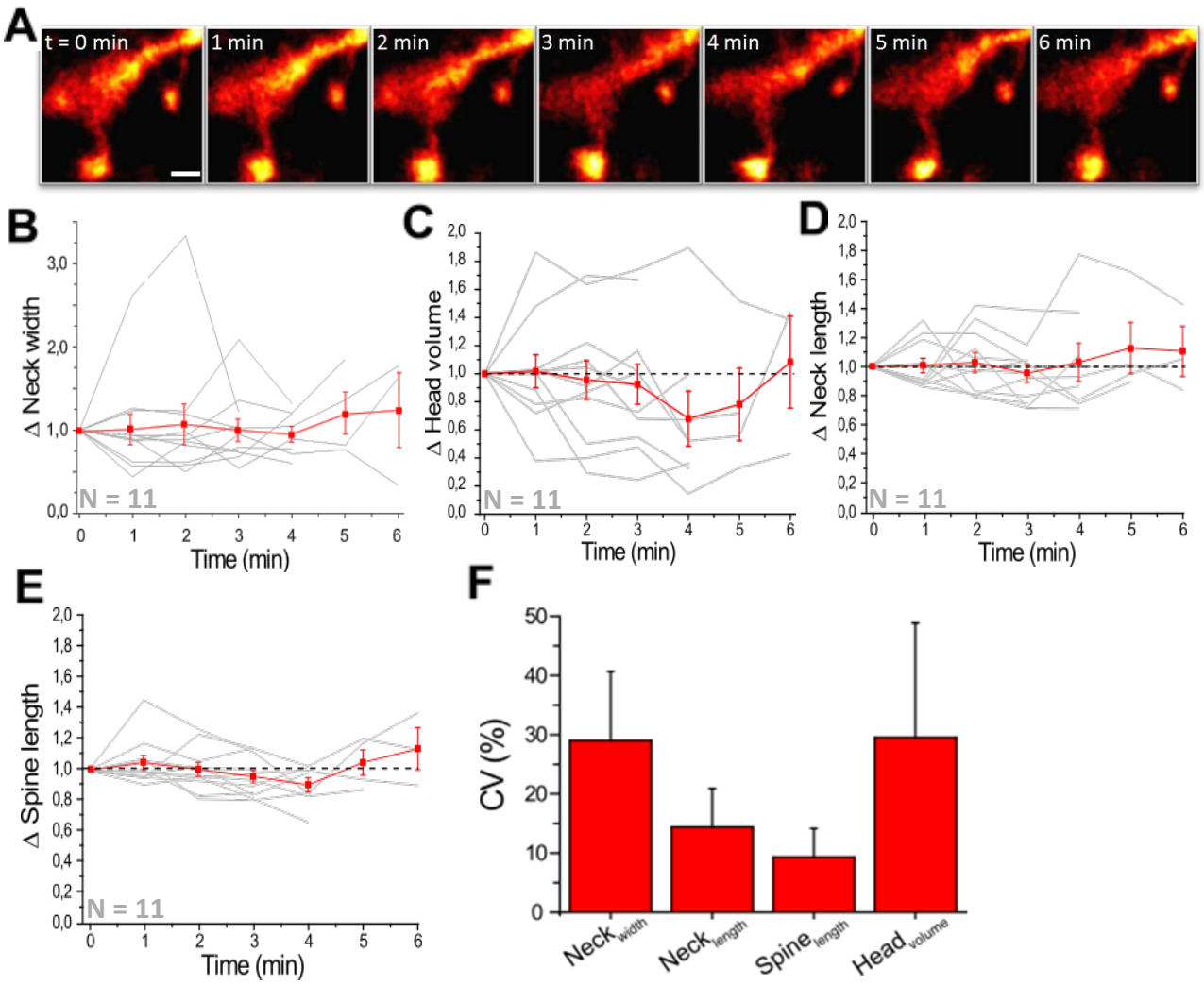

Figure 30: Spine morphological parameters investigated at higher temporal resolution show lower variability. *(A) 2P-STED images of a dendritic spine followed for 6 min, showing low variability and stability of spine morphological parameters over time. Scalebar = 2 µm. (B-E) Timelapse imaging for up to 6 min showing all traces for the individual spines (grey) and mean ± s.e.m. (red). N = 11 spines from 5 animals, 1-way repeated measures ANOVA with post-hoc Bonferroni correction to test differences between each and every time point. (B) Variability of neck width (overall F = 0.65, p = 0.63; comparison of each time point to each other time point: p >> 0.05). (C) Head volume variability (F = 0.40, p = 0.86; comparison of each time point to each other time point: p ranging from 0.15 – 0.69). (D) Variability of neck length (overall F = 0.32, p = 0.86; each time point compared to each other time point did not show any significant differences (p >> 0.05). (E) Spine length variability (overall F = 1.90, p = 0.14; comparison of each time point to each other time point: p >> 0.05). (F) Variability of morphological parameters within spines as indicated by the coefficient of variation (CV) in mean + s.d. (red + black).* $CV_{neck\ width}$ *= 29.0 ± 11.7 %,* $CV_{head\ volume}$ *= 29.5 ± 19.3 %,* $CV_{neck\ length}$ *= 14.4 ± 6.52 %,* $CV_{spine\ length}$ *= 9.29 ± 4.86 %.*

$_{50\ min}$ = 0.048 and $p_{20\text{-}50\ min}$ = 0.030). Even though morphological parameters differed greatly between spines, little variation was found within spines over time, as indicated by the coefficient of variation (CV), except for neck width and head volume, which were more variable ($CV_{neck\ width}$ = 30.9 ± 15.0 % (s.d.), $CV_{head\ volume}$ = 32.8 ± 23.1 %, $CV_{neck\ length}$ = 23.0 ± 18.6 %, $CV_{spine\ length}$ = 16.4 ± 16.1 %; Fig. 29f). Altogether, this indicates that in these experiments, the morphology of each spine does slightly vary over time, but is stable on average over periods of almost an hour when monitored every 10 minutes. Furthermore, the data thus show that repeated 2P-STED imaging of dendritic spines is possible.

The transient changes I observed are unlikely to be due to photo toxicity, since spines on the same dendritic stretch did not all show the same transient changes (Fig. 29a). One should keep in mind, that subtle variations over time might still be due to the rotation of spines over time (Arellano et al. 2007). In addition, to rule out that we missed large changes in spine morphology due to under-sampling, I also followed spines with a higher temporal resolution. Single spines were monitored every minute for 4 – 6 minutes in total (Fig. 30a). At this higher temporal resolution, none of the morphological parameters showed any directional changes, with each time point compared to the other also not showing any significant differences (n = 11 spines from 5 animals, 1-way repeated measures ANOVA with post-hoc Bonferroni correction, overall $F_{neck\ width}$ = 0.65 with $p_{neck\ width}$ = 0.63, overall $F_{head\ volume}$ = 0.40 with $p_{head\ volume}$ = 0.86, overall $F_{neck\ length}$ = 0.32 with $p_{neck\ length}$ = 0.86 and overall $F_{spine\ length}$ = 1.90 with $p_{spine\ length}$ = 0.14; comparison of each time point to each other time point: p >> 0.05; Fig. 30b-e). I also observed that at higher temporal resolution, morphological parameters greatly differed between spines, but again showed little variation within spines, except for neck width and head volume, which were also at higher temporal resolution more variable ($CV_{neck\ width}$ = 29.0 ± 11.7 % (s.d.), $CV_{head\ volume}$ = 29.5 ± 19.3 %, $CV_{neck\ length}$ = 14.4 ± 6.52 %, $CV_{spine\ length}$ = 9.29 ± 4.86 %; Fig. 30f). This variation in spine morphology might possibly be related to changes in synaptic transmission and spine compartmentalization, but I cannot confirm this here as I did not have a functional readout yet.

6.2.3 Biochemical and electrical compartmentalization of spines *in vivo*

The biochemical compartmentalization of spines can be quantified by FRAP experiments using YFP. In order to study spine compartmentalization, I thus performed *in vivo* FRAP experiments combined with 2P-STED microscopy in the barrel cortex of Thy1$^{eYFP/eYFP}$ anesthetized mice who were implanted with a cranial window. The baseline florescence of the YFP signal within the spine head was monitored by 2P line scanning (2P power ~12 mW at the back aperture) for 500 ms prior to photo bleaching for 20-30 ms at a higher 2P power (40 mW at the back aperture). This was followed by continuous 2P line scanning (~12 mW at the back aperture) to monitor the recovery of the YFP signal within the spine head for 3-4 s. The recovery time course of the YFP signal can be described by an exponential fit with a single time constant τ_{meas}. Since the bleaching pulse is rather long, I included a non-fixed offset value to take into account possible incomplete recovery of fluorescence upon bleaching due to additional depletion of YFP in the dendrite. The fitted time constant (τ), obtained as described in the methods section of this thesis, subsequently reflects the degree

of biochemical compartmentalization in the individual spine. In parallel, I used the formulas as previously described (see methods section) to estimate biochemical compartmentalization and electrical resistance of the spine neck based on the spine nanoscale morphology, as exemplified in Fig. 31a-c. From this point on, $\tau_{calculated}$ refers to the recovery time constant as predicted by a simple diffusion model incorporating

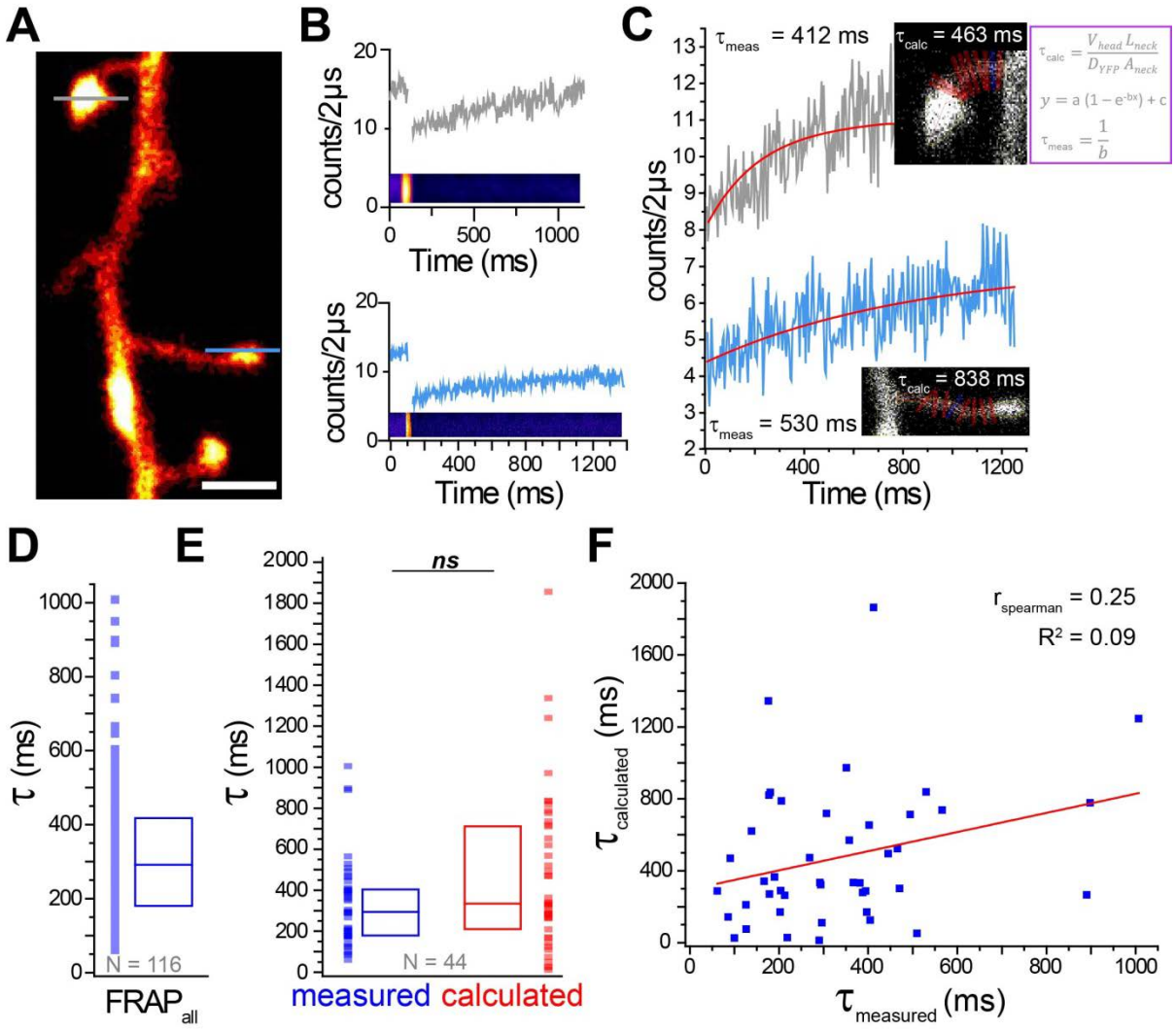

Figure 31: Spine morphology and biochemical compartmentalization in vivo. *(A) Example of YFP-labeled spines, gray and blue line indicating where FRAP traces were recorded. Scalebar = 1 µm. (B, C) Examples of FRAP traces in spines with variable morphology showing related variability in compartmentalization. (B) Examples of full FRAP signal and relative fluorescence of the line scan (intensity bar) of the two different spines shown in (A) with a grey and a blue 'bleaching' line. (C) Recovery traces of the spine with a relatively short neck and large head (top) and of the spine on the same dendritic stretch with a long neck and small head (bottom). The rising phase of the FRAP trace is fitted with a mono-exponential (red), which yields the time constant $\tau_{measured}$. The same time constant is also calculated based on the morphological parameters from the 2P-STED images ($\tau_{calculated}$). Formulas indicated in the purple toolbox. (D, E) Box plots show interquartile range and median of the non-normally distributed measurements. (D) Range (all data points visualized in a scatter plot) and distribution of all FRAP measurements (n = 116 spines from 4 animals, inter quartiles range = 185 – 419 ms). (E) Paired data showing that calculated τ and measured τ do not significantly differ from each other (n = 44 spines from 2 animals, median $\tau_{measured}$ = 295 ms, interquartile range = 179 – 408 ms; median $\tau_{calculated}$ = 334 ms, interquartile range = 237 – 716 ms; Sign Test: Z = 1.66, p = 0.10). (F) Calculated τ did only correlate weakly positive with measured τ ($r_{spearman}$ = 0.25, p = 0.10 ; Linear fit function: R^2 = 0.09), possibly due to the fact that the calculations do not take into account the possible presence of organelles in the spine neck and/or head.*

experimentally measured spine morphological parameters, while $\tau_{measured}$ refers to actual experimental measurements (Fig. 31c). Individual spines exhibited different values for τ as derived from the FRAP experiments, spanning a broad range around a median of 293 ms (n = 116 spines from 4 animals, interquartile being 185 – 419 ms; Fig. 31d). This differs from studies from other laboratories (Grunditz et al., 2008), possibly due to the differences in approach (see Discussion). Diffusion time constants were however within the range of those found in hippocampal organotypic slice cultures (Tønnesen et al. 2014), but differed with hippocampal P14/P37 and P37 L5 cells in acute slices (Wijetunge et al. 2014). However, since the super-resolution based approach from our lab previously showed that spine compartmentalization can be predicted by spine morphology (Tønnesen et al., 2014), I aimed to verify that here in the *in vivo* preparation. Assuming the diffusion coefficient of YFP to be 16 $\mu m^2/s$ (Petrásek & Schwille, 2008), indeed estimates of τ based on spine nanoscale morphology were in a similar range as found with the FRAP experiments (the median of $\tau_{measured}$ = 295 ms with interquartile being 179 – 408 ms, while median of $\tau_{calculated}$ = 334 ms with interquartile range = 237 – 716 ms, Sign Test: Z = 1.66, p = 0.10; Fig. 31e). However, the calculated τ only weakly correlated in a positive manner with the measured compartmentalization factor ($r_{spearman}$ = 0.25, p = 0.10 and linear fit function, R^2 = 0.09; Fig. 31f); this could be explained by the fact that there are multiple other factors contributing to biochemical compartmentalization besides morphology alone. For example, the calculations do not take into account the possible presence of organelles in spine neck and/or head (Grunditz et al., 2008). The presence of these organelles might impede and slow down diffusion, so that the measured time constants are lower than what is predicted by the simple diffusion model. This model only takes the outer morphology of the spine into account and assumes that the inside can be described by a spatially uniform cytoplasmic resistivity. If one would include these other factors in our calculation of τ, this will probably optimize the model for spine compartmentalization and accordingly give a higher correlation between the then newly calculated τ and measured τ. Despite the weak correlation we found, it has been argued that spine morphology and spine compartmentalization are at least related to each other. Indeed, I observed a moderate positive correlation between spine neck length and the diffusion time constant, $\tau_{measured}$ ($r_{spearman}$ = 0.40, p = 0.007; Fig. 32a). However, neck length explained only 4 % of the variation in τ (linear regression, R^2 = 0.04; Fig. 32a). Further, no correlation was found between spine head volume and diffusion time constant as determined by $\tau_{measured}$ ($r_{spearman}$ = 0.062, p = 0.66; linear fit, R^2 = -0.02 (minus sign indicating that robust fitting was not possible); Fig. 32b). Lastly, there was only a weak negative correlation observed between spine neck width and $\tau_{measured}$ ($r_{spearman}$ = -0.15, p = 0.33; Fig. 32c). This parameter was fitted with an allometric fit (due to its quadratic dependency) and had to include a constant in order to allow for robust fitting of the data, once again indicating that other parameters should be taken into account when defining a proper model for diffusion in spines *in vivo*. Similarly to neck length, spine neck width only accounted for little of the variation in diffusion rates (R^2 = 0.016; Fig. 32c).

Based on the spine morphology, I could also estimate spine neck resistance (Ohm's law, formula 1). It can also be estimated based on the diffusion rates (Fick's law, formula 2; Svoboda et al., 1996), as described in the methods section and reformulated here as follows:

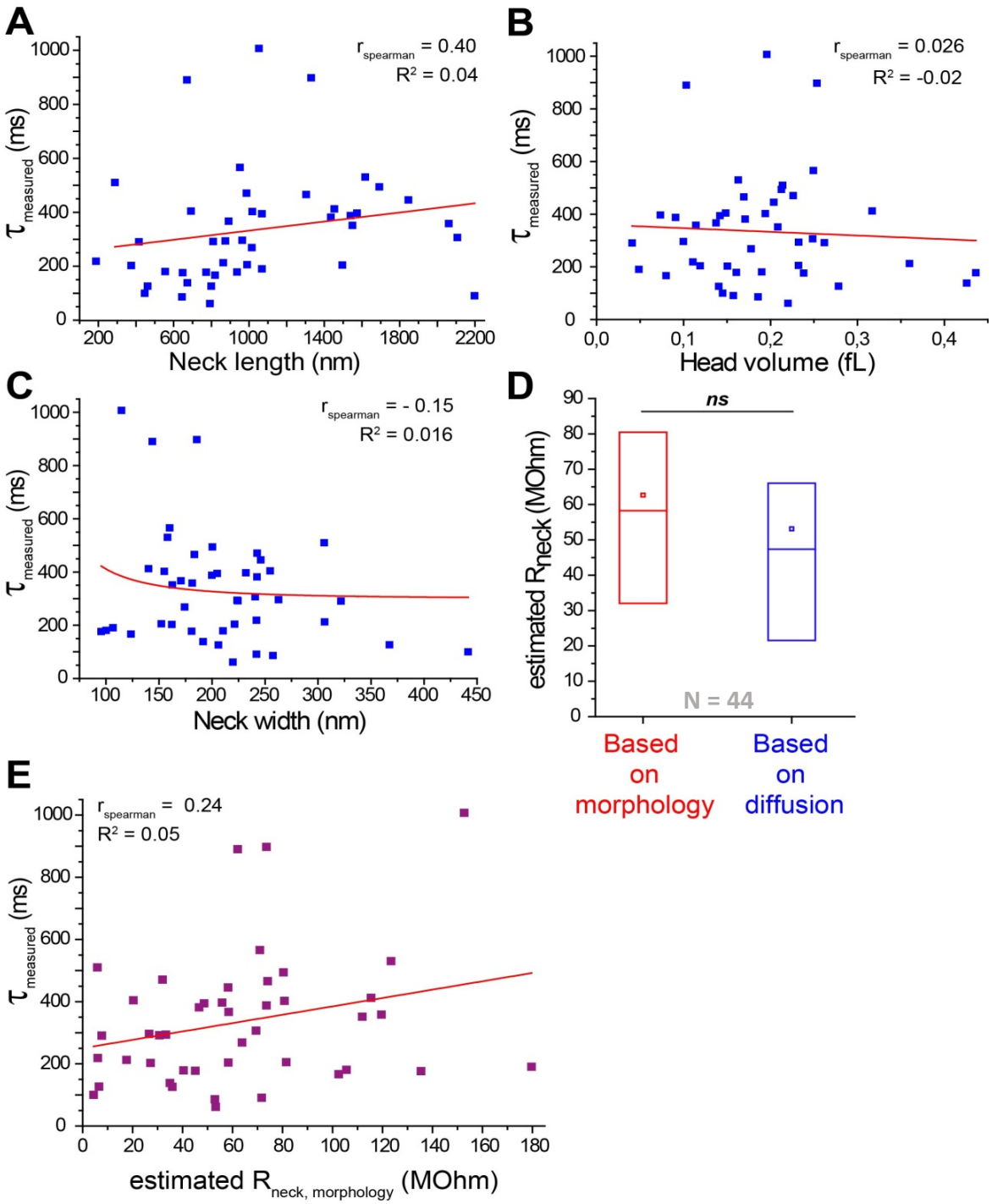

Figure 32: Spine morphology and spine compartmentalization. *(A-C) Correlation of morphological parameters to biochemical compartmentalization. (A) $\tau_{measured}$ plotted as a function of neck length, showing a moderate positive correlation ($r_{spearman}$ = 0.40, p = 0.007), but only little explanation of the variation in $\tau_{measured}$ (linear regression, R^2 = 0.04). (B) Head volume did not correlate with $\tau_{measured}$ ($r_{spearman}$ = 0.026; linear fit, R^2 = -0.02). (C) $\tau_{measured}$ plotted as a function of neck width showing a weak negative correlation ($r_{spearman}$ = -0.15, p = 0.33) and explaining only a small proportion of the variation in τ (allometric fit including a constant, R^2 = 0.016). (D) Estimation of electrical neck resistance based on morphological parameters (Ohm's law) and diffusional rates (Fick's law), similar to (Tønnesen et al., 2014). Box plots show median and interquartile range of R_{neck} estimates, which did not differ significantly between morphological and diffusion based calculations (n = 44 spines from 2 animals, median $R_{neck,morphology}$ = 58 MOhm with interquartile range = 32.4 – 80.7 MOhm; median $R_{neck,diffusion}$ = 48.6 MOhm with interquartile range = 21.8 – 66.5 MOhm; Wilcoxon Signed Rank test: Z = 1.66, p = 0.097). (E) Correlative plot of $R_{neck,morphology}$ and $\tau_{measured}$, showing a weak positive correlation between the two estimates ($r_{spearman}$ = 0.24), but neck resistance only explained 5 % of the diffusion (linear fit, R^2 = 0.05).*

$$R_{morph} = \frac{\rho L}{A} \qquad (1)$$

and

$$R_{\tau} = \frac{\tau \rho D}{V} \qquad (2)$$

where ρ is cytoplasmic resistivity (assumed to be 150 Ω cm; Major et al., 1994; Nevian et al., 2007), L is neck length, A is the neck cross-sectional area, τ the diffusion time constant, D the diffusion coefficient (assumed to be 16 $\mu m^2/s$, (Petrásek & Schwille, 2008), and V is the spine head volume. Using formulas 1 and 2, I found that estimates of R_{neck} based on morphology (n = 44 spines from 2 animals; median $R_{neck,morphology}$ = 58 MOhm, interquartile range = 32.4 – 80.7 MOhm) were not significantly different from estimates based on the diffusion time

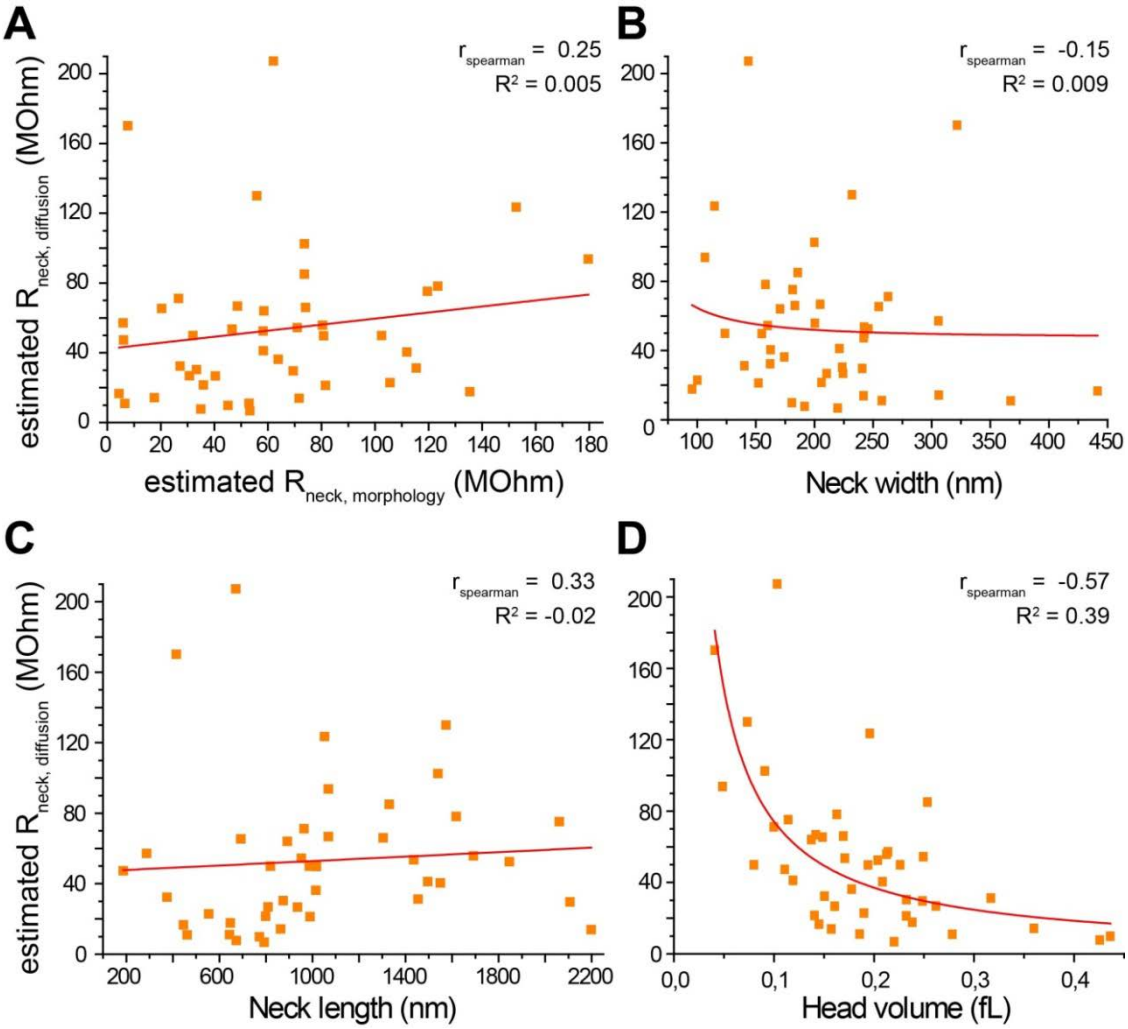

Figure 33: Spine neck resistance and spine morphological parameters. *(A) Correlative plot of $R_{neck,morphology}$ and $R_{neck,diffusion}$ showing a weak positive correlation between the two estimates ($r_{spearman}$ = 0.25), but neck resistance based calculations only explain 0.5 % of the diffusion based calculations (linear fit, R^2 = 0.005). (B-D) Correlation of spine morphological parameters to estimated neck resistance.(B) $R_{neck,diffusion}$ plotted as a function of neck width, showing a very weak negative correlation ($r_{spearman}$ = - 0.15), and only little explanation of the variation in R_{neck} (R^2 = 0.009). (C) $R_{neck,diffusion}$ plotted as a function of neck length showing a weak positive correlation ($r_{spearman}$ = 0.33) and not explaining the variation in $R_{neck,diffusion}$ (R^2 = - 0.02). (D) Head volume did correlate strongly negatively with $R_{neck,diffusion}$ ($r_{spearman}$ = - 0.57) and explained a large proportion of its variability (R^2 = 0.39).*

constant (median of $R_{neck,diffusion}$ = 48.6 MOhm, interquartile range = 21.8 – 66.5 MOhm; Sign Test: Z = 1.66, p = 0.097; Fig. 32d). Estimates of R_{neck} based on spine morphology were not strongly correlated to diffusion in spines as defined by $\tau_{measured}$, indicating that biochemical and electrical compartmentalization vary independently from each other ($r_{spearman}$ = 0.24 and R^2 = 0.05; Fig. 32e). The different types of estimates for R_{neck} were weakly correlated with each other, with only 0,5 % of the variation in estimated neck resistance based on diffusion being explained by estimated neck resistance based on morphology ($r_{spearman}$ = 0.25, linear fit R^2 = 0.005; Fig. 33a). Morphological parameters each correlated differently to the estimates of R_{neck} based on diffusion (neck width: $r_{spearman}$ = -0.15, R^2 = 0.009; neck length: $r_{spearman}$ = 0.33, R^2 = -0.02; Fig. 33b,c). Naturally, head volume is strongly correlated to estimated R_{neck}, as this parameter is part of the formula to estimate R_{neck} based on diffusion, and it did explain 39 % of the variability in the estimated R_{neck} ($r_{spearman}$ = -0.57 and R^2 = 0.39; Fig. 33d).

6.2.4 Conclusion

Taken together, the 2P-STED images showed that spine morphological parameters span a broad range, the findings being in accordance with previous EM studies (Harris et al., 1992; Trommald & Hulleberg, 1997; Arellano et al., 2007). Furthermore, spines were shown to be stable over time on average, across a large population. However, at the level of individual spines the morphological parameters exhibited appreciable temporal fluctuations. One should keep in mind that spine shapes are region and age specific (Wijetunge et al. 2014), and thus a direct comparison with previous studies in hippocampus cannot be made. We can however consider 2P-STED microscopy a useful tool to study spine morphology and morphological dynamics at the nanoscale, which is an improvement on imaging spines with conventional light microscopy, which has a diffraction-limited resolution.

Furthermore, I here explored the link between spine morphology and biochemical compartmentalization in the intact environment (*in vivo*), which had only been explored in organotypic slice cultures using STED (Tønnesen et al., 2014). I do not see a direct correlation between $\tau_{calculated}$ and $\tau_{measured}$. Despite the moderate correlation between neck length and $\tau_{measured}$, the variation in diffusion is only weakly explained by spine morphological parameters, which might explain the lack of correlation between $\tau_{measured}$ and $\tau_{calculated}$. Based on previous studies in organotypic slice cultures and acute slices (Tonnesen et al. 2014; Wijetunge et al. 2014), I think that spine nanoscale morphology and biochemical compartmentalization are nevertheless linked to each other. However, in order to confirm this for the *in vivo* preparation, further experiments are needed.

6.3 Further applications of *in vivo* 2P-STED microscopy

6.3.1 Validating the capability of the 2P-STED setup to perform dual color imaging *in vivo*

Part 1 and 2 of the result section showed the capability of the setup to image different brain structures in two colors in acute slices and demonstrated super-resolution 2P-STED microscopy *in vivo*. However, a combination of the two approaches (dual color imaging and *in vivo* preparation) was not yet verified for our specific setup. In order to validate that dual color 2P microscopy *in vivo* was possible with our setup, I used crossbred mice, which labelled a subset of neurons and all microglia (Thy1H$^{+/YFP}$ x Cx3Cr1$^{+/eGFP}$; Fig. 34a). In addition, I show that 2P-STED microscopy *in vivo* with two colors was also possible in differently sized field of views (Fig. 34b,c). The 2P-STED microscopy approach allowed us to observe the

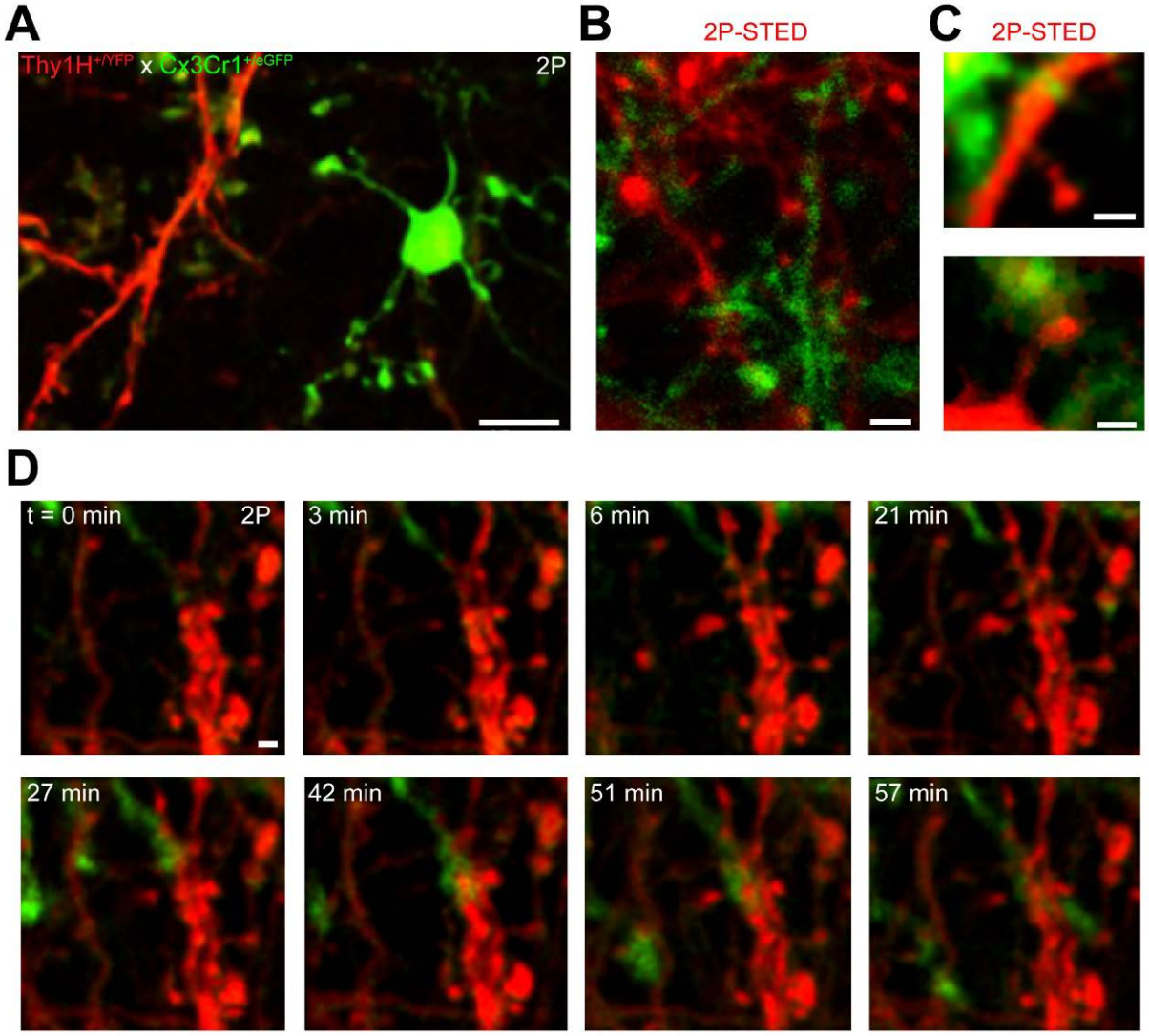

***Figure 34: Validation setup – two color 2P-STED microscopy* in vivo.** *(A) Image acquired in 2P mode and linearly unmixed to visualize neural and glial structures in two colors. Maximum intensity projection (MIP) of a 10 µm z-stack showing dendritic stretches (red) and microglia (green). Scalebar = 10 µm. (B-D) Images were acquired in 2P-STED mode and two channel signal detection was linearly unmixed to visualize spine-microglia interactions. (B) Smaller field of view (FOV) overview of both neural (red) and microglial (green) structures, showing complexity of interactions. Scalebar = 2 µm. (C) Zoom on dendrite (red) - microglia (green) proximity (top) and spine head – microglia proximity (bottom). Scalebars represent 1 µm. (D) Time lapse acquisition of neuron (red) – microglia (green) interaction, showing approach and retraction of microglial processes over time. Scalebar = 1 µm.*

interaction of microglia and spines at the nanoscale, and revealed that microglial processes were in contact with both the dendritic shaft as well as the dendritic spines *in vivo* (Fig. 34c). Microglia – spine interaction has been shown to be activity-dependent and influenced by neuronal activity *in vivo* (Wake et al. 2009). The authors proposed that microglia monitor and respond to the functional state of the synapse and might contribute to spine turnover (Wake et al. 2009). Even though our approach allows for the quantification of the interactions with great detail, which can add to the previous findings of Wake and colleagues, I here only use this model to show that our setup is capable of performing multiple types of acquisitions, in two colors, and with nanoscale resolution *in vivo*. In addition to microglia-spine snapshots, I could indeed follow the microglia-spine interactions for up to 1 hour (Fig. 34d). Having validated the setup, I can now use this *in vivo* dual color 2P-STED approach to study spine – glia interactions in more detail.

6.3.2 The tripartite synapse *in vivo*

Until fairly recently, most studies of the brain have been mainly neuron-centric. However, mounting evidence indicates that glial cells are not only the support cells in the brain but also play an important role in regulating synaptic physiology more directly. Here I mainly focus on one glial type, the astrocyte, which has nowadays been accepted as to be involved in several synapse-related processes, including the regulation of synaptic efficacy. Since astrocytes occupy a key position between blood vessels and synapses, they are amongst others in charge of coupling neuronal activity and local blood flow changes (Petzold & Murthy 2011). Astrocytic processes can have diameters well below the resolution limit, requiring super-resolution techniques to image their fine structure.

Our *in vivo* 2P-STED approach is a promising tool to study the tripartite synapse because of its ability to image neuronal structures at the nanoscale and *in vivo*. In order to investigate the tripartite synapse *in vivo* with 2P-STED, I additionally needed to establish a STED suitable labelling approach for astrocytes.

6.3.2.1 Development of an astrocytic label suitable for STED microscopy

To study the tripartite synapse, I started out by imaging double transgenic mice ($Thy1H^{+/YFP}$ x $GFAP^{+/eGFP}$) expressing YFP in a subset of neurons under the Thy1 promoter and GFP in most astrocytes under the glial fibrillary acidic protein (GFAP) promoter. Unfortunately, astrocytic labelling was not sufficiently bright to acquire images of the tripartite synapse (Fig. 37a). GFP expression under the GFAP promoter was bright enough in single transgenic animals to perform 2P imaging (data not shown), but not bright enough to perform long-term imaging or STED-imaging.

I then tried a viral approach to label the astrocytes. First, several constructs based on the $gfaABC_1D$ promoter, the shortened version of the GFAP promoter, and adeno-associated virus (AAV) serotypes were tested for suitability (Fig. 35a-c). This shorter promoter was published to be specific for, and allow for bright labelling of, the astrocytes (Shigetomi et al. 2013). This property made it an interesting promoter for our 2P-STED imaging purpose. Suitability was determined based on the specificity and brightness of the labels. In addition, the reactivity of astrocytes upon injection of the newly created virus was tested at the time

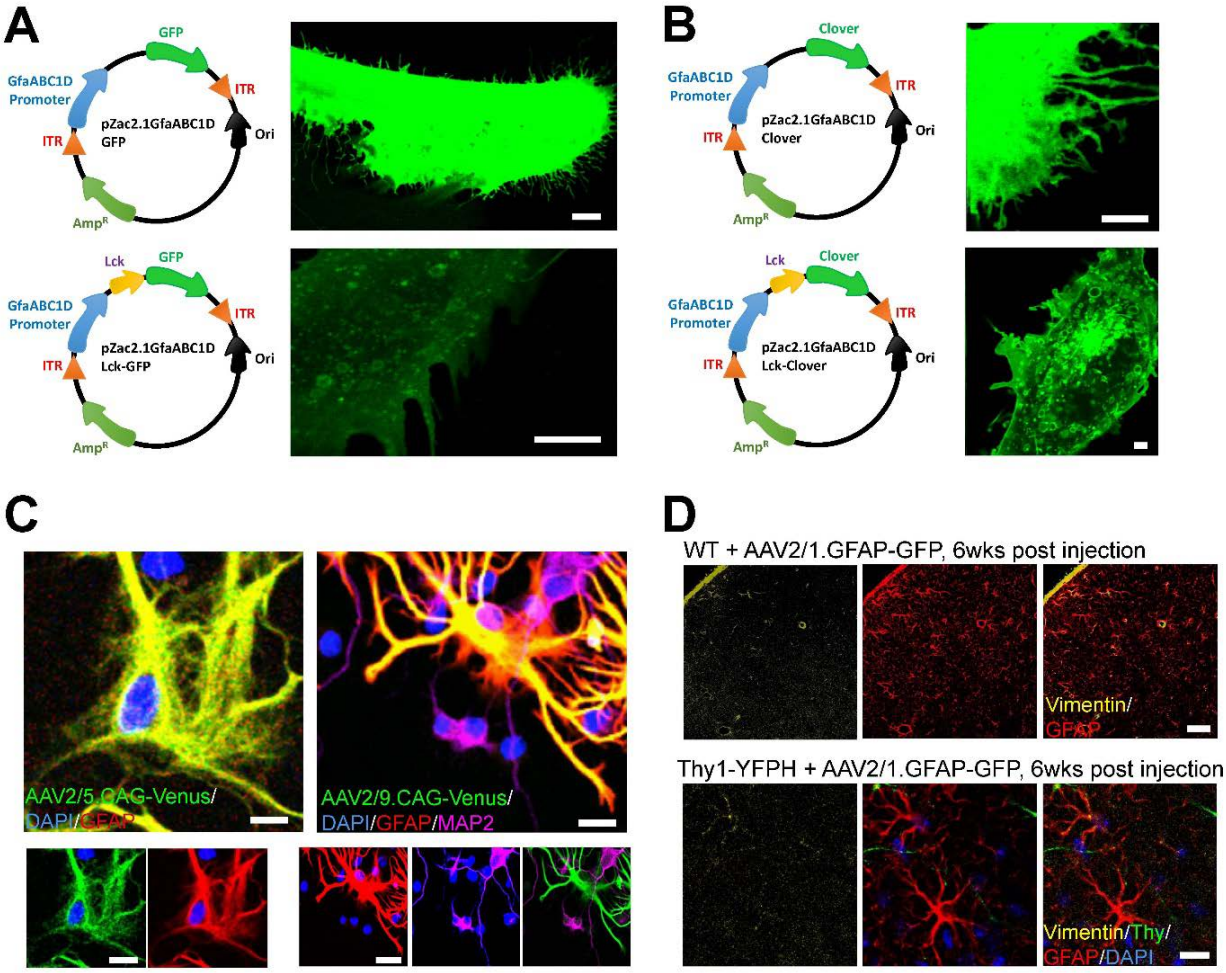

Figure 35: Testing and validating viral labelling approach for astrocytes. *(A) Testing of cytosolic and membrane bound constructs of GFP under gfaABC$_1$D promoter, showing weaker expression of membrane bound GFP. Scalebars represent 5 µm. (B) Testing of cytosolic and membrane bound constructs of Clover under gfaABC$_1$D promoter. Detailed organelles can be seen with the membrane bound label, brightness similar in cytosolic and membrane-bound labelling. Scalebars are 5 µm (top) and 2 µm (bottom). (C) Testing of different associated adeno virus (AAV) serotypes 2/5 (left) and 2/9 (right) in mixed cultures, showing preference of serotypes under ubiquitous promoter for astrocytes as tested with immunochemistry. Scalebars are 10 µm. (D) Validating non-reactivity of astrocytes upon injection (of AAV2/1.GFAP-GFP to label astrocytes) at time point of imaging (6 weeks post-injection) in WT and Thy1-YFPH mice. Using vimentin as a marker for astrocyte reactivity, I find no apparent reactivity as compared to activated labelling as seen in literature. Scalebars are 10 µm.*

point of planned image acquisition (Figure 35d). The antibody used for immunohistochemistry to verify astrocyte reactivity, vimentin, was chosen based on several research articles (Yamada et al. 1992; Lewén 2013; Martinez et al. 1998; Herpers et al. 1986) but nevertheless also tested for its suitability in my hands as a reactivity marker (Figure 36a-c).

After having verified that both the constructs and different virus serotypes were suitable for astrocytic labelling, and having checked that 6 weeks after injection of the virus astrocytes had recovered from activation by the injection, 3 different viruses were tested for *in vivo* imaging. The adeno associated viruses AAV2/1.GFAP-GFP, AAV2/1.gfaABC$_1$D-Clover, and AAV2/1.gfaABC$_1$D-Lck-Clover were stereotactically injected in the barrel cortex of wild type (WT) animals and astrocytes were imaged *in vivo* 6 weeks later. Clover has similar spectral

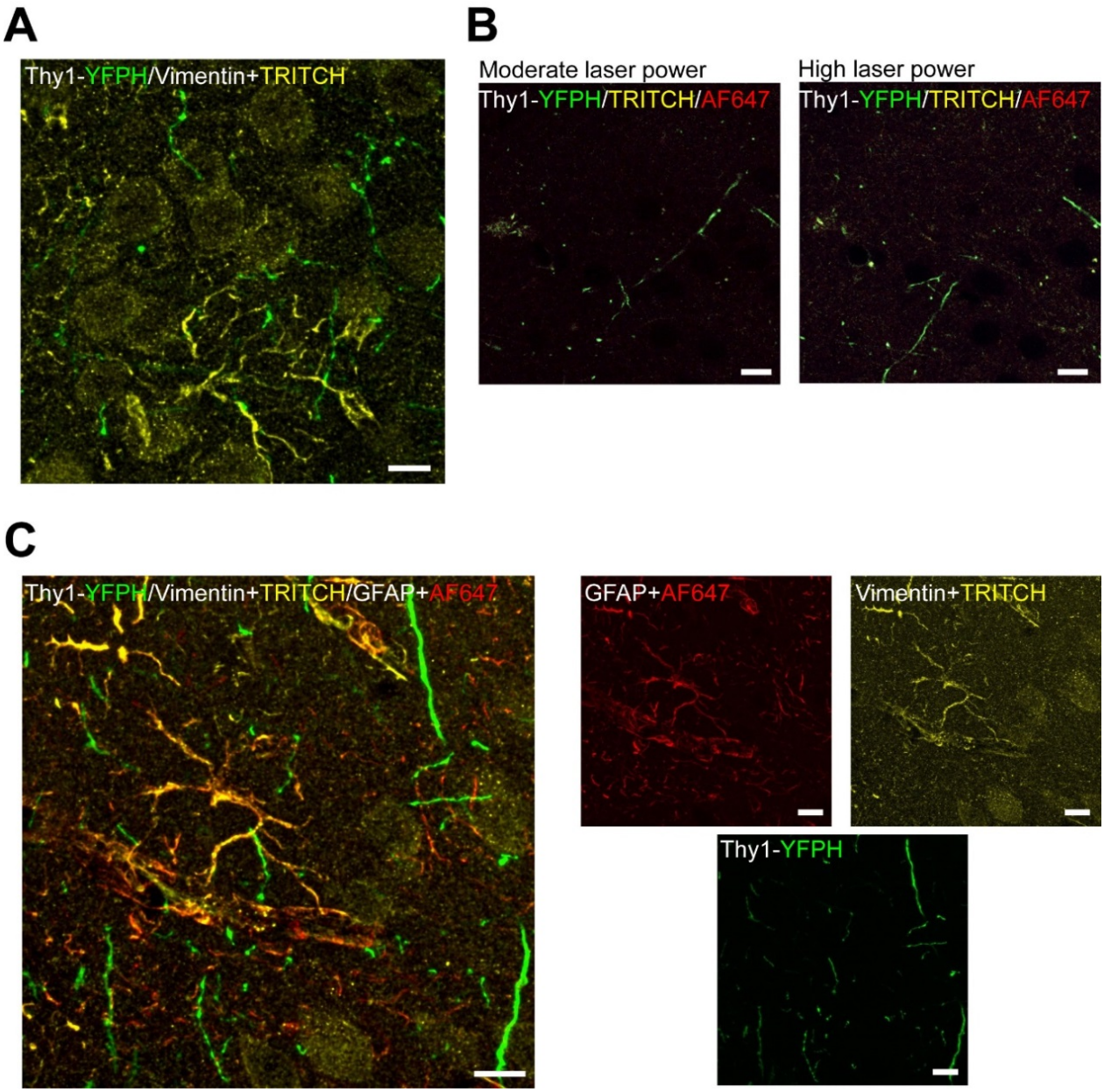

Figure 36: Validation of vimentin antibody. *(A) Immunostaining of brain slices from Thy1-YFPH mice after injection of saline solution showing little astrocyte reactivity indicating the injection itself is not harmful. (B) Immunostaining of Thy1-YFPH brain slices incubated with secondary antibodies alone, showing that vimentin is specific, as indicated by the absence of secondary antibody labelling, even at high laser power (right). (C) Verification astrocyte specificity by co-staining astrocytes based on GFAP and vimentin promoters in Thy1-YFPH mice, confirming specificity of vimentin as astrocytic reactivity label. All scalebars represent 10 µm.*

properties as GFP, but seems to be brighter and more stable than the GFP label. Both cytosolic and membrane-bound Clover were tested because I expected the membrane label to express even in finer processes at the end of the astrocytic arbor where the volume label might not be well expressed. Due to the high surface-to-volume ratio of the thin processes, this viral membrane labeling approach may allow for a higher chance of finding the tiny astrocytic protrusions nearby dendritic spines, and thus a higher chance of imaging tripartite synapse structure *in vivo*. Upon stereotactic injection at age ~P25, all viruses were properly expressed in the barrel cortex of anesthetized mice at age P55 – P75 and allowed for 2P-

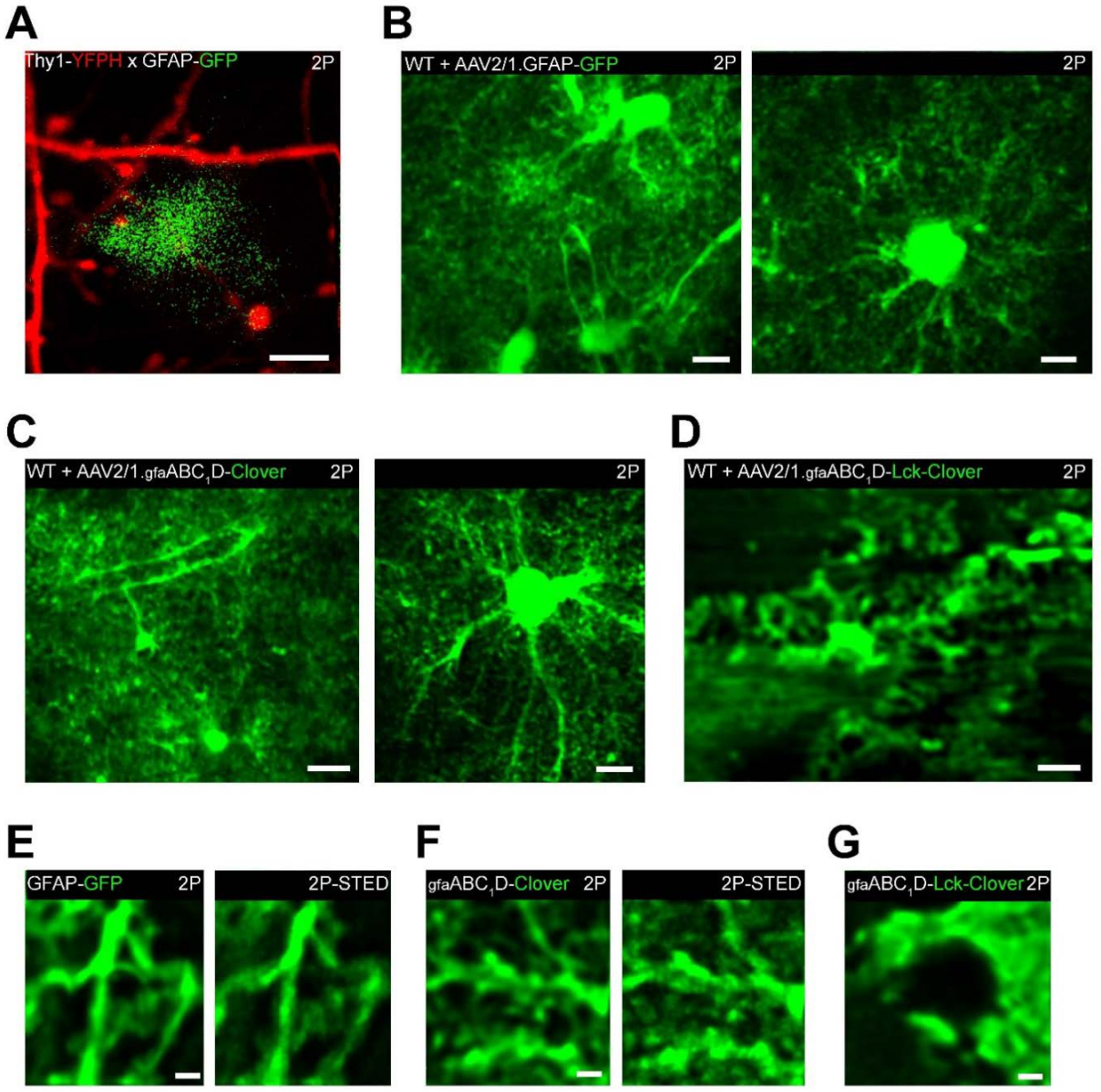

***Figure 37: Establishment of an astrocytic label for 2P-STED microscopy* in vivo.** *(A) MIP of 2P image of dendritic stretches (red) and astrocytes (green) acquired in double transgenic Thy1-YFPHxGFAP-GFP mouse. Scalebar = 2 µm. (B-D) Testing different viruses to label astrocytes, MIPs of 10 µm (left) and 20 µm (right) z-stacks acquired in 2P mode in barrel cortex of anesthetized wildtype (WT) mice. Scalebars are 10 µm (B left, C left, D) and 5 µm (B right, C right). (B) Cytosolic GFP under GFAP promoter. (C) Cytosolic Clover under gfaABC$_1$D promoter. (D) Membrane bound Clover under gfaABC$_1$D promoter. (E-G) Astrocytic processes visualized as MIPs of 1 µm z-stacks acquired in 2P and 2P-STED mode. Images are deconvolved (3 iterations) for visualization purposes only and all scalebars represent 1 µm. (E) Cytosolic GFP. (F) Cytosolic Clover. (G) Membrane bound Clover, 2P-STED acquisition in small FOV failed.*

imaging in different FOVs *in vivo* (Fig. 37b-d). Cytosolic Clover labeled astrocytes slightly brighter than the two other constructs (Fig. 37c), but all constructs showed large and smaller astrocytic processes around the cell body as well as astrocytic end-feet around the blood vessels. Because of its 3D complex arborization, astrocytic labeling with the membrane-bound label appeared as sheets at the larger processes and supposed cell body, while volume labels created a densely labelled arbor-like structure and a clear cell body. The typical morphology of astrocytes, that is, the dense arborization, and the fact that their domains are distinguishable from each other, can be visualized with 2P microscopy *in vivo*.

Since I was interested in the fine details of the astrocytes, I performed 2P-STED microscopy on astrocytic processes. No apparent photo bleaching or photo damage was detected upon 2P-STED imaging of astrocytes labelled with cytosolic GFP or Clover, but neither did I see a clear STED effect (Fig. 37e,f). I did not manage to obtain clear STED images of the membrane bound labelled astrocytes in WT mice either, but could zoom in on the astrocytic processes with 2P microscopy (Fig. 37g). The dense structure of the astrocyte causing stronger background fluorescence affects the signal-to-noise ratio and thereby impeded imaging in 2P-STED mode. Despite these results, I thought that the viral labelling approach was promising and thus I proceeded to use these labels in Thy1H$^{+/YFP}$ mice in order to be able to study the nanoscale morphology of the tripartite synapse.

6.3.2.2 2P-STED microscopy as a tool to study tripartite synapse in vivo

Using cytosolic GFP as a label for astrocytes, I was able to image both neuronal and astrocytic structures in layer 1 of mouse barrel cortex *in vivo*, with label density of the astrocytes increasing when going deeper into the tissue (Fig. 39a). Nevertheless, I was able to visualize the astrocytic domain in relation to the neuronal structures with 2P microscopy (Fig. 39b). However, spine-astrocyte interactions were harder to visualize than global neuron-astrocyte co-localization, especially because astrocytic processes bleached fast when imaged with 2P-STED (Fig. 38). I could resolve the co-localization at a single time point, but it was not possible to study spine-astrocyte interactions over time. I succeeded in visualizing

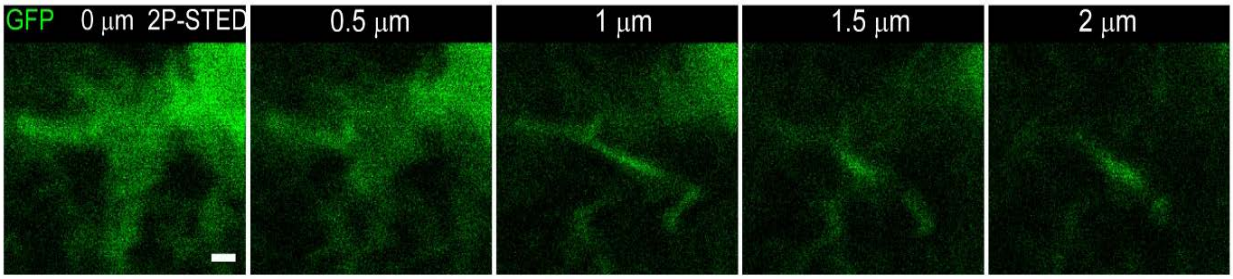

***Figure 38: Bleaching of astrocytic label**. Cytosolic GFP expressed under the GFAP promoter. Images are MIPs of 2 µm z-stack of astrocytic process showing rapid loss of signal over depth. Scalebar = 1 µm.*

with great detail the proximity of spine and astrocytic processes (Fig. 39c), where due to the use of 2P-STED I could well resolve the dendritic spine neck, but astrocytic processes remained harder to resolve. That said, I discarded the cytosolic GFP label as a suitable label to follow tripartite synapse dynamics at the nanoscale over time *in vivo*. Considering the brightness of cytosolic Clover as shown in figure 37 and cytosolic labels being less prone to bleaching than membrane-bound labels, I expected that visualizing the tripartite synapse structure with it will be possible, at least in single snapshots. Unfortunately, I did not arrive to perform these experiments. I did however also expect membrane-bound Clover to be a suitable label to image the astrocytes at high resolution, since the label will get expressed in the fine processes, which the cytosolic label might not label as well. Indeed, I could express the membrane bound Clover in astrocytes next to the Thy1-YFP labelled pyramidal neurons. Because of the sheet-like appearance and all astrocytic processes getting labeled, label density was very high (Fig. 40a). While distinguishing neuronal structures within the meshwork of astrocytic processes was challenging, I succeeded at visualizing spine-astrocytic

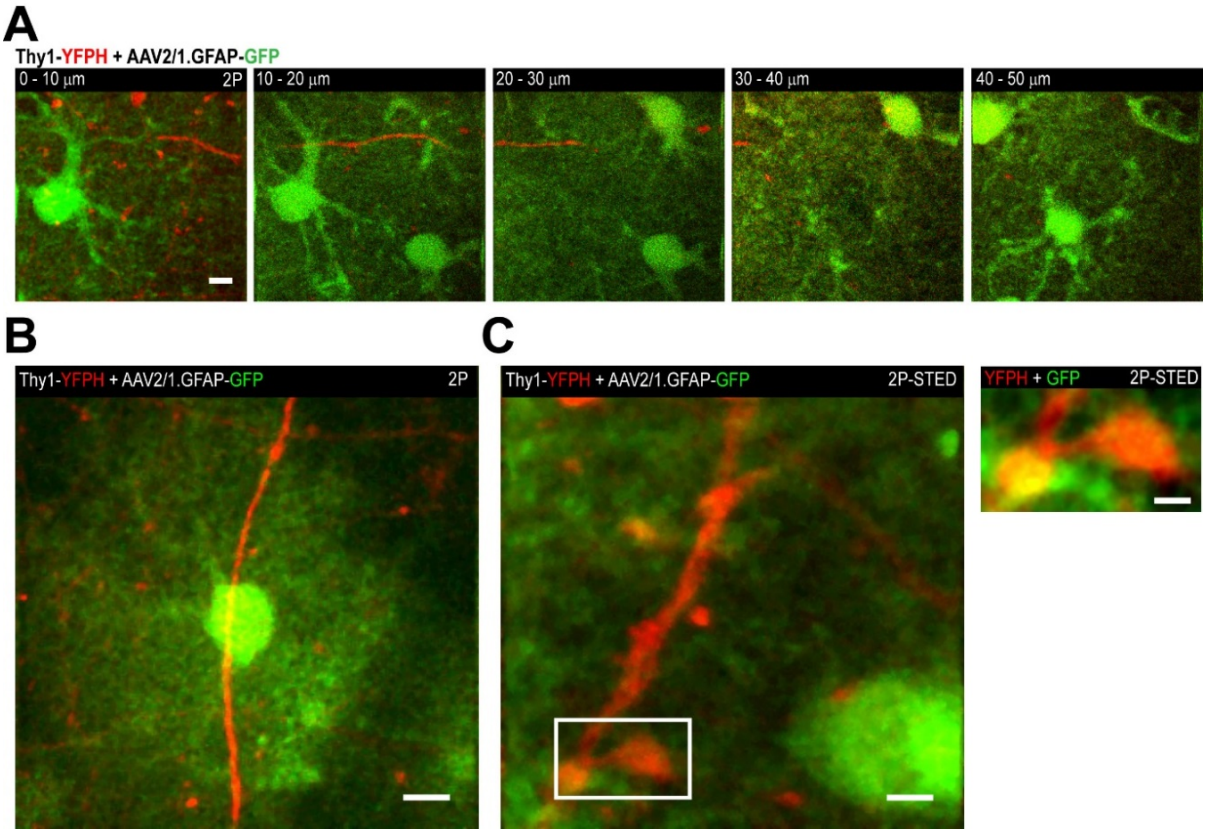

Figure 39: Imaging of dendritic spines and astrocytes labelled with cytosolic GFP. *(A) MIPs of 10 µm z-stacks acquired with 2P microscopy, showing neuronal structures (red) and astrocytes (green). At different depths, astrocytic labelling becomes stronger, and unmixing of the signals more difficult. Scalebar = 5 µm. (B) Typical example of astrocytic domain (green) submerging neuronal structures (red), image acquired in 2P mode, scalebar = 5 µm. (C) Small field of view (FOV) MIP of dendritic stretch close to astrocytic cell body (left) and zoom in on dendritic spine surrounded by astrocytic processes (right). Images acquired in 2P-STED mode, showing well resolved dendritic spine neck. Scalebars are 2 µm (left) and 500 nm (right).*

process co-localization with 2P-microscopy (Fig. 40a). I proceeded to image spine-astrocyte interaction with 2P to find regions of interest (ROIs), which would be suitable for 2P-STED microscopy. That is, ROIs at the edge of the injection site, away from vascular structures, and not within 10 µm of the surface of the brain. In those regions I was able to visualize both dendritic spines surrounded by, and interacting with, astrocytic processes (Fig. 40b,c). I observed diverse types of coverage of neuronal structures by the astrocytes, while resolving the fine details of the neuronal structures such as the spine neck width (Fig. 40c, left). Astrocytic processes were found to be proximal to the different neuronal structures (dendritic spines and axonal boutons), as well as to oppose them, as seen in the merged signal images (Fig. 40c, center). Further studies on spine-astrocyte interactions should be performed with our 2P-STED approach in order to quantify the different type of astrocytic coverages of spines *in vivo*.

6.3.3 Conclusion

Altogether, the presented data showed the feasibility of dual color 2P-STED microscopy *in vivo* to study spine – glia interactions with high resolution. Both dendritic spines and their opposing microglial processes could indeed be resolved at the nanoscale, allowing for

interesting follow-up studies such as whether microglia preferentially interact with spines of specific morphologies and how dynamic these contacts are.

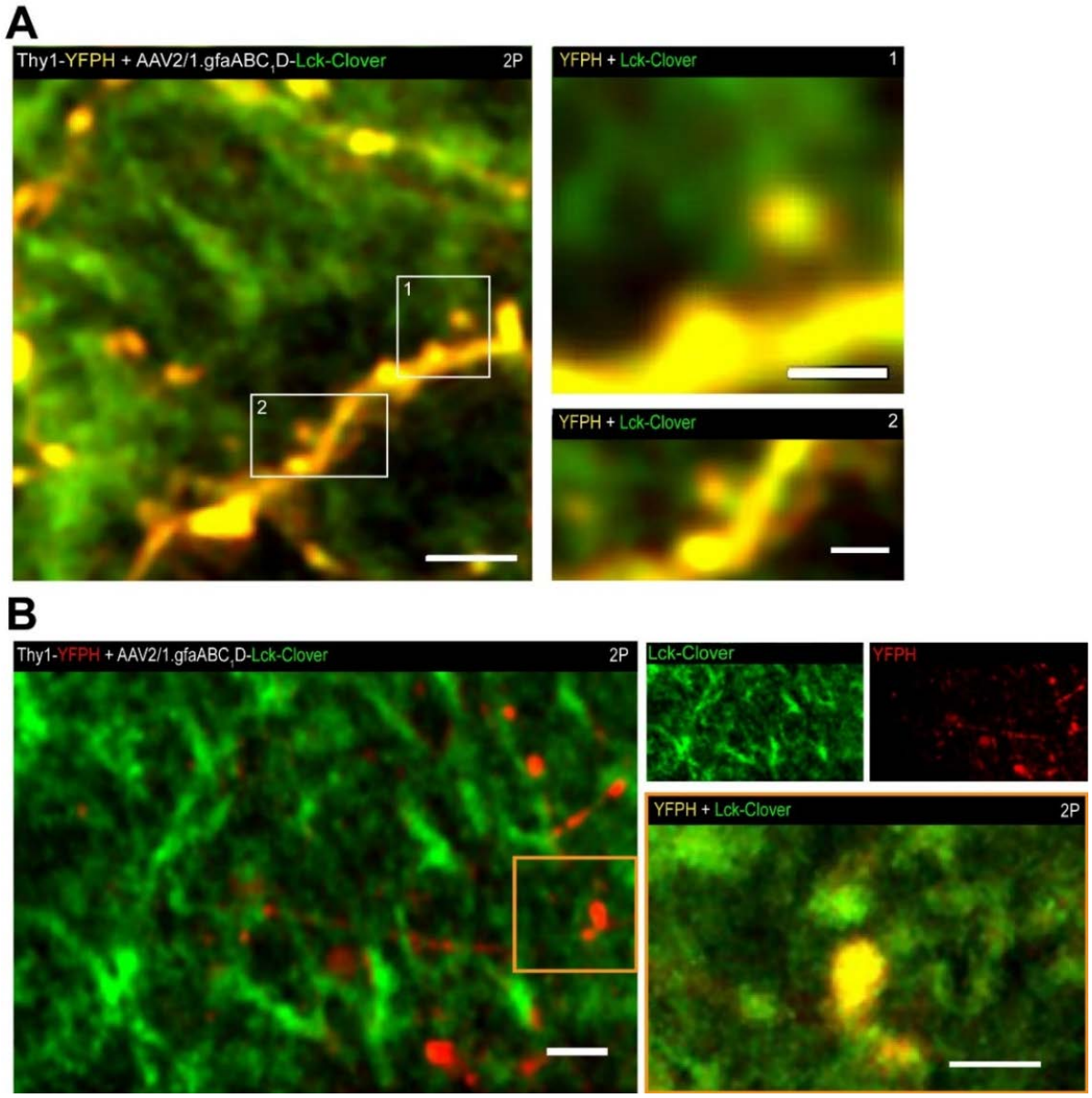

Figure 40, part I: Astrocytic coverage of neuronal processes visualized with membrane bound Clover as label for astrocytes.*(A) MIPs showing spines (yellow) on the same dendritic stretch and axonal boutons (yellow) all being differently covered by the astrocytic processes (green). Scalebars are 3 µm (left) and 1 µm (upper and lower right). (B) MIP of a 20 µm z-stack showing dense labelling of astrocytic processes by membrane bound Clover (left), making unmixing of the two labels (Lck-Cklover (green), upper center; YFPH (red), upper right) more complicated as visualized in the lower right image. Scalebars are 5 µm (left) and 2 µm (right). Figure continued on next page.*

Unfortunately, imaging of the tripartite synapse remained challenging, but I did show a promising novel strategy to co-label astrocytes and neurons in the mouse barrel cortex. Utilizing a viral labeling approach for the astrocytes, I could visualize spines which were volume-labeled with YFP in transgenic mice together with astrocytic processes which were labeled with Clover. Within the cloud of densely membrane-labeled astrocytes, I could resolve dendritic spine necks with great detail, but to resolve the morphology of astrocytic processes at the nanoscale remained challenging.

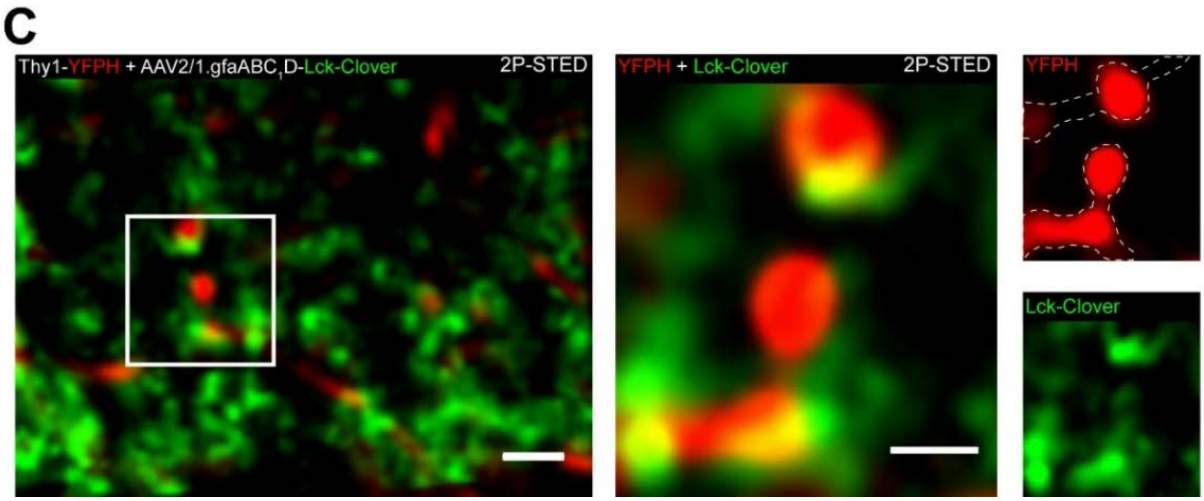

Figure 40 continued: Astrocytic coverage of neuronal processes visualized with membrane bound Clover as label for astrocytes. *(C) MIP of neuron - astrocyte interaction (left) imaged in 2P-STED mode at the edge of the injection side (less crowded). Zoom in (right) shows that astrocytes (green) are proximal to both dendritic spines (red) as well as axonal boutons (red). Small FOV images were deconvolved (4 iterations) and scalebars are 2 µm (left) and 1 µm (right).*

I do however believe that the *in vivo* dual color 2P-STED microcopy approach in combination with the novel labelling approach for the astrocytes, will eventually allow for visualization and quantification of astrocytic processes their fine morphology. These preliminary experiments namely helped identifying some of the pitfalls to imaging astrocytes with 2P-STED microscopy, which accordingly may help identify a suitable approach to study spine-astrocyte interactions *in vivo* at the nanoscale in the future.

7 DISCUSSION

The building blocks of the mammalian brain, neurons and glial cells, are constantly adapting their properties in response to environmental stimuli and internally generated neuronal activity. These dynamics and the communication in the brain takes mainly place at synapses, which in the case of an excitatory synapse typically are formed by presynaptic axonal boutons and postsynaptic dendritic spines. It has been shown that those structures have a variable and dynamic morphology and it has been proposed that spine morphology plays a key role in synaptic functioning. Furthermore, the thin spongiform processes emanating from glial cells can be in close apposition and/or interact with the synapse. Unfortunately, the study of synapses as well as their glial partners is often hindered by their small size and the optical inaccessibility by conventional diffraction-limited light microscopy. Thus, it is of great interest to study the neuronal and glial nanoscale structures, as the structural parameters of dendritic spines can define their biochemical and electrical properties, and the glial coverage of spines can regulate synaptic efficacy. The recent development of stimulated emission depletion (2P-STED) microscopy can bypass the diffraction barrier of conventional light microscopy and allows for imaging inside living biological tissue. It thereby enables the investigation of neuronal and glial structures at the nanoscale in living brain tissue. To investigate the morphological dynamics of dendritic spine morphology as well as spine compartmentalization in the barrel cortex of living mice, I used an approach which combined super-resolution 2P-STED microscopy and FRAP experiments *in vivo*. To study spine-glia interactions with our custom-built 2P-STED microscope *in vivo*, we aimed to set up a novel labelling approach for the glial cells. I searched for an approach that will label the structures strongly and stably, and would thus be suitable for STED imaging.

7.1 Summary of the findings

In this thesis, I first introduced the basic principles and implementation of *in vivo* 2P-STED microscopy in the laboratory. In the first results section I described the optimization of *in vivo* surgery and imaging, and the use of a silicon-oil objective to visualize dendritic spines in layer 1 of mouse barrel cortex. I also showed the acquisition of nanoscale (time-lapse) images of YFP and GFP labeled structures in acute brain slices and *in vivo*.

I then showed in the second section of the results that 2P-STED imaging could reveal the morphological parameters (i.e. neck width, neck length, spine length, and head volume) of dendritic spines with great detail in the barrel cortex of anesthetized Thy1-YFPH mice. Those morphological parameters were found to span a broad range and all of them - except for total spine length – showed a significant difference between measurements from 2P data compared to 2P-STED data. This difference in measurements is expected from the improved resolution obtained in STED microscopy. Total spine length is expected to show the same results in both imaging modalities since spine length sizes are well above the resolution limit. Spine morphology was imaged every 10 minutes for up to 50 minutes, and every minute for up to 6 minutes. I did not find any correlation between the different morphological parameters. Even though the population of spines showed large heterogeneity, all of the morphological parameters were on average stable over time. Spine morphology did show subtle fluctuations from one time point to another for a given spine, but again remained on

average stable over time. Similar to spine morphology, my exploratory experiments showed that the values for the biochemical compartmentalization factor (diffusion time constant, τ) spanned a broad range, with similar ranges found in calculated τ (from 2P-STED data) and measured τ (from FRAP data). Calculated and measured τ were not correlated, which could be explained by morphological data not taking into account what fraction of space inside the spine is effectively involved in diffusion, or taken up by intracellular structures such as the actin-rich spine apparatus, the endoplasmic reticulum (ER), mitochondria, and other organelles. A moderate correlation was found between spine neck length and measured τ, while a weak correlation was found between spine neck width and measured τ. Spine neck length seemed to only explain 4 % of the variation in diffusion rates and spine neck width seemed to account for only 1.6 % of the variability. Head volume did not correlate with, neither explained the variability in, the diffusion time constant τ. In addition to the diffusion time constant, neck resistance was calculated either based on Ohm's law or on Fick's law, and was found to not be significantly different when comparing the two approaches.

Finally, I verified that our system is capable of performing dual color 2P-STED microscopy *in vivo* and I demonstrated its capability by imaging spine – glia co-localization. The interaction between spines and microglial processes could be visualized, but astrocytes were highly sensitive to the STED light. It was therefore challenging to image the tripartite synapse in 2P-STED mode. With the novel labelling approach I did however succeed in the visualization of the apposition of neuronal structures and astrocytic processes.

Taken together, the results described in this thesis thus showed that our 2P-STED approach allows for the study of brain structures, in particular dendritic spines, with super-resolution microscopy *in vivo*. It was shown that spine morphology is on average stable at the nanoscale and that subtle fluctuations in spine morphology can account for a small part of the variability in spine compartmentalization. Furthermore, we extended the approach to two color imaging based on spectral detection and linear unmixing of spectrally similar fluorophores like YFP and GFP. With this extended approach, I studied the morphological co-localization of dendritic spines and glial processes in layer 1 of the barrel cortex of anesthetized mice. These findings pave the way for a better understanding of how synaptic morphological rearrangements contribute to brain physiology and thus shows the value of the 2P-STED approach as a tool in neuroscience.

Having showed the implementation of *in vivo* 2P-STED microscopy in the laboratory, it would be good to mention here that besides familiarization with a novel system, setting up the surgery for a cranial window in mouse barrel cortex, and thus an *in vivo* imaging approach for our laboratory, other basic technical issues were dealt with as well. Besides imaging, our setup also allowed for patch-clamping experiments. Together with another PhD student in the lab (Thomas Pfeiffer), we started out implementing other optical beam paths in order to be able to perform uncaging experiments with our system in the near future. Those adaptations of the setup were however not discussed in this thesis. Further, there was ample opportunity to learn about the alignment of laser cavities, basic functioning of the different lasers included in the setup, the working principles of pressured air tables, and getting a much deeper insight into general optics, as we were unfortunate to have for in total more than ten months of challenging issues with the different lasers included in our setup. Environmental factors destabilized our system, giving me the chance to evaluate

different kinds of sources for noise and system instability, as well as to come up with new ideas of how to solve or circumvent those challenges.

Besides these general technical challenges, the system requires intense alignment on a daily basis. Since one needs both spatial and temporal alignment of the different laser beams (2P and STED), the components in the optical path have to be optimized for a good performance of the system each and every day. Furthermore, to obtain high-quality images, it is of great importance that the sample preparation is mechanically stable and the mouse is maintained as close as possible to its physiological health. Another technical limitation of our 2P-STED microscope is the depth penetration and the chance for losing resolution when going deeper into tissue. In order to benefit more from the advantages of 2P microscopy, it would be beneficial to make use of adaptive optics. Another limitation of the presented work is the labelling of astrocytes. Even though astrocytes were brightly labeled, it remained challenging to image them in 2P-STED mode. I did not yet arrive to stably image the fine details of astrocytic processes over time, but did show the first steps in this direction.

All in all, this complex, but valuable, 2P-STED system thus performed well regarding the imaging of dendritic spines but needs further optimization for stable repeated imaging of the tripartite synapse. The presented system also allowed me to improve tremendously my troubleshooting skills, and I see some opportunities to improve the 2P-STED approach even more.

7.2 Improvements of the *in vivo* STED approach as a tool in neuroscience

Ever since its first theoretical description, STED microscopy has been increasingly applied to the life sciences. Its application to neuroscience specifically is only a decade old, which can be explained by the fact that STED is technically challenging and was originally limited to fixed preparations. Fixed samples can be imaged on an inverted system while using high numerical aperture (NA) oil objectives, while *in vivo* imaging requires longer working distance water immersion objectives and an upright system. The high NA oil objectives (refractive index (n) = 1.51) are not compatible with live tissue imaging and the water-immersion (n = 1.33) objectives, even though well suited for live tissue imaging in an upright system, often come at the cost of having a lower NA than the oil objectives. Nevertheless, water-immersion objectives are nowadays used in our laboratory for STED microscopy applied to live tissue, including the intact brain. With the usage of a silicon-oil objective, it is now also possible to have both a high NA and reduced refractive index mismatch (1.40 for the silicon-oil objective versus ca. 1.36 for brain tissue) and have a high performance while imaging through a glass coverslip (n = 1.51). Here, I showed mainly results based on imaging with the water-immersion objective, since the physical size (5.4 mm at the front lens to 22.8 mm within the first 0.17 mm of the front lens) and short working distance (0.3 mm) of the silicon-oil objective made *in vivo* imaging challenging. Nevertheless, experiments performed with the silicon-oil objective were promising regarding the obtained resolution and correction of spherical aberrations on fluorescent nano-spheres. Using the silicon-oil objective I could also show crisp images of dendritic spines in layer 1 of mouse barrel cortex. I therefore believe that the silicon-oil objective is very promising for further *in vivo* experiments.

7.2.1 Optimization of the preparation

In order to benefit from the optical properties of the silicon-oil objective, it is of importance to create a fixation mechanism for the head holder, which should take up as little space as possible. In my trials, I created a much thinner helmet than I would usually do for the water-immersion objective, but this comes with the risk of the helmet being more fragile and thus offering less mechanical stability during image acquisition. One could try to use a different type of dental cement for the helmet, which can be applied in a thin fashion but still ensures a robust fixation. Furthermore, it might be beneficial to adapt the imaging platform in such a way that the head holder can be fixed on the nasal bone instead of, or in addition to, the parietal bone. It is thereby positioned further away from the barrel cortex and would thus create more space for the objective to image through the cranial window. A combined fixation of the nasal bone, premaxilla and the top of the skull (see Fig. 41) will allow for stable head fixation (Howles et al. 2009). Preferably, the mouse is stabilized in a stereotactic

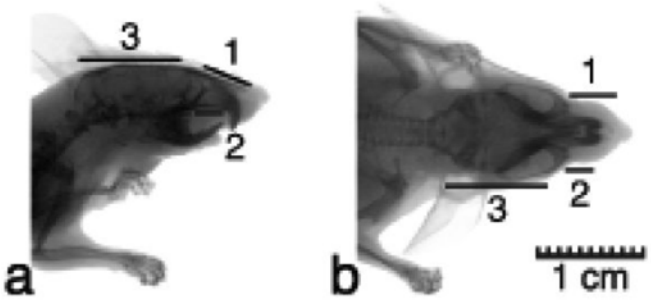

Figure 41: X-ray images showing boney structures that could be used to head-fix a mouse. *1 = nasal bone, 2 = premaxilla, 3 = top of the skull. Optimal angle for 1 was measured to be 22 ± 2° and for 2 preferable angle was measured to be 0 ± 1°. Figure taken from (Howles et al. 2009).*

frame, which can be adjusted in x, y, z, and angle, in order to stably fix and perfectly fit the mouse below the objective. In addition, increasing the size of the craniotomy to 5 mm will facilitate imaging with the silicon-oil objective. However, this has the disadvantage of covering almost the full mouse hemisphere and thereby hinders the application of equal pressure to the brain below the window due to the brain its curvature. If size restrictions turn out to be the only restriction for using a silicon-oil objective, it might be worth considering to change the animal model and use rats instead of mice.

Besides adjusting the brain preparation for the purpose of a better fit with a different type of objective, the cranial window itself could already be improved in order to allow for stable and long-term imaging of the mouse neocortex. A striking paper by Heo and colleagues (Heo et al. 2016) showed the use of a “soft, transparent, freely accessible cranial window for chronic imaging and electrophysiology”. This novel approach made use of silicone-based polydimethylsiloxane (PDMS) to substitute the skull and dura, thereby having a penetrable window with long-term high optical clarity (see Fig. 42). Imaging was reportedly stable, and the material that was used for the window allowed for insertion of multiple micropipettes and/or microelectrodes at any position without any leakage of the cerebral spinal fluid (Heo et al. 2016). I share the optimism of the authors that this approach will contribute to a better insight into brain functioning when combined with other technologies often used in the field of neuroscience. It remains to be tested whether STED light does not interfere with the PDMS, but this approach for a cranial window sounds very promising, especially because it will allow the combined use of an imaging approach with functional measurements like electrophysiology. A functional read-out of neuronal activity and the dendritic spines would

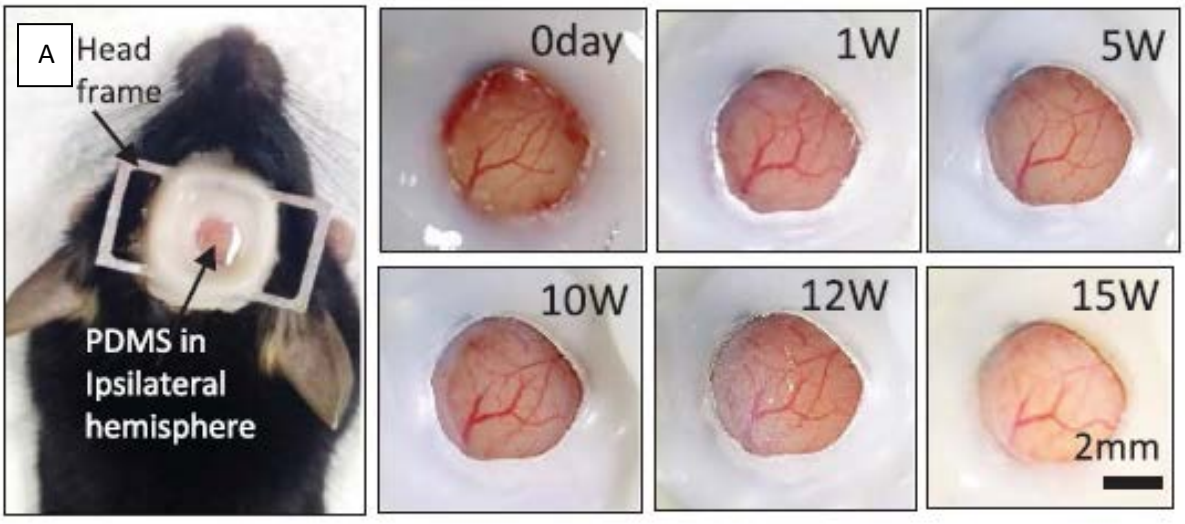

Figure 42: A cranial window with PDMS. *(A) Example of a mouse implanted with a PDMS window, clarity of the brain followed from the day of the surgery (0day) until 15 weeks after the surgery, showing high optical clarity. Image adapted from* (Heo et al. 2016).

be helpful to confirm my estimations of neck resistance based on 2P-STED microscopy and the influence of tri-synaptic morphological changes at the nanoscale on synaptic function. Indeed, electrophysiological techniques have a perfectly matching temporal resolution. However, they lack proper spatial resolution, which could be overcome by making use of optical imaging methods to study the activity of multiple cells simultaneously, even in processes too small for electrode recording (Cossart et al. 2005).

7.2.2 Adding optical imaging methods to study brain cell physiology

One optical strategy to study the electrical properties of spines, would be the use of voltage-sensitive dyes and genetically encoded voltage indicators (VSDs and GEVIs; see e.g. Kuhn et al. 2008; Ferezou et al. 2006; Knöpfel et al. 2015). When exciting the dye and monitoring the emitted fluorescence, one can determine the voltage of the cell with a fast response time in the microseconds range. However, VSDs used to have a low signal to noise ratio (Kuhn et al. 2004), bound unspecific to all membranes, and mainly gave information about the larger dendrites and axon terminals. The last few years, optical voltage imaging has gained momentum with the development of the GEVIs (e.g. see Knöpfel et al. 2015). GEVIs have a subcellular spatial resolution, millisecond temporal resolution, and allow for the simultaneous recording of hundreds of neurons (Inagaki & Nagai 2016). The GEVIs thus enable voltage recordings that are challenging to achieve with other techniques, and could allow greater experimental throughput (Yang & St-Pierre 2016). The performance of the indicator does however depend on many factors, including the imaging modality (Yang & St-Pierre 2016). It therefore remains to be elucidated whether they can be used in combination with 2P-STED microscopy. If possible, this would enable investigating whether or not there is a direct relation between spine morphology and spine function *in vivo*. Possibly, in baseline conditions this will not be obvious to see, but by using for example 2P-uncaging of glutamate, one could specifically activate single spines and study their electrical activity (with GEVIs), as well as subtle fluctuations in their morphology (with STED microscopy).

Another optical approach to monitor neuronal activity is the usage of Ca^{2+} indicators to image calcium concentrations (early work in Yuste & Katz 1991). This approach relies on the calcium influx upon depolarization of the cell, with the calcium influx in the soma of the active cell being directly related to the number of action potentials fired (discussed in e.g. Cossart et al. 2005). A large range of calcium indicators is nowadays available for regular confocal and 2P microscopy, but here I only discuss the yellow/green fluorophores as these would be compatible with our setup. To fully benefit from the capabilities of our setup, preferably one uses a calcium indicator that is especially stable and bright enough to be imaged with 2P-STED light. Such an indicator will allow for simultaneously imaging the nanoscale morphology and calcium levels in for example dendritic spines. In addition, calcium is an important astrocytic signaling molecule and would thus allow for a functional read-out of those glial cells as well. In order to monitor changes in calcium levels, one can make use of calcium-sensitive fluorescent indicators or genetically encoded calcium indicators (GECIs). The acetoxymethyl (AM) fluorescent calcium probes, such as for example Oregon Green BAPTA-1-AM (OGB1-AM), can be simultaneously bolus-loaded into many cells by virtue of the fact that they are initially membrane permeable (but then become trapped inside the cells after enzymatic cleavage of the ester group) (Stosiek et al. 2003). They have a high affinity for calcium and show large responses. Several other AM esters, including Fluo-4 AM, Fura-2 AM and Indo-1 AM, were also successfully loaded *in vivo* and imaged with 2P microscopy to study neuronal activity in layer 2/3 of the mouse barrel cortex (Stosiek et al. 2003). Despite their membrane permeability, the AM indicators require acute loading into the sample. To save this step and to be able to do chronic imaging, one might thus prefer using the genetic method. One successful class of GECIs for calcium imaging are the yellow cameleons (YCs; Horikawa et al. 2010; Nagai et al. 2004; Yamada et al. 2011). For example, the YC 3.60 ratiometric FRET (fluorescence resonance energy transfer) indicator is stably expressed in neurons (Margolis et al. 2010) and has been found to allow for the study of calcium signals on the long term (Andermann et al. 2010; Margolis et al. 2010; O'Connor et al. 2010; Margolis et al. 2012), with high spatio-temporal resolution (Minderer et al. 2012) and sensitivity (Lütcke et al. 2010; Minderer et al. 2012) in the anesthetized mouse somatosensory cortex. YC indicators are generally less sensitive to motion artefacts than non-ratiometric sensors and thus allow for the quantification of calcium concentrations in *in vivo* preparations. In addition to YC3.60, YCX2.60 has been shown to display strong expression in different types of neurons in layer 2/3 of the somatosensory cortex in transgenic mice, while also having an expanded dynamic range (Madisen et al. 2015). Furthermore, the latest generation of GECIs, such as the single wavelength calcium indicator GCaMP6 (Chen et al. 2013), showed improved performance over the previous GCaMP generations (discussed in e.g. Madisen et al. 2015; Lin & Schnitzer 2016). One of the variants, GCaMP6f, was shown to exhibit fluorescence changes of almost 3 % for calcium concentrations up to 1 µM with half decay times of approximately 70 ms *in vitro* at 37 °C (Chen et al. 2013; Badura et al. 2014). The GCaMP6 variants could report single action potentials with at least 20 % ΔF/F with a half decay time of 142 ms or larger in the mouse cortex *in vivo*, which is superior to the performance of organic dyes (Chen et al. 2013). The *in vivo* dynamic range of the GCaMP6 variants (13 ± 0.9 % until 23 ± 3.2 %) was further 3. 6 fold higher than the dynamic range of its predecessor GCaMP5K (3.6 ± 1.9 %) (Chen et al. 2013).

Another variant of GCaMP6f was recently shown to allow for more temporally accurate calcium reporting, while maintaining high responsiveness *in vitro* and *in vivo* (Badura et al. 2014). Complementary to the previously shown Thy1-GCaMP6 mouse line (Dana et al. 2014), Madisen and colleagues further showed the stable transgenic expression of GCaMP6 variants in neurons with increased sensitivity (Madisen et al. 2015). In addition, GCaMP6 could even be used to study hippocampal dentate gyrus granule cells *in vivo*, which gave similar results when comparing to red fluorescent indicators which reportedly facilitate the imaging deep inside tissue (Pilz et al. 2016). The red-shifted calcium indicators will however not be further discussed here, as they are not compatible with our setup. Altogether, the GCaMP6 indicators are having an improved performance over synthetic dyes and previous generations of GECIs and allow for the long-term imaging of small synaptic compartments as well as large groups of neurons (Chen et al. 2013). Recently, a new design has been proposed for a green calcium indicator (Barykina et al. 2016). The so-called NTnC sensor showed higher brightness and pH-stability *in vitro* compared with GCaMP6s and allowed for the visualization of neuronal activity *in vivo* in mouse primary visual cortex in freely moving awake mice (Barykina et al. 2016). The calcium indicators described above mainly focused on the functional read-outs of neurons, but can possibly be modified in such a way that they allow for the visualization of calcium levels in astrocytes as well. Indeed, for example the GCaMPs have been used to study astrocytic calcium activity. Recently, using a GCaMP6 variant, previously unknown characteristics of subcellular astrocytic calcium signals where revealed upon long-term imaging of astrocyte populations *in vivo* (Stobart et al. 2016). Using either one of the above mentioned calcium indicators, many interesting follow-up experiments can be thought of. For example, combined with the usage of our 2P-STED approach we could study the nanoscale morphology of the tripartite synapse, while simultaneously following the calcium levels in either the astrocytic processes or the dendritic spines. Further, one could use the 2P-STED approach together with the calcium imaging to study how both these parameters (morphology and calcium levels) change over time.

7.2.3 Optimization of the setup

Besides linking nanoscale morphology to neuronal and astrocytic function, it is important to allow for the most optimal visualization of the fine details of different brain structures. An improved visualization of the subtle morphology of brain structures can be obtained by increasing the axial resolution of the microscope, that is, create a 3D STED beam. In our laboratory, preliminary results show the feasibility of 3D STED in brain slices, which can possibly be extended to *in vivo* imaging as well. The creation of a 3D STED beam can be established by the use of an additional phase plate in the STED beam path, which creates a bottleneck beam via a phase shift. This phase shift is a π phase shift in a central disc, causing excited molecules to be quenched below and above the focal spot. The combination of a 2D STED beam with the bottle beam will enhance the resolution of the microscope in both lateral and axial direction (e.g. (Klar et al. 2000)). The axial bottle beam is however even more susceptible to aberrations than the lateral donut beam (Antonello et al. 2016), and thus has a higher need for aberration corrections. One strategy to correct for aberrations is the use of adaptive optics (Yan et al. 2016) such as spatial light modulators (SLMs). SLMs are electrically programmable devices that spatially modulate a coherent beam of light via liquid

crystals. These crystals can change the polarization of reflected (or transmitted) light dependent on the electric field. SLMs can modulate both the phase and the intensity of a light beam, which is advantageous for a more profound depth penetration. They will further allow for improved STED microscopy in complex structures, by correcting aberrations coming from the optical inhomogeneity of tissue (Patton et al. 2016). The performance of the STED microscope can further be improved by optimizing the temporal alignment of the excitation and STED pulses. This can be achieved via trial and error, or by using simulations (Gao et al. 2016). Temporal adjustments can further be made in the detection pathway, with time-gated detection having been shown to circumvent the issue of temporal misalignment (Galiani et al. 2012). The authors further suggested that synchronization jittering, in STED systems with different sources for the excitation and depletion beam, could be reduced through temporal adjustments (Galiani et al. 2012). In addition, care should be taken that polarization of the light beams is optimized, as is it key to a good zero intensity center of the doughnut and thus resolution enhancement (Galiani et al. 2012). Another improvement in the detection pathway specific for our setup would be the implementation of proximity-detection. This will circumvent the de-scanning of the fluorescence signal, does not need to focus the emitted light into an optical fiber, and will thus allow for more efficient detection of the scattered photons deep inside the intact brain. A high quality detector with a large active window, such as the GaAsP photomultiplier tube (PMT), can easily be implemented in the system since only one additional dichroic mirror will need to be installed behind the objective to send the emitted fluorescence to the detector(s). Besides the GaAsP detectors, one could also consider a hybrid detector, which unites the advantages of avalanche photodiodes and PMTs (Borlinghaus et al. 2012). Altogether, by technically developing the setup it will thus be possible to resolve brain structures even better with high(er) resolution and improved signal intensities.

7.3 Imaging dendritic spine morphology and compartmentalization *in vivo*

Spine necks, and in particular the electrical resistance they impose on synaptic currents, have been suggested to be a key mechanism for synaptic plasticity. This may not affect so much somatic electrical activity directly, but can regulate local voltages and thereby influence dendritic integration of synaptic signals (Grunditz et al. 2008; Tønnesen et al. 2014; Tønnesen et al. 2016). To study the effect of spine neck changes on synaptic function, a detailed read-out of the spine morphology should be combined with functional assays. So far, studies on spine dynamics have mainly focused on dendritic spines in the hippocampus, but it is of great interest to also investigate spines in layer 1 of the mouse neocortex since it is a key layer for integration of sensory inputs and intra-cortical activity. One big advantage of studies in layer 1 is its accessibility for both *in vivo* 2P- and STED microscopy. I here performed snapshot and time-lapse analysis of dendritic spines in the living brain with a lateral resolution around 70 nm and a temporal resolution in the minute range.

7.3.1 Resolving spine morphology at the nanoscale *in vivo*

Even though EM studies of spines in fixed samples provided us with detailed information about their nanoscale morphology (Harris et al. 1992; Arellano et al. 2007), similar results were scarce in live tissue. Our lab established the investigation of fine structures in living

brain slices with STED-microscopy, mainly in the hippocampus (Tønnesen & Nägerl 2013; Bethge et al. 2013; Wijetunge et al. 2014), and could argue against morphological categorization schemes commonly used in the literature of light microscopy (Tønnesen et al. 2014). Work of the Hell group showed an *in vivo* example of spine morphology being variable over time, as well as rearrangements of actin in dendritic spines (Berning et al. 2012; Willig et al. 2014). In addition to this work, I now presented here a much more comprehensive analysis of spine morphology and structural dynamics. I showed that spine sizes and shapes were stable over time on average, across a large population. However, at the level of individual spines the morphological parameters exhibited appreciable temporal fluctuations. Using the 2P-STED approach, I was able to resolve well the differences in spine morphological parameters and changes in spine morphology in depth *in vivo*. While the values I found for spine neck width *in vivo* were in a similar range as compared to those in hippocampal organotypic slice cultures and acute slices (Tønnesen et al. 2014), neck length values differed greatly between different preparations. Neck width values were also comparable with those found in brain slices of P37 WT mice in both the hippocampus and L5 cells of the cortex (Wijetunge et al. 2014). On the contrary, neck width values in WT mice at the age of P14 were slightly more different and neck length values were different for both P14 and P37 hippocampal and L5 cells (Wijetunge et al. 2014). These differences might be explained by the fact that my *in vivo* preparation differs in both age (Tønnesen et al. 2014 & Wijetunge et al. 2014) and region (Tønnesen et al. 2014) from the previous work.

7.3.2 Dynamics of spine morphological parameters *in vivo*

Several studies have already implied that spine morphology is reflecting its function (Nusser et al. 1998; Majewska et al. 2000; Yuste et al. 2000), making the investigation of morphological dynamics a relevant study to better understand synaptic functioning. At lower resolution, several groups indeed showed the link between spine structural plasticity and learning and memory (Holtmaat et al. 2006; Xu et al. 2009; Yang et al. 2009; Lai et al. 2012; Moczulska et al. 2013), but they did not focus on the effect of subtle changes in spine morphology. To this end, Lauterbach and colleagues used a very elegant approach to both optically stimulate and simultaneously non-invasively observe neuronal structures with great detail in primary cultured cells, and showed that indeed nanoscale morphology is structurally plastic (Lauterbach et al. 2016). Since primary cultured cells are not in their physiological environment, it would be advantageous to study these effects in a more intact environment as well. It was shown that subtle changes in spine morphology could be followed in brain slices upon stimulation through 2P glutamate uncaging (Tønnesen et al. 2014). However, I am now the first to quantify the dynamics of several morphological parameters at the nanoscale *in vivo*, which might be indicative of continuous adaptations in the connectivity of the neuronal network. Furthermore, I did not artificially control for all the vital functions of the mice, unlike Berning and colleagues, making my preparation more similar to the actual physiological environment. Others confirmed the usage of STED microscopy for repeated imaging of spines in cultured neurons and brain slices (Westphal et al. 2008; Ding et al. 2009; Tønnesen et al. 2014), but studies in the intact brain are still scarce. Albeit imaged at lower resolution, dendritic spines were found to be persistent in the adult animal, but nevertheless prone to overall structural changes and changes in spine

length. This suggests a maintenance of structural plasticity in the adult cortex in order to be able to adapt synaptic strength when necessary (Majewska et al. 2006). I did indeed show that spines were prone to nanoscale fluctuations in morphological parameters, but in the population did not significantly change their average size over time. In this study I could not only investigate spine length and overall shape, but also spine neck width and neck length, which are possibly involved in synaptic plasticity in different ways. Previous studies in addition showed the coupling of spine head structural plasticity to synaptic plasticity in hippocampus (Van Harreveld & Fifkova 1975; Desmond & Levy 1983; Matsuzaki et al. 2004; Nägerl et al. 2004; Zhou et al. 2004; Hayama et al. 2013), the mechanism of which could possibly be extended to my work. The spine dynamics might thus be linked to synaptic plasticity in mouse neocortex as well. In addition to structural plasticity of the spine head affecting synaptic plasticity, spine necks have been shown to be structurally plastic as well. Changes in spine morphology have been shown to be regulated dynamically by neuronal activities (Bloodgood & Sabatini 2005). These changes do also regulate spine compartmentalization, thereby mainly regulating local voltage changes and biochemical compartmentalization (Grunditz et al. 2008; Tønnesen et al. 2014). Again, these studies were performed in brain slices, but the ideas could possibly be extended to my *in vivo* findings.

7.3.3 Spine morphological parameters' link to spine compartmentalization *in vivo*

Indeed, the narrow spine neck has already early on been suggested and later been shown to isolate the spine head biochemically and electrically from the dendrite (but see Popovic et al. 2015). This is due to the spine neck morphology, which is leading to it having a role as a diffusional barrier and an electrical resistor (Segev & Rall 1988; Svoboda et al. 1996; Bloodgood & Sabatini 2005; Araya et al. 2006; Grunditz et al. 2008; Harnett et al. 2012; Araya et al. 2014; Tønnesen et al. 2014). This isolation mechanism can lead to compartmentalized signaling, which has been shown to regulate synaptic strength independent of their neighboring synapses (Matsuzaki et al. 2004; Harvey & Svoboda 2007). Here I focused on single spines alone, and found a broad range of values for biochemical compartmentalization as expressed by the diffusion time constant τ. My findings differed from previous studies (Grunditz et al. 2008), which can be explained by the completely different experimental procedure. Where Grunditz and colleagues used a thinned skull window and ketamine/xylazine anesthesia (Grunditz et al. 2008), I used a chronic cranial window and isoflurane anesthesia. Different types of preparation/anesthesia may affect the activation of spines differently. These differences in the (history of) activation of spines might be reflected in differences in spine morphology and accordingly lead to differences in spine compartmentalization. Additionally, synaptopodin – a spine apparatus associated protein - was shown to alter the local organization of the cytoskeleton and thereby influenced diffusion rates in the membrane (Wang et al. 2016). Possibly a similar mechanisms is present in the cytosol, but this needs to be confirmed. Each of these parameters might influence the FRAP measurements, thereby causing a difference in the ranges of τ-values found. The estimation of τ based on the morphology was only weakly correlated with the measured τ. This might partly be explained by the presence of intracellular organelles, which affect diffusion but are not taken into account for the calculation. In addition, in the time lapse acquisitions I observed that neck width and head

volume, the main determinants of compartmentalization, showed more fluctuations over time than spine length and neck length. This variation might cause the observed morphology to mismatch with the morphology during the measured FRAP. Even though image acquisition is on the seconds time scale, and I observed morphological changes at the minute scale, I cannot rule out this possibility. Using the *in vivo* 2P-STED approach, I found a modest and weak correlation between τ and spine neck length and spine neck width, respectively. Consistent with previous findings in hippocampus (Tønnesen et al. 2014), I showed that neck width seems to be an important parameter for diffusion rates in spines in layer 1 of mouse barrel cortex. These findings were thus in accordance with previous work in brain slices, while the differences I found are most probably coming forth from the fact that spine morphology, and thus also spine compartmentalization, are age and region specific (Wijetunge et al. 2014).

In summary, I showed that even though *in vivo* spine morphology is on average stable over time, spines nevertheless show subtle fluctuations, suggesting that synaptic connections in the brain are continuously being adapted. Furthermore, the findings in the exploratory experiments suggested that spine neck length and spine neck width are possibly not only *ex vivo* but also in the intact living mouse brain of importance for spine biochemical compartmentalization. To confirm my findings, experiments combining 2P-STED microscopy with FRAP experiments *in vivo* should be continued. It should then become more clear whether the relation between spine morphology and function, which has also been suggested by others (e.g. (Hugel et al. 2009), is a true correlation or not. Increasing the number of experiments will make the data more robust and conclusions more solid. Furthermore, one should not forget that estimates of spine neck resistance were based on assumptions about resistivity of the cytoplasm, which might differ between the slender spine neck and other, larger structures (Grunditz et al. 2008). Technical advances might help elucidate the resistivity of spine neck cytoplasm and thus rule out the effect of the assumptions. Additional experiments with either GEVIs, GECIs, or *in vivo* patch-clamp experiments, will further add a functional read-out and help verify the estimates which were based on morphological data and diffusion measurements. A recent study in cortical slices already used an electrochromic VSD and found no electrical isolation by the spine neck of dendritic spines on the thin basal dendrites of L5 pyramidal neurons (see Fig. 43; (Popovic et al. 2015)). These findings argue against the hypothesized spine electrical compartmentalization and its role in synaptic transmission (e.g. as simulated in (Gulledge et al. 2012)), but the authors already point out the need for further investigations of spines on other parts of the dendritic tree and other neuronal types, since they might behave differently (Popovic et al. 2015). Besides more in depth studies focused on the relationship between spine nanoscale morphology and spine compartmentalization, an interesting follow-up study for the work presented here would be to investigate subtle morphological changes upon sensory stimulation (e.g. whisker stimulation) *in vivo*. One could use the 2P-STED approach and study the subsequent effects of these changes on spine compartmentalization with the FRAP approach. If successful, this approach might eventually be extended to two-color 2P-STED and include the possible influence of glial cells on spine morphology and function. The STED approach combined with dual color detection and spectral unmixing indeed allowed for a better insight in the fine details of the structural

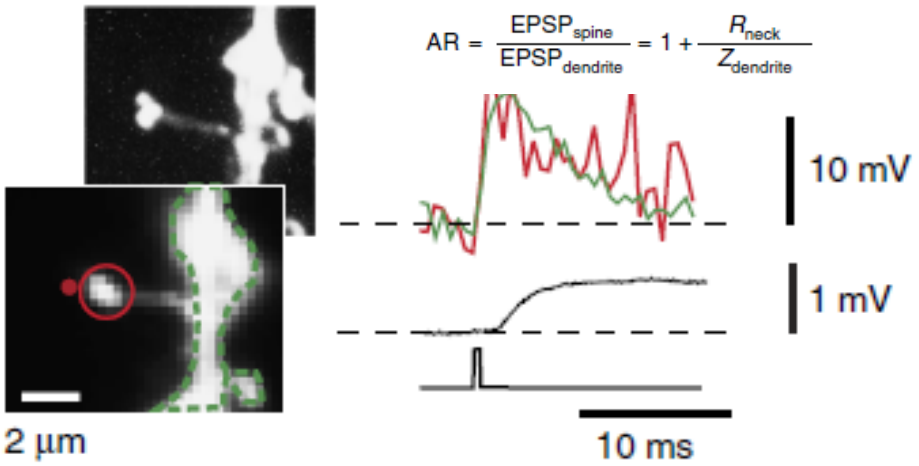

Figure 43: Attenuation of electrical signals through spines. *Attenuation of electrical signals is calculated as indicated by the equation at the top of the image. Images show z- stack of confocal images (upper) and single frame image of a spine in recording position (lower), with the red dot indicating the glutamate uncaging spot. Green trace = dendritic EPSP, red trace = spine EPSP, first black trace = somatic patch electrode recording, second black trace = timing of uncaging pulse. Image adapted from* (Popovic et al. 2015).

interactions with other brain structures, such as glial cells, in brain slices (see e.g. Panatier et al. 2014).

7.4 Studying neuron – glia interactions *in vivo*

In the last section of the results I showed that dual color 2P-STED microscopy *in vivo* is also possible with our system. As a proof of concept, I showed that by using double transgenic mice with a subset of pyramidal neurons and one type of glial cells, namely all microglia, being labelled, I could image and reveal microglia-spine interaction at the nanoscale and over time. Another type of glial cell, the astrocyte, has nowadays been accepted to play a role in synaptic communication, as suggested first by Alfonso Araque in the late nineties (Araque et al. 1999), and is thus an interesting structure to study. More recently it has in addition been suggested that astrocytes, similar to neurons, also have a topographical representation of the body and that indeed a strong reciprocal neuron-glial communication mechanism exists (Ghosh et al. 2013), all the more reason to study spine-astrocyte interactions. It has been shown that subtle changes in the morphology of astrocytic processes, as determined in EM images, are related to a reduced synaptic strength, as determined by field EPSPs in live tissue (Pannasch et al. 2014). However, this was a comparison between two different populations (fixed and live) and thus showed the need for live super-resolution imaging approaches. Our 2P-STED approach was thought to be the perfect tool to study spine-astrocyte interaction at the nanoscale *in vivo*, where neurovascular coupling by the astrocyte is still intact. Unfortunately, existing labelling strategies for the astrocytes were not compatible with our 2P-STED microscope, and thus I opted for a different labelling approach.

I tested several constructs and studied their suitability regarding brightness and stability for STED microscopy. All constructs (cytosolic GFP, cytosolic Clover, membrane-bound GFP, and membrane-bound Clover) did express well in cultures, and viral expression was bright

enough for 2P imaging in the intact brain. However, astrocytes were very sensitive to the STED light, and imaging sessions upon viral injection were not always successful. The unsuccessful imaging sessions might originate from different expression levels of the virus in individual mice. In addition, the depth of injection was stereotactic regulated but could nevertheless vary, thereby possibly causing some mice to express the label in astrocytes located too deep for STED microscopy to reach. Further trials with higher concentrations of the viral particles or multiple injection sites instead of just one, might improve the brightness of the label and the amount of labeled cells, respectively. Unfortunately, upon (too) dense labelling of the astrocytes at the surface, signal-to-noise ratio will decrease because of the stronger background signal. To avoid the usage of viruses, another possibility would be to test other transgenic mouse lines (e.g. see examples in (Li et al. 2013)) for their suitability with *in vivo* 2P-STED microscopy. In addition, combining the development of the setup with the optimization of the labelling approach for astrocytes might allow for an improved visualization of tripartite synapse structure in the intact brain, thereby opening many doors for further applications of our 2P-STED microscope in neuroscience.

7.5 Outlook for 2P-STED microscopy as an imaging tool in neuroscience

The work presented here has been mainly descriptive, but exploratory experiments showed its potential capabilities when combined with other techniques. In neuroscience, there are many outstanding questions related to spines alone, and to spine-glia interactions. Many of those questions could not yet be answered because of diffraction-limited resolution. Our 2P-STED approach will thus be an important addition to the available imaging tools in neuroscience. For example, we previously showed with a STED approach that in fixed tissue originating from a mouse model of fragile X syndrome (FXS) the developmental trajectory of dendritic spines is subtly compromised in an age- and region-specific manner, a finding which is likely to go unnoticed when using diffraction-limited microscopy approaches (Wijetunge et al. 2014). Since fine changes in dendritic spine morphology appear during development and are predicted to affect biochemical compartmentalization of spines (Wijetunge et al. 2014), it is of great interest to study this mechanism in live tissue (e.g. see (Nagaoka et al. 2016)). Promising tools to study those structure-function relations in the barrel cortex include intra- and juxtacellular recordings *in vivo* (Agmon & Connors 1992; Crochet & Petersen 2006; de Kock & Sakmann 2008; Houweling et al. 2010) and the previously discussed calcium imaging approach (Stosiek et al. 2003; Kerr et al. 2005; Sato et al. 2007) with for example GCaMPs or YCs (Tian et al. 2009; Nagai et al. 2004; Lütcke et al. 2010). Furthermore, the use of a variety of techniques in awake rodents (Helmchen et al. 2001; Krupa et al. 2004; Lee et al. 2006; Ferezou et al. 2006; Leiser & Moxon 2007; Dombeck et al. 2007) helps elucidating the functioning of barrel columns in different behavioral contexts. In addition, I believe that our 2P-STED approach combined with other measurements, such as FRAP experiments, will be a powerful tool to study the functional consequences of morphological changes *in vivo*. Additionally, it will help address more directly the functional consequences of subtle changes in spine morphology to neuropathology, and thus their role in neurodevelopmental disorders. This approach could be applied to other mouse models as well, to elucidate spine pathology and its functional consequences in neurological disorders such as autism spectrum disorder, schizophrenia,

Alzheimers's disease, Parkinson's disease, Huntington's disease, frontotemporal dementia and prion diseases (e.g. see (Penzes et al. 2011; Herms & Dorostkar 2016)).

Spine morphology and its interactions with other structures are not only of importance in pathology, but also in the healthy brain. For example, remodeling of dendritic spines and axonal boutons upon synaptic activation has been studied separately (e.g. (Matsuzaki et al. 2004; Becker et al. 2008)), but the question whether or not the nanoscale morphological changes of those two structures are synchronized is not yet fully answered. The dual color 2P-STED approach *in vivo* will allow for the study of the fine structural changes of both synaptic elements in an intact environment simultaneously and thereby enable the investigation of interactions between the two synaptic compartments during structural remodeling. Fine adaptations of their morphology are possibly representative for the functional adaptability of the pre- and post-synaptic element, and thus of great interest for further studies. Combining dual color 2P-STED microscopy with the FRAP experiments will help to elucidate the functional changes of spines and relate them to morphological changes of axonal boutons. In addition, this dual color approach will help elucidate questions in the field of neuron-glia interactions (see also (Panatier et al. 2014)). Electron microscopy does enable visualization of the tripartite synapse its structure with high resolution, but does not allow for the dissection of dynamic events in the physiologically intact environment. First of all, the 2P-STED approach will be a useful tool to study the variability in the tripartite synapse its structure. It will help elucidating whether or not astrocytic processes cover all synapses, and if this coverage depends on the type of synapse (excitatory versus inhibitory) or the shape (large spines versus small/thin spines). Likewise, we could try to follow the dynamics of the tripartite structure *in vivo*, which will help to understand better neuron-glia interactions under realistic experimental conditions. Furthermore, the usage of our imaging approach in combination with for example whisker stimulation, will allow for the investigation of how astrocytic processes are affected by sensory input and how neuronal activity influences the structure of the full tripartite synapse. By combining 2P-STED microscopy with calcium imaging, it would even be possible to study the functional consequences of subtle changes in the structure of the tripartite synapse. Similar to the interactions between astrocytic processes and spines, it can be studied what type of spines are contacted by microglial processes, and whether or not this interaction changes upon stimulation of the spine. Those findings could be of importance for comparisons with mechanisms in neurological disorders where glial cells are involved.

Astrocytes, being a key component for the maintenance of homeostasis in the brain, can underlay many neurological disorders when they are dysfunctional. Understanding neuron-astrocyte interactions and malfunctioning might help therapeutic targeting for epilepsy, Alzheimer's disease, and other neurodegenerative approaches (discussed in (Pekny et al. 2016)). Astrocytopathies contribute for example to neurodegenerative processes in amyotrophic lateral sclerosis and Huntington's disease, and can play a role in neuropsychiatric disorders such as schizophrenia and depression as well (reviewed in (Verkhratsky & Parpura 2016)). Depression would be a very interesting neurological disorder to study, as it has been discussed to include adaptations of the so-called quad-partite synapse composed by a pre- and post-synapse, an astrocytic process, and a microglial

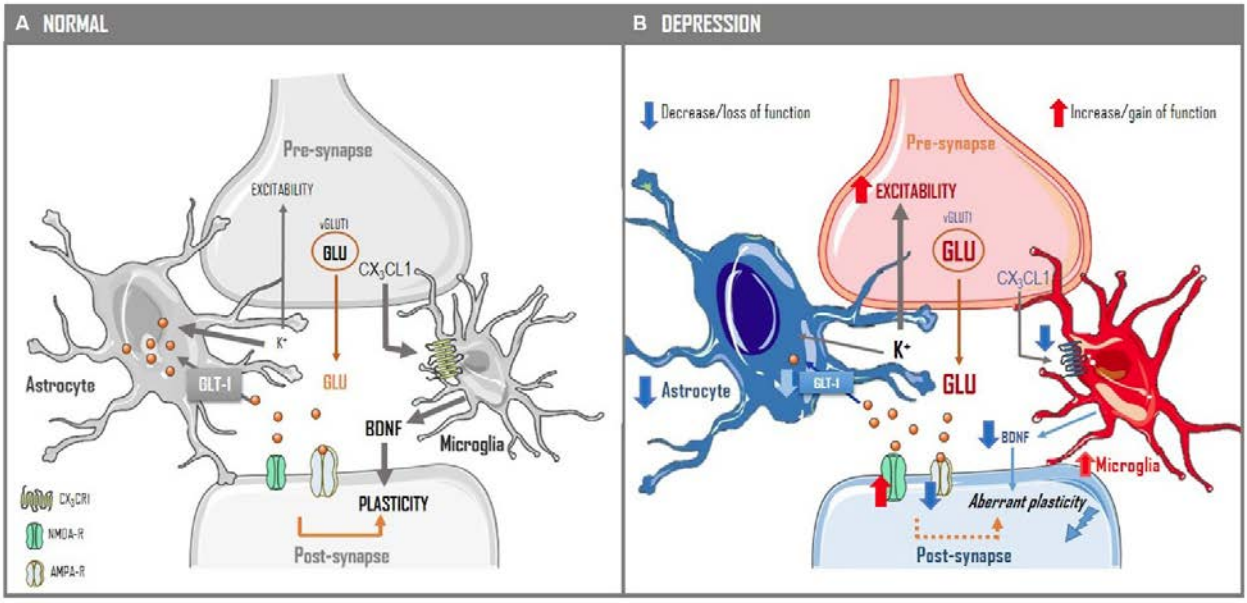

Figure 44: The quad-partite synapse and its modifications in depression*. Synaptic transmission is defined by the pre- and post-synapse as well as the microglial and astroglial processes, via various pathways. (A) Neuron-glial communication in the healthy quad-partite synapse. (B) Alterations of the quad-partite synapse its inter-relations in depression, translating into inadequate encoding of information. Figure taken from* (Rial et al. 2015)*.*

process (see Fig. 44; (Rial et al. 2015)). With our *in vivo* 2P-STED approach and double transgenic mice labelling neurons and microglia (e.g. Thy1H$^{+/eYFP}$ x Cx3Cr1$^{+/eGFP}$) injected with a virus targeting astrocytes (e.g. gfaABC$_1$D.Lck-Clover), we could then for example study the morphological changes of the quad-partite synapse with great detail in the intact environment and elucidate the interaction between those four elements.

7.6 Concluding remarks

In conclusion, the work presented here showed the establishment of *in vivo* super-resolution microscopy in mouse barrel cortex. The 2P-STED approach could be used to examine the morphological fluctuations and compartmentalization of dendritic spines with great detail, and could be used to image spine-glia interactions *in vivo*. The correlation found between the nanoscale morphology of dendritic spines and their biochemical compartmentalization factor can possibly be confirmed by combining 2P-STED microscopy with *in vivo* patch-clamp electrophysiology, 2P uncaging, calcium- and/or VSD imaging for a functional read-out.

Even though the novel labelling strategy for astrocytes and the usage of 2P-STED microscopy allowed me already to study the fine details of neuronal and glial cells in the intact environment, the emergence of stronger astrocytic labels in the green spectral range and adaptations of our microscope will help to discover many interesting facets of tripartite synapse morphology and its relation to brain physiology.

Altogether, our approach will be useful for the *in vivo* study of many relevant biological questions. This includes the types of coverage of spines by glial processes, the dynamics of those variable structures, and the type of interaction of specific spines with (multiple) glial cells, at the nanoscale. This will help to get a better insight in (tri-) synaptic morphological dynamics, the consequences of those dynamics for synapse function, and possibly a better understanding of synaptic communication and thus brain physiology and pathology.

REFERENCES

Abbe, E., 1873. Beiträge zur Theorie des Mikroskops und der mikroscopischen Wahrnehmung. *Archiv für Mikroskopische Anatomie*.

Adrian, M. et al., 2014. Barriers in the brain : resolving dendritic spine morphology and compartmentalization. , 8(December), pp.1–12.

Agmon, a & Connors, B.W., 1992. Correlation between intrinsic firing patterns and thalamocortical synaptic responses of neurons in mouse barrel cortex. *Journal of neuroscience*, 12(1), pp.319–329.

Alvarez, V. a & Sabatini, B.L., 2007. Anatomical and physiological plasticity of dendritic spines. *Annual review of neuroscience*, 30, pp.79–97.

Andermann, M.L., Kerlin, A.M. & Reid, R.C., 2010. Chronic cellular imaging of mouse visual cortex during operant behavior and passive viewing. *Front Cell Neurosci*, 4, pp. 3 -

Anderson, C.M. & Swanson, R.A., 2000. Astrocyte glutamate transport: review of properties, regulation, and physiological functions. *Glia*, 32(1), pp.1–14.

Angulo, M.C. et al., 2004. Glutamate released from glial cells synchronizes neuronal activity in the hippocampus. *Journal of neuroscience*, 24(31), pp.6920–7.

Antonello, J. et al., 2016. Coma aberrations in combined two- and three-dimensional STED nanoscopy. *Optics Letters*, 41(15), p.3631.

Araque, A. et al., 1999. Astrocyte-induced modulation of synaptic transmission. *Canadian journal of physiology and pharmacology*, 77(9), p.7.

Araque, A., Carmignoto, G. & Haydon, P.G., 2001. Dynamic Signaling Between Astrocytes and Neurons. *Annual Review of Physiology*, 63(1), pp.795–813.

Araya, R., 2014. Input transformation by dendritic spines of pyramidal neurons. *Frontiers in neuroanatomy*, 8(December), p.141.

Araya, R. et al., 2006. The spine neck filters membrane potentials. *Proceedings of the National Academy of Sciences of the United States of America*, 103(47), pp.17961–6.

Araya, R., Vogels, T.P. & Yuste, R., 2014. Activity-dependent dendritic spine neck changes are correlated with synaptic strength. *Proceedings of the National Academy of Sciences of the United States of America*, 111(28), pp.E2895-904.

Arellano, J.I. et al., 2007. Ultrastructure of dendritic spines: correlation between synaptic and spine morphologies. *Frontiers in neuroscience*, 1(1), pp.131–143.

Ashby, M.C. et al., 2006. Lateral diffusion drives constitutive exchange of AMPA receptors at dendritic spines and is regulated by spine morphology. *Journal of neuroscience*, 26(26), pp.7046–55.

Azevedo, F.A.C. et al., 2009. Equal numbers of neuronal and nonneuronal cells make the human brain an isometrically scaled-up primate brain. *Journal of Comparative Neurology*, 513(5), pp.532–541.

Badura, A., et al., 2014. Fast calcium sensor proteins for monitoring neural activity. *Neurophotonics*, 1, 025008

Barykina, N.V. et al., 2016. A new design for a green calcium indicator with a smaller size and a reduced number of calcium-binding sites. *Scientific Reports*, 6(September), pp. 34447

Bay, V. & Butt, A.M., 2012. Relationship between glial potassium regulation and axon excitability: a role for glial Kir4.1 channels. *Glia*, 60(4), pp. 651–60.

Becker, N. et al., 2008. LTD Induction Causes Morphological Changes of Presynaptic Boutons and Reduces Their Contacts with Spines. *Neuron, 60(4),* pp. 590–7

Benavides-Piccione, R. et al., Cortical area and species differences in dendritic spine morphology. *Journal of*

neurocytology, 31(3–5), pp.337–46.

Bernardinelli, Y. et al., 2014. Activity-dependent structural plasticity of perisynaptic astrocytic domains promotes excitatory synapse stability. *Current Biology*, 24(15), pp.1679–1688.

Bernardinelli, Y., Magistretti, P.J. & Chatton, J.-Y., 2004. Astrocytes generate Na+-mediated metabolic waves. *Proceedings of the National Academy of Sciences of the United States of America*, 101(41), pp.14937–42.

Bernardo, K.L. et al., 1990. Local intra- and interlaminar connections in mouse barrel cortex. *Journal of Comparative Neurology*, 291(2), pp.231–255.

Berning, S. et al., 2012. Nanoscopy in a Living Mouse Brain. *Science*, 335(6068), p.551.

Bethge, P. et al., 2013. Two-Photon Excitation STED Microscopy in Two Colors in Acute Brain Slices. *Biophysical Journal*, 104(4), pp.778–785.

Bethge, P. & Nägerl, U.V., 2014. Two-Photon Excitation STED Microscopy for Imaging Synapses and Glia in Acute Brain Slices. In pp. 205–220.

Betzig, E. 1995. Proposed method for molecular optical imaging. *Optics Letters*, 20 (3), pp. 237 – 239

Betzig, E. et al., 2006. Imaging Intracelllular Fluorescent Proteins at Nanometer Resolution. *Science*, 313(5793), pp. 1642 – 1645

Bezzi, P. & Volterra, A., 2001. A neuron-glia signalling network in the active brain. *Current opinion in neurobiology*, 11(3), pp.387–94.

Bhatt, D.H., Zhang, S. & Gan, W.-B., 2009. Dendritic spine dynamics. *Annual review of physiology*, 71, pp.261–282.

Bianchini, P. et al., 2012. Single-wavelength two-photon excitation-stimulated emission depletion (SW2PE-STED) superresolution imaging. *Proceedings of the National Academy of Sciences of the United States of America*, 109(17), pp.6390–3.

Blanpied, T.A., Kerr, J.M. & Ehlers, M.D., 2008. Structural plasticity with preserved topology in the postsynaptic protein network. *Proceedings of the National Academy of Sciences of the United States of America*, 105(34), pp.12587–92.

Blom, H. et al., 2012. Nearest neighbor analysis of dopamine D1 receptors and Na +-K +-ATPases in dendritic spines dissected by STED microscopy. *Microscopy Research and Technique*, 75(2), pp.220–228.

Blom, H. et al., 2013. Spatial Distribution of DARPP-32 in Dendritic Spines. *PLoS ONE*, 8(9), pp.1–9.

Blom, H. et al., 2011. Spatial distribution of Na+-K+-ATPase in dendritic spines dissected by nanoscale superresolution STED microscopy. *BMC neuroscience*, 12(1), p.16.

Blomberg, F., Cohen, R.S. & Siekevitz, P., 1977. The structure of postsynaptic densities isolated from dog cerebral cortex. II. Characterization and arrangement of some of the major proteins within the structure. *The Journal of cell biology*, 74(1), pp.204–25.

Bloodgood, B.L. & Sabatini, B.L., 2007. Ca(2+) signaling in dendritic spines. *Current opinion in neurobiology*, 17(3), pp.345–51.

Bloodgood, B.L. & Sabatini, B.L., 2005. Neuronal activity regulates diffusion across the neck of dendritic spines. *Science (New York, N.Y.)*, 310(5749), pp.866–9.

van den Bogaart, G. et al., 2011. Membrane protein sequestering by ionic protein–lipid interactions. *Nature*, 479(7374), pp.552–555.

Booth, M.J., 2007. Adaptive optics in microscopy. *Phil. Trans. R. Soc. A*, 365, pp. 2829 – 2843

Booth, M.J. 2014. Adaptive optical microscopy: the ongoing quest for a perfect image. *Light: Science and Applications*, 3, e165, doi: 10.1038/lsa.2014.46

Borlinghaus, R.T., Birk, H. & Schreiber, F., 2012. Detectors for Sensitive Detection : HyD. *Current microscopy contributions to advances in science and technology, Vol. 2*, pp.818–825.

Bosch, M. & Hayashi, Y., 2012. Structural plasticity of dendritic spines. *Current Opinion in Neurobiology*, 22(3), pp.383–388.

Bosman, L.W.J. et al., 2011. Anatomical pathways involved in generating and sensing rhythmic whisker movements. *Frontiers in integrative neuroscience*, 5, p.53.

Bourne, J.N. & Harris, K.M., 2008. Balancing structure and function at hippocampal dendritic spines. *Annual review of neuroscience*, 31, pp.47–67.

Brecht, M., Roth, A. & Sakmann, B., 2003. Dynamic receptive fields of reconstructed pyramidal cells in layers 3 and 2 of rat somatosensory barrel cortex. *The Journal of physiology*, 553(Pt 1), pp.243–65.

Bückers, J. et al., 2011. Simultaneous multi-lifetime multi-color STED imaging for colocalization analyses. *Optics express*, 19(4), pp.3130–43.

Bushong, E.A. et al., 2002. Protoplasmic astrocytes in CA1 stratum radiatum occupy separate anatomical domains. *Journal of neuroscience*, 22(1), pp.183–92.

Bushong, E.A., Martone, M.E. & Ellisman, M.H., 2004. Maturation of astrocyte morphology and the establishment of astrocyte domains during postnatal hippocampal development. *International journal of developmental neuroscience : the official journal of the International Society for Developmental Neuroscience*, 22(2), pp.73–86.

Carter, B.C. et al., 2012. Transient sodium current at subthreshold voltages: activation by EPSP waveforms. *Neuron*, 75(6), pp.1081–93.

Di Castro, M.A. et al., 2011. Local Ca2+ detection and modulation of synaptic release by astrocytes. *Nature neuroscience*, 14(10), pp.1276–84.

Chang, F.L. & Greenough, W.T., 1984. Transient and enduring morphological correlates of synaptic activity and efficacy change in the rat hippocampal slice. *Brain research*, 309(1), pp.35–46.

Chang, H.T., 1952. Cortical neurons with particular reference to the apical dendrites. *Cold Spring Harbor symposia on quantitative biology*, 17, pp.189–202.

Chen, C.-C., Lu, J. & Zuo, Y., 2014. Spatiotemporal dynamics of dendritic spines in the living brain. *Frontiers in neuroanatomy*, 8(May), p.28.

Chen, X. et al., 2012. LOTOS-based two-photon calcium imaging of dendritic spines in vivo. *Nature Protocols*, 7(10), pp.1818–1829.

Chen, T.W. et al., 2013. Ultrasensitive fluorescent proteins for imaging neuronal activity. *Nature*, 499, pp. 295–300.

Chmyrov, A. et al., 2013. Nanoscopy with more than 100,000 “doughnuts”. *Nature methods*, 10(8), pp.737–40.

Cohen, R.S., Chung, S.K. & Pfaff, D.W., 1985. Immunocytochemical localization of actin in dendritic spines of the cerebral cortex using colloidal gold as a probe. *Cellular and Molecular Neurobiology*, 5(3), pp.271–284.

Connor, J.R. & Diamond, M.C., 1982. A comparison of dendritic spine number and type on pyramidal neurons of the visual cortex of old adult rats from social or isolated environments. *The Journal of comparative neurology*, 210(1), pp.99–106.

Cossart, R., Ikegaya, Y., Yuste, R., 2005. Calcium imaging of cortical networks dynamics. *Cell Calcium*, 37, pp. 451 – 457

Covelo, A. & Araque, A., 2016. Lateral regulation of synaptic transmission by astrocytes. *Neuroscience*, 323(March), pp.62–66.

Crick, F., 1982. Do dendritic spines twitch? *Trends in Neurosciences*, 5, pp.44–46.

Crochet, S. & Petersen, C.C.H., 2006. Correlating whisker behavior with membrane potential in barrel cortex of awake mice. *Nature neuroscience*, 9(5), pp.608–610.

Dana, H. et al., 2014. Thy1-GCaMP6 transgenic mice for neuronal population imaging in vivo. *PLoS ONE*, 9, e108697

Danbolt, N.C., 2001. Glutamate uptake. *Progress in Neurobiology*, 65(1), pp.1–105.

Dani, J.W., Chernjavsky, A. & Smith, S.J., 1992. Neuronal activity triggers calcium waves in hippocampal astrocyte networks. *Neuron*, 8(3), pp.429–40.

Denk, W. et al., 1994. Anatomical and functional imaging of neurons using 2-photon laser scanning microscopy. *Journal of neuroscience methods*, 54(2), pp.151–62.

Denk, W., Strickler, J.H. & Webb, W.W., 1990. Two-photon laser scanning fluorescence microscopy. *Science (New York, N.Y.)*, 248(4951), pp.73–6.

Denk, W., Sugimori, M. & Llinás, R., 1995. Two types of calcium response limited to single spines in cerebellar Purkinje cells. *Proceedings of the National Academy of Sciences of the United States of America*, 92(18), pp. 8279–82.

Denk, W., 1996. Two-photon excitation in functional biological imaging. *J. Biomed. Opt.*, 1, pp. 296 – 304

Denk, W. & Svoboda, K., 1997. Photon upmanship: why multiphoton imaging is more than a gimmick. *Neuron*, 18, pp. 351 – 357

Derouiche, A. & Frotscher, M., 2001. Peripheral astrocyte processes: Monitoring by selective immunostaining for the actin-binding ERM proteins. *Glia*, 36(3), pp.330–341.

Desmond, N. L. & Levy, W. B., 1983. Synaptic correlates of associative potentiation/depression: an ultrastructural study in the hippocampus. *Brain Res.*, 265, 21–30

Desmond, N.L. & Levy, W.B., 1986. Changes in the numerical density of synaptic contacts with long-term potentiation in the hippocampal dentate gyrus. *The Journal of Comparative Neurology*, 253(4), pp.466–475.

Dillon, C. & Goda, Y., 2005. The actin cytoskeleton: integrating form and function at the synapse. *Annual review of neuroscience*, 28(February), pp.25–55.

Ding, J.B., Takasaki, K.T. & Sabatini, B.L., 2009. Supraresolution imaging in brain slices using stimulated-emission depletion two-photon laser scanning microscopy. *Neuron*, 63(4), pp.429–37.

Dombeck, D.A. et al., 2007. Imaging large-scale neural activity with cellular resolution in awake, mobile mice. *Neuron*, 56(1), pp.43–57.

Donnert, G. et al., 2006. Macromolecular-scale resolution in biological fluorescence microscopy. *Proc Natl Acad Sci U S A*, 103(31), pp.11440–11445.

Donnert, G. et al., 2007. Two-color far-field fluorescence nanoscopy. *Biophysical journal*, 92, pp.L67--9.

Dunaevsky, a et al., 1999. Developmental regulation of spine motility in the mammalian central nervous system. *Proceedings of the National Academy of Sciences of the United States of America*, 96(23), pp.13438–43.

Eggeling, C. et al., 2009. Direct observation of the nanoscale dynamics of membrane lipids in a living cell. *Nature*, 457(7233), pp.1159–62.

Engert, F. & Bonhoeffer, T., 1999. Dendritic spine changes associated with hippocampal long-term synaptic plasticity. *Nature*, 399(6731), pp.66–70.

Ewers, H. et al., 2014. A Septin-Dependent Diffusion Barrier at Dendritic Spine Necks L. Mei, ed. *PLoS ONE*, 9(12), p.e113916.

Feldmeyer, D. et al., 2013. Barrel cortex function. *Progress in Neurobiology*, 103, pp.3–27.

Feldmeyer, D., 2012. Excitatory neuronal connectivity in the barrel cortex. *Frontiers in Neuroanatomy*, 6(July), p.24.

Fellin, T. et al., 2004. Neuronal synchrony mediated by astrocytic glutamate through activation of extrasynaptic NMDA receptors. *Neuron*, 43(5), pp.729–43.

Feng, G. et al., 2000. Imaging Neuronal Subsets in Transgenic Mice Expressing Multiple Spectral Variants of GFP. *Neuron*, 28(1), pp.41–51.

Ferezou, I., Bolea, S. & Petersen, C.C.H., 2006. Visualizing the cortical representation of whisker touch: voltage-sensitive dye imaging in freely moving mice. *Neuron*, 50(4), pp.617–29.

Fifková, E. & Anderson, C.L., 1981. Stimulation-induced changes in dimensions of stalks of dendritic spines in the dentate molecular layer. *Experimental neurology*, 74(2), pp.621–7.

Fifková, E. & Delay, R.J., 1982. Cytoplasmic actin in neuronal processes as a possible mediator of synaptic plasticity. *The Journal of cell biology*, 95(1), pp.345–50.

Fifková, E. & Van Harreveld, A., 1977. Long-lasting morphological changes in dendritic spines of dentate granular cells following stimulation of the entorhinal area. *Journal of neurocytology*, 6(2), pp.211–30.

Fischer, M. et al., 1998. Rapid actin-based plasticity in dendritic spines. *Neuron*, 20(5), pp.847–54.

Fox, K., 2008. *Barrel Cortex*

Friedrich, M. et al., 2011. STED-SPIM: Stimulated emission depletion improves sheet illumination microscopy resolution. *Biophysical Journal*, 100(8), pp.L43–L45.

Fu, M. & Zuo, Y., 2011. Experience-dependent structural plasticity in the cortex. *Trends in Neurosciences*, 34(4), pp.177–187.

Galiani, S. et al., 2012. Strategies to maximize the performance of a STED microscope. *Optics Express*, 20(7), p.7362.

Genoud, C. et al., 2006. Plasticity of astrocytic coverage and glutamate transporter expression in adult mouse cortex. *PLoS Biology*, 4(11), pp.2057–2064.

Ghosh, A., Wyss, M.T. & Weber, B., 2013. Somatotopic astrocytic activity in the somatosensory cortex. *Glia*, 61(4), pp.601–610.Genoud, C. et al., 2006. Plasticity of astrocytic coverage and glutamate transporter expression in adult mouse cortex. *PLoS Biology*, 4(11), pp.2057–2064.

Giaume, C. et al., 2010. Astroglial networks: a step further in neuroglial and gliovascular interactions. *Nature Reviews Neuroscience*, 11(2), pp.87–99.

Gilbert, C.D. & Sigman, M., 2007. Brain states: top-down influences in sensory processing. *Neuron*, 54(5), pp.677–96.

Golgi, C., 1873. Sulla struttura della sostanza grigia dell cervello. *Gaz. Med. Lomb.*, 33, pp.244–246.

Gould, T.J. et al., 2012. Adaptive optics enables 3D STED microscopy in aberrating specimens. *Optics Express*, 20(19), p.20998.

Gray, E.G., 1959a. Axo-somatic and axo-dendritic synapses of the cerebral cortex: an electron microscope study. *Journal of anatomy*, 93(Pt 4), pp.420–33.

Gray, E.G., 1959b. Electron microscopy of synaptic contacts on dendrite spines of the cerebral cortex. *Nature*, 183(4675), pp.1592–3.

Gray, E.G. & Guillery, R.W., 1963. A NOTE ON THE DENDRITIC SPINE APPARATUS. *Journal of anatomy*, 97, pp.389–92.

Greenough, W.T. & Volkmar, F.R., 1973. Pattern of dendritic branching in occipital cortex of rats reared in complex environments. *Experimental neurology*, 40(2), pp.491–504.

Grienberger, C., Chen, X. & Konnerth, A., 2015. Dendritic function in vivo. *Trends in Neurosciences*, 38(1), pp.45–54.

Grosche, J. et al., 1999. Microdomains for neuron-glia interaction: parallel fiber signaling to Bergmann glial cells. *Nature neuroscience*, 2(2), pp.139–43.

Grotjohann, T. et al., 2012. rsEGFP2 enables fast RESOLFT nanoscopy of living cells. *eLife*, 2012(1), pp.1–14.

Grunditz, A. et al., 2008. Spine Neck Plasticity Controls Postsynaptic Calcium Signals through Electrical Compartmentalization. *Journal of Neuroscience*, 28(50), pp.13457–13466.

Grutzendler, J. & Gan, W.-B., 2006. Two-photon imaging of synaptic plasticity and pathology in the living mouse brain. *NeuroRx : the journal of the American Society for Experimental NeuroTherapeutics*, 3(4), pp.489–96.

Grutzendler, J., Kasthuri, N. & Gan, W.-B., 2002. Long-term dendritic spine stability in the adult cortex. *Nature*, 420(6917), pp.812–816.

Gu, L. et al., 2014. Long-term in vivo imaging of dendritic spines in the hippocampus reveals structural plasticity. *Journal of neuroscience*, 34(42), pp.13948–53.

Gulledge, A.T., Carnevale, N.T. & Stuart, G.J., 2012. Electrical advantages of dendritic spines. *PLoS ONE*, 7(4).

Gustafsson, M.G.L., 2005. Nonlinear structured-illumination microscopy: wide-field fluorescence imaging with theoretically unlimited resolution. *Proceedings of the National Academy of Sciences of the United States of America*, 102(37), pp. 13081 – 86

Halassa, M.M., Fellin, T. & Haydon, P.G., 2007. The tripartite synapse: roles for gliotransmission in health and disease. *Trends in Molecular Medicine*, 13(2), pp.54–63.

Halassa, M.M. & Haydon, P.G., 2010. Integrated brain circuits: astrocytic networks modulate neuronal activity and behavior. *Annual review of physiology*, 72(2), pp.335–55.

Hall, A., 1994. Small GTP-binding proteins and the regulation of the actin cytoskeleton. *Annual review of cell biology*, 10, pp.31–54.

Hama, K. et al., 2004. Tri-dimensional morphometric analysis of astrocytic processes with high voltage electron microscopy of thick Golgi preparations. *Journal of neurocytology*, 33(3), pp.277–85.

Harke, B. et al., 2008. Resolution scaling in STED microscopy. *Optics Express*, 16(6), p.4154.

Harms, K.J. & Dunaevsky, A., 2007. Dendritic spine plasticity: looking beyond development. *Brain research*, 1184, pp.65–71.

Harnett, M.T. et al., 2012. Synaptic amplification by dendritic spines enhances input cooperativity. *Nature*, 491(7425), pp.599–602.

Van Harreveld, A. & Fifkova, E., 1975. Swelling of dendritic spines in the fascia dentata after stimulation of the perforant fibers as a mechanism of post-tetanic potentiation. *Exp. Neurol.*, 49, pp. 736–49

Harris, K.M., 1999. Structure, development, and plasticity of dendritic spines. *Current Opinion in Neurobiology*, 9(3), pp.343–348.

Harris, K.M., Jensen, F.E. & Tsao, B., 1992. Three-dimensional structure of dendritic spines and synapses in rat hippocampus (CA1) at postnatal day 15 and adult ages: implications for the maturation of synaptic physiology and long-term potentiation. *Journal of neuroscience*, 12(7), pp.2685–705.

Harris, K.M. & Kater, S.B., 1994. Dendritic spines: cellular specializations imparting both stability and flexibility to synaptic function. *Annual review of neuroscience*, 17, pp.341–371.

Harris, K.M. & Stevens, J.K., 1989. Dendritic spines of CA 1 pyramidal cells in the rat hippocampus: serial electron microscopy with reference to their biophysical characteristics. *Journal of neuroscience*, 9(8), pp.2982–97.

Harvey, C. D. & Svoboda, K., 2007. Locally dynamic synaptic learning rules in pyramidal neuron dendrites. *Nature*, 450, pp. 1195–200

Hayama, T. et al., 2013. GABA promotes the competitive selection of dendritic spines by controlling local Ca2+ signaling. *Nat. Neurosci.*, 16, pp. 1409–16

Hayashi-Takagi, A et al., 2015. Labelling and optical erasure of synaptic memory traces in the motor cortex. *Nature*, 525(7569), pp.333-8.

Hein, B., Willig, K.I. & Hell, S.W., 2008. Stimulated emission depletion (STED) nanoscopy of a fluorescent protein-labeled organelle inside a living cell. , 105(38).

Hell, S.W. & Wichmann, J., 1994. Breaking the diffraction resolution limit by stimulated emission: stimulated-emission-depletion fluorescence microscopy. *Optics letters*, 19(11), pp.780–2.

Helmchen, F. et al., 2001. A Miniature Head-Mounted Neurotechnique Two-Photon Microscope : High-Resolution Brain Imaging in Freely Moving Animals. , 31, pp.903–912.

Helmchen, F. & Denk, W., 2005. Deep tissue two-photon microscopy. *Nature Methods*, 2(12), pp. 932 – 940

Henneberger, C. et al., 2010. Long-term potentiation depends on release of D-serine from astrocytes. *Nature*, 463(7278), pp.232–6.

Heo, C. et al., 2016. A soft, transparent, freely accessible cranial window for chronic imaging and electrophysiology. *Scientific reports*, 6(February), p.27818.

Hering, H. & Sheng, M., 2001. Dendritic spines: structure, dynamics and regulation. *Nature reviews. Neuroscience*, 2(12), pp.880–888.

Herms, J. & Dorostkar, M.M., 2016. Dendritic Spine Pathology in Neurodegenerative Diseases. *Annual Review of Pathology: Mechanisms of Disease*, 11(1), pp.221–250.

Herpers, M.J.H.M. et al., 1986. Co-expression of glial fibrillary acidic protein- and vimentin-type intermediate filaments in human astrocytomas. *Acta Neuropathologica*, 70(3–4), pp.333–339.

Higley, M.J. & Contreras, D., 2003. Nonlinear integration of sensory responses in the rat barrel cortex: an intracellular study in vivo. *Journal of neuroscience*, 23(32), pp.10190–200.

Hirase, H. et al., 2004. Calcium dynamics of cortical astrocytic networks in vivo. *PLoS biology*, 2(4), p.E96.

Hofer, S.B. et al., 2009. Experience leaves a lasting structural trace in cortical circuits. *Nature*, 457(7227), pp.313–7.

Hofmann, M. et al., 2005. Breaking the diffraction barrier in fluorescence microscopy at low light intensities by using reversibly photoswitchable proteins. *Proceedings of the National Academy of Sciences*, 102(49), pp.17565–17569.

Holcman, D. & Schuss, Z., 2011. Diffusion laws in dendritic spines. *Journal of mathematical neuroscience*, 1(1), p.10.

Holthoff, K., Tsay, D. & Yuste, R., 2002. Calcium Dynamics of Spines Depend on Their Dendritic Location. *Neuron*, 33(3), pp.425–437.

Holthoff, K., Zecevic, D. & Konnerth, A., 2010. Rapid time course of action potentials in spines and remote dendrites of mouse visual cortex neurons. *J Physiol*, 588(7), pp.1085–1096.

Holtmaat, A. et al., 2009. Long-term, high-resolution imaging in the mouse neocortex through a chronic cranial window. *Nature protocols*, 4(8), pp.1128–44.

Holtmaat, A. & Svoboda, K., 2009. Experience-dependent structural synaptic plasticity in the mammalian brain. *Nature reviews. Neuroscience*, 10(9), pp.647–58.

Holtmaat, A.J.G.D. et al., 2005. Transient and persistent dendritic spines in the neocortex in vivo. *Neuron*, 45(2), pp.279–291.

Holtmaat, A. et al., 2006. Experience-dependent and cell-type-specific spine growth in the neocortex. *Nature*, 441, pp. 979 – 83

Honkura, N. et al., 2008. The subspine organization of actin fibers regulates the structure and plasticity of dendritic spines. *Neuron*, 57(5), pp.719–29.

Hooks, B.M. et al., 2011. Laminar Analysis of Excitatory Local Circuits in Vibrissal Motor and Sensory Cortical Areas C. C. C. H. Petersen, ed. *PLoS Biology*, 9(1), p.e1000572.

Hoopmann, P. et al., 2010. Endosomal sorting of readily releasable synaptic vesicles. *Proceedings of the National Academy of Sciences of the United States of America*, 107, pp.19055–19060.

Horikawa, K. et al., 2010. Spontaneous network activity visualized by ultrasensitive Ca(2+) indicators, yellow Cameleon-Nano. *Nature Methods*, 7, pp. 729–732

Hosokawa, T. et al., 1995. Repeated confocal imaging of individual dendritic spines in the living hippocampal slice: evidence for changes in length and orientation associated with chemically induced LTP. *Journal of neuroscience*, 15(8), pp.5560–73.

Houweling, A.R. et al., 2010. Nanostimulation: Manipulation of Single Neuron Activity by Juxtacellular Current Injection. *Journal of Neurophysiology*, 103(3).

Howles, G. et al., 2009. Rapid Production of specialized animal handling devices using computer-aided design and solid freeform fabrication. *J Magn Reson Imaging.*, 30(2), pp.466–471.

Hugel, S. et al., 2009. Dendritic spine morphology determines membrane-associated protein exchange between dendritic shafts and spine heads. *Cerebral Cortex*, 19(3), pp.697–702.

Humeau, Y. et al., 2005. Dendritic Spine Heterogeneity Determines Afferent-Specific Hebbian Plasticity in the Amygdala. *Neuron*, 45(1), pp.119–131.

Husi, H. et al., 2000. Proteomic analysis of NMDA receptor-adhesion protein signaling complexes. *Nature neuroscience*, 3(7), pp.661–9.

Inagaki, S. & Nagai, T., 2016. Current progress in genetically encoded voltage indicators for neural activity recording. *Current Opinion in Chemical Biology*, 33, pp. 95 – 100

Jones, E.G. & Powell, T.P., 1969. Morphological variations in the dendritic spines of the neocortex. *Journal of cell science*, 5(2), pp.509–29.

Jung, S. et al., 2000. Analysis of fractalkine receptor CX(3)CR1 function by targeted deletion and green fluorescent protein reporter gene insertion. *Molecular and cellular biology*, 20(11), pp.4106–14.

Kamin, D. et al., 2010. High- And low-mobility stages in the synaptic vesicle cycle. *Biophysical Journal*, 99(2), pp.675–684.

Kasai, H. et al., 2010. Learning rules and persistence of dendritic spines. *The European journal of neuroscience*, 32(2), pp.241–9.

Keck, T. et al., 2008. Massive restructuring of neuronal circuits during functional reorganization of adult visual cortex. *Nature neuroscience*, 11(10), pp.1162–7.

Kellner, R.R. et al., 2007. Nanoscale organization of nicotinic acetylcholine receptors revealed by stimulated emission depletion microscopy. *Neuroscience*, 144(1), pp.135–143.

Kennedy, M.B. et al., 2005. Integration of biochemical signalling in spines. *Nature Reviews Neuroscience*, 6(6), pp.423–434.

Kennedy, M.B., 1998. Signal transduction molecules at the glutamatergic postsynaptic membrane. *Brain Research Reviews*, 26(2), pp.243–257.

Kennedy, M.B., 2000. Signal-Processing Machines at the Postsynaptic Density. *Science*, 290(5492), pp.750–754.

Kerr, J.N.D., Greenberg, D. & Helmchen, F., 2005. Imaging input and output of neocortical networks in vivo.

Proceedings of the National Academy of Sciences of the United States of America, 102(39), pp.14063–8.

Kessels, M.M. et al., 2011. Controlling actin cytoskeletal organization and dynamics during neuronal morphogenesis. *European journal of cell biology*, 90(11), pp.926–33.

Kittel, R.J. et al., 2006. Bruchpilot promotes active zone assembly, Ca2+ channel clustering, and vesicle release. *Science (New York, N.Y.)*, 312(5776), pp.1051–4.

Klar, T.A. et al., 2000. Fluorescence microscopy with diffraction resolution barrier broken by stimulated emission. *Proceedings of the National Academy of Sciences*, 97(15), pp.8206–8210.

Kleinfeld, D. et al., 1998. Fluctuations and stimulus-induced changes in blood flow observed in individual capillaries in layers 2 through 4 of rat neocortex. *Proceedings of the National Academy of Sciences of the United States of America*, 95, pp. 15741 – 46

Knöpfel, T., Gallero-Salas, Y. & Song, C., 2015. Genetically encoded voltage indicators for large scale cortical imaging come of age. *Current Opinion in Chemical Biology*, 27, pp. 75 – 83

Knott, G.W. et al., 2006. Spine growth precedes synapse formation in the adult neocortex in vivo. *Nature neuroscience*, 9(9), pp.1117–24.

Koch, C., Poggio, T., 1983. A theoretical analysis of electrical properties of spines. *Proc.R Soc. Lond., B, Biol. Sci.*, 213, pp.455–477.

Koch, C., 2004. *Biophysics of computation information processing in single neurons*,

Koch, C. & Zador, A., 1993. The function of dendritic spines: devices subserving biochemical rather than electrical compartmentalization. *Journal of neuroscience*, 13(2), pp.413–22.

de Kock, C.P.J. & Sakmann, B., 2008. High frequency action potential bursts (>or= 100 Hz) in L2/3 and L5B thick tufted neurons in anaesthetized and awake rat primary somatosensory cortex. *The Journal of physiology*, 586(14), pp.3353–64.

Koester, H.J. & Sakmann, B., 1998. Calcium dynamics in single spines during coincident pre- and postsynaptic activity depend on relative timing of back-propagating action potentials and subthreshold excitatory postsynaptic potentials. *Proceedings of the National Academy of Sciences of the United States of America*, 95(16), pp.9596–601.

Kopec, C.D. et al., 2007. GluR1 links structural and functional plasticity at excitatory synapses. *Journal of Neuroscience*, 27(50), pp.13706–13718.

Korkotian, E., Holcman, D. & Segal, M., 2004. Dynamic regulation of spine-dendrite coupling in cultured hippocampal neurons. *The European journal of neuroscience*, 20(10), pp.2649–63.

Korkotian, E. & Segal, M., 2001. Regulation of dendritic spine motility in cultured hippocampal neurons. *Journal of neuroscience*, 21(16), pp.6115–24.

Korkotian, E. & Segal, M., Structure-Function Relations in Dendritic Spines: Is Size Important?

Korobova, F. & Svitkina, T., 2010. Molecular architecture of synaptic actin cytoskeleton in hippocampal neurons reveals a mechanism of dendritic spine morphogenesis. *Molecular biology of the cell*, 21(1), pp.165–76.

Krupa, D.J. et al., 2004. Layer-specific somatosensory cortical activation during active tactile discrimination. *Science (New York, N.Y.)*, 304(5679), pp.1989–92.

Kuhn, B., Fromherz, P., Denk, W., 2004. Large voltage-sensitive dye signals measured with one and two-photon excitation. *Soc. Neurosci. Abstr.*

Kuhn, B., Denk, W. & Bruno, R.M., 2008. In vivo two-photon voltage-sensitive dye imaging reveals top-down control of cortical layers 1 and 2 during wakefulness. *Proceedings of the National Academy of Sciences of the United States of America*, 105(21), pp.7588–93.

Kusters, R. et al., 2014. Forced transport of deformable containers through narrow constrictions. *Physical Review E - Statistical, Nonlinear, and Soft Matter Physics*, 90(3), pp.1–8.

Kusters, R. et al., 2013. Shape-induced asymmetric diffusion in dendritic spines allows efficient synaptic AMPA receptor trapping. *Biophysical journal*, 105(12), pp.2743–50.

Lai, C.S.W., Franke, T.F. & Gan, W.-B., 2012. Opposite effects of fear conditioning and extinction on dendritic spine remodelling. *Nature*, 483(7387), pp.87–91.

Lalo, U. et al., 2006. NMDA receptors mediate neuron-to-glia signaling in mouse cortical astrocytes. *Journal of neuroscience*, 26(10), pp.2673–83.

Landis, D.M. & Reese, T.S., 1983. Cytoplasmic organization in cerebellar dendritic spines. *The Journal of cell biology*, 97(4), pp.1169–78.

Latour, I. et al., 2001. Differential mechanisms of Ca2+ responses in glial cells evoked by exogenous and endogenous glutamate in rat hippocampus. *Hippocampus*, 11(2), pp.132–45.

Lauterbach, M.A. et al., 2016. Superresolving dendritic spine morphology with STED microscopy under holographic photostimulation. *Neurophotonics*, 3(4), p.41806.

Lee, A.K. et al., 2006. Whole-cell recordings in freely moving rats. *Neuron*, 51(4), pp.399–407.

Lee, K.F.H., Soares, C. & Béïque, J.C., 2012. Examining form and function of dendritic spines. *Neural Plasticity*, 2012.

Lee, S.-J.R. et al., 2009. Activation of CaMKII in single dendritic spines during long-term potentiation. *Nature*, 458(7236), pp.299–304.

Lehre, K.P. et al., 1995. Differential expression of two glial glutamate transporters in the rat brain: quantitative and immunocytochemical observations. *Journal of neuroscience*, 15(3 Pt 1), pp.1835–53.

Lehre, K.P. & Rusakov, D.A., 2002. Asymmetry of glia near central synapses favors presynaptically directed glutamate escape. *Biophysical journal*, 83(1), pp.125–34.

Leiser, S.C. & Moxon, K.A., 2007. Responses of trigeminal ganglion neurons during natural whisking behaviors in the awake rat. *Neuron*, 53(1), pp.117–33.

Lendvai, B. et al., 2000. Experience-dependent plasticity of dendritic spines in the developing rat barrel cortex in vivo. *Nature*, 404(6780), pp.876–881.

Lewén, S.E., 2013. *Cellular Reactions and Behavioral Changes in Focal and Diffuse Traumatic Brain Injury*,

Li, B. et al., 2007. The neuregulin-1 receptor erbB4 controls glutamatergic synapse maturation and plasticity. *Neuron*, 54(4), pp.583–97.

Li, D. et al., 2013. New tools for investigating astrocyte-to-neuron communication. *Frontiers in Cellular Neuroscience*, 7(October), p.Article 193.

Li, K.W. & Jimenez, C.R., 2008. Synapse proteomics: current status and quantitative applications. *Expert Review of Proteomics*, 5(2), pp.353–360.

Li, Q., Wu, S.S.H. & Chou, K.C., 2009. Subdiffraction-limit two-photon fluorescence microscopy for GFP-tagged cell imaging. *Biophysical Journal*, 97(12), pp.3224–3228.

Lin, X. et al., 2007. Sema4D-plexin-B1 implicated in regulation of dendritic spine density through RhoA/ROCK pathway. *Neuroscience letters*, 428(1), pp.1–6.

Lin, M.Z. & Schnitzer, M.J., 2016. Genetically encoded indicators of neuronal activity. *Nature Neuroscience*, 19 (9), pp. 1142 – 1153

Lisman, J.E. & Harris, K.M., 1993. Quantal analysis and synaptic anatomy--integrating two views of hippocampal plasticity. *Trends in neurosciences*, 16(4), pp.141–7.

Liu, K.S.Y. et al., 2011. RIM-binding protein, a central part of the active zone, is essential for neurotransmitter release. *Science (New York, N.Y.)*, 334(6062), pp.1565–9.

Lütcke, H. et al., 2010. Optical recording of neuronal activity with a genetically-encoded calcium indicator in anesthetized and freely moving mice. *Frontiers in neural circuits*, 4, p.9.

Madisen, L. et al., 2015. Transgenic mice for intersectional targeting of neural sensors and effectors with high specificity and performance. *Neuron*, 85, pp. 942–958

Majewska, A., Brown, E., et al., 2000. Mechanisms of calcium decay kinetics in hippocampal spines: role of spine calcium pumps and calcium diffusion through the spine neck in biochemical compartmentalization. *Journal of neuroscience*, 20(5), pp.1722–34.

Majewska, A. & Sur, M., 2003. Motility of dendritic spines in visual cortex in vivo: changes during the critical period and effects of visual deprivation. *Proceedings of the National Academy of Sciences of the United States of America*, 100(26), pp.16024–16029.

Majewska, A., Tashiro, A. & Yuste, R., 2000. Regulation of spine calcium dynamics by rapid spine motility. *Journal of neuroscience*, 20(22), pp.8262–8.

Majewska, A.K., 2006. Remodeling of Synaptic Structure in Sensory Cortical Areas In Vivo. *Journal of Neuroscience*, 26(11), pp.3021–3029.

Major, G. et al., 1994. Detailed passive cable models of whole-cell recorded CA3 pyramidal neurons in rat hippocampal slices. *J. Neurosci.*, 14, pp. 4613–4638

Margolis D.J. et al., 2010. Chronic two-photon calcium imaging of stability and plasticity of sensory representations in mouse barrel cortex. *Neuroscience Meeting Planner. Society for Neuroscience, San Diego, CA, USA*, Online.

Margolis, D.J. et al., 2012. Reorganization of cortical population activity imaged throughout long-term sensory deprivation. *Nature Neuroscience*, 15(11), pp.1539–1546.

Martinez, G. et al., 1998. GFAP, S-100 and vimentin proteins in rat after cerebral post-ischemic reperfusion. *International Journal of Developmental Neuroscience*, 16(6), pp.519–526.

Matsuzaki, M. et al., 2001. Dendritic spine geometry is critical for AMPA receptor expression in hippocampal CA1 pyramidal neurons. *Nature neuroscience*, 4(11), pp.1086–92.

Matsuzaki, M. et al., 2004. Structural basis of long-term potentiation in single dendritic spines. *Nature*, 429(6993), pp.761–6.

Matus, A., 2000. Actin-based plasticity in dendritic spines. *Science (New York, N.Y.)*, 290(5492), pp.754–8.

Matus, A. et al., 1982. High actin concentrations in brain dendritic spines and postsynaptic densities. *Proceedings of the National Academy of Sciences of the United States of America*, 79(23), pp.7590–4.

McAllister, A.K., 2007. Dynamic Aspects of CNS Synapse Formation. *Annu Rev Neurosci*, 30, pp.425–450.

Minderer, M. et al., 2012. Chronic imaging of cortical sensory map dynamics using a genetically encoded calcium indicator. *J. Physiol.*, 590 (1), pp. 99 – 107

Moczulska, K.E. et al., 2013. Dynamics of dendritic spines in the mouse auditory cortex during memory formation and memory recall. *Proceedings of the National Academy of Sciences of the United States of America*, 110(45), pp.18315–20.

Moneron, G. et al., 2010. Fast STED microscopy with continuous wave fiber lasers. *Optics express*, 18(2), pp.1302–1309.

Moneron, G. & Hell, S.W., 2009. Two-photon excitation STED microscopy. *Optics express*, 17(17), pp.14567–14573.

Moore, C.I. & Nelson, S.B., 1998. Spatio-temporal subthreshold receptive fields in the vibrissa representation of rat primary somatosensory cortex. *Journal of neurophysiology*, 80(6), pp.2882–92.

Müller, T., Schumann, C. & Kraegeloh, A., 2012. STED microscopy and its applications: new insights into cellular processes on the nanoscale. *Chemphyschem : a European journal of chemical physics and physical*

chemistry, 13(8), pp.1986–2000.

Müller, W. & Connor, J.A., 1991. Dendritic spines as individual neuronal compartments for synaptic Ca2+ responses. *Nature*, 354(6348), pp.73–6.

Murphy-Royal, C. et al., 2015. Surface diffusion of astrocytic glutamate transporters shapes synaptic transmission. *Nature neuroscience*, 18(2), pp.219–26.

Mysore, S.P., Tai, C.Y. & Schuman, E.M., 2007. Effects of N-cadherin disruption on spine morphological dynamics. *Front Cell Neurosci*, 1(December), p.1.

Nagai, T. et al., 2004. Expanded dynamic range of fluorescent indicators for Ca(2+) by circularly permuted yellow fluorescent proteins. *Proceedings of the National Academy of Sciences of the United States of America*, 101(29), pp.10554–9.

Nagaoka, A. et al., 2016. Abnormal intrinsic dynamics of dendritic spines in a fragile X syndrome mouse model in vivo. *Scientific Reports*, 6(November 2015), p.26651.

Nägerl, U.V., Eberhorn, N., Cambridge, S.B., Bonhoeffer, T., 2004. Bidirectional activity-dependent morphological plasticity in hippocampal neurons. *Neuron*, 44(5), pp.759-67

Nägerl, U.V. et al, 2007. Protracted synaptogenesis after activiti-dependent spinogenesis in hippocampal neurons. *The journal of neuroscience : the official journal of the Society for Neuroscience*, 27(30), pp.8149-56

Nägerl, U.V. et al., 2008. Live-cell imaging of dendritic spines by STED microscopy. *Proceedings of the National Academy of Sciences of the United States of America*, 105(48), pp.18982–7.

Navarrete, M. & Araque, A., 2008. Endocannabinoids mediate neuron-astrocyte communication. *Neuron*, 57(6), pp.883–93.

Neil, M.A.A., Juškaitis, R. & Wilson, T., 1997. Method of obtaining optical sectioning by using structured light in a conventional microscope. *Optics Let.*, 22(24), pp. 1905–1907.

Nevian, T. & Sakmann, B., 2004. Single spine Ca2+ signals evoked by coincident EPSPs and backpropagating action potentials in spiny stellate cells of layer 4 in the juvenile rat somatosensory barrel cortex. *Journal of neuroscience*, 24(7), pp.1689–99.

Nevian, T., Larkum, M.E., Polsky, A. & Schiller, J., 2007. Properties of basal dendrites of layer 5 pyramidal neurons: a direct patch-clamp recording study. *Nat. Neurosci.*, 10, pp. 206–214

Nishiyama, J. & Yasuda, R., 2015. Biochemical Computation for Spine Structural Plasticity. *Neuron*, 87(1), pp.63–75.

Noguchi, J., Nagaoka, A., Watanabe, S., Ellis-Davies, G.C.R., et al., 2011. In vivo two-photon uncaging of glutamate revealing the structure–function relationships of dendritic spines in the neocortex of adult mice. *The Journal of Physiology*, 589(10), pp.2447–2457.

Noguchi, J. et al., 2005. Spine-neck geometry determines NMDA receptor-dependent Ca2+ signaling in dendrites. *Neuron*, 46(4), pp.609–22.

Nusser, Z. et al., 1998. Cell Type and Pathway Dependence of Synaptic AMPA Receptor Number and Variability in the Hippocampus. *Neuron*, 21(3), pp.545–559.

Oberheim, N.A. et al., 2008. Loss of astrocytic domain organization in the epileptic brain. *Journal of neuroscience*, 28(13), pp.3264–76.

O'Connor, D.H. et al., 2010. Neural activity in barrel cortex underlying vibrissa-based object localization in mice. *Neuron*, 67(6), pp.1048–1061.

Oheim, M., Beaurepaire, E., Chaigneau, E., Mertz, J. & Charpak, S., 2001. Two-photon microsocpy in brain tissue: parameters influencing the imaging depth. *J. Neurosci. Methods*, 111, pp 29 – 37

Oliet, S.H.R., Piet, R. & Poulain, D.A., 2001. Control of Glutamate Clearance and Synaptic Efficacy by Glial

Coverage of Neurons. *Science*, 292(5518), pp.923–926.

Oray, S., Majewska, A. & Sur, M., 2004. Dendritic spine dynamics are regulated by monocular deprivation and extracellular matrix degradation. *Neuron*, 44(6), pp.1021–30.

Pan, F. & Gan, W.-B., 2008. Two-photon imaging of dendritic spine development in the mouse cortex. *Developmental neurobiology*, 68(6), pp.771–8.

Panatier, A. et al., 2011. Astrocytes are endogenous regulators of basal transmission at central synapses. *Cell*, 146(5), pp.785–98.

Panatier, A. et al., 2006. Glia-derived D-serine controls NMDA receptor activity and synaptic memory. *Cell*, 125(4), pp.775–84.

Panatier, A., Arizono, M. & Nägerl, U.V., 2014. Dissecting tripartite synapses with STED microscopy. *Philosophical transactions of the Royal Society of London. Series B, Biological sciences*, 369(1654), p.20130597-.

Panatier, A. & Robitaille, R., 2016. Astrocytic mGluR5 and the tripartite synapse. *Neuroscience*, 323, pp.29–34.

Pannasch, U. et al., 2014. Connexin 30 sets synaptic strength by controlling astroglial synapse invasion. *Nature neuroscience*, 17(4), pp.549–58.

Patton, B.R. et al., 2016. Three-dimensional STED microscopy of aberrating tissue using dual adaptive optics. *Optics Express*, 24(8), p.8862.

Parnass, Z., Tashiro, A. & Yuste, R., 2000. Analysis of spine morphological plasticity in developing hippocampal pyramidal neurons. *Hippocampus*, 10(5), pp.561–8.

Pascual, O. et al., 2005. Astrocytic purinergic signaling coordinates synaptic networks. *Science (New York, N.Y.)*, 310(5745), pp.113–6.

Pasti, L. et al., 1997. Intracellular calcium oscillations in astrocytes: a highly plastic, bidirectional form of communication between neurons and astrocytes in situ. *Journal of neuroscience*, 17(20), pp.7817–30.

Pekny, M. et al., 2016. Astrocytes: a central element in neurological diseases. *Acta Neuropathologica*, 131(3), pp.323–345.

Pellett, P.A. et al., 2011. Two-color STED microscopy in living cells. *Biomedical optics express*, 2(8), pp.2364–2371.

Penzes, P. et al., 2011. Dendritic spine pathology in neuropsychiatric disorders. *Nature neuroscience*, 14(3), pp.285–93.

Perea, G. & Araque, A., 2005. Properties of synaptically evoked astrocyte calcium signal reveal synaptic information processing by astrocytes. *Journal of neuroscience*, 25(9), pp.2192–203.

Perea, G., Navarrete, M. & Araque, A., 2009. Tripartite synapses: astrocytes process and control synaptic information. *Trends in neurosciences*, 32(8), pp.421–31.

Perez-Alvarez, A. et al., 2014. Structural and functional plasticity of astrocyte processes and dendritic spine interactions. *Journal of neuroscience*, 34(38), pp.12738–44.

Peters, A; Palay, SL; Webster, H., 1991. *The fine structure of the nervous system: the neurons and supporting cells*,

Peters, A., Feldman, M. & Saldanha, J., 1976. The projection of the lateral geniculate nucleus to area 17 of the rat cerebral cortex. II. Terminations upon neuronal perikarya and dendritic shafts. *Journal of Neurocytology*, 5(1), pp.85–107.

Peters, A. & Kaiserman-Abramof, I.R., 1970. The small pyramidal neuron of the rat cerebral cortex. The perikaryon, dendrites and spines. *The American journal of anatomy*, 127(4), pp.321–55.

Peters, A. & Kaiserman-Abramof, I.R., 1969. The small pyramidal neuron of the rat cerebral cortex. The

synapses upon dendritic spines. *Zeitschrift für Zellforschung und mikroskopische Anatomie (Vienna, Austria : 1948)*, 100(4), pp.487–506.

Petersen, C.C.H. et al., 2003. Interaction of sensory responses with spontaneous depolarization in layer 2/3 barrel cortex. *Proceedings of the National Academy of Sciences of the United States of America*, 100(23), pp.13638–43.

Petersen, C.C.H.H., 2007. The functional organization of the barrel cortex. *Neuron*, 56(2), pp.339–355.

Petrásek, Z. & Schwille, P., 2008. Precise measurement of diffusion coefficients using scanning fluorescence correlation spectroscopy. *Biophys. J.*, 94, pp. 1437–1448

Petzold, G.C. et al., 2008. Coupling of Neural Activity to Blood Flow in Olfactory Glomeruli Is Mediated by Astrocytic Pathways. *Neuron*, 58(6), pp.897–910.

Petzold, G.C. & Murthy, V.N., 2011. Role of astrocytes in neurovascular coupling. *Neuron*, 71(5), pp.782–796.

Pfeiffer, T., Avignone, E. & Nägerl, U.V., 2016. Induction of hippocampal long-term potentiation increases the morphological dynamics of microglial processes and prolongs their contacts with dendritic spines. *Scientific Reports*, (February), pp.1–9.

Pilz, G-A. et al., 2016. Functional imaging of dentate granule cells in the adult mouse hippocampus. *The Journal of Neuroscience*, 36 (28), pp. 7407 – 7414

De Pittà, M. et al., 2012. Computational quest for understanding the role of astrocyte signaling in synaptic transmission and plasticity. *Frontiers in computational neuroscience*, 6(December), p.98.

Popovic, M.A. et al., 2015. Electrical behaviour of dendritic spines as revealed by voltage imaging. *Nature Communications*, 6, p.8436.

Porter, J.T. & McCarthy, K.D., 1996. Hippocampal astrocytes in situ respond to glutamate released from synaptic terminals. *Journal of neuroscience*, 16(16), pp.5073–81.

Rall, W., 1978. Dendritic spines and synaptic potency. In R. Porter, ed. *Studies in Neurophysiology*. Cambridge University, pp. 203–209.

Ramón y Cajal, S., 1888. Estructura de los centros nerviosos de las aves. *Rev. Trim. Histol. Norm. Pat.*, 1, pp.1–10.

Ramón y Cajal, S., 1899. *La Textura del Sistema Nerviosa del Hombre y los Vertebrados*,

Ramón y Cajal, S., 1892. *Nuevo concepto de la Histología de los centros nerviosos*,

Ramón y Cajal, S., 1891. Significación fisiológica de las expansiones protoplásmicas y nerviosas de la sustancia gris. *Revista de Ciencias Médicas de Barcelona*, 22, p.23.

Rankin, B.R. et al., 2011. Nanoscopy in a living multicellular organism expressing GFP. *Biophysical Journal*, 100(12), pp.63–65.

Reichenbach, A., 1989. Attempt to classify glial cells by means of their process specialization using the rabbit retinal Müller cell as an example of cytotopographic specialization of glial cells. *Glia*, 2(4), pp.250–259.

Rial, D. et al., 2015. Depression as a Glial-Based Synaptic Dysfunction. *Frontiers in cellular neuroscience*, 9(January), p.521.

Richards, D.A. et al., 2004. AMPA-receptor activation regulates the diffusion of a membrane marker in parallel with dendritic spine motility in the mouse hippocampus. *The Journal of physiology*, 558(Pt 2), pp.503–12.

De Robertis, E.D. & Bennett, H.S., 1955. Some features of the submicroscopic morphology of synapses in frog and earthworm. *The Journal of biophysical and biochemical cytology*, 1(1), pp.47–58.

Rothstein, J.D. et al., 1994. Localization of neuronal and glial glutamate transporters. *Neuron*, 13(3), pp.713–725.

Rouach, N. et al., 2008. Astroglial metabolic networks sustain hippocampal synaptic transmission. *Science (New York, N.Y.)*, 322(5907), pp.1551–5.

Rusakov, D.A., 2001. The Role of Perisynaptic Glial Sheaths in Glutamate Spillover and Extracellular Ca2+ Depletion. *Biophysical Journal*, 81(4), pp.1947–1959.

Sabatini, B.L., Maravall, M. & Svoboda, K., 2001. Ca2+ signaling in dendritic spines. *Current Opinion in Neurobiology*, 11(3), pp.349–356.

Sabatini, B.L., Oertner, T.G. & Svoboda, K., 2002. The Life Cycle of Ca2+ Ions in Dendritic Spines. *Neuron*, 33(3), pp.439–452.

Sachdev, R.N.S., Ebner, F.F. & Wilson, C.J., 2004. Effect of subthreshold up and down states on the whisker-evoked response in somatosensory cortex. *Journal of neurophysiology*, 92(6), pp.3511–21.

Sala, C. & Segal, M., 2014. Dendritic Spines: The Locus of Structural and Functional Plasticity. *Physiological Reviews*, 94(1), pp.141–188.

Sapoznik, S., Ivenshitz, M. & Segal, M., 2006. Age-dependent glutamate induction of synaptic plasticity in cultured hippocampal neurons. *Learning & memory (Cold Spring Harbor, N.Y.)*, 13(6), pp.719–27.

Sato, T.R. et al., 2007. The functional microarchitecture of the mouse barrel cortex. *PLoS biology*, 5(7), p.e189.

Schikorski, T. & Stevens, C.F., 1997. Quantitative ultrastructural analysis of hippocampal excitatory synapses. *Journal of neuroscience*, 17(15), pp.5858–67.

Schmidt, R. et al., 2008. Spherical nanosized focal spot unravels the interior of cells. *Nature methods*, 5(6), pp.539–544.

Schnorrenberg, S. et al., 2016. In vivo super-resolution RESOLFT microscopy of drosophila melanogaster. *eLife*, 5(JUNE2016), pp.1–11.

Schröder, J. et al., 2009. In vivo labeling method using a genetic construct for nanoscale resolution microscopy. *Biophysical Journal*, 96(1), pp.1–3.

Segal, M., 2005. Dendritic spines and long-term plasticity. *Nature reviews. Neuroscience*, 6(4), pp.277–84.

Segev, I. & Rall, W., 1988. Computational study of an excitable dendritic spine. *Journal of neurophysiology*, 60(2), pp.499–523.

Serrano, A. et al., 2006. GABAergic network activation of glial cells underlies hippocampal heterosynaptic depression. *Journal of neuroscience*, 26(20), pp.5370–82.

Shi, S.H. et al., 1999. Rapid spine delivery and redistribution of AMPA receptors after synaptic NMDA receptor activation. *Science (New York, N.Y.)*, 284(5421), pp.1811–6.

Shigetomi, E. et al., 2013. Imaging calcium microdomains within entire astrocyte territories and endfeet with GCaMPs expressed using adeno-associated viruses. *The Journal of general physiology*, 141(5), pp.633–647.

Sidenstein, S.C. et al., 2016. Multicolour Multilevel STED nanoscopy of Actin/Spectrin Organization at Synapses. *Scientific Reports*, 6(May), p.26725.

Sieber, J.J. et al., 2006. The SNARE Motif Is Essential for the Formation of Syntaxin Clusters in the Plasma Membrane. *Biophysical Journal*, 90(8), pp.2843–2851.

Simons, D.J., 1978. Response properties of vibrissa units in rat SI somatosensory neocortex. *Journal of neurophysiology*, 41(3), pp.798–820.

Smith, K.R. et al., 2014. Psychiatric risk factor ANK3/ankyrin-G nanodomains regulate the structure and function of glutamatergic synapses. *Neuron*, 84(2), pp.399–415.

Sobczyk, A., Scheuss, V. & Svoboda, K., 2005. NMDA receptor subunit-dependent [Ca2+] signaling in individual hippocampal dendritic spines. *Journal of neuroscience*, 25(26), pp.6037–46.

Sorra, K.E. & Harris, K.M., 2000. Overview on the structure, composition, function, development, and plasticity of hippocampal dendritic spines. *Hippocampus*, 10(5), pp.501–11.

Špaček, J., 1985. Three-dimensional analysis of dendritic spines. *Anatomy and Embryology*, 171(2), pp.235–243.

Spacek, J. & Harris, K.M., 1998. Three-Dimensional Organization of Cell Adhesion Junctions at Synapses and Dendritic Spines in Area CA1 of the Rat Hippocampus. , 68(November 1997), pp.58–68.

Spacek, J. & Harris, K.M., 1997. Three-dimensional organization of smooth endoplasmic reticulum in hippocampal CA1 dendrites and dendritic spines of the immature and mature rat. *Journal of neuroscience*, 17(1), pp.190–203.

Spacek, J. & Hartmann, M., 1983. Three-dimensional analysis of dendritic spines. I. Quantitative observations related to dendritic spine and synaptic morphology in cerebral and cerebellar cortices. *Anatomy and embryology*, 167(2), pp.289–310.

Steinhäuser, C. et al., 1992. Heterogeneity in the Membrane Current Pattern of Identified Glial Cells in the Hippocampal Slice. *The European journal of neuroscience*, 4(6), pp.472–484.

Stobart, J. L et al., 2016. Long-term in vivo calcium imaging of astrocytes reveals distinct cellular compartment responses to sensory stimulation. *Cerebral Cortex,* Epub ahead of print. DOI: 10.1093/cercor/bhw366

Stosiek, C. et al., 2003. In vivo two-photon calcium imaging of neuronal networks. *Proceedings of the National Academy of Sciences of the United States of America*, 100(12), pp.7319–24.

Sullivan, R. et al., 2004. Cloning, transport properties, and differential localization of two splice variants of GLT-1 in the rat CNS: implications for CNS glutamate homeostasis. *Glia*, 45(2), pp.155–69.

Svoboda, K., Mainen, Z.F. & Malinow, R., 1999. Synaptic calcium transients in single spines indicate that NMDA receptors are not saturated. *Nature*, 399(6732), pp.151–155.

Svoboda, K., Tank, D.W. & Denk, W., 1996. Direct measurement of coupling between dendritic spines and shafts. *Science (New York, N.Y.)*, 272(5262), pp.716–9.

Svoboda, K. & Yasuda, R., 2006. Principles of tow-photon excitation microscopy and its applications to neuroscience. *Neuron*, 50, pp. 823 – 839.

Tada, T. et al., 2007. *Role of Septin Cytoskeleton in Spine Morphogenesis and Dendrite Development in Neurons*,

Tada, T. & Sheng, M., 2006. Molecular mechanisms of dendritic spine morphogenesis. *Current opinion in neurobiology*, 16(1), pp.95–101.

Takasaki, K. & Sabatini, B.L., 2014. Super-resolution 2-photon microscopy reveals that the morphology of each dendritic spine correlates with diffusive but not synaptic properties. *Frontiers in neuroanatomy*, 8(May), p.29.

Takasaki, K.T., Ding, J.B. & Sabatini, B.L., 2013. Live-cell superresolution imaging by pulsed STED two-photon excitation microscopy. *Biophysical Journal*, 104(4), pp.770–777.

Takumi, Y. et al., 1999. The arrangement of glutamate receptors in excitatory synapses. *Annals of the New York Academy of Sciences*, 868, pp.474–82.

Testa, I. et al., 2012. Nanoscopy of Living Brain Slices with Low Light Levels. *Neuron*, 75(6), pp.992–1000.

Theodosis, D.T., Poulain, D.A. & Oliet, S.H.R., 2008. Activity-dependent structural and functional plasticity of astrocyte-neuron interactions. *Physiological reviews*, 88(3), pp.983–1008.

Tian, L. et al., 2009. Imaging neural activity in worms, flies and mice with improved GCaMP calcium indicators. *Nature methods*, 6(12), pp.875–81.

Toni, N. et al., 2001. Remodeling of synaptic membranes after induction of long-term potentiation. *Journal of neuroscience*, 21(16), pp.6245–6251.

Tønnesen, J. & Nägerl, U. V., 2013. Two-color STED imaging of synapses in living brain slices. Methods Mol. Biol.

950, 65–80

Tønnesen, J. et al., 2014. Spine neck plasticity regulates compartmentalization of synapses. *Nature neuroscience*, 17(5), pp.678–85.

Tønnesen, J. et al., 2011. Two-Color STED Microscopy of Living Synapses Using A Single Laser-Beam Pair. *Biophysical Journal*, 101(10), pp.2545–2552.

Trachtenberg, J.T. et al., 2002. Long-term in vivo imaging of experience-dependent synaptic plasticity in adult cortex. *Nature*, 420(6917), pp.788–794.

Tran, T.S. et al., 2009. Secreted semaphorins control spine distribution and morphogenesis in the postnatal CNS. *Nature*, 462(7276), pp.1065–9.

Triller, A. & Choquet, D., 2005. Surface trafficking of receptors between synaptic and extrasynaptic membranes: and yet they do move! *Trends in neurosciences*, 28(3), pp.133–9.

Tsay, D. & Yuste, R., 2004. On the electrical function of dendritic spines. *Trends in Neurosciences*, 27(2), pp.77–83.

Urban, N.T. et al., 2011. STED nanoscopy of actin dynamics in synapses deep inside living brain slices. *Biophysical journal*, 101(5), pp.1277–84.

Vanderklish, P.W. & Edelman, G.M., 2002. Dendritic spines elongate after stimulation of group 1 metabotropic glutamate receptors in cultured hippocampal neurons. *Proceedings of the National Academy of Sciences of the United States of America*, 99(3), pp.1639–44.

Ventura, R. & Harris, K.M., 1999. Three-dimensional relationships between hippocampal synapses and astrocytes. *Journal of neuroscience*, 19(16), pp.6897–906.

Verkhratsky, A. & Parpura, V., 2016. Astrogliopathology in neurological, neurodevelopmental and psychiatric disorders. *Neurobiology of Disease*, 85, pp.254–261.

Volfovsky, N. et al., 1999. Geometry of dendritic spines affects calcium dynamics in hippocampal neurons: theory and experiments. *Journal of neurophysiology*, 82(1), pp.450–462.

Volterra, A., Liaudet, N. & Savtchouk, I., 2014. Astrocyte Ca(2+) signalling: an unexpected complexity. *Nature reviews. Neuroscience*, 15(5), pp.327–35.

Volterra, A. & Meldolesi, J., 2005. Astrocytes, from brain glue to communication elements: the revolution continues. *Nature reviews. Neuroscience*, 6(8), pp.626–40.

Wake, H. et al., 2009. Resting Microglia Directly Monitor the Functional State of Synapses *In Vivo* and Determine the Fate of Ischemic Terminals. *The Journal of Neuroscience*, 29(13), pp.3974-39800

Walikonis, R.S. et al., 2000. Identification of proteins in the postsynaptic density fraction by mass spectrometry. *Journal of neuroscience*, 20(11), pp.4069–80.

Wang, D.D. & Bordey, A., 2008. The Astrocyte Odyssey. *Prog Neurobiol.*, 86(4), pp.342–367.

Wang, X. et al., 2006. Astrocytic Ca2+ signaling evoked by sensory stimulation in vivo. *Nature neuroscience*, 9(6), pp.816–23.

Wang, L. et al. 2016. The Role of Synaptopodin in Membrane Protein Diffusion in the Dendritic Spine Neck. *PLoS One*, 11, e0148310

Weber, B. & Barros, L.F., 2015. The Astrocyte: Powerhouse and Recycling Center. *Cold Spring Harbor perspectives in biology*, 7(12), p.a020396.

Westphal, V. et al., 2008. Video-rate far-field optical nanoscopy dissects synaptic vesicle movement. *Science (New York, N.Y.)*, 320(5873), pp.246–9.

Westrum, L.E. et al., 1980. Microtubules, dendritic spines and spine apparatuses. *Cell and Tissue Research*, 208(2), pp.171–181.

Wijetunge, L.S. et al., 2014. Stimulated emission depletion (STED) microscopy reveals nanoscale defects in the developmental trajectory of dendritic spine morphogenesis in a mouse model of fragile X syndrome. *Journal of neuroscience*, 34(18), pp.6405–12.

Wilbrecht, L. et al., 2010. Structural plasticity underlies experience-dependent functional plasticity of cortical circuits. *Journal of neuroscience*, 30(14), pp.4927–32.

Wildanger, D. et al., 2009. A compact STED microscope providing 3D nanoscale resolution. *Journal of Microscopy*, 236(1), pp.35–43.

Willig, K.I. et al., 2014. Nanoscopy of filamentous actin in cortical dendrites of a living mouse. *Biophysical Journal*, 106(1), pp.L01–L03.

Willig, K.I. et al., 2006. STED microscopy reveals that synaptotagmin remains clustered after synaptic vesicle exocytosis. *Nature*, 440(7086), pp.935–9.

Willig, K.I. & Nägerl, U.V., 2012. Stimulated emission depletion (STED) imaging of dendritic spines in living hippocampal slices. *Cold Spring Harbor Protocols*, 7(5), pp.576–582.

Winship, I.R., Plaa, N. & Murphy, T.H., 2007. Rapid astrocyte calcium signals correlate with neuronal activity and onset of the hemodynamic response in vivo. *Journal of neuroscience*, 27(23), pp.6268–72.

Witcher, M.R., Kirov, S.A. & Harris, K.M., 2007. Plasticity of perisynaptic astroglia during synaptogenesis in the mature rat hippocampus. *Glia*, 55(1), pp.13–23.

Woolsey, T.A. & Van der Loos, H., 1970. The structural organization of layer IV in the somatosensory region (SI) of mouse cerebral cortex. The description of a cortical field composed of discrete cytoarchitectonic units. *Brain research*, 17(2), pp.205–42.

Wyatt, R.M., Tring, E. & Trachtenberg, J.T., 2012. Pattern and not magnitude of neural activity determines dendritic spine stability in awake mice. *Nature neuroscience*, 15(7), pp.949–51.

Xie, Y. et al., 2007. *The GTP-Binding Protein Septin 7 Is Critical for Dendrite Branching and Dendritic-Spine Morphology*,

Xu, H.-T. et al., 2007. Choice of cranial window type for in vivo imaging affects dendritic spine turnover in the cortex. *Nature neuroscience*, 10(5), pp.549–551.

Xu, T. et al., 2009. Rapid formation and selective stabilization of synapses for enduring motor memories. *Nature*, 462(7275), pp.915–9.

Yamada, T. et al., 1992. Vimentin immunoreactivity in normal and pathological human brain tissue. *Acta Neuropathologica*, 84(2), pp.157–162.

Yamada, Y. et al., 2011. Quantitative comparison of genetically encoded Ca indicators in cortical pyramidal cells and cerebellar Purkinje cells. *Front. Cell. Neurosci.*, 5, pp. 18 -

Yan, W. et al., 2016. Aberration correction for stimulated emission depletion microscopy with coherent optical adaptive technique. In T. G. Bifano, J. Kubby, & S. Gigan, eds. *SPIE Coherent Optical Adaptive Techniques*. International Society for Optics and Photonics, p. 97170K.

Yang, B. et al., 2014. Large parallelization of STED nanoscopy using optical lattices. *Optics express*, 22(5), pp.5581–9.

Yang, G., Pan, F. & Gan, W.-B., 2009. Stably maintained dendritic spines are associated with lifelong memories. *Nature*, 462(7275), pp.920–4.

Yang, Y. et al., 2008. Spine expansion and stabilization associated with long-term potentiation. *Journal of neuroscience*, 28(22), pp.5740–51.

Yang, H.H. & St-Pierre, F., 2016. Genetically encoded voltage indicators: opportunities and challenges. *Journal of neuroscience*, 36(39), pp. 9977–89

Yaroslavsky, A.N. et al., 2002. Optical properties of selected native an coagulated human brain tissues in vitro in

the visible and near infrared spectral range. *Phys. Med. Biol.*, 47, pp. 2059 – 2073

Yasuda, R. & Murakoshi, H., 2011. The mechanisms underlying the spatial spreading of signaling activity. *Current opinion in neurobiology*, 21(2), pp.313–21.

Yu, X. & Zuo, Y., 2011. Spine plasticity in the motor cortex. *Current Opinion in Neurobiology*, 21(1), pp.169–174.

Yuste, R., 2013. Electrical Compartmentalization in Dendritic Spines. *Annual Review of Neuroscience*, 36(1), pp.429–449.

Yuste, R. & Bonhoeffer, T., 2001. Morphological changes in dendritic spines associated with long-term synaptic plasticity. *Annual review of neuroscience*, 24, pp.1071–89.

Yuste, R. & Denk, W., 1995. Dendritic spines as basic functional units of neuronal integration. *Nature*, 375(6533), pp.682–4.

Yuste, R., Majewska, A. & Holthoff, K., 2000. From form to function: calcium compartmentalization in dendritic spines. *Nature neuroscience*, 3(7), pp.653–9.

Yuste, R., Katz, L.C., 1991. Control of postsynaptic Ca2+ influx in developing neocortex by excitatory and inhibitory neurotransmitters, *Neuron*, 6, pp. 333–344.

Zembrzycki, A. et al., 2013. Sensory cortex limits cortical maps and drives top-down plasticity in thalamocortical circuits. *Nature neuroscience*, 16(8), pp.1060–7.

Zhang, X. et al., 2013. Essential role for synaptopodin in dendritic spine plasticity of the developing hippocampus. *Journal of neuroscience*, 33(30), pp.12510–8.

Zhou, Q., Homma, K. J. & Poo, M, 2004. Shrinkage of dendritic spines associated with long-term depression of hippocampal synapses. *Neuron*, 44, pp. 749–57

Zhu, J.J. et al., 2002. Ras and Rap Control AMPA Receptor Trafficking during Synaptic Plasticity. *Cell*, 110(4), pp.443–455.

Zhu, J.J. & Connors, B.W., 1999. Intrinsic firing patterns and whisker-evoked synaptic responses of neurons in the rat barrel cortex. *Journal of neurophysiology*, 81(3), pp.1171–83.

Zhuo, L. et al., 1997. Live Astrocytes Visualized by Green Fluorescent Protein in Transgenic Mice. *Developmental Biology*, 187(1), pp.36–42.

Zuo, Y. et al., 2005. Development of long-term dendritic spine stability in diverse regions of cerebral cortex. *Neuron*, 46(2), pp.181–189.

APPENDICES

APPENDIX 1: Springer - Methods in Molecular Biology manuscript

Two-photon STED microscopy for nanoscale imaging of neural morphology *in vivo*

Mirelle J.T. ter Veer [1,2]*, Thomas Pfeiffer [1,2]* and U. Valentin Nägerl [1,2]#

[1]Interdisciplinary Institute for Neuroscience, UMR 5297 CNRS, Bordeaux, France

[2]Université de Bordeaux, Bordeaux, France

* Equal contribution

Corresponding author:

Dr. U. Valentin Nägerl, Professor of Neuroscience and Bioimaging,

valentin.nagerl@u-bordeaux.fr

Interdisciplinary Institute for Neuroscience, UMR 5297 CNRS

University of Bordeaux

146 rue Leo Saignat, 33077 Bordeaux, France

Phone: +33 / 55 75 71 097

ABSTRACT

The detailed study of morphology and function of neuronal synapses in the living brain tissue and the contribution of the adjacent glial protrusions to neuronal communication is often hindered by the small size of these structures (< 200 nm) and the confined optical accessibility in intact brain tissue by conventional diffraction-limited light microscopy. The recent development of two-photon excitation STED (2P-STED) microscopy accommodates super-resolved imaging and depth penetration, thereby for the first time enabling the investigation of these structures at the nanoscale in the living brain tissue. This permits to study the dynamic structure and function of synapses and their interactions with glial processes at unprecedented resolution.

In this protocol, we introduce the basic principle of 2P-STED microscopy and give practical advice on how to operate these types of microscopes. In addition, we highlight putative applications by presenting dual-color time-lapse image acquisition of dendritic spines and microglial processes, in acute brain slices and *in vivo*.

Key words: STED, super-resolution microscopy, nanoscopy, two-photon (2P) microscopy, dendritic spines, acute brain slice, *in vivo* brain imaging, dual-color imaging, microglial processes.

1. Introduction:

Following Ramon y Cajal's pioneering description of neuronal morphology and synapses which constitute the building blocks of neuronal communication, one of the principle endeavors in Neuroscience research has been to decipher the relationship of synaptic function and morphology in health and disease. The development of two-photon (2P) microscopy (Denk et al., 1990, 1994) and the possibility to image synapses in living brain tissue led to the discovery of activity-dependent morphological changes of synapses. This dynamic adaption of synaptic morphology is considered as the cellular substrate for learning and memory in the mammalian brain (Engert and Bonhoeffer, 1999; Trachtenberg et al., 2002; Matsuzaki et al., 2004; Becker et al., 2008). While 2P microscopy allows for the visualization and basic description of synaptic structures, its diffraction-limited resolution prohibits their study at the finest detail. The development of super-resolution STED microscopy enables to bypass this diffraction limit, i.e. to resolve structures well below 200 nm using light microscopy. Thus, enabling in the first instance the visualization of dendritic spines at the nanoscale *in vivo* (Berning et al., 2012) and secondly advancing our understanding of how neurons work, e.g. with the discovery of spine neck plasticity (Tønnesen et al., 2014). Employing super-resolution dual-color 2P-STED microscopy *in vivo* permits a swift progression in the investigation of the functional relevance of nanoscale morphological dynamics of synapses and the impact of glial processes in its immediate vicinity.

1.1. Principle of 2P-STED microscopy

Similar to conventional fluorescence microscopy, in 2P-STED microscopy fluorophores are used to label and visualize biological structures of interest. 2P excitation of the fluorophores moves the fluorescent molecules from their ground state (S_0) to their excited state (S_1). The fluorescence signal originates from the subsequent return of the excited molecules to their

ground state, while emitting a red-shifted photon (see Figure 1A). 2P excitation with femtosecond pulsed lasers allows for deeper penetration into the sample and reduces photo toxicity and photo bleaching because the fluorescence generation from the non-linear 2P absorption is restricted to the focal spot only. Since the amount of time molecules spend in their excited state is very short, using pulsed multi-photon excitation and pulsed single-photon depletion has the advantage of more efficient quenching of the fluorescent signal. In STED microscopy, the molecules are forced back to the ground state before spontaneous emission can occur. This is achieved via so called stimulated emission using, a laser which has a longer wavelength than the excitation laser (STED laser, see Figure 1A). The red-shifted STED light can be separated from the fluorescence signal by standard optical filters and dichroic mirrors. Therefore, the little direct excitation of the fluorophore, whose excitation spectrum is far away from the STED wavelength, does not contribute to the collected emitted fluorescence signal.

The goal of the STED approach is to improve the spatial resolution of the microscope by decreasing the size of its point-spread function (PSF). The minimal distance between two point sources of light that can still be resolved by conventional light microscopy is classically given by Abbe's formula (Abbe, 1873):

$$\Delta r = \frac{\lambda}{2 \times NA},$$

where λ is the wavelength of the excitation light and NA the numerical aperture of the objective. The size of the PSF can be reduced by spatially constricting the fluorescence signal, which is accomplished by superimposing the red-shifted STED beam on top of the excitation laser (see Figure 1A). The STED beam is doughnut-shaped with zero light intensity in the center, which makes it possible to quench the fluorescence everywhere except for the center. This leads to a greatly diminished size of the resulting fluorescent spot. The effective size, which was spared from the quenching effect by the STED light, correlates with the intensity

of the STED doughnut beam. As a result the minimal resolvable distance between two fluorescent objects is described by the following modified formula:

$$\Delta r = \frac{\lambda}{2 \times NA \times \sqrt{1 + I_{STED}/I_S}},$$

where I_{STED} is the intensity of the STED laser and I_S the intensity at which half of the molecules are quenched (Harke et al., 2008).

1.2. Overview of the application of STED microscopy in neuroscience

The theory of STED was first proposed in 1994 by Stefan Hell (Hell and Wichmann, 1994) and the proof of principle followed in 2000 (Klar et al., 2000), which brought him the shared Nobel Prize in Chemistry in 2014. Initially, STED microscopy has been applied to neuroscience research in a series of immuno-histochemical studies examining the nanoscale distribution of synaptic proteins in fixed neuronal cell cultures (Kittel et al., 2006; Sieber et al., 2006; Willig et al., 2006). First works in living cultured brain slices highlighting the dynamics of synaptic vesicles in nerve terminals and the fine morphological changes of dendritic spines (Nägerl et al., 2008; Westphal et al., 2008) helped the STED approach to gain momentum in its application to living tissues preparation. Nowadays, STED microscopy has already been successfully extended to thick tissue preparations such as acute slices and *in vivo* preparations (Urban et al., 2011; Berning et al., 2012) in single and dual-color (Tønnesen et al., 2011). Importantly, the STED approach can be readily combined with other opto-physiological techniques, such as patch-clamp electrophysiology paired with 2P glutamate uncaging, and fluorescent recovery after photobleaching (FRAP) (Tønnesen et al., 2014). Notably, the combined use of those techniques allowed the discovery of the plasticity of the dendritic spine neck and its role in the electrical and biochemical compartmentalization of synapses (Tønnesen et al., 2014). The recent synergistic combination of 2P excitation and

super-resolution STED microscopy in an upright system (Bethge et al., 2013) permits the conception of super-resolution acute brain slices and *in vivo* imaging experiments.

In this protocol, we will first share a summary of the optical components needed to establish a 2P-STED system, and describe the optical architecture of our homebuilt microscope. We will then provide the reader with a detailed guide for daily aligning routines which are generally applicable for custom-built or purchased microscopy setups and include how to practically handle and optimize the microscope for imaging deep inside living brain tissue. Finally, we highlight possible applications of this super-resolution imaging method by sharing image acquisitions of dendritic spines and microglial processes in intact brain tissue *in vivo*, both in single and dual color.

2. Materials:

In the following we list the main components and tools needed for a 2P-STED microscope and imaging experiments in living brain tissue.

2.1. Microscope equipment

1. Pulsed laser light sources
    - 2P excitation: 2P laser tuned to 910 nm at 80 MHz (Millennia eV combined with a Tsunami, SpectraPhysics)
    - STED depletion: 2P laser (Chameleon, Coherent) tuned to 834 nm which is converted by an optical parametric oscillator (OPO, APE) to obtain light at 598 nm at 80 MHz
2. Microscope base and objective
    - Modular research-grade upright microscope (e.g. Olympus BX-51WI)
    - Motorized sample stage (e.g. 380FM, Luigs & Neumann)

- High NA water-dipping objective with correction collar (e.g. Olympus LUMFI 60x, NA 1.1, working distance 1.5 mm)

3. Optical elements
    - Pulse stretching:
        - SF 6 glass rod, 12 cm, to stretch femtosecond STED pulses to ~1 ps.
        - 20 m long polarization-maintaining single-mode fiber to stretch the STED pulses to ~70 ps (Pure silica core, NA 0.12, Schäfter & Kirchhoff)
        - fiber coupler (Schäfter & Kirchhoff)
    - Light modulation:
        - Electrical Optical Modulator, Pockels cell (e.g. Conoptics)
        - 2π delay vortex phase mask (RPC Photonics)
        - λ/2-wave plate and λ/4-wave plate (e.g. Qioptiq)
    - Beam expansion and scanning:
        - lenses (e.g. Qioptiq): STED beam collimation after the fiber with a f = 40 mm convex lens; emitted fluorescence is focused with f = 300 mm convex lenses
        - telescopes for beam expansion: 2P beam expansion = 1:2 (f = 75 mm concave and f = 150 mm convex), Scan- and Tubelens combination with beam expansion = 1:5 (f = 40 mm convex and f = 200 mm convex)
        - Telecentric beam scanner for x,y plane with beam expansion = 2:1 due to the combination of a spherical mirror and two galvo-mirrors (Yanus IV digital scan head, Till Photonics)

        - Piezo-driven objective positioner for z-scans (P-725, Physik Instrumente)
    - Mirrors adapted to the light in the respective beam path: di-electric visual (STED), 2-photon (2P), silver (combined 2P, STED, and emitted fluorescence)
    - Pellicle beam splitter (55% / 45%, Thorlabs)
    - Dichroic mirrors and filters
        - Band-pass filter (593/40, F37-593, AHF Analysentechnik)
        - Short-pass dichroic (700/10, T700dcspxruv, AHF Analysentechnik)
        - Long-pass dichroic (580/10, 580dcxru, AHF Analysentechnik)
        - Short-pass filter (680, FF01-680/SP-25, Semrock)
        - Single Notch filter (594, NF02-594S-25, Semrock)
        - Emission band-filter (520/70, FF01-520/70-25, Semrock)
        - Long-pass dichroic (514, LP02-514RS-25, Semrock)
    - 2x Ø 62.5 µm multi-mode fiber
    - Detectors:
        - Photodiode (3932 BSM, SpectraPhysics) with a detection range from 400 – 1100 nm to capture STED light and allow for synchronization with 2P light.
        - PMT (Photosensor modules H10722 series, Hamamatsu Photonics K.K.) with a detection range suited for STED and 2P wavelengths to visualize reflections of gold beads.
        - 2x APDs (SPCM-AQR-13, PerkinElmer) with a detection range from 400 - 1060 nm to visualize emitted fluorescent signals.

4. Opto-mechanical components

- Optical mounts, post assemblies, optical rails and other helpful standard optical equipment (e.g. from Thorlabs, Newport and Qioptiq)
- 2x motorized mirror mounts for high-precision beam walking of the STED and 2P beams (Newport)

5. Additional hardware / tools
    - Phase-lock-loop for synchronization of the laser pulses (SpectraPhysics, Model3930 Lok-to-Clock)
    - Nanosphere samples immobilized on regular microscopy glass slides (150 nm gold, 40 nm and 170 nm fluorescent nanospheres)
    - High milli-molar sea of fluorescence (e.g. 10 mM calcein or fluorescein dissolved in distilled H_2O)
    - Power meters with sensitivity ranging from microwatts to 3 watts
6. Software
    - ImageJ
    - Imspector
    - Agilis
    - SpectraSuite

2.2. Sample preparation

1. Acute brain slices
    - Mice: Thy1H$^{+/eYFP}$ and Thy1H$^{+/eYFP}$ x Cx3Cr1$^{+/eGFP}$
    - Preparation of sagittal brain slices (350 µm thick) cut on a vibratome (e.g. Leica VT1200S)
    - Acute slice maintenance:
        - Slicing solutions

        - Carbogenated ACSF containing (in mM): 124 NaCl, 3 KCl, 26 $NaHCO_3$, 1.25 NaH_2PO_4, 10 glucose, 2 $CaCl_2$ and 1 $MgCl_2$ (pH 7.4, osmolarity ~305 mOsm/L). Perfusion (3 - 4 ml/min) and heated chamber (32 - 33 °C)
    - Dissection tools
    - Stage for acute slices and electrophysiology (Motorized sample stage (e.g. 380FM, Luigs & Neumann))
2. *In vivo* preparation
    - Mice: $Thy1H^{+/eYFP}$
    - Maintenance of health of mice
        - Anaesthetics:
            - Lidocaine 2% (Lurocaïne®) / Lidocaïne 2% (Xylocaïne®)
            - Isoflurane 4% and 1.5%
        - Analgetics:
            - Buprecare 10 times dilutated in PBS, 100uL per 30gr mouse
        - Other drugs:
            - Dexamethasone sodium phosphate, 20uL at 4mg/mL
            - Ocry-gel
        - Solutions:
            - Cortex buffer consisting of (in mM): 123 NaCl, 5 KCl, 10 glucose, 10 Hepes, 2 $CaCl_2$, and 2 $MgSO_4$
    - Surgery tools
    - Head-holder, *in vivo* platform and stage (customized from Luigs & Neumann)

3. Methods:

3.1. Step-by-step procedure for working with a 2P-STED microscope

The quality of the super-resolution images is dependent on stringent specifications of the optical elements and hardware in the first place, and secondly on highly accurate alignment and coupling of the lasers beams (in x, y, z and t) and detectors. We have described the conception and building of a 2P-STED microscope from scratch previously (Bethge and Nägerl, 2014).

3.1.1. Description of the laser beam paths

The 2P beam clears an electrical optical modulator (EOM, e.g. a pockels cell) which enables a quick and convenient power modulation of the 2P light (see Figure 1B). The 2P beam diameter is expanded with a telescope by a factor 2 to sufficiently overfill the back aperture of the objective. By slightly de-collimating the beam with the telescope, the z-focus of the 2P beam can be adjusted to coincide with the STED doughnut in the focal plane. In order to increase the depletion efficiency, the polarization of the 2P beam can be adjusted to the polarization of the STED beam by using a λ/2-wave plate. Eventually, the 2P beam is combined with the STED beam path via a dichroic mirror.

The STED light pulses are stretched in time by sending them through a 12 cm long SF6 glass rod before passing through an EOM, which allows for rapid power modulation (see Figure 1B). Subsequently, the beam is coupled into a 20 m long polarization maintaining single-mode optical fiber to obtain a pulse length of ~70 ps. After the fiber the re-collimated beam acquires its characteristic doughnut shape by clearing a helical 2π phase mask. The shape of the doughnut is fine-tuned by adjusting a λ/2-wave and λ/4-wave plate. Specifically, they serve to modify the circular polarization of the STED beam (see Notes). The STED and 2P beam are combined by a short-pass dichroic mirror. The focus of both beams is moved over

the sample in all three dimensions by the telecentric x,y scanner and the piezo z-positioner for image acquisition. De-scanned emitted fluorescence is sent via a long-pass dichroic mirror towards the detectors. The emitted fluorescence of two green fluorophores, such as GFP and YFP, can be spectrally separated via a dichroic mirror and is eventually focused into optical multi-mode fibers coupled to avalanche photodiodes (APDs).

3.1.2. Preparation of the microscope

1. Determine the laser power of the STED and 2P light and calibrate the transmission through the Pockels cells by maximizing their transmission. A correct alignment of the Pockels cell can be evaluated by the transmission and extinction ratio, which should be >90% and >1000x , respectively.
2. Verify regularly that the laser beams are centered on the mirrors and optical elements. The installation of pinholes will facilitate the assessment of beam misalignment and its correction (see also Notes). Superior long-term alignment stability can be achieved by the elimination of unequally distributed heat sources.
3. Coupling of the STED beam into the single-mode optical fiber (see also Notes): At low laser power, ensure that at least 50% of the light is transmitted. If necessary, align the beam (“beam walking”) until maximal transmission of the light is reached (> 65%).
4. STED doughnut design and optimization: A homogeneous shape in three dimensions (x, y and z) and a deep intensity minimum at the center (the “null”) are crucial for obtaining a high gain in resolution and signal-to-noise ratio. The doughnut is visualized by illuminating with minimum STED light intensity 150 nm gold nanospheres immobilized on a glass slide. The evoked reflection is sent via a pellicle beam splitter to a photon multiplier tube (PMT) (see Figure 2B). A

homogeneous doughnut with a tight and low-intensity null can be created by adjusting the wavefront shaping optical elements. First, rotation of the quarter-wave plate serves to improve the symmetry and thus diameter of the anticipated intensity null. Second, repositioning of the helical phase mask will adjust the position of the null. Third, optimization of the quality of the null can be obtained by rotating the half-wave plate. Preferably, the null will have a maximum intensity of less than 1% of the signal on the rim of the doughnut. Fourth, the correction collar on the water-immersion objective should be adapted for an optimal z-profile. By repositioning a subset of lenses inside the objective, the correction collar will adjust for spherical aberrations, which will be seen in the reflected signals as a tighter and more symmetrical z-profile. All elements should be iteratively re-visited until the optimal doughnut shape has been reached in x, y, and z (see Figure 2A).

5. Co-alignment of the 2P and STED beam: Utilizing the reflection of the illuminated gold bead sample using minimum laser powers, verify that the 2P and the STED beam overlap in x, y, and z. If this is not the case, we suggest to move the 2P beam using a motorized mirror external to the common beam path (see Figure 5). The telescope in the 2P beam path can serve to overcome misalignment in z by slight de-collimation (see Figure 2A).
6. Detector alignment: The emitted fluorescence is de-scanned and spectrally detected in two APDs. For two-channel detector alignment, a highly concentrated sea of fluorescence is used (e.g. 10 mM calcein or fluorescein). Note, while using a water-dipping lens, the objective is directly immersed into the sea, which needs to be properly rinsed afterwards. Performing x, y scans in a large field of view (e.g. 100 x 100 µm), it can be assessed by visual inspection whether the signals are

centered on both detection channels (see Figure 2C). If both channels are not well aligned, the emission beam can be moved with the last common mirror in the detection beam path. Ultimately, both YFP and GFP signals are centered in their respective channels by moving the beam with the respective mirrors in front of the multimode fibers connected to the APDs. To verify that both channels are superimposed, we directly overlay the channels in Imspector and double check by exporting and overlaying the two images in ImageJ (see Figure 2C).

7. Test of the quenching efficacy of the STED doughnut: While performing rapid z-scans on the interface of the sea of fluorescence and the glass slide, we evaluate whether the efficacy of the STED doughnut to quench the 2P excitation-derived emitted fluorescence is sufficient (> 60%). Applied laser powers should be similar to the acquisition parameters in the biological sample. At this stage the co-alignment of the detectors in the z-dimension can be verified by exciting the sea of fluorescence with the 2P beam. An offset of the position of the edge of the interface between fluorophore and glass slide between both channels is rectified by adjusting the distance of the collection lens in front of the multimode fibers. The time-delay system (Lok-to-Clock, SpectraPhysics) phase-locks the 2P and STED beam and is as such used to synchronize the two beams in time. The use of a rough (12 ns) and fine (2 ns) delay allows to overlap the 2P and STED pulses in time in order to reach the most optimal quenching effect (quenching of 60 - 80% of the original fluorescent signal) (see Figure 2D). Low quenching efficiency can be improved by adjusting the time delay between the pulses from the two 2P and STED laser. Furthermore, it is important to optimize the relative intensities of the excitation and STED beams. While too little STED power will not efficiently quench the 2P light, too much STED power can produce direct excitation of the

fluorophores, thereby reducing the effective quenching capacity as well. If both of these adaptations do not allow for sufficient fluorescent quenching by the STED beam, we recommend going back to the doughnut design on the gold beads. Low quenching efficacy can originate from a bad quality doughnut and/or that the 2P and STED beam are imperfectly superimposed.

8. Evaluation of the spatial resolution achieved by 2P-STED imaging using fluorescent nanospheres: First, while imaging 170 nm fluorescent beads in a small field of view (FOV, 10 x 10 µm) with both the 2P and STED beam , we can test whether the two beams are well co-aligned. Small corrections can be carried out by using the two respective motorized mirrors in the 2P and STED beam path. Z-scans of single beads allow for validation of the co-alignment of the detectors in the z-dimension (see Figure 2F). Possibly one needs to re-adapt the correction collar here again, to correct for spherical aberrations at the different depths. As a result of all optimizations, the beads should be resolved at approximately 170 nm (measured by full-width half max (FWHM)) and the peak of the intensity should be centered (see Figure 2E).

   To evaluate the level of sub-diffraction resolution, we recommend using 40 nm fluorescent nanospheres and image them with a 20 nm pixel size. They are about ten times smaller than the resolution limit of regular 2P microscopy, yet still fairly bright and produce robust signals with sufficient signal-to-noise ratio. The same beads are imaged by 2P and 2P-STED light and line profiles with their FWHM measurements are used to quantitatively assess the PSF. This resolution enhancement can be ameliorated by finding the optimal power ratio between the 2P and STED light as mentioned before (see 7). Using our 2P-STED microscope, we achieve a lateral resolution of 60 - 90 nm (see Figure 2G).

3.2. Sample preparation

The presented 2P-STED setup can accommodate the imaging of living brain tissue, both in acute slice preparations as well as the intact brain using a cranial window. Below we shortly describe how to prepare the different samples for imaging.

3.2.1. Acute brain slice preparation

Acute sagittal brain slices are prepared from P25 - P35 aged Thy1H$^{+/YFP}$ or Thy1H$^{+/YFP}$ x Cx3Cr1$^{+/eGFP}$ mice. In both transgenic mice a subset of pyramidal neurons is labelled with YFP while in the latter in addition all microglia are labelled with GFP. Microglia are the resident immune cells of the brain and are sensitive to damage originating from the acute slicing procedure. Therefore, outmost care has to be taken during the preparation. Slices are prepared as described previously (Pfeiffer et al., 2016). In brief, after the slicing procedure slices are kept in carbogenated (95% O_2 and 5% CO_2) artificial cerebrospinal fluid (aCSF) until use. Experiments are to be performed in a submerged recording chamber at 33 °C with continuous perfusion of carbogenated aCSF (3 - 4 ml/min).

3.2.2. Preparation for in vivo brain imaging

Standard procedures for *in vivo* brain imaging include thinned skull preparations, the implementation of a cranial (glass) window, or an open skull preparation. We utilize a cranial window (see Figure 3A) in P55 – P75 aged Thy1H$^{+/YFP}$ male mice, which allows for keeping the cranial pressure constant, thereby reducing significantly the chance of movement artifacts of the brain compared to other preparations. The window is based on a 170 µm thick glass coverslip which also permits easier and more reproducible light penetration of 2P and STED light to structures deeper in the brain than in a thinned skull preparation. Mice are chosen in this age-range based on their skull thickness and therefore ease of surgery. In this age range

the skull is thin enough to easily penetrate it with the drill, but at the same thick enough to not easily break it and, thereby possibly damaging the underlying cortical tissue.

In general, any type of mouse which expresses a fluorophore can be used for *in vivo* experiments with conventional light microscopy. For 2P-STED imaging we strongly recommend relying on a bright, photostable, and sparsely expressed fluorescent label. The Thy1H$^{+/YFP}$ mouse line (Feng et al., 2000), which trans-genetically targets a subset of pyramidal neurons with YFP, fulfills this prerequisites and is, thus, a suitable label for volume-metric STED imaging.

The freely diffusible YFP-label (YFP) can be easily replenished from the cytosolic pool and allows in our hands the use of laser intensities sufficiently high to obtain super-resolution images of neuronal morphologies, and at the same time suffering only little from photo bleaching and photo toxicity.

Next to the importance of choosing a suitable label, successful *in vivo* experiments are greatly dependent on the mechanical stability of the sample. A headholder, which is glued to the brain via a helmet-like structure allows for the fixation of the mouse to the microscopy platform and ultimately for the physical stabilization of the skull. In addition, the sample stability and eventually the quality of the acquired images can be optimized by considering the following parameters. First, the head of the mouse is turned in such a way that breathing is not obstructed, but the region of interest can still be easily accessed by the objective. Second, the body posture of the mice is adjusted so that the lungs can easily expand while breathing, while the front paws are still resting on the heating pad for a stable body posture. The anesthesia mask should cover the nostrils of the mice and anesthesia is set to oxygen supply at 0.6 L/min and ~1.5 % isoflurane. At these rates the breathing of the mouse is calm and abdominal, thereby reducing vibrations of the brain compared to diaphragmatic breathing. Having

established a stable and optically accessible cranial window, one can visualize neural dendrites, spines, and glial processes (see Figure 3B).

3.3. Super-resolution image acquisition

For STED imaging experiments the sample quality is of outmost importance. Layers of damaged cells on the surface and non-healthy brain tissue introduce background fluorescence and can be excited by the high-intensity STED light. In general, laser intensities, field of view (FOV), pixel size and dwell time are dependent on the goal of the experiment, depth in the tissue, label intensity of the structure of interest and whether single images or time-lapse experiments are envisaged. For the imaging of dendritic spines we choose FOVs located at least 20 and up to 80-90 μm below the surface of the brain slice and the *in vivo* brain preparation. Imaging of spine-microglia interaction was performed at least 50 μm below the slice surface, where microglia are less likely to be affected by the slicing procedure. Employing 2P-STED microscopy enables the observation of dynamic microglia-spine interactions at the nanoscale (see Figure 3G). Slice health and more moderate laser powers (2P and STED) are key for succeeding in these super-resolution time-lapse experiments.

For *in vivo* image acquisition, the breathing pattern of the mouse (1 Hz) and blood pulsations (5 – 7.5 Hz) degrade the image quality. Beyond doubt, motion artifacts are a serious limitation for obtaining nanoscale resolution images. Here, the requirements for mechanical stability are much more stringent than for structures investigated by regular 2P microscopy. To suppress the effects of motion artifacts, the region of interest should be far from major blood vessels and the acquisition parameters (pixel size and dwell time) need to be revisited regularly dependent on the conditions. By continuously controlling and adapting the anesthesia settings a stable breathing pattern can be ensured. Scanning faster, i.e. the reduction of the FOV and/or the pixel dwell time, will allow for a reduced negative impact of the before-mentioned

vibrational sources. However, by scanning faster higher 2P and STED laser intensities might be necessary. The needed power depends both on the intensity and the stability of the label; on the imaging depth and whether the sample is an acute brain slices or the intact mouse brain. Typically, they range between ~5 - 20 mW (2P) and ~15 - 30 mW (STED) (measured at the back aperture of the objective). Image stacks are acquired with voxel sizes between 20 x 20 x 500 nm and 40 x 40 x 1000 nm (x, y, and z) and pixel dwell times vary between 10 - 50 µs. Time-lapse imaging can be performed at a temporal resolution of 5 - 10 min for 1.5 hours. We advise to acquire small stacks of 3 µm for *in vivo* acquisitions in order to be able to compare frames in the same focal plane in case breathing artifacts changed the focus while imaging.

3.4. Super-resolution images and image analysis in live tissue

Acquired 2P-STED images of dendritic stretches and spines are exported as 16-bit tiff files from the IMSpector software to NIH ImageJ. For illustration purposes, brightness and contrast can be adjusted and a 1 pixel median filter applied to improve image quality. Z-image stacks can be visualized in maximal intensity projections (see Figure 3B and D). For the visualization of time-lapse acquisitions (see Figure 3C, E, F and G), we use the ImageJ plugin StackReg to correct for lateral drift of the image sections.

To quantify the nanoscale morphology of dendritic spines (over time) it is possible to measure the full width at half maximum (FWHM) of spine neck width (see Figure 4B), which is done on raw data of single z-sections. To automatically measure FWHM a custom made ImageJ plugin was used (courtesy of Florian Levet). At multiple positions on the spine neck, the plugin automatically estimates the best orthogonal fit and plots the intensity profile. Having multiple parallel lines helps to reduce the noise coming from single measurements and the

acquisition. The FWHM value can then be extracted from the non-linear Gaussian fits of the intensity profiles (see Figure 4A).

4. Notes

1. Backward-forward alignment is a procedure necessary for first setting up a STED microscope, but it is also regularly carried out to maintain a good performance of the system. To this end, a collimated beam from a 600 nm light source and an additional optical multimode fiber are used. The beam, which is coupled in the fiber, is sent backward through the beam path by clearing centrally the objective, the scanner, and the detection and excitation beam paths. Ultimately, the backward propagating beam has to be aligned into the 20 m polarization-maintaining single-mode fiber. The two pinholes to be installed before the scanner in the common beam path are positioned accordingly (see Figure 5A). They will serve as a reference for the forward alignment and all minor daily alignment routines. Subsequently the STED beam will be aligned forward to the reference pinholes (see Figure 5B). The backward-forward alignment is repeated until both beams clear the pinholes and couple into the optical fibers. At this stage, the 2P beam is superimposed on the STED beam path. Subsequently, the overlap of the 2P and the STED beam is ensured on a large distance before to continue the regular beam alignment (see preparation of the microscope).
2. In order to facilitate alignment procedures, we recommend inserting pinholes at strategic positions of the common (see Figure 5A) and external beam paths. This allows verifying whether the laser beams are still aligned to the centers of the optical elements and, more importantly in the common beam path, whether the 2P and STED beam are still co-aligned. By iterative beam walking perfect clearing of the pinholes can be achieved (see Figure 5A and B). Replacing the objective by a fluorescing

alignment target makes it possible to check whether the co-alignment of the two beams on the pinholes holds true until reaching the sample (see Figure 5C).

3. Fiber-coupling can be facilitated by using a power meter suitable for the pulsed STED beam in order to measure the input power and the amount of transmitted light. In order to couple the light properly into the fiber, as well as in order to align to pinholes, one should walk the beam. More specifically, two different mirrors are used to move the beam in x- and y-direction, without introducing an angle to the beam path. The two mirrors are a chosen close and far mirror with respect to the fiber (or any other optical element ones wishes to align to).
4. In 2P-STED microscopy, the efficiency of the STED effect can be optimized by taking into account the polarization and circularity of light. The circularity of light is achieved by the insertion of a rotatable λ/4-wave plate into the beam path. The circularity can be read out via the combined used of a motorized polarizer and an oscilloscope. In case of perfect circularity, a flat line will appear on the oscilloscope, since all polarization directions are equally represented. If this is not the case, you will obtain a sine-wave, which indicates insufficient beam circularity. As some polarizations are easier to transform than others, adapting the polarization in the STED path with the λ/2-wave plate, will help to obtain optimal circularity. The circular polarization is mainly of importance for the doughnut-shaped STED beam, since it is needed to achieve a deep null and thus perfect destructive interference for the marginal rays coming in at shallow angles in the high NA objective.

References

Abbe E (1873) Beitraege zur Theorie des Mikroskops und der mikroskopischen Wahrnehmung.

Becker N, Wierenga CJ, Fonseca R, Bonhoeffer T, Nägerl UV (2008) LTD induction causes morphological changes of presynaptic boutons and reduces their contacts with spines. Neuron 60:590–597.

Berning S, Willig KI, Steffens H, Dibaj P, Hell SW (2012) Nanoscopy in a living mouse brain. Science 335:551.

Bethge P, Chéreau R, Avignone E, Marsicano G, Nägerl UV (2013) Two-Photon Excitation STED Microscopy in Two Colors in Acute Brain Slices. Biophys J 104:778–785.

Bethge P, Nägerl UV (2014) Two-photon STED microscopy for imaging synapses and glia in acute brain slices. In: Nanoscale imaging of Synapses.

Denk, Delaney KR, Gelperin A, Kleinfeld D, Strowbridge BW, Tank DW, Yuste R (1994) Anatomical and functional imaging of neurons using 2-photon laser scanning microscopy. J Neurosci Methods:151–162.

Denk, Strickler, Webb (1990) Two-photon laser scanning fluorescence microscopy. Science (80-) 248:73–76.

Engert F, Bonhoeffer T (1999) Dendritic spine changes associated with hippocampal long-term synaptic plasticity. Nature 399:66–70.

Feng G, Mellor RH, Bernstein M, Keller-Peck C, Nguyen QT, Wallace M, Nerbonne JM, Lichtman JW, Sanes JR (2000) Imaging Neuronal Subsets in Transgenic Mice Expressing Multiple Spectral Variants of GFP. Neuron 28:41–51.

Harke B, Keller J, Ullal CK, Westphal V, Schönle A, Hell SW (2008) Resolution scaling in STED microscopy. Opt Express 16:4154.

Hell SW, Wichmann J (1994) Breaking the diffraction resolution limit by stimulated emission: stimulated-emission-depletion fluorescence microscopy. Opt Lett 19:780.

Kittel RJ, Wichmann C, Rasse TM, Fouquet W, Schmidt M, Schmid A, Wagh D a, Pawlu C, Kellner RR, Willig KI, Hell SW, Buchner E, Heckmann M, Sigrist SJ (2006) Bruchpilot promotes active zone assembly, Ca2+ channel clustering and Vesicle Release. Science (80-) 312:1051–1054.

Klar T a., Jakobs S, Dyba M, Egner A, Hell SW (2000) Fluorescence microscopy with diffraction resolution barrier broken by stimulated emission. Proc Natl Acad Sci 97:8206–8210.

Matsuzaki M, Honkura N, Ellis-Davies GC, Kasai H (2004) Structural basis of long-term potentiation in single dendritic spines. Nature 429.

Nägerl UV, Willig KI, Hein B, Hell SW, Bonhoeffer T (2008) Live-cell imaging of dendritic spines by STED microscopy. Proc Natl Acad Sci U S A 105:18982–18987.

Pfeiffer T, Avignone E, Nägerl UV (2016) Induction of hippocampal long-term potentiation increases the morphological dynamics of microglial processes and prolongs their

contacts with dendritic spines. Sci Rep 6:32422.

Sieber JJ, Willig KI, Heintzmann R, Hell SW, Lang T (2006) The SNARE motif is essential for the formation of syntaxin clusters in the plasma membrane. Biophys J 90:2843–2851.

Tønnesen J, Katona G, Rózsa B, Nägerl UV (2014) Spine neck plasticity regulates compartmentalization of synapses. Nat Neurosci 17:678–685.

Tønnesen J, Nadrigny F, Willig KI, Wedlich-Söldner R, Nägerl UV (2011) Two-color STED microscopy of living synapses using a single laser-beam pair. Biophys J 101:2545–2552.

Trachtenberg JT, Chen BE, Knott GW, Feng G, Sanes JR, Welker E, Svoboda K (2002) Long-term in vivo imaging of experience-dependent synaptic plasticity in adult cortex. Nature 420:788–794.

Urban NT, Willig KI, Hell SW, Nägerl UV (2011) STED nanoscopy of actin dynamics in synapses deep inside living brain slices. Biophys J 101:1277–1284.

Westphal V, Rizzoli SO, Lauterbach MA, Kamin D, Jahn R, Hell SW (2008) Video-rate far-field optical nanoscopy dissects synaptic vesicle movement. Science 320:246–249.

Willig KI, Rizzoli SO, Westphal V, Jahn R, Hell SW (2006) STED microscopy reveals that synaptotagmin remains clustered after synaptic vesicle exocytosis. Nature 440:935–939.

Figure legends

Figure 1. 2P-STED microscopy: The principle and the setup (A) Simplified Jablonski diagram of the energy transitions of fluorophores during a fluorescence cycle. Spatially and temporally simultaneous absorbance of two photons of the same (long) wavelength excites fluorophores from their ground state (S_0) to their first excited singlet state (S_1). Decay in the vibrational states and further fall back to S_0 allows for spontaneous emission of a photon on the nanosecond timescale. Stimulated emission prevents this transition by forcing the fluorophore back to its ground state and emitting a photon identical to the incident one. The doughnut-shaped STED beam enables the quenching of the fluorescence only in the outer rim of the excitation beam, which effectively enhances the spatial resolution up to 50 – 60 nm. **(B)** Setup schematic of a homebuilt 2P-STED microscope which enables for performing two-color super-resolution imaging of green and yellow emitting probes in living brain tissue. A Titanium:Sapphire (Ti:Sapph) laser tuned to 910 nm at ~80 MHz provides the 2P excitation light, of which the intensity and beam size are adjusted by an electrical optical modulator (EOM) and telescope, respectively. The polarization of the 2P light is modulated by the λ/2-wave plate. The 2P and STED beam are combined by a dichroic mirror (DM 1). The STED beam originates from a Ti:Sapph laser tuned to 834 nm at ~80 MHz pumping an optical parametric oscillator (OPO) to obtain light at 598 nm. The light pulses are stretched by a SF6 glass rod and a 20 meter long polarization-maintaining single-mode fiber to obtain approximately 70 ps pulses. The characteristic doughnut-shaped STED beam is introduced by a helical vortex phase plate and its polarization and circularity can be adjusted by the λ/2-wave plate and λ/4-wave plate. The combined beams are scanned across the sample using a telecentric xy-scanner and a fast nano z-positioner for image acquisition through a water-immersion objective with a numerical aperture (NA) of 1.1 and 60x magnification. De-

scanned detection and spectral separation of the emitted fluorescence is done with a dichroic mirror (DM 2 and 3) and avalanche photodiodes (APDs).

Figure 2. Daily alignment routine and performance of the microscope. (A) Lateral and axial views of reflected point spread functions (PSFs) of gold beads illuminated by 2P and STED light. A symmetric STED doughnut with a zero-intensity center (left). Gold bead illuminated by 2P light showing a Gaussian beam profile (middle). For 2P-STED imaging, it is crucial to perfectly overlap the two beams in x-, y-, and z-dimension (right). **(B)** Gold bead PSF imaging is performed by using a flip pellicle beam splitter (55% / 45% transmission / reflection) to guide the reflected light to a photon multiplier tube (PMT). **(C)** Lateral scans of the sea of fluorescence in a large field of view (FOV) are performed to co-align the two channels. **(D)** The quenching efficiency of the STED beam is assessed by scanning axially the sea of fluorescence at the coverslip interface using the 2P and 2P-STED mode. Exemplary z-scan images show approximately 80% quenching in the 2P-STED mode quantified by the fluorescent signal intensity. **(E)** Two close 170 nm beads can only be resolved using 2P-STED. **(F)** Axial alignment is verified on 170 nm beads. **(G)** Consecutively imaging 40 nm fluorescent beads in 2P and 2P-STED mode allows for the assessment of a substantial gain in resolution in 2P-STED mode. The line profile and the FWHM of the lorentzian fit provide a quantitative measure of the resolution, which is usually around 60 - 80 nm. Scale bars: 500 nm (E, F, and G).

Figure 3. 2P-STED imaging in living brain tissue. (A) Implementation of a cranial window in Thy1H$^{+/YFP}$ transgenic mice (top), crucial positioning of the mouse below the objective (bottom left), and typical view through the cranial window of an operated mouse (bottom

right). **(B)** 2P and 2P-STED image of YFP-labeled dendritic spines in layer 1 of the barrel cortex *in vivo*, showing the resolution improvement when comparing the two modes. **(C)** Nanoscale time-lapse imaging of the morphology of dendritic spines in layer 1 of the barrel cortex *in vivo* at 40 µm depth. **(D)** Super-resolved L5 dendrite and dendritic spines 45 µm deep in an acute brain slice obtained from a Thy1H$^{+/YFP}$ mouse. Maximal intensity projections (MIP). **(E)** Time-lapse imaging of dendritic spines of a L5 apical oblique showing that nanoscale morphological changes can be followed up to 60 minutes in acute brain slices. MIP of three z-planes approximately 30 µm deep. **(F)** Dendritic spines can be followed with a temporal resolution enabling the assessment of their fine morphological dynamics during changes in their synaptic transmission. Single z-plane approximately 35 µm deep in an acute brain slice. **(G)** Two-color 2P-STED time-lapse imaging can be used to dissect the dynamic morphological interactions between microglial processes and dendritic spines in acute brain slices (Thy1H$^{+/YFP}$ x Cx3Cr1$^{+/eGFP}$ mouse). MIP of two z-planes 45 µm deep. All images are taken during basal synaptic transmission. Scale bars: 500 nm (F, G); 1 µm (B, C, D); 2 µm (E).

Figure 4. Analysis of 2P-STED images of dendritic spines in living brain tissue. (A) A custom-made ImageJ plugin facilitates the analysis of distinct morphological parameters. After the definition of a region of interest (ROI), the plugin delivers the outline of the ROI and creates its skeleton. Orthogonal lines are drawn on the skeleton and the spine head outline is fitted with an ellipse. The intensity distribution of the orthogonal lines is plotted and the FWHM is extracted from the Gaussian fit. **(B)** Exemplary image showing the difference in FWHM of different spine neck widths on the same dendritic stretch. Scale bar: 1 µm.

Figure 5. Alignment procedures. (A) Schematic explanation of the backward alignment procedure. A collimated beam from a laser diode is sent backward through the setup. The beam propagates centered through the objective, z-positioner, telecentric scanner, and the STED beam path. Pinholes are inserted based on the backward beam, and serve as reference for the forward beam. **(B)** Forward alignment. The STED beam is aligned to the reference pinholes and propagates centered through all optical elements. Back- and forward-alignment is repeated until the pinholes are perfectly cleared. **(C)** 2P beam alignment. The 2P beam is subsequently co-aligned to the STED beam by utilizing the reference pinholes and a fluorescent target to verify co-alignment holds true until the sample.

- Figure 1-

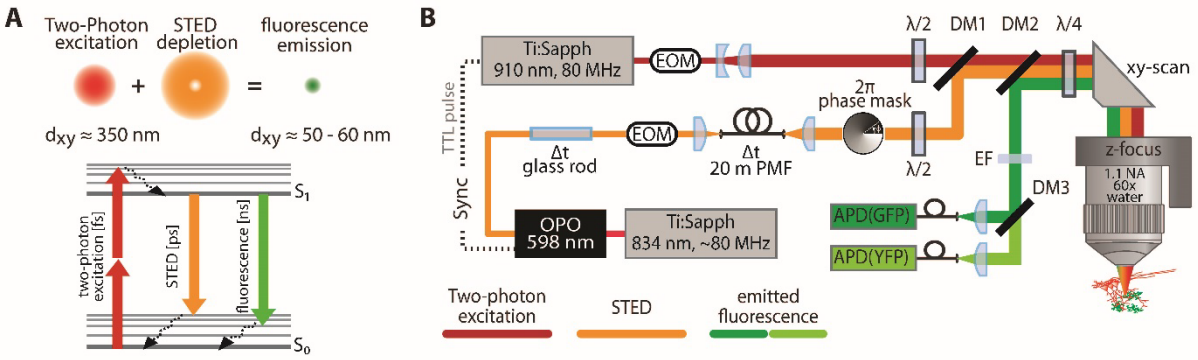

- Figure 2 -

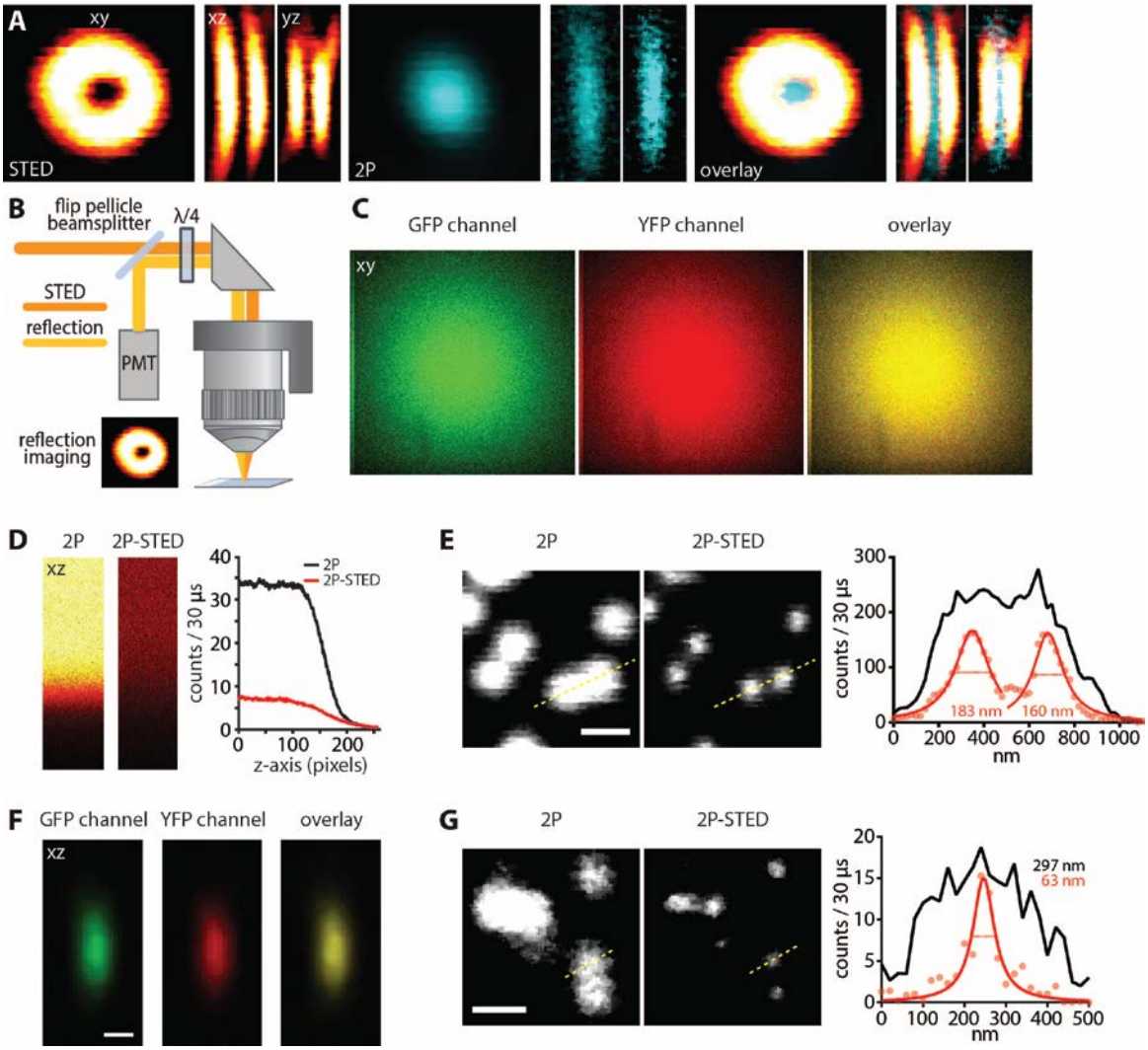

- Figure 3 -

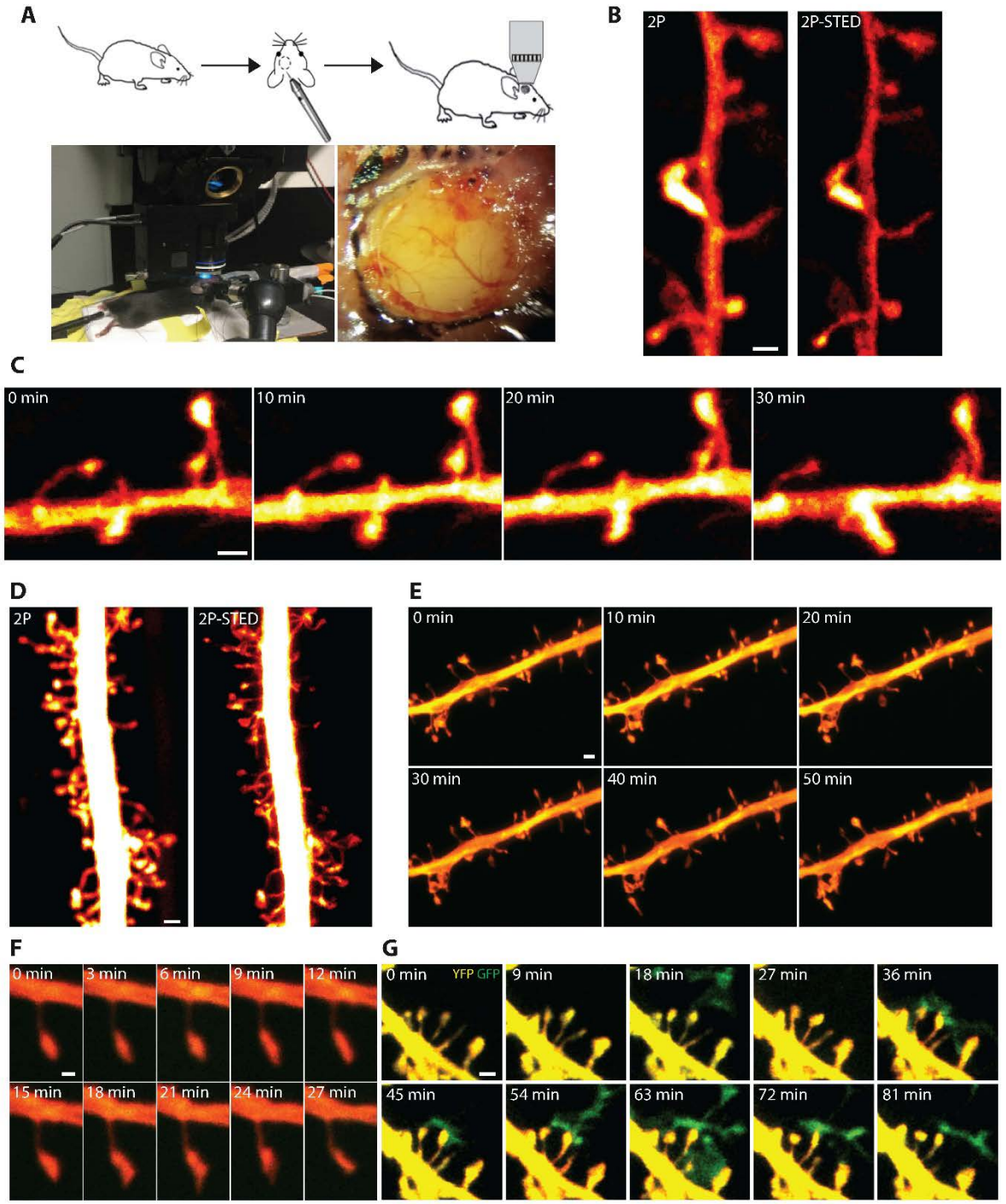
A
B
2P
2P-STED
C
0 min
10 min
20 min
30 min
D
2P
2P-STED
E
0 min
10 min
20 min
30 min
40 min
50 min
F
0 min
3 min
6 min
9 min
12 min
15 min
18 min
21 min
24 min
27 min
G
0 min
YFP GFP
9 min
18 min
27 min
36 min
45 min
54 min
63 min
72 min
81 min

- Figure 4 -

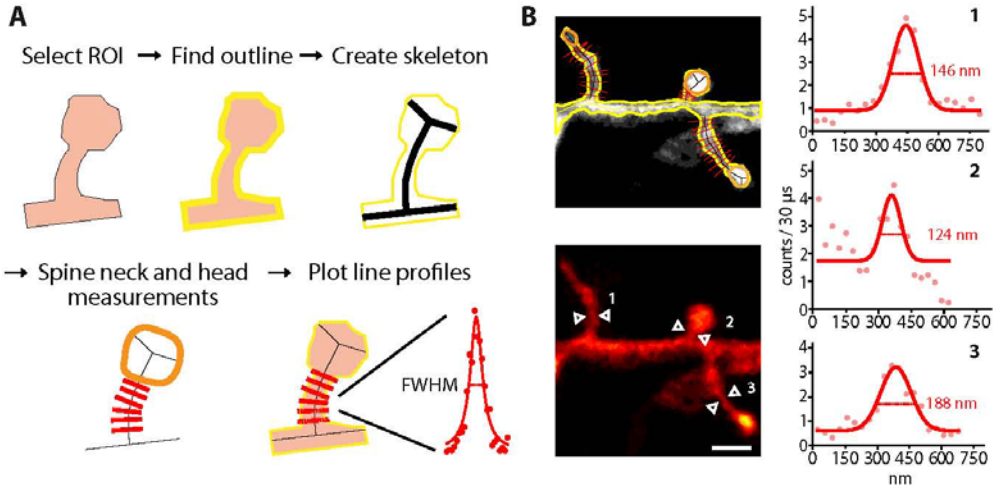

- Figure 5 -

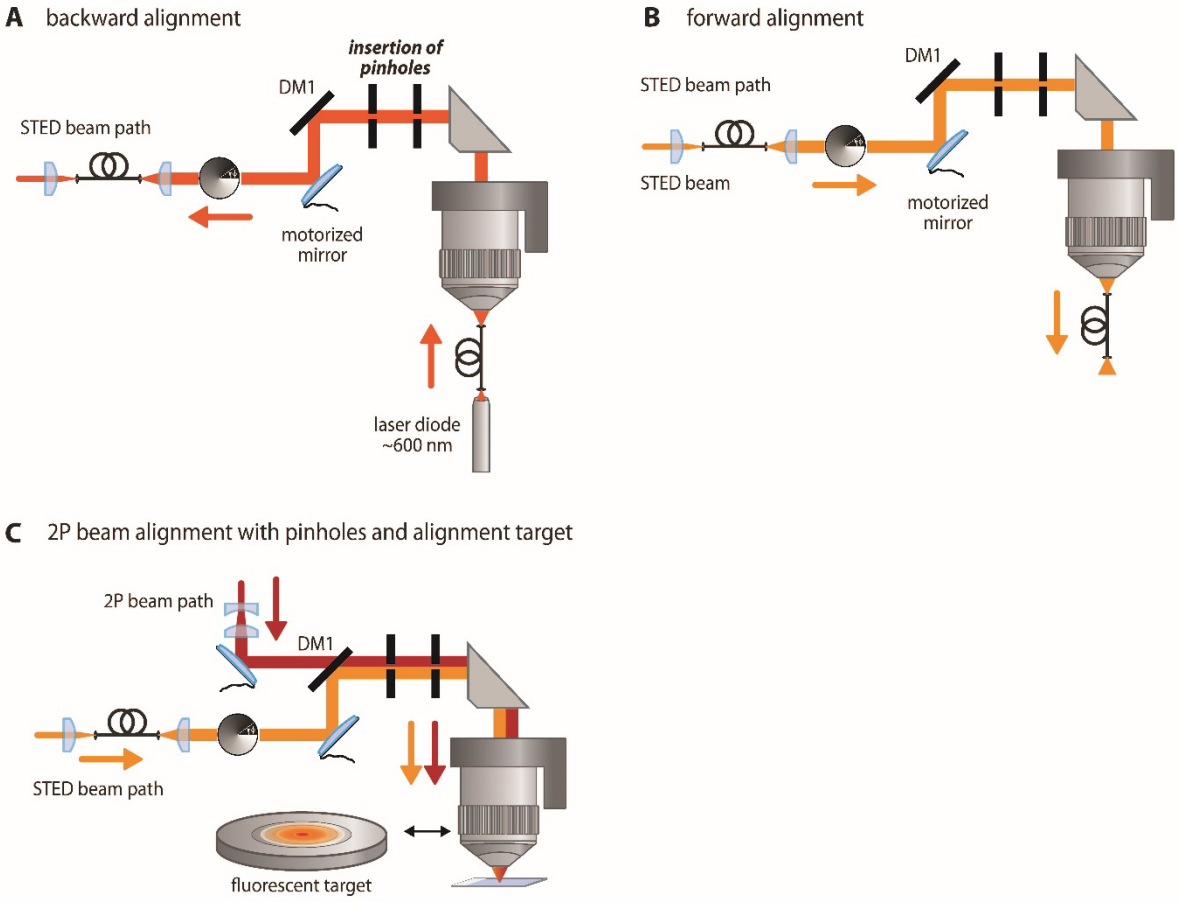

APPENDIX 2 – Time lines of experiments

In order to estimate the amount of time it will take to reproduce those experiments, one can study the time lines I am presenting here. They represent all experiments which were described in this thesis.

2P-STED (timelapse) imaging *in vivo* of dendritic spines w/o astrocytes:

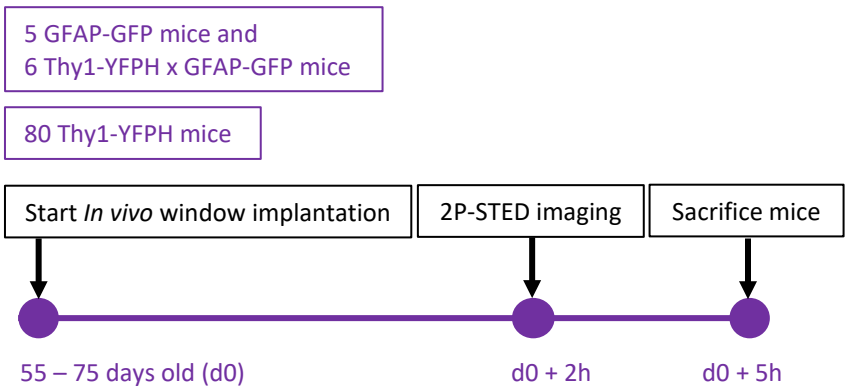

Defining amount of expression virus and 2P-STED (timelapse) imaging *in vivo* of neuron-astrocyte interaction:

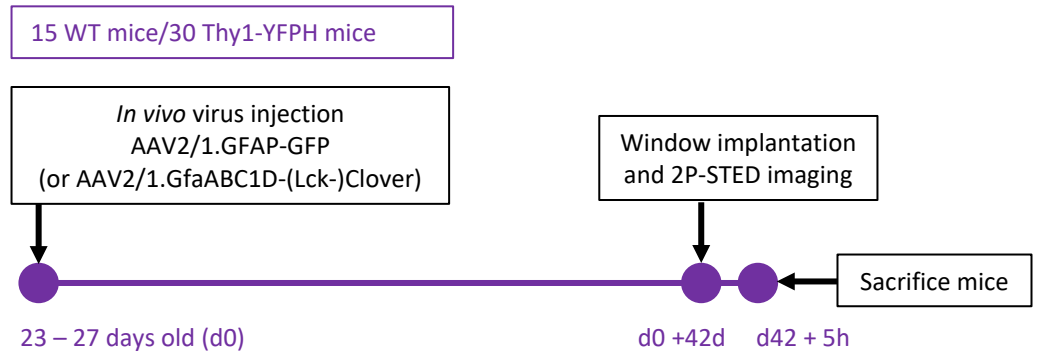

Testing new constructs in astrocytic cultures:

APPENDIX 2 – Time lines of experiments

Testing AAV serotypes in mixed cultures:

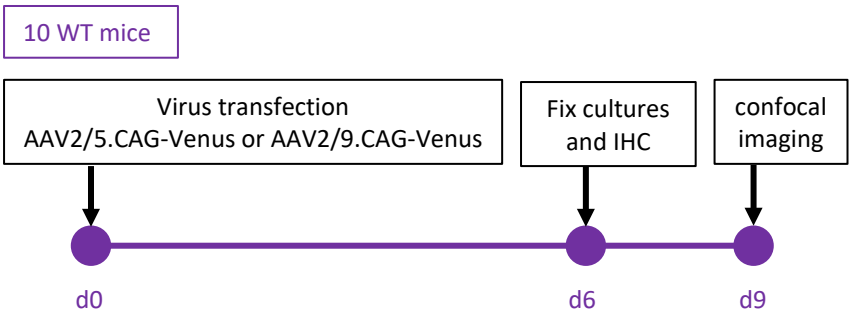

Defining optimal time point of expression virus and reactivity of astrocytes: